Copyright is owned by the Author of the thesis. Permission is given for a copy to be downloaded by an individual for the purpose of research and private study only. The thesis may not be reproduced elsewhere without the permission of the Author.

From Triangles to Rings: Colourful Clusters of Substituted Naphthalenediols

Author:
Tyson DAIS

Supervisor:
Prof. Paul PLIEGER

A thesis submitted in partial fulfillment of the requirements for the degree of

Doctor of Philosophy

in

Chemistry

School of Natural Sciences
Massey University

2022

Declaration of Authorship

I, Tyson DAIS, declare that this thesis titled, “From Triangles to Rings: Colourful Clusters of Substituted Naphthalenediols” and the work presented in it are my own. I confirm that:

- This work was done wholly or mainly while in candidature for the research degree of PhD in Chemistry at Massey University.
- Where I have consulted the published work of others, this is always clearly attributed.
- Where I have quoted from the work of others, the source is always given. With the exception of such quotations, this thesis is entirely my own work.
- I have acknowledged all main sources of help.
- All work presented in this thesis was completed by the author, except:
  - In collaboration with the University of Electro-Communications, Tokyo, Japan, Professor Takayuki Ishida and his students Rina Takano and Yoshiki Yamaguchi collected the magnetic data presented in Chapters 3 – 5. This includes the simulation and curve fitting performed with MAGPACK, and production of the susceptibility and magnetization plots.

Signed: Tyson Dais

Date: 4th of July 2022

"The natural audience size might be less than one on this one"

Bill Gates

Abstract

Coordination chemistry is perhaps one of the most base-level fields within chemistry, with a rich past and an ever expanding future. Existing in a relatively newer niche, however, is the field of single molecule magnetism, sitting at an intersection between synthetic chemistry and chemical physics with an aspiring road leading to materials chemistry and advanced information technology. While the fundamentals of the field are established, it has not yet reached the stage of implementing single molecule magnet technology, for which a broader understanding is needed. A crucial part of this is the ability to interpret magneto-structural correlations, to understand the ways in which molecular structure effects the electronic structure of the metal ions, and hence their performance as single molecule magnets.

A series of new homo- and heterometallic complexes are reported; which, where possible, have been magnetically characterized. A non-macrocyclic triangular complex featuring a planar Cu_3TbO_6 core represents the first of its class to exhibit slow relaxation of magnetization in zero applied field, a characteristic of single molecule magnets, while similar Cu_3Gd, Cu_3Dy, and Ni_3Gd complexes show field supported magnetic properties. The regularity with which the Cu_3Ln and Ni_3Ln complexes crystallize, and the observation of ferromagnetic ground states for each, exemplifies the reliability of the present synthetic strategy to produce potential single molecule magnets. The Co_3Ln complexes presented here were found to have variable cobalt coordination geometries, a subtle effect induced by the size of each lanthanide, with the $\mathbf{Co_3Dy}$ complex being the sole example of purely octahedral cobalt centres. Magnetic measurements of $\mathbf{Co_3La}$ revealed a ground state spin of $S = 3/2$ with a relatively large zero-field splitting parameter, likely associated with the presence of a trigonal bipyramidal cobalt centre.

A number of higher nuclearity complexes are also reported. Four variations of a Ni_{16} molecular wheel have been crystallographically identified, three of which are nearly-isostructural acetate containing polymorphs and the last of which is a formate analogue. One polymorph exhibited a capsule like packing arrangement within its crystal structure, however, attempts to drive the inclusion of a guest molecule were unsuccessful. Synthetic efforts to produce a copper based analogue resulted in the unexpected formation of a Cu_{14} cluster which exhibited the same binding pattern as $\mathbf{Ni_{16}}$. Two manganese containing complexes, $\mathbf{Mn_8}$ and $\mathbf{MnLa_6}$, were also obtained where the former exhibited the relatively uncommon homometallic square-in-square architecture.

Acknowledgements

First, I would like to express my gratitude to my supervisor, Professor Paul Plieger, for his endless support and enthusiasm. While giving me freedom to discover on my own, his knowledge and guidance throughout has been crucial in my PhD journey. I would also like to thank my co-supervisor, Associate Professor Gareth Rowlands, for being a great source of guidance in all areas of academia, but particularly for patiently troubleshooting the organic synthesis woes early in my PhD.

While many people have helped contribute to my research, I am immensely grateful to Emeritus Professor Geoff Jameson for his unending guidance in all aspects of X-ray crystallography and Professor Takayuki Ishida for carrying out magnetic characterization on a number of my compounds. Thanks also to Pat Edwards for assistance with NMR and Dave Lun for HR-MS.

My thanks especially go out to the members of the Plieger and Rowlands groups past, present, and honourary, for their support, advice, and willingness to drink.

Finally, to Hamish, for his support and patience throughout this long journey.

Publication List

Publications relevant to this thesis

- T. N. Dais, R. Takano, T. Ishida and P. G. Plieger. Self-assembly of non-macrocyclic Cu_3Ln clusters. *Dalton Trans.*, 2022, **51**, 1446-1453.
- T. N. Dais, R. Takano, Y. Yamaguchi, T. Ishida and P. G. Plieger. Metallocyclic Cu^{II}–Ln^{III} single-molecule magnets from the self-assembly of 1,4-diformylnaphthalene-2,3-diol. *ACS Omega*, 2022, **7**(*6*), 5537-5546.
- T. N. Dais, R. Takano, T. Ishida and P. G. Plieger. Lanthanide induced variability in localised Co^{II} geometries of four triangular $L_3Co^{II}{}_3Ln^{III}$ complexes. *RSC Advances*, 2022, **12**(*8*), 4828-4835.

Additional publications by author

- J. K. Buchanan, T. N. Dais and P. G. Plieger. Computational studies of the magneto-structural correlations in a manganese dimer with Jahn–Teller distortions. *Phys. Chem. Chem. Phys.*, 2022, **24**, 4407-4414.
- S. S. Woodhouse, J. K. Buchanan, T. N. Dais, E. W. Ainscough, A. M. Brodie, G. H. Freeman and P. G. Plieger. Structural trends in a series of bulky dialkylbiarylphosphane complexes of Cu^I. *Acta Crystallogr. C*, 2021, **77**(*9*), 513-521.
- S. Patel, T. N. Dais, P. G. Plieger and G. J. Rowlands. Breaking paracyclophane: The unexpected formation of non-symmetric disubstituted nitro[2.2]metaparacyclophanes. *Beilstein J. Org. Chem.*, 2021, **17**, 1518-1526.
- D. N. T. De Silva, T. N. Dais, G. B. Jameson, D. J. Cutler, E. K. Brechin, C. G. Davies, G. N. L. Jameson and P. G. Plieger. Synthesis and characterization of symmetrically *versus* unsymmetrically proton-bridged hexa-iron clusters. *ACS Omega*, 2021, **6**(*25*), 1661-16669.
- S. S. Woodhouse, T. N. Dais, E. H. Payne, M. K. Singh, E. K. Brechin and P. G. Plieger. The structural manipulation of a series of Ni_4 defective dicubanes: Synthesis, X-ray structures, magnetic and computational analyses. *Dalton Trans.*, 2021, **50**(*15*), 5318-5326.

- T. N. Dais, D. J. Nixon, P. J. Brothers, W. Henderson and P. G. Plieger. Towards more effective beryllium chelation: an investigation of second-sphere hydrogen bonding. *RSC Advances*, 2020, **10**, 40142-40147.
- D. J. Nixon, L. C. Perera, T. N. Dais, P. J. Brothers, W. Henderson and P. G. Plieger. Tuning receptors for the encapsulation of Be^{+2}. *Phys. Chem. Chem. Phys.*, 2019, **21**(*35*), 19660-19666.
- T. N. Dais, M. J. Brown, M. P. Coles, F. Laur, J. R. Price, G. J. Rowlands and P. G. Plieger. Synthesis and characterization of Co(II) and Mn(II) $[M_3L_3]$ triangles. *J. Incl. Phenom. Macrocycl. Chem.*, 2019, **94**(*3*), 175-182.

Contents

List of Figures

List of Tables

List of Abbreviations

AC	Alternating Current
ATR-FTIR	Attenuated Total Reflectance Fourier Transform Infrared spectroscopy
CHN	Carbon, Hydrogen, and Nitrogen elemental analysis
CShM	Continuous Shape Measurement calculation
DC	Direct Current
DFT	Density Functional Theory
EPR	Electron Paramagnetic Resonance spectroscopy
HR-MS	High Resolution Mass Spectrometry
NMR	Nuclear Magnetic Resonance spectroscopy
HMBC	Heteronuclear Multiple Bond Correlation
HMQC	Heteronuclear Multiple Quantum Coherence
NOESY	Nuclear Overhauser Effect Spectroscopy
QTM	Quantum Tunelling of Magnetization
SOC	Spin-Orbit Coupling
SQUID	Superconducting Quantum Interference Device
XRD	X-ray Diffraction
PXRD	Powder X-ray Diffraction
SCXRD	Single Crystal X-ray Diffraction
ZFS	Zero-Field Splitting

Physical Constants

Avogadro's number	$N_A = 6.022 \times 10^{-23}\,\mathrm{mol}^{-1}$
Bohr magneton	$\mu_\mathrm{B} = 9.274 \times 10^{-24}\,\mathrm{J\,T}^{-1}$
Boltzmann constant	$k_\mathrm{B} = 1.381 \times 10^{-23}\,\mathrm{J\,K}^{-1}$
Electron g-factor	$g_e = 2.002\,318$

Chapter 1

An Introduction

The history of magnetic materials dates back to earlier than 600 B.C., when magnetism was first observed in a form of the mineral magnetite, called lodestone. It was not until the early nineteenth century that is was formulated that magnetism and electricity represent different aspects of the force of electromagnetism, which is one part of the electroweak force. By the twentieth century, scientists had begun systematically studying magnetism, finally beginning to understand it at a fundamental level, and develop technologies based on this understanding. Research surrounding magnetic materials encompasses nearly all areas of modern science, with a particular focus on the development of novel magnetic materials and the ability to tune their properties. Despite the vast amount of applications classical magnets have in our lives, they suffer, primarily, from two major drawbacks: their chemical reactivity, and high energy cost.

1.1 Magnetic Materials and Their Properties

At its root, magnetism can arise from two sources: electric currents (I), or the spin magnetic moments ($\vec{\mu}_\mathrm{s}$) of elementary particles. In the simplest terms, the attractive or repulsive magnetic interactions between two objects originates from the interaction between each objects electrons or an objects electrons with a magnetic field (B).[1] When an object is subjected to a relatively strong magnetic field, the spins of the objects ground state electrons align with the magnetic field, however, the ground state electron spins of most objects will become rapidly disordered when removed from the applied field and thus quench the observed magnetism.[2]

1.1.1 Magnetism in Bulk Solids

At the atomic level there exists two fundamental types of magnetism: diamagnetism and paramagnetism, each of which have unique effects on the arrangement of electron spins. Diamagnetic materials contain only anti-parallel paired electrons, thus have a net magnetic moment of zero, and are not attracted towards an applied magnetic field. Paramagnetism, however, describes the attractive interaction between an applied magnetic field and the unpaired electrons within the material. This paramagnetic interaction also has a strong temperature dependence.[3–5] Bulk solids may be characterized into further subgroups of magnetism which are most commonly combinations of properties of diamagnetic and paramagnetic materials. The magnetic properties of both diamagnetic and paramagnetic compounds can be determined by measuring the magnetic response of the compound with respect to an applied magnetic field, known as the magnetic susceptibility, χ, and defined by Eq. 1.1:

$$\chi = \frac{\partial M}{\partial \boldsymbol{H}} \tag{1.1}$$

Where M is the magnetization of the sample and $\boldsymbol{H}$ is the strength of the applied field. In the case of a weak applied field, the change in sample magnetization as a function of applied field is constant thus χ is defined by the dimensionless quantity in Eq. 1.2:

$$\chi = \frac{M}{\boldsymbol{H}} \tag{1.2}$$

The most commonly expressed form of χ is the molar susceptibility, χ_M, which is the sum of diamagnetic and paramagnetic susceptibilities (χ_D and χ_P, respectively) and has units $\mathrm{cm^3\ mol^{-1}}$ (Eq. 1.3):[6–8]

$$\chi_\mathrm{M} = \chi_\mathrm{D} + \chi_\mathrm{P} \tag{1.3}$$

1.1.2 Classes of Magnetic Materials

The most common classes of magnetic interactions observed in the bulk phase (excluding diamagnetism) are; paramagnetism, ferromagnetism, antiferromagnetism, and ferrimagnetism (Figure 1.1). In general, these systems require non-zero electron spins typically observed in organic radicals, transition metal ions, or lanthanide ions.[3]

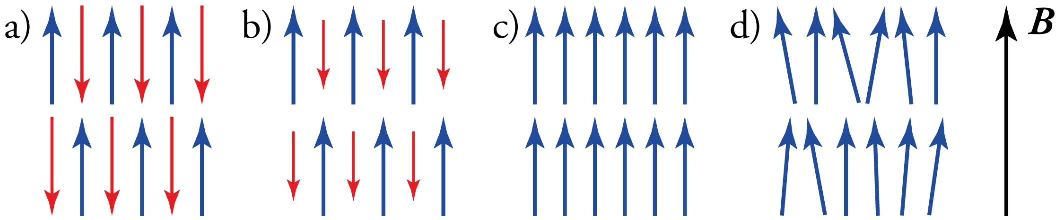

FIGURE 1.1: Representation of the alignment of spins in an applied field (**B**) for a) antiferromagnetic, b) ferrimagnetic, c) ferromagnetic, and d) paramagnetic solids.

Paramagnetism

In paramagnetic compounds, unpaired electron spins are oriented randomly and independently of the neighbouring spins. If a sufficiently strong magnetic field, ***H***, is applied to the sample then the random thermal motion can be overcome and the spins of unpaired electrons will align parallel or anti-parallel to ***H***. At zero applied field thermal motion will once again dominate the system, and the unpaired electron spins will randomize, thus the molar susceptibility of paramagnetic materials is both temperature and field dependent.[3–5] The Curie law (Eq. 1.4) defines this temperature dependence as:

$$\chi_{\mathrm{M}} = \frac{N_{\mathrm{A}} g^2 \mu_{\mathrm{B}}^2}{3k_{\mathrm{B}}T} \boldsymbol{S}(\boldsymbol{S}+1) \tag{1.4}$$

Where N_{A} is Avogadro's number (6.022×10^{23} mol^{-1}), g is the Landé g-factor, μ_{B} is the Bohr magneton (9.274×10^{-24} J T^{-1}), k_{B} is the Boltzmann constant (1.380×10^{-23} J K^{-1}), T is the system temperature, and **S** is the spin quantum number. The Curie constant, C (emu K mol^{-1}), can then be defined as Eq. 1.5:

$$\mathrm{C} = \frac{N g^2 \mu_{\mathrm{B}}^2}{3k_{\mathrm{B}}} \boldsymbol{S}(\boldsymbol{S}+1) \tag{1.5}$$

Which allows Eq. 1.4 to simplify to:

$$\chi_{\mathrm{M}} = \frac{C}{T} \tag{1.6}$$

This equation more directly shows the inverse temperature dependence of the molar susceptibility for paramagnetic compounds. This leads to a linear field dependence of magnetization at low applied fields, however, at high applied field strengths (with constant temperature) the magnetization increases and reaches a saturation value, M_{sat}, that depends on the spin quantum number, $\boldsymbol{S}$:

$$\frac{M_{\text{sat}}}{N_{\text{A}}\mu_{\text{B}}} = Sg = n \tag{1.7}$$

Where ${}^{M_\text{s}}/_{N_\text{A}\mu_\text{B}}$ is the reduced magnetization and n is the number of unpaired electrons in the system.[3,8]

Ferro-, Antiferro-, and Ferrimagnetism

Long-range ordering of magnetic spins in bulk materials is commonly observed and leads to the phenomena of ferro-, antiferro-, and ferrimagnetism. These three classes of magnetic materials behave similarly to paramagnetic compounds and lose their magnetic ordering above a specific temperature, again, due to thermal motion overcoming magnetic ordering. For ferro- and ferrimagnets this is the Curie temperature, T_C, and for antiferromagnets this is the Néel temperature, T_N. Bulk ferromagnetic materials are divided into Weiss domains, in the absence of an applied field each domain has a non-zero magnetic moment in a somewhat random orientation leading to a net sample magnetization of zero. When a magnetic field is applied and the sample is kept below T_C the domain walls are displaced and a new domain structure is formed, whereby the magnetic moments of each domain align parallel with the direction of the applied field. Below the Curie temperature, when the applied field is removed, the magnetization is retained. In contrast, the unpaired spins in an antiferromagnet will arrange anti-parallel when below T_N, thus will give a net magnetization of zero in an applied magnetic field. Ferrimagnets behave similarly to antiferromagnets with their anti-parallel spins in an applied field, however the magnetization vector of the domains can have different magnitudes leading to a net non-zero magnetic moment. Similar to ferromagnets, below their ordering temperature, this magnetization is retained upon removal from the applied field.

1.1.3 Single Molecule Magnetism

Almost three decades ago magnetization experiments were carried out by Sessoli *et al.*[9] on the compound first reported over a decade earlier by Lis,[10] now commonly known as Mn_{12}. This system was the first of its kind observed to retain magnetization, at the molecular level, in zero applied field.[11,12] This discovery kick-started the now flourishing field of molecular magnetism, with Web of Science showing over 10,000 documents matching the search term ’single molecule magnet’ published prior to 2022.[13]

Single molecule magnets primarily differ from classical bulk magnetic materials in the nature of the magnetic interactions and ordering. SMMs rely on short range ordering, where each individual molecular unit acts as a single magnetic domain, without the need for long range ordering and interactions as in bulk magnets. SMMs are commonly characterized by an effective barrier to the reversal of magnetization (U_{eff}) and their blocking temperature (T_B), above which they behave like regular superparamagnets and below which they exhibit single-molecule-domain ferromagnetic behaviour.

1.2 Electronic Structure, Interactions, and Hamiltonians

At its core, magnetism requires the presence of unpaired electrons, which are typically considered to be localized to magnetic orbitals (Figure 1.2). The unpaired electrons can reside in *p*-orbitals, as in reactive radical compounds, transition metal *d*-orbitals, or the highly shielded *f*-orbitals of the lanthanide and actinide series. Complexes can be formed with any number of spin centres containing various combinations of *p*-, *d*-, or *f*-magnetic orbitals with unique electronic structures. The subtle effects of spin-orbit, spin-spin, ligand field, and crystal field interactions are paramount to the fundamental understanding of such systems; where small apparent changes can lead to vastly different molecular properties.

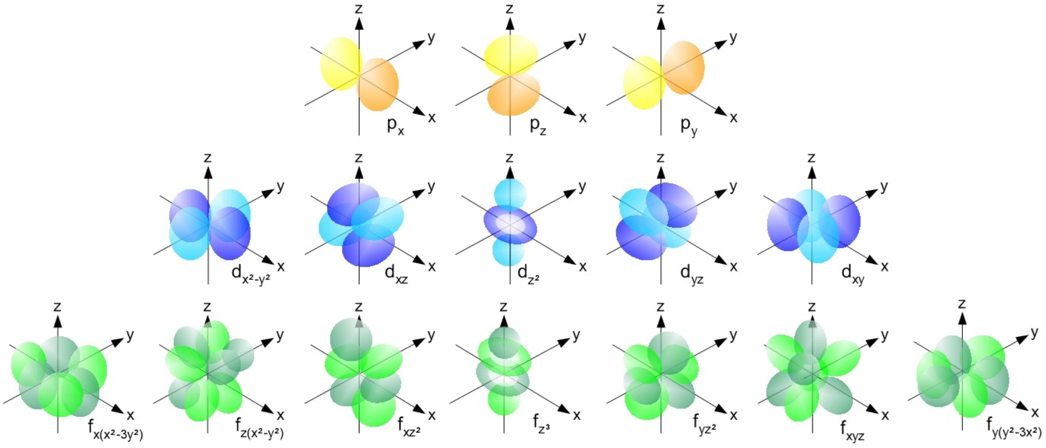

FIGURE 1.2: Real valued functions depicting the general shape of the *p*-, *d*-, and *f*-orbitals.

Magnetically interesting compounds with unpaired electrons in their *p*-orbitals are almost exclusively nitrogen based, most commonly nitronyl-nitroxide derivatives,[14–17] due to their relative stability over other highly reactive light element radical species. Magnetic *d*-orbitals encompass the transition metal rows, with the 3*d* metals being the most well studied due to the generally well understood nature of their coordination chemistry. The vast range of oxidation states available to many transition metals makes them an attractive target for electrochemical considerations, while their often well defined coordination geometries simplifies the rationalizing of their electronic structures. Heavier transition metals, i.e. those in the 4*d* and 5*d* series, have also been explored but much less often in heterometallic systems. Finally, the highly shielded and relatively unreactive *f*-orbitals of the lanthanide and actinide metals paired with their unquenched orbital momentum makes them a highly attractive target for the construction of magnetic complexes.

1.2.1 Spin-orbit Couplings

The spin-orbit coupling (SOC) of light atoms (generally $Z \leq 30$), known as *LS* coupling or Russell-Saunders coupling,[18] is small so the total orbital angular momentum (***L***) and total spin (***S***) are said to be ″good quantum numbers″.[19] For much heavier elements, with many electrons and a larger nuclear charge, the spin-orbit interaction becomes as strong as the interaction between individual spins and dominates the Coulomb interactions. Thus a *j-j* coupling scheme is used to describe the interaction between spin and orbital angular momenta of individual electrons in heavy elements.[19]

Russell-Saunders Coupling

In multi-electron atoms with weak spin-orbit coupling, the total angular momentum (***J***) can be visualized as the vector addition of the total orbital angular momentum (***L***) and the total spin angular momentum (***S***), as in Fig. 1.3. This coupling regime holds true for weak applied magnetic fields. In the presence of stronger external magnetic fields, ***L*** and ***S*** can decouple, giving rise to a different splitting of energy levels called the Paschen-Back effect.[19]

j-j coupling

For heavier elements (generally $Z \geq 40$) spin-orbit coupling becomes more important as relativistic effects must be taken into account when calculating orbital energies. Spin-orbit coupling constants (ζ) tend to increase across and down the periodic table, for example $\zeta = 460$ cm^{-1} for Fe$^{\text{III}}$ ($Z = 26$) and $\zeta = 1900$ cm^{-1} for Dy$^{\text{III}}$ ($Z = 66$).[20,21] The effect of ζ on the energy level of the electron is computed using the Hamiltonian in Eq. 1.8, giving energies of the ***J*** states as in Eq. 1.9

$$\begin{aligned} \mathcal{H}_{\boldsymbol{LS}} &= \lambda_{\boldsymbol{LS}} \boldsymbol{L} \cdot \boldsymbol{S} \\ \text{where } \lambda_{\boldsymbol{LS}} &= \frac{\pm \zeta_{nl}}{2S} \end{aligned} \tag{1.8}$$

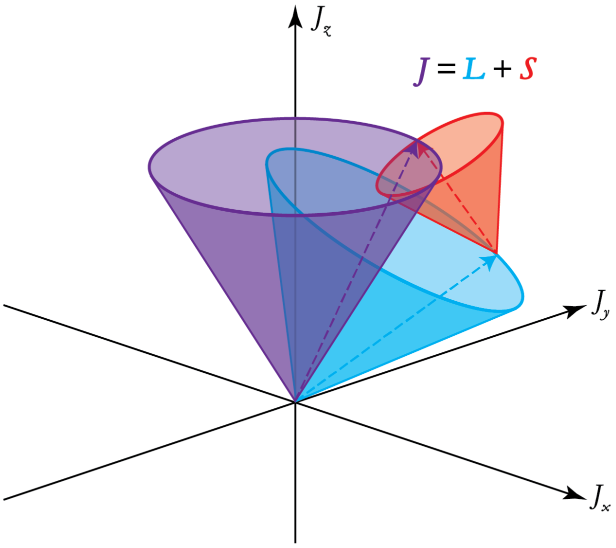

FIGURE 1.3: Illustration of Russell-Saunders type coupling.

$$E(J) = \left(\frac{\lambda}{2}\right)[J(J+1) - L(L+1) - S(S+1)] \quad (1.9)$$

1.2.2 Exchange and Superexchange

Exchange interactions between metal centres occur in complexes as a result of the direct overlap of partially occupied atomic orbitals within the metal ions. In contrast, superexchange interactions occur as a result of the overlap of partially occupied metal ion orbitals with intermediary ligand orbitals. Superexchange interactions occur in polynuclear clusters in two distinct ways: antiferromagnetic exchange occurs when two metal ions and a ligand are colinear, i.e. a 180° M–L–M angle (Figure 1.4, top). Ferromagnetic exchange occurs when this angle is reduced to near 90°, involving the interaction of a second orthogonal p-orbital of the ligand (Figure 1.4, bottom). The Pauli exclusion principle dictates that for two magnetic ions with half-occupied orbitals which are coupled through a non-magnetic ion, the superexchange will be strongly antiferromagnetic in nature whereas the coupling between an ion with a filled orbital and one with a half-filled orbital will be strongly ferromagnetic.[22,23] Ferromagnetic exchange typically dominates when an ion with either a fully or partially occupied orbital couples to a vacant orbital, however when multiple types of interactions are simultaneously present antiferromagnetic interactions will dominate due to its dependence of the intra-atomic exchange term.[23,24]

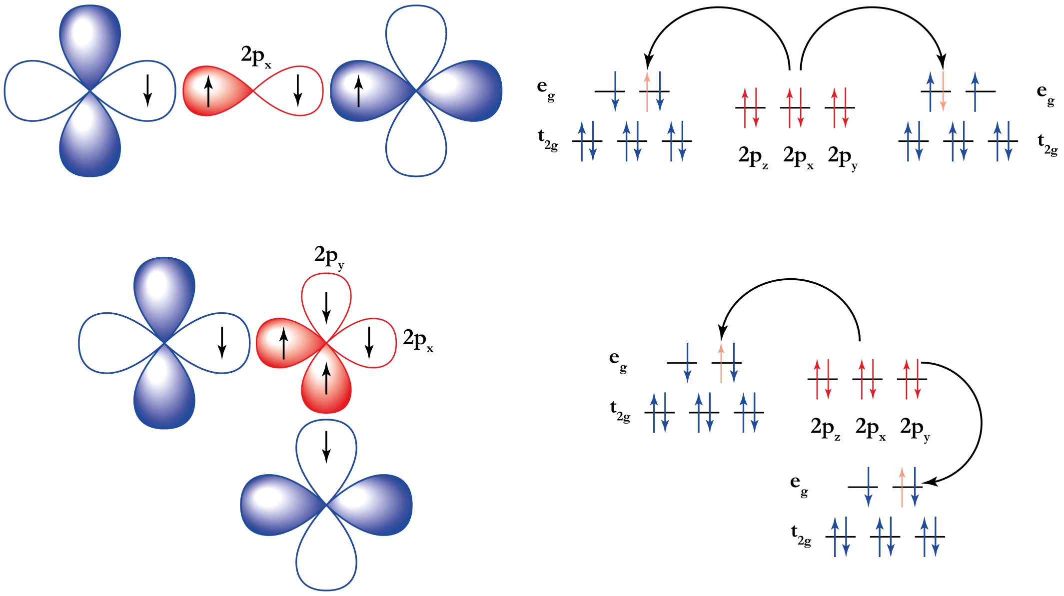

FIGURE 1.4: Schematic representation of a linear exchange pathway involving two $3d^8$ metal d-orbitals and one $2p^6$ ligand centred p-orbital (top) and a nonlinear exchange pathway involving two $3d^8$ metal d-orbitals and two $2p^6$ ligand centred p-orbitals (bottom).

1.2.3 Magnetic Anisotropy

In the absence of an applied field and any form of spin-orbit coupling, an electron spin has spherical symmetry and is therefore totally isotropic. However, the interaction between electron spin and orbital motion must be considered for real systems. A consequence of SOC is the splitting of otherwise degenerate energy levels of the electrons, and it is this interaction that leads to the anisotropic behaviour observed in metal ions. The primary contributors to magnetic anisotropy are the zero-field splitting (ZFS) effect and the Zeeman effect (Figure 1.5), which can be collectively described by the spin-Hamiltonian in Eq. 1.10:

$$\begin{aligned}\mathcal{H} &= \mathcal{H}_{Zeeman} + \mathcal{H}_{ZFS} \\ &= \mu_{\mathrm{B}}\vec{B}\boldsymbol{g}\boldsymbol{S} + \boldsymbol{S}\boldsymbol{D}\boldsymbol{S}\end{aligned} \tag{1.10}$$

ZFS causes a loss of degeneracy in the spin microstates in systems with non-zero spins, without an applied field, originating from either a direct interaction between the magnetic dipoles of unpaired electrons or from another contribution arising as a consequence of SOC. A series expansion of the ZFS spin Hamiltonian leads to an equation (Eq. 1.11) described by a quadrupolar (axial) term, D, which applies for $\boldsymbol{S} \geq 1$ and a hexadecapolar (rhombic) term, E, for $\boldsymbol{S} \geq 2$, of the form:

$$\mathscr{H}_{\mathrm{ZFS}} = D\left[\mathcal{S}_z^2 - \frac{1}{3}S(S+1)\right] + E\left(\mathcal{S}_x^2 - \mathcal{S}_y^2\right) \tag{1.11}$$

where the D parameter is non-zero in cases with symmetry lower than cubic, for which a positive value results in the lowest spin ground state (0 or 1/2) and a negative value indicates a $M = S$ ground state, and the E parameter is non-zero for any symmetry lower than axial. This implies that in the low temperature regime, a system with a negative D value will have spins aligned parallel to z (as in an easy-axis system) and with a positive value of D the system will be easy-plane, with spins oriented perpendicular to z. If the directional g-values and SOC constant, λ, are known for a given system, then the sign and magnitude of the ZFS can be estimated using the equations in Eq. 1.12

$$\begin{aligned} D &= \frac{\lambda}{2}\left[g_z - \frac{g_x + g_y}{2}\right] \\ E &= \frac{\lambda}{4}\left(g_x - g_y\right) \end{aligned} \tag{1.12}$$

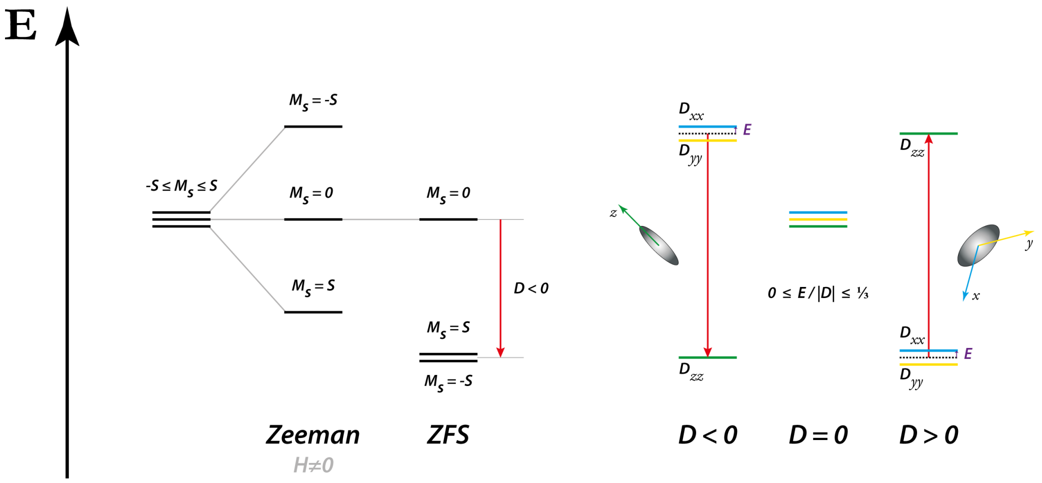

FIGURE 1.5: Simplified representation of the relative energy levels split by the Zeeman effect and zero-field splitting, and the corresponding change in D from easy-axis to easy-plane.

The Zeeman effect is only operative in an applied magnetic field, i.e. $\boldsymbol{H} \neq 0$. As previously discussed; in the weak field limit the Zeeman splitting takes the form of LS coupling, while in the limit of an applied field comparable to the internal field of the atom, it converges to the Paschen-Back effect.[19] The Zeeman term of the spin-Hamiltonian in Eq. 1.10 can be rewritten such that it no longer depends on the $\boldsymbol{g}$ value of the element, but rather the g value of the free electron, g_e, as in Eq. 1.13:

$$\mathcal{H}_{Zeeman} = \mu_{\mathrm{B}} \left(g_e 2\boldsymbol{S} + \boldsymbol{L} \right) \cdot \boldsymbol{B} \tag{1.13}$$

Furthermore, if the ${}^{2S+1}L_J$ multiplet is a pure J state, then the Wigner-Eckart theorem can be applied to further simplify the Hamiltonian to Eq. 1.14:

$$\mathcal{H}_{Zeeman} = -\mu_{\mathrm{B}} \boldsymbol{J} \cdot \boldsymbol{B} \tag{1.14}$$

1.3 Selected Characterization for Metal Clusters

1.3.1 Single-crystal X-ray Diffraction

Single-crystal X-ray diffraction (SCXRD) is perhaps the most important characterization tool for determining the molecular structure of crystalline solids in all fields of chemistry and indeed has far reaching effects in other fundamental sciences. Although the technique as we know it was only developed in the early 20th century, observations about the regularity of crystal morphologies date back to the 17th century.[25] Max von Laue pioneered SCXRD when he demonstrated the diffraction of X-rays through a copper sulfate crystal, and observed a series of concentric circles, now known as Laue rings.[26] The theory was further developed by Bragg (Eq. 1.15) who determined that a crystal would diffract X-rays if the inter-atomic spacing in the crystal, at the relevant angle, matched the wavelength of the incident beam then the resulting constructive interference would lead to an observable spot, commonly referred to as a reflection.

$$n\lambda = 2d \sin\theta \tag{1.15}$$

By definition, crystals are periodic structures, meaning the electron density of molecular sub units can be related to the electron density of crystal as a whole. The electron density at a given point in the crystal, relative to the origin of its unit cell, can be given by $\rho(x, y, z)$. By considering the periodicity, this electron density can be represented by the Fourier sum of atomic structure factors as in Eq. 1.16:

$$\rho(x, y, z) = \frac{1}{V} \sum_{h} \sum_{k} \sum_{l} F_{hkl} e^{2\pi i (hx+ky+lz)} \tag{1.16}$$

where the indices h, k, and l define planes through the crystal lattice, and F_{hkl} defines the structure factors for the planes that intersect some multiple of the points $1/h$, $1/k$, and 1/*l*. The atomic structure factor, F_{hkl}, can be further defined as the Fourier sum of the atomic scattering factors, f, as in Eq. 1.17:

$$F_{hkl} = \sum_{j=1}^{n} f_j e^{2\pi i (hx_j + ky_j + lz_j)} \tag{1.17}$$

Atomic scattering factors largely depend on the both angle of incidence (as in the Bragg equation, Eq. 1.15) and the number of electrons that the atom has. Consequently, this makes it difficult to distinguish between atoms with similar atomic numbers, particularly at high values of Z. There is also a contribution from the anomalous scattering factors, f' and f'', which are wavelength dependent:

$$f(\theta, \lambda) = f_0(\theta) + f'(\lambda) + if''(\lambda) \tag{1.18}$$

Euler's formula can be used to express the exponent in Eq. 1.17 as a complex number, meaning that F_{hkl} can be defined as the sum of complex vectors (Figure 1.6).

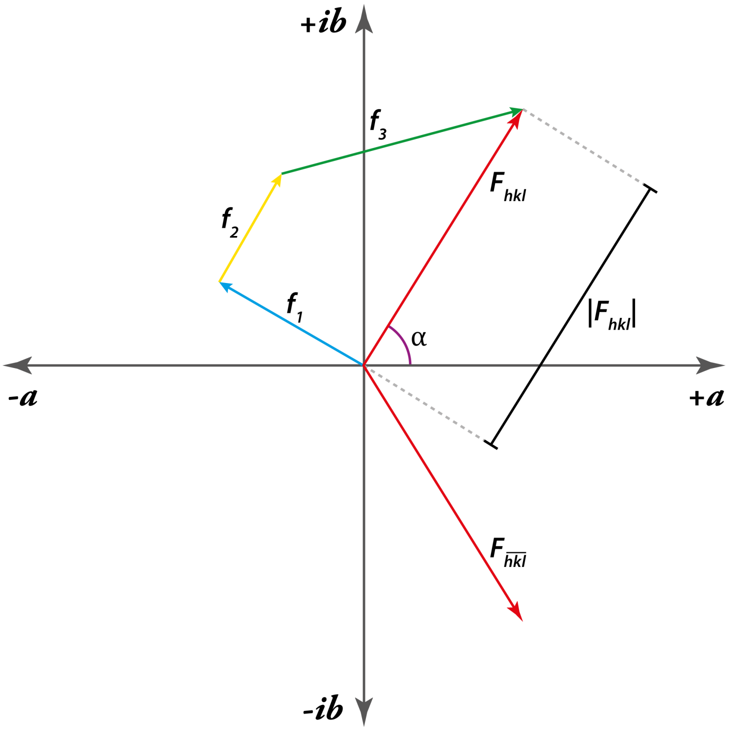

FIGURE 1.6: Vector representation of a structure factor, F_{hkl}, and its Friedel pair, $F_{\overline{hkl}}$.

Ordinarily, the same reflection in the opposite direction ($-h$,$-k$,$-l$) should have the same intensity. Experimentally, the diffraction pattern shows the intensity or $|F_{hkl}|$ information but the phase of the reflection, corresponding to the angle α in Figure 1.6, is not observed. The position of each reflection is determined by the intensity of the electron density and the indices of the plane which it corresponds to, however the phase information which is determined by the relative distance between the peak of the electron density and the plane of the reflection is lost.[27]

1.3.2 SQUID Magnetometry

Superconducting quantum interference device (SQUID) magnetometers provide the most effective way to measure subtle changes in magnetic fields with high sensitivity and precision. SQUID, along with its micro- and nano-SQUID counterparts, provides the only method to experimentally determine the overall magnetic moment of a sample in absolute units – with further advances leading to the measurement of individual spins.[28–30] A SQUID magnetometer consists of two semiconducting half-ring structures separated by a thin insulating material, which form two parallel Josephson junctions (Figure 1.7). Brian Josephson, whom the Josephson junction is named after, found that the electrical current density through an insulating medium separating two superconductors is directly proportional to the phase difference $\Delta\phi$ of the two superconducting wave functions, and hence the time derivative of this phase difference would correspond to the voltage across the insulating layer. Additionally, $\Delta\phi$ will be influenced by a magnetic flux, Φ, through the ring, producing an observable change in voltage across the insulating layers. In principle, a sample passed sinusoidally through a superconducting pickup coil will produce an alternating magnetic flux through the coil that is then transferred to the SQUID coil, which is acting as a flux-to-voltage converter, and the corresponding voltage can be amplified and read out via a computer. SQUIDs typically operate at liquid helium to liquid nitrogen temperatures (4.2 – 77 K), utilize magnetic fields of the same order as typical NMR spectroscopy (2 – 14 T), and can operate in direct current (DC) and alternating current (AC) modes. The discovery of the Josephson junction also lead to the realization that magnetic flux, Φ_0, is quantized (Equation 1.19); where $\hbar$ is the reduced Planck constant, and e is the elementary charge.

$$\Phi_0 = \frac{2\pi\hbar}{2e} \cong 2.0678 \times 10^{-15}\ \mathrm{T \cdot m^2} \tag{1.19}$$

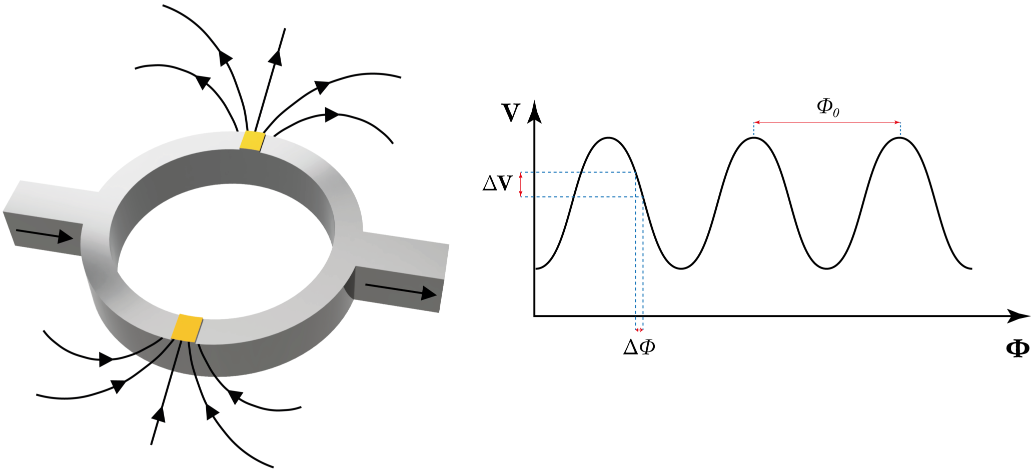

FIGURE 1.7: Schematic representation of a Josephson junction and a representative plot of the large observed voltage drop, ΔV for a small change in magnetic flux, $\Delta\phi$.

For the purpose of characterizing SMMs, there are three routine SQUID experiments: DC magnetic susceptibility ($\chi_{\mathrm{m}}T$ vs T, Figure 1.8, left), DC magnetization (M vs H, Figure 1.8, right), and AC magnetic susceptibility measurements ($\chi(\omega)$ vs ω or T, Figure 1.10). For a crystalline sample with well separated molecular units, avoiding any intermolecular spin-dipole interactions, the DC measurements give information about the total spin state of the sample in both high and low temperature regimes. Insight into the spin states of individual spin centres, for example in a heterobinuclear $\mathrm{Mn^{II}Tb^{III}}$ complex (where $S_{\mathrm{total}} = 12$), can also be gained from these measurements.

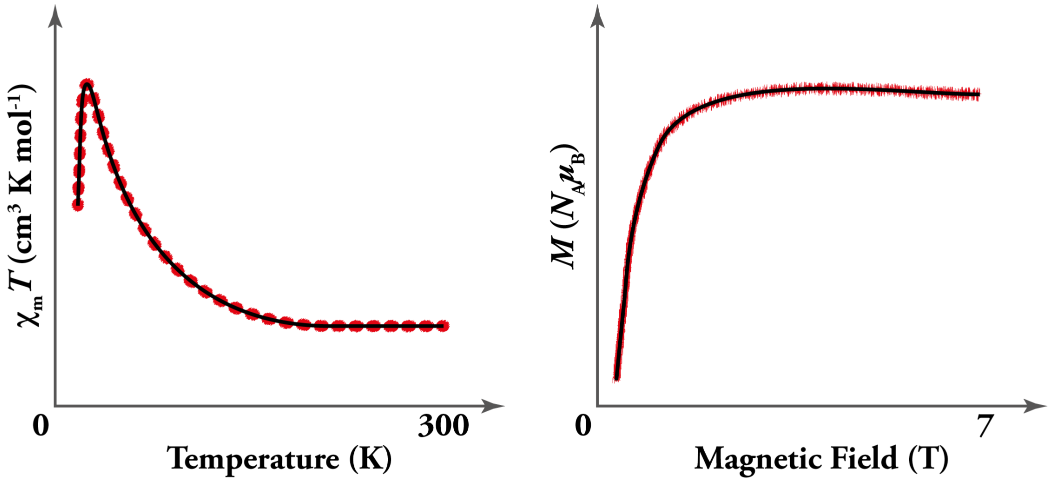

FIGURE 1.8: Schematic representation of a DC magnetic susceptibility plot (left) and DC magnetization plot (right) for an arbitrary ferromagnetically coupled system.

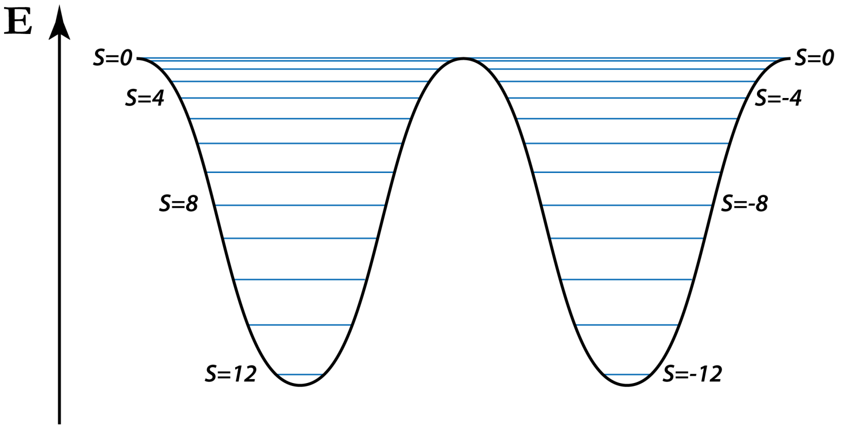

FIGURE 1.9: Schematic representation of the magnetic double-well potential for a ferromagnetically coupled theoretical $Mn^{II}Tb^{III}$ complex with $S_{total} = 12$ ground state.

It is the AC magnetic susceptibility data which gives true insight into the ability of a sample to act as an SMM. The dynamical properties of a sample can be probed by placing it between two coils which have a current flow with angular frequency ω. By operating at a frequency where the magnetic field oscillates too fast for the magnetic dipoles of individual molecules to align to it, the spins will be redistributed over the available energy levels, which will be associated with a relaxation process and hence a relaxation time, τ. For a sinusoidally oscillating magnetic field, $H(t) = H_0 + he^{i\omega t}$ where H_0 is the static field and $\omega = 2\pi\nu$ is the angular frequency of the alternating field, the dynamic magnetization of the sample will take a similar form: $M(t) = M_0 + m(\omega)e^{i\omega t}$. For a given system with an arbitrary relaxation pathway, the applied field ($H(t)$) and the sample magnetization ($M(t)$) cannot be in phase, thus $m(\omega)$ is a complex quantity and the AC susceptibility, $\chi(\omega)$, will also be a complex quantity dependant on an in-phase (χ') and out-of-phase (χ'') component (Eq. 1.20):

$$\begin{aligned}\chi(\omega) &= \frac{m(\omega)}{h} \\ &= \chi'(\omega) - i\chi''(\omega) \\ &= \chi_S + \frac{\chi_T - \chi_S}{1 + (i\omega\tau)^{1-\alpha}}\end{aligned} \tag{1.20}$$

The greatest benefit of AC susceptibility measurements for the characterization of SMMs lies in their ability to probe different values of τ by varying the measurement frequency, ω, which is often necessary for an accurate determination of the blocking temperature, which corresponds to χ''_{max}, and effective barrier (Eq. 1.21). Above the blocking temperature, the out-of-phase component is small and the the in-phase component follows the Curie law (Eq. 1.6) where $\chi' \propto T^{-1}$. Because the blocking temperature has a dependence on the measurement frequency, the peak in a χ'' vs T plot occurs at different values of ω.

$$T_B = \frac{U_{\text{eff}}}{\ln(\tau/\tau_0)k_{\text{B}}} \tag{1.21}$$

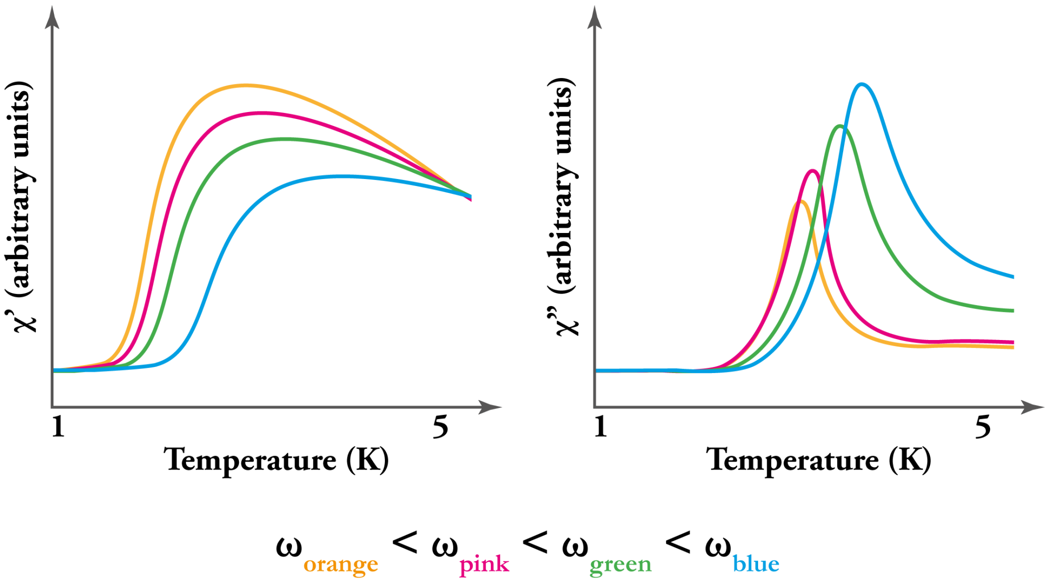

FIGURE 1.10: Schematic representation of plots for the in-phase (left) and out-of-phase (right) components for an AC magnetic susceptibility measurement, of an imaginary system, to illustrate the temperature and frequency dependence.

1.3.3 Electron Paramagnetic Resonance Spectroscopy

Electron paramagnetic resonance (EPR) is a spectroscopic method for studying systems containing unpaired electrons. The use of an external magnetic field (B_0) allows the Zeeman effect (Equation 1.22) to be exploited due to electrons having a spin quantum number of $s = \frac{1}{2}$ which is split by the magnetic component $m_\mathrm{s} = \pm\frac{1}{2}$, the sign of which is dependant on its alignment with the applied magnetic field.

$$E = m_\mathrm{s} g_e \mu_\mathrm{B} B_0 \tag{1.22}$$

where g_e is the electron spin g-factor, and μ_B is the Bohr magneton. For unpaired electrons, the separation between the $m_\mathrm{s} = +\frac{1}{2}$ and $m_\mathrm{s} = -\frac{1}{2}$ states is therefore given by Equation 1.23

$$\Delta E = g_e \mu_\mathrm{B} B_0 \tag{1.23}$$

As both μ_B and g_e are constants, this splitting is directly proportional to the applied field and is typically on the order of microwave energies (9 –10 GHz). An unpaired electron can transition between these two energy levels by either emitting or absorbing a photon such that $h\nu = \Delta E$, leading to the realization of Equation 1.24

$$h\nu = g_e \mu_\mathrm{B} B_0 \tag{1.24}$$

In real world chemical systems, particularly those containing metal ions, electrons are often associated with more than one atom. This has important consequences on the EPR spectrum of such a system:

1. The angular momentum of an unpaired electron is a not a constant, thus can have g-factors which differ from g_e.
2. Electron-electron interactions can occur for systems with more than one unpaired electron, and gives rise to fine structure as zero field splitting (ZFS) and exchange coupling.
3. A non-zero nuclear spin will cause a magnetic moment which perturbs unpaired electron associated with that nucleus, leading to hyperfine coupling which splits the EPR resonance signals, analogous to *J*-coupling in NMR.

4. The interaction between unpaired electrons and the greater chemical environment changes the shape of the EPR spectral lines.
5. The above effects can be orientation dependant in the case of systems with large anisotropy, hence can provide information about the molecular or atomic orbital containing the unpaired electron.

1.3.4 ^{57}Fe Mössbauer Spectroscopy

The Mössbauer effect describes the recoilless emission and resonant absorption of gamma radiation by atomic nuclei in solids.[31,32] Mössbauer spectroscopy can be used to elucidate various magnetic, electronic, and structural properties of solids containing certain (Mössbauer active) nuclei across a wide temperature range (typically 2 – 300 K, although temperatures in excess of 1000 K have been reported).[33–35] Mössbauer spectroscopy is most commonly used for the analysis of ^{57}Fe, which has both a very low energy gamma-ray emission and long-lived excited state. The analysis of ^{57}Fe requires a Rh source doped with radioactive ^{57}Co, which decays via electron capture to an excited state of ^{57}Fe, which in turn relaxes to the ground state via emission of a gamma ray. By oscillating the position of the gamma source, the emitted gamma radiation can be modulated by the Doppler effect. The gamma rays are allowed to pass through the sample chamber and are detected by a scintillation detector, the signal is then amplified and analyzed by a multichannel analyser thus generating the Mössbauer spectrum. The Mössbauer spectrum (Figure 1.11) plots count rate or transmittance against source velocity. With the aid of curve fitting software three Mössbauer parameters can be obtained: the isomer shift (IS), the quadrupole splitting (QS), and the magnetic hyperfine splitting (Figure 1.12). For selected nuclei these parameters can be used to obtain information about the oxidation state, nature of chemical bonding, electronic and crystallographic structure, coordination geometry and symmetry of the selected nuclei, and the presence or absence of magnetic ordering.[36,37]

The isomer shift, IS (δ), describes the shift in resonance energy of a nucleus due to electron transitions within its s-orbitals, that is, IS is a result of the changing interaction between the nucleus and inner electron cloud due to slight variations in the electron cloud density. The isomer shift is used to help determine the oxidation state, valency states, and the electron withdrawing and shielding power of electronegative groups.[31,36,38] Quadrupole splitting, QS (ΔE_Q), occurs when an applied electric field gradient or non-uniform electric field causes a non-spherical charge distribution, i.e. a non-zero nuclear quadrupole moment. The quadrupole splitting can be used to determine the oxidation state, spin state, site symmetry, and hence the arrangement of ligands.[31,36,38]

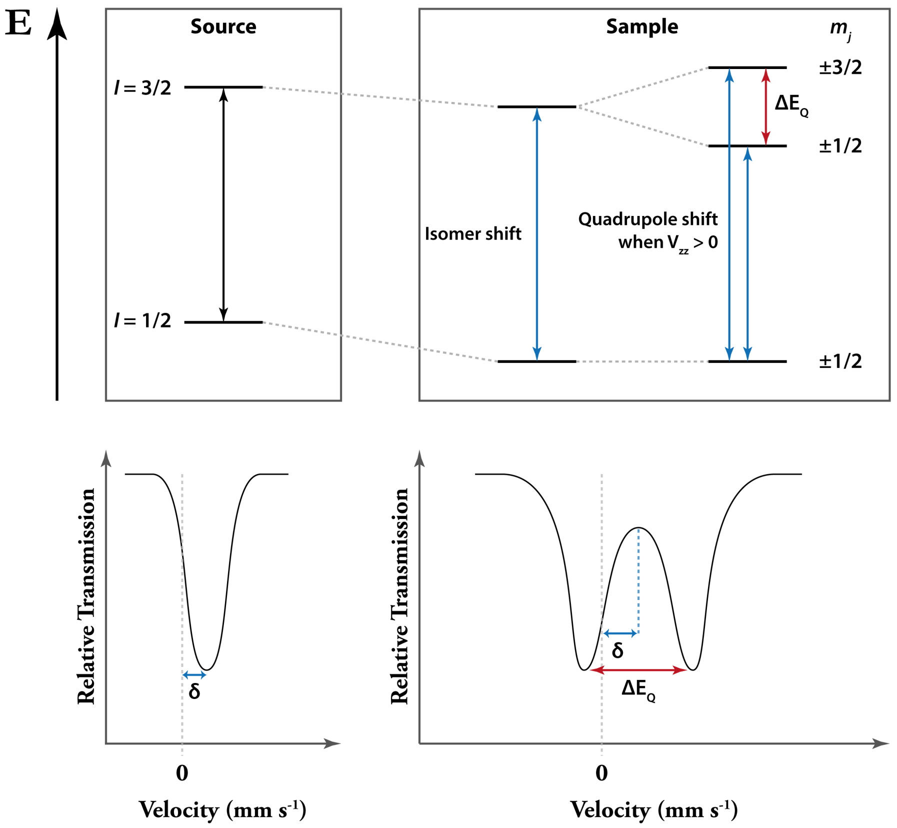

FIGURE 1.11: Schematic diagram showing the relative energies of the m_j states, and plots showing the effects of the isomer shift and quadrupole shift on the Mössbauer spectra.

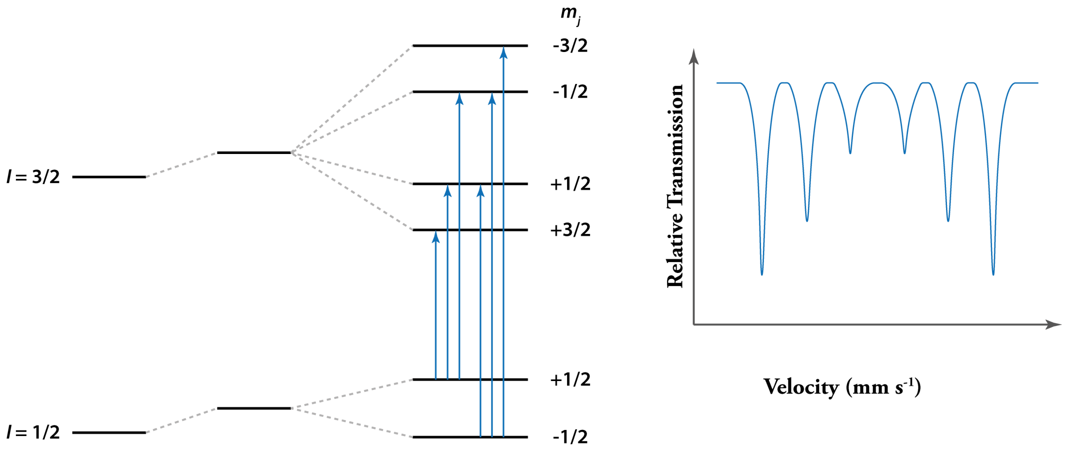

FIGURE 1.12: Schematic representation of hyperfine splitting and the resulting Mössbauer spectra.

The complex splittings present in Mössbauer spectra all rise from subtle changes in the electronic structure of the iron centres. Along with oxidation state, spin state, and crystal field effects, the electronic structure of each iron centre can be uniquely affected by the presence of applied electric or magnetic fields, as well as dipolar or superexchange interactions. As previously discussed, temperature dependent magnetic ordering will also influence the electronic structure.[39,40] The Powell and Mereacre groups have extensively investigated ^{57}Fe Mössbauer spectroscopy as a potential aid in determining the magnetic ground state of various high-nuclearity homometallic[41] and heterometallic clusters.[42–46] Through this technique insight can be gained into not only the anisotropy of the iron centres, but also the anisotropy and spin structure of the elements they interacts with, as well as the relaxation dynamics of the total molecular spin system.

1.4 Molecular Clusters and Their Magnetic Properties

With its innumerable sub-fields and broad reaching applications, coordination chemistry has a rich past and a seemingly ever flourishing future. Coordination complexes, or molecular clusters, find applications across all areas of science and life; from antibacterial agents[47–49] and molecular machines,[50–52] to heterogeneous catalysts for material or fuel production[53–57] and spintronic devices for new technologies.[58–62] Amongst some of the more recently discovered niches is the field of molecular magnetism, which in itself contains a multitude of sub-fields. Molecular magnets come in many flavours, ranging from mononuclear single-ion magnets (SIMs) to discrete polynuclear clusters (SMMs) and also include polymeric single-chain magnets (SCMs), with many further sub-distinctions that can be made.

Perhaps the most important distinction in the chemistry of SMMs and metal clusters is the difference between homo- and heterometallic systems. While not strictly true for all cases, homometallic complexes tend to have more approachable synthetic requirements, often utilizing small rigid ligands or flexible but symmetric ligands which can bind without the need for considering binding pocket specificity, and can allow for predictable nuclearities and topologies. Heterometallic complexes on the other hand, often require a more conscientious approach to ligand synthesis by designing distinct binding sites for each of the desired metals. The result is an often richer and more complex structure and set of properties, particularly for molecular magnets.

1.4.1 Homometallic Complexes

Homometallic complexes are common across essentially all molecular architectures, with new architectures often first discovered using homometallic systems. High anisotropy barriers and blocking temperatures approaching liquid nitrogen temperatures have been found in two similar $\mathrm{Dy^{III}}$ metallocene SMMs reported by Layfield *et al.*[63] (Figure 1.13, left) and Chilton *et al.*[64] (Figure 1.13, right).

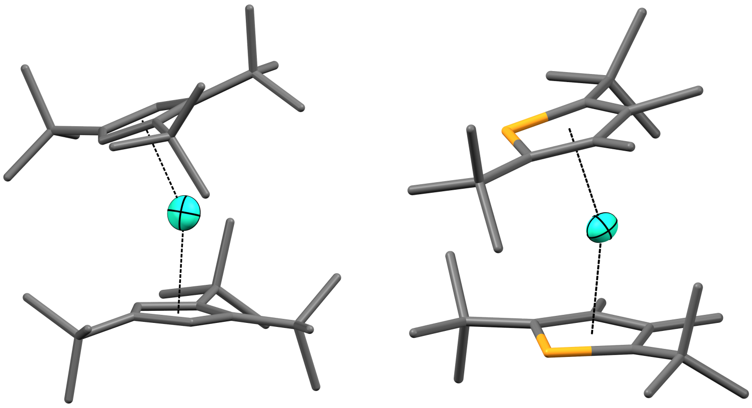

FIGURE 1.13: X-ray crystal structures of the $\mathrm{Dy^{III}}$ metallocenes reported by Layfield (left) and Chilton (right). Non-coordinating anions and hydrogen atoms have been omitted for clarity. Thermal ellipsoids of $\mathrm{Dy^{III}}$ atoms shown at 70%. C = grey, Dy = turquoise, P = orange.

Both groups similarly prepared their metallocene complexes by the reaction of dysprosium halide salts with the appropriate cyclopentadienyl-like derivative (1,2,4-tri(*tert*-butyl)cyclopentadienide or 1,4-bis(*tert*-butyl)-2,3-dimethylphospholyl) to produce 3-coordinate complexes where the ligands bind in an η_5 fashion and a halide group remains bound to the $\mathrm{Dy^{III}}$ centre. To obtain the desired 2-coordinate complexes each group performed a halide abstraction and subsequent metathesis reaction to provide a non-coordinating anionic species to balance the complexes +1 charge. Layfield *et al.* found that by decreasing the coordination number of the relatively oblate $\mathrm{Dy^{III}}$ centre,[65] which increased the axiality of the coordinating groups, the magnetic properties were greatly enhanced with a reported blocking temperature (T_B) of 60 K and an effective barrier to the reversal of magnetization (U_eff) of 1277 $\mathrm{cm^{-1}}$.[63] *Ab initio* calculations indicated that the enhanced axiality effectively suppressed QTM, leading to a dominant relaxation pathway through a high energy Kramer's doublet. A similar U_eff of 1223 $\mathrm{cm^{-1}}$ was reported by Chilton *et al.* for the monophospholyl derivative containing complex,[64] however magnetic hysteresis was only observed up to 48 K, 12 K below the cyclopentadienyl metallocene. Chilton *et al.* also reported the results of *ab initio* calculations which were in line with those of the cyclopentadienyl metallocene, however, the weaker crystal field provided by the monophospholyl ligand caused a compression in energy between the electronic states, leading to faster relaxation and consequently a lower T_B.

As nuclearities increase, a number of supramolecular architectures become synthetically accessible. In particular, use of the molecular library model[66–68] to inform ligand design and metal choice can often result in the self-assembly of complexes in the form of common convex polygons in two dimensions and polyhedra in three dimensions. Among the common complexes of the simple polygons are molecular M_3L_3 triangles and M_4L_4 squares. Four related M_3L_3 complexes in the form of cyclohelicate triangles have been reported by the Plieger[69] and Brooker[70] groups, in which the same bis-pyridyl appended pyrazine ligand (*N*,*N*′-(pyrazine-2,5-diylbis(methanylylidene))bis(2-(pyridin-2-yl)ethanamine)) was found to self-assemble into molecular triangles with Mn^{II} and Co^{II} (Figure 1.14, left) by Plieger *et al.* and Fe^{II} or Zn^{II} (Figure 1.14, right) by Brooker *et al.*

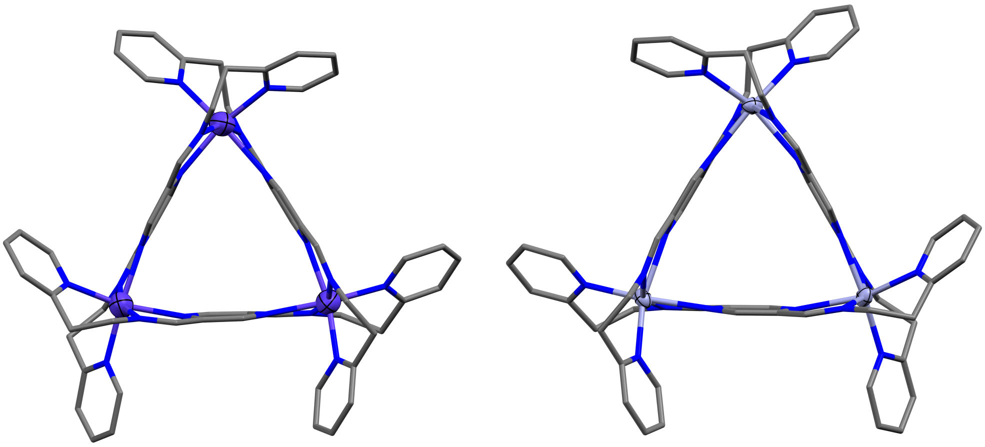

FIGURE 1.14: X-ray crystal structures of the triangular Co_3L_3 (left) and Zn_3L_3 (right) cyclohelicates reported by Plieger *et al.* and Brooker *et al.*, respectively. Non-coordinated species and hydrogen atoms have been omitted for clarity. Thermal ellipsoids of metal atoms shown at 70%. C = grey, Co = dark purple, N = blue, Zn = light purple.

These complexes are good examples of when model chemistry can yield unexpected results. When considering the arrangement of binding sites within the ligand and the choice of typical octahedral transition metals, one might expect an M_4L_4 square to form like in previously reported works containing the amide analogue of this ligand.[71,72] Brooker *et al.* reported DFT calculations which indicated the formation of triangles was likely due to an entropic driving force dominating the enthalpic costs of any geometrically induced strain in the ligand.[70]

At higher nuclearities the number of possible discrete architectures increases further, with common motifs including coordination cages[66,73,74] and supramolecular rings or wheels.[75–81] In 2004 Christou *et al.* reported the synthesis of a Mn^{III}_{84}-acetate wheel shaped SMM (Figure 1.15).[76] With crystallographic six-fold symmetry and an outer diameter of $\sim$ 4.2 nm, this complex crystallizes into perfectly aligned nanotubes. DC magnetic measurements indicated an $S_{\text{total}} = 6$ ground state at 1.8 K, and single-crystal magnetometry carried out with an array of micro-SQUIDs revealed open hysteresis loops below 1.5 K. The profile of the observed hysteresis loops did not feature any notable step-wise behaviour, which would be indicative of QTM, and has been attributed to the size of the complex and the void space within the cavity which is likely filled with heavily disordered solvent molecules, a common drawback of such large structures with open geometries. AC susceptibility measurements further indicated the presence of a thermally activated relaxation pathway above 0.5 K, which allowed fitting of the data to an Arrhenius relationship giving an effective relaxation barrier of 12.5 cm^{-1}.

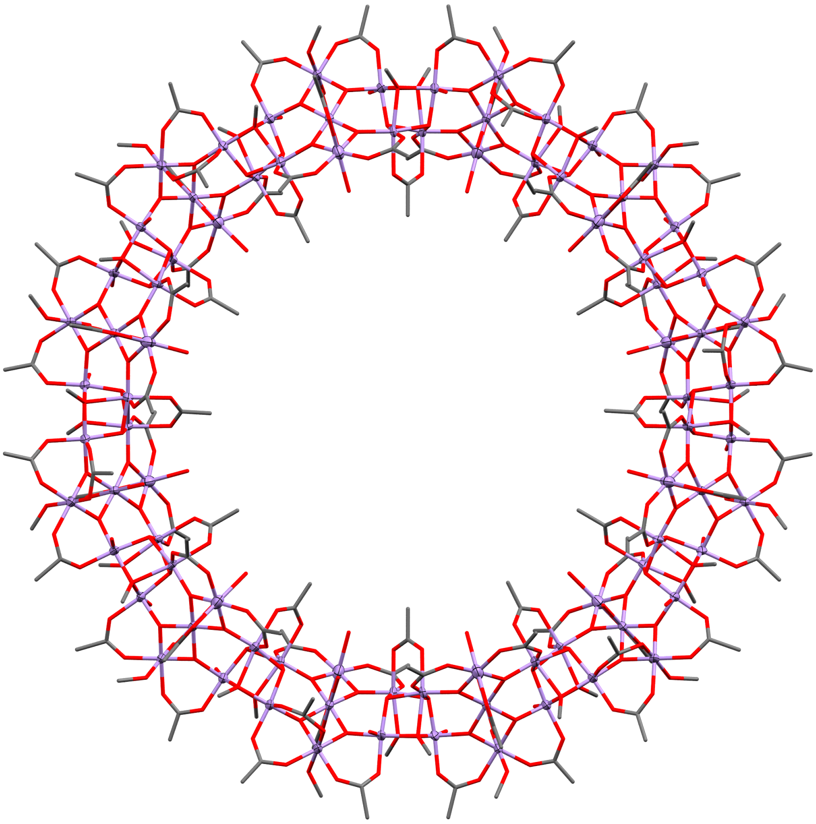

FIGURE 1.15: X-ray crystal structures of the Mn_{84} molecular wheel. Disordered species and hydrogen atoms have been omitted for clarity. Thermal ellipsoids of metal atoms shown at 70%. C = grey, Mn = light purple, O = red.

An even larger molecular wheel was reported by Zheng *et al.* in 2017, featuring 140 Gd^{III} centres in a 10-fold symmetric 6.0 nm ring (Figure 1.16).[81] This giant molecular wheel self-assembled from a mixture of $Gd(NO_3)_3 \cdot 6\,H_2O$ and *myo*-inositol (*cis*-1,2,3,5-*trans*-4,6-cyclohexanehexol) in the presence of sodium acetate. The complex also features carbonate groups which bind in a $5.2_{1,2}2_{2,3}2_{4,5}$ mode in Harris notation[82] (see Appendix A). Incorporation of carbonate anions into the complex was achieved by *in situ* generation from refluxing in atmosphere allowing for CO_2 fixation, which is a method that has previously been reported for a Ln_4 clusters.[83] With a large void diameter of $\sim$ 3.4 nm inside of the Gd_{140} wheel, this complex suffers the same structurally ambiguity, in the contents of the void space, as the Mn_{84} complex. Thermogravimetric analysis and CHN indicate the presence of approximately 80 water molecules distributed through the lattice and void space, which necessitated the use of a solvent mask to account for both the water molecules, and the 80 nitrate anions required to balance the charge of the complex. Magnetic characterization indicated a $\chi_m T$ value of 1042 cm^3 K mol^{-1}, which is close to the expected value for 140 non-coupled Gd^{III} ions. Upon cooling to 2 K the $\chi_m T$ profile was reported to decrease sharply to a value of 498 cm^3 K mol^{-1}, indicating weak antiferromagnetic interactions were present, which was further evidenced with simulations using a modified genetic algorithm.

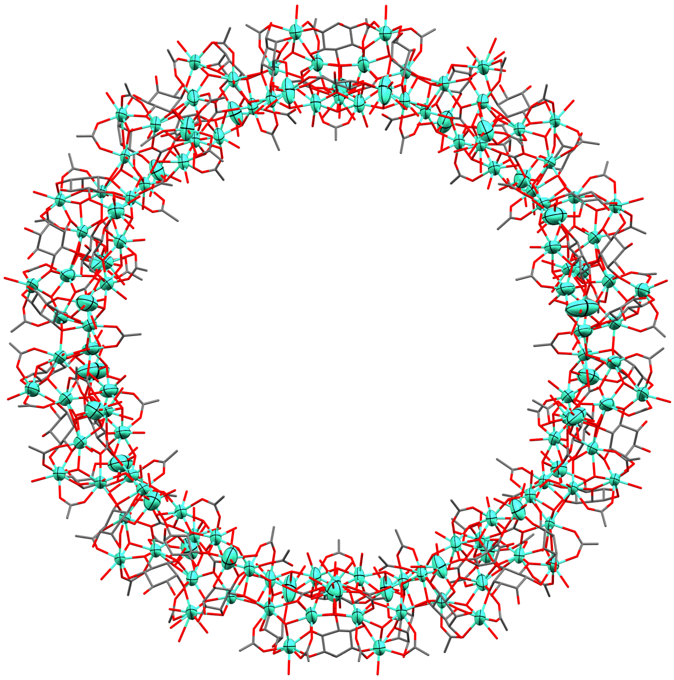

FIGURE 1.16: X-ray crystal structures of the Gd_{140} molecular wheel. Disordered species and hydrogen atoms have been omitted for clarity. Thermal ellipsoids of metal atoms shown at 70%. C = grey, Gd = turquoise, O = red.

1.4.2 The Mixed Valence Interface

Mixed valence complexes constitute a somewhat different class of homometallic cluster complexes, where from the perspective of formulation and atomic number they are the same, while also being isoelectronic with potential heterometallic analogues (e.g. a $Co^{II}Co^{III}$ complex and a $Co^{II}Fe^{II}$ complex). Mixed valence complexes are most common among the transition metals,[84–89] although mixed valence lanthanide complexes have been reported.[90–92] A prime example of a mixed valence cluster is the archetypal SMM, Mn_{12} (Figure 1.17), with its central $Mn^{IV}{}_4O_4$ cube surrounded by an octagonal $Mn^{III}{}_8(OAc)_8$ ring.[10,85] The Mn^{IV} centres were found to ferromagnetically interact with each other ($S_{Mn^{IV}} = 4 \times 3 = 12$), and antiferromagnetically couple to the Mn^{III} centres ($S_{Mn^{III}} = 8 \times 4 = 32$), resulting in an overall $S_{total} = 10$ ground state. This demonstrates how the presence two different oxidation states can add to the complexity of the molecular properties, through varying coordination number and geometry, as well as changing the electronic structure of potentially interacting spin centres.

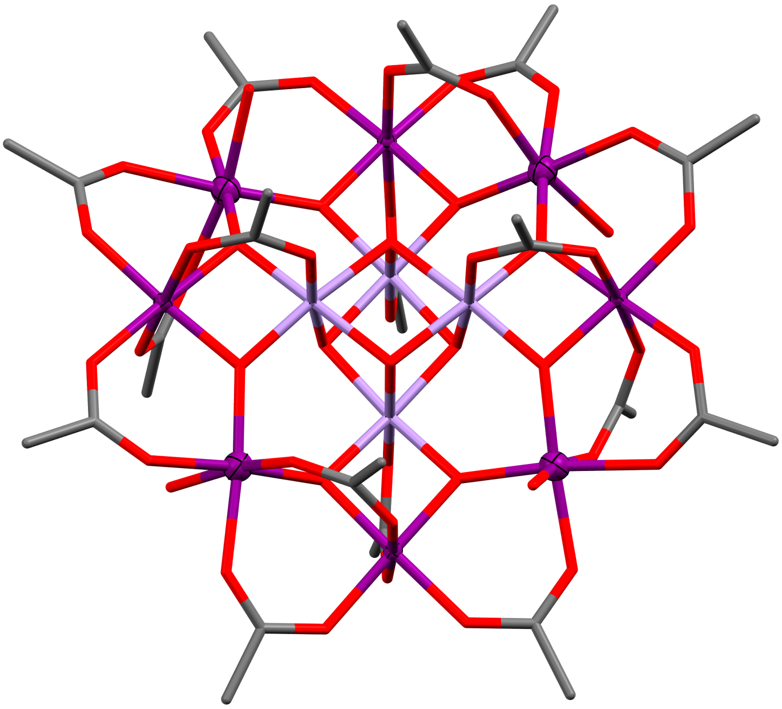

FIGURE 1.17: Neutron crystal structure of Mn_{12} reported by Christou *et al.*[93] Disordered species and hydrogen atoms have been omitted for clarity. Thermal ellipsoids of metal atoms shown at 99%. C = grey, Mn^{IV} = dark purple, Mn^{III} = light purple, O = red.

1.4.3 Heterometallic Complexes

The use of two or more different metals in the formation of coordination compounds provides an attractive target, particularly when utilizing metals from different regions of the periodic table, and especially in the field of molecular magnetism. Individually, homometallic 3*d* or 4*f* clusters have a number of shortcomings in the search for a highly functional SMM, such as the easily quenched orbital angular momentum of first row transition metals or the often unavoidable QTM present in purely lanthanide complexes. It's believed that these can be overcome by incorporating both types of metals, in relatively close proximity to each other, and using a ligand system which is sufficiently bulky so as to minimize any intermolecular interactions. 3*d*-4*f* SMMs were first reported in 2004 as $[CuL^1Ln(hfac)_2]_2$ squares (Ln = Tb or Dy, H_3L^1 = 1-(2-hydroxybenzamido)-2-(2-hydroxy-3-methoxybenzylideneamino)-ethane) by Matsumoto *et al.*[94] and $[Dy_6Mn^{III}_4Mn^{IV}_2(H_2L^2)_4(HL^2)_2L_{10}(MeOH)_{10}(H_2O)_2]$ (H_3L^2 = salicylhydroxamic acid) by Pecoraro *et al.*[95] While ligands can often be carefully designed to include binding pockets of the appropriate size containing the desired donor groups, formation of the predicted architecture is not always guaranteed, particularly when utilizing small mono- or bidentate ligands. While theoretically any architecture with some arbitrary 3*d*:4*f* stoichiometry could be obtained, triangular M_3Ln clusters (M = first row transition metal) with near planar M_3LnO_6 cores (Figure 1.18) are of particular interest.

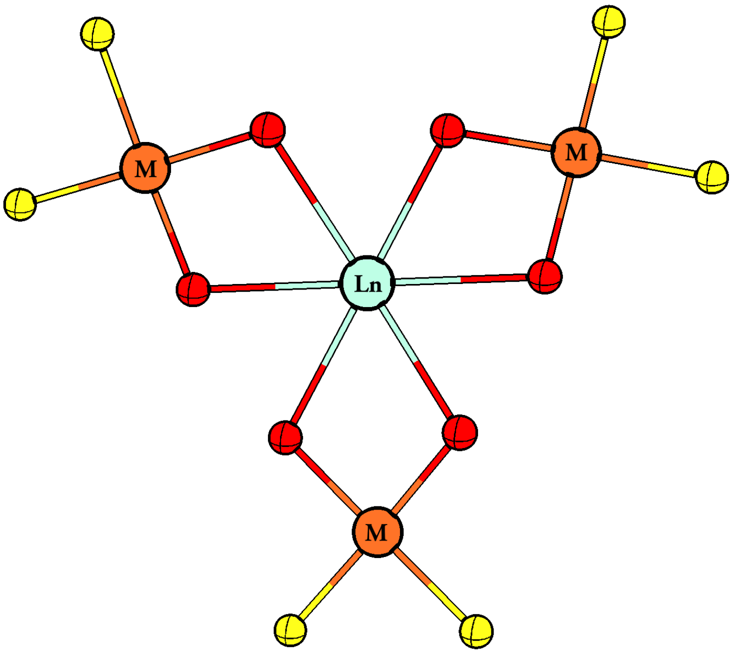

FIGURE 1.18: Schematic representation of a near planar M_3LnO_6 core with other groups bound to the transition metal equatorial sites in yellow.

When M is diamagnetic, the complexes possesses only 4*f* single ion character, conversely, when Ln is diamagnetic (or isotropic and non-coupled) the complex possesses purely 3*d* magnetic character with a triangular arrangement, thus necessitating a non-zero spin. Finally, the more complex but magnetically interesting case, where both 3*d* and 4*f* are paramagnetic and coupled with the potential for strong superexchange interactions and large S_{total} values. This metallacyclic M_3LnO_6 triangle motif was first reported by Nabeshima *et al.*, who used Zn_3La to template the [3 + 3] Schiff base condensation of 1,4-diformylbenzene-2,3-diol with various diamine linkers (Figure 1.19).[96] Inspired by the predictable formation of macrocyclic Zn_3La complexes, this motif was first extended to include other lanthanide ions,[97–103] and later to use Cu^{II},[104–110] Ni^{II},[111,112] and more recently Co^{II} as the 3*d* ions.[113,114]

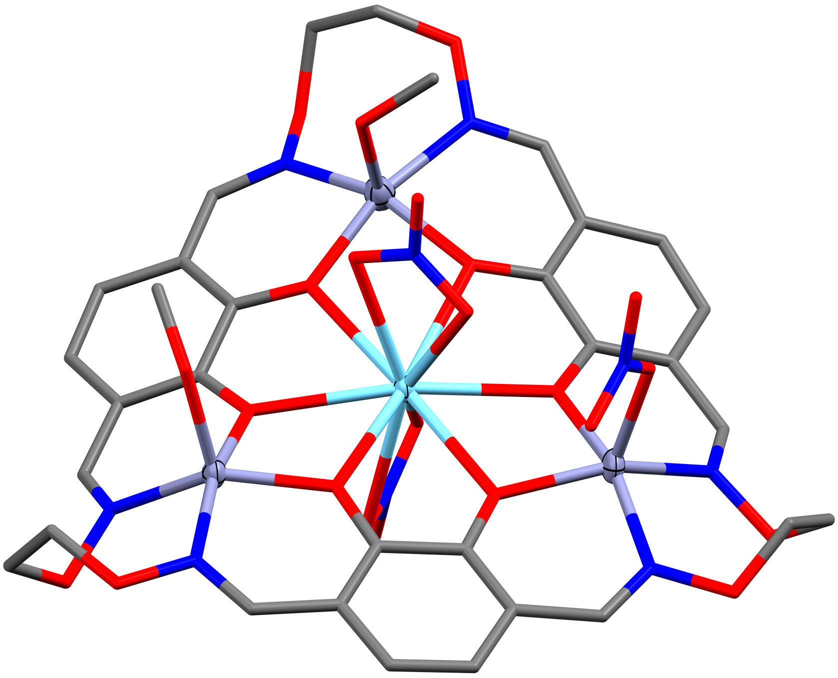

FIGURE 1.19: X-ray crystal structure of the first Zn_3La complex reported by Nabeshima *et al.* Hydrogen atoms have been omitted for clarity. Thermal ellipsoids of metal atoms shown at 70%. C = grey, La = light blue, N = blue, O = red, Zn = purple.

Throughout the literature, the target complexes of this type all involve [3 + 3] macrocyclic ligand systems, templated by the M_3Ln ions, with limited non-macrocyclic analogues sometimes isolated and reported as intermediate species. Mashima *et al.* has utilized M_3LnL^{macro} complexes ($M = Co^{II}$ or Zn^{II}) as catalysts for the co-polymerization of epoxides and CO_2,[103,113] while Brooker *et al.* focused on investigating the magnetic properties of discrete M_3LnL^{macro} complexes ($M = Zn^{II}$, Cu^{II}, or Ni^{II}) as well as six two-component one-dimensional polymer derivatives of the most promising SMM candidate, Cu_3Tb.[107–109] Of the M_3Ln complexes containing paramagnetic 3*d* metal centres reported by Brooker *et al.*, only some of those based on the Cu_3TbO_6 core exhibited slow relaxation of magnetization and were capable of acting as SMMs. The first triangular Cu_3Tb complex reported of this type involved the [3 + 3] macrocycle formed from 1,4-diformylbenzene-2,3-diol and 1,3-diaminopropane (Figure 1.20).[104] The properties of this core structure were further investigated by altering the strength of the ligand field through varying the size of diamine linker involved in the macrocyclization, with the 1,4-diaminobutane linker providing the first reported macrocyclic 3*d*-4*f* SMM which exhibited the slow relaxation of magnetization in zero applied field.[106] The series of reported macrocyclic Co_3Ln complexes do not include any magnetic characterization, and although the reported Ni_3Ln complexes do, no slow relaxation of magnetization was observed.

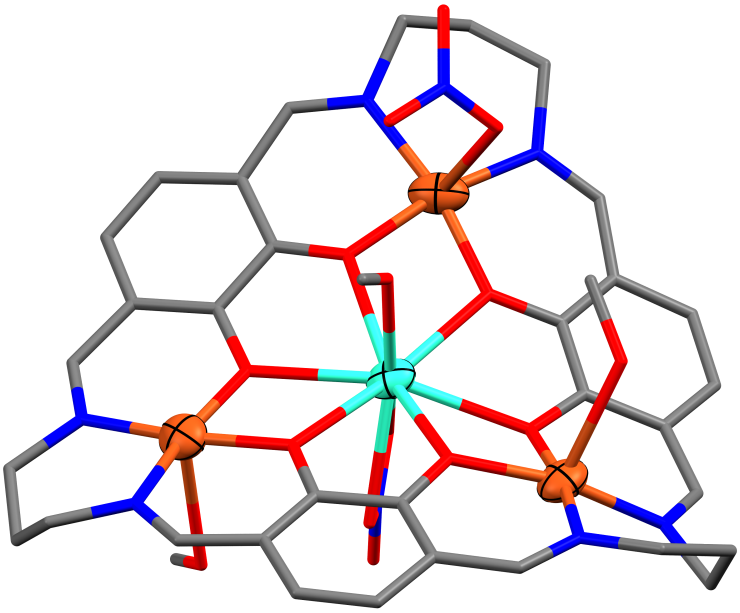

FIGURE 1.20: X-ray crystal structure of the first Cu_3Tb complex reported by Brooker *et al.* Non-coordinated species and hydrogen atoms have been omitted for clarity. Thermal ellipsoids of metal atoms shown at 70%. C = grey, Cu = orange, N = blue, O = red, Tb = turquoise.

Compared to the large number of macrocyclic M_3Ln metallacycles with this planar triangle topology, only three analogous non-macrocyclic aldehyde containing complexes have been isolated and structurally reported, without any magnetic characterization, excluding the work presented in Chapters 3 – 5 of this thesis. These three complexes were prepared from the methanolic 3:3:1 reaction of 1,4-diformylbenzene-2,3-diol with $Zn(NO_3)_2 \cdot 6\,H_2O$ or $Ni(NO_3)_2 \cdot 6\,H_2O$ and the appropriate lanthanide nitrate salt. The $[Zn_3La]^{ald}$ complex (Figure 1.21) reported by Nabeshima *et al.*[115] is nearly isostructural with the $[Ni_3Dy]^{ald}$ and $[Ni_3Yb]^{ald}$ complexes reported by Brooker *et al.*[111] All feature near-octahedral transition metal ions bound within the O_4 pocket provided by a phenol and an aldehyde donor each from two separate ligands, axially capped by methanol molecules (or crystallographically disordered 1:1 MeOH:H_2O caps in $[Ni_3Yb]^{ald}$), and a 10-coordinate Ln^{III} centre, with six equatorial phenol/catechol donors in the ligand plane, and an η_2-NO_3 anion capping on each side of the plane. The +1 charge on the complexes are balanced by a non-coordinated nitrate anion.

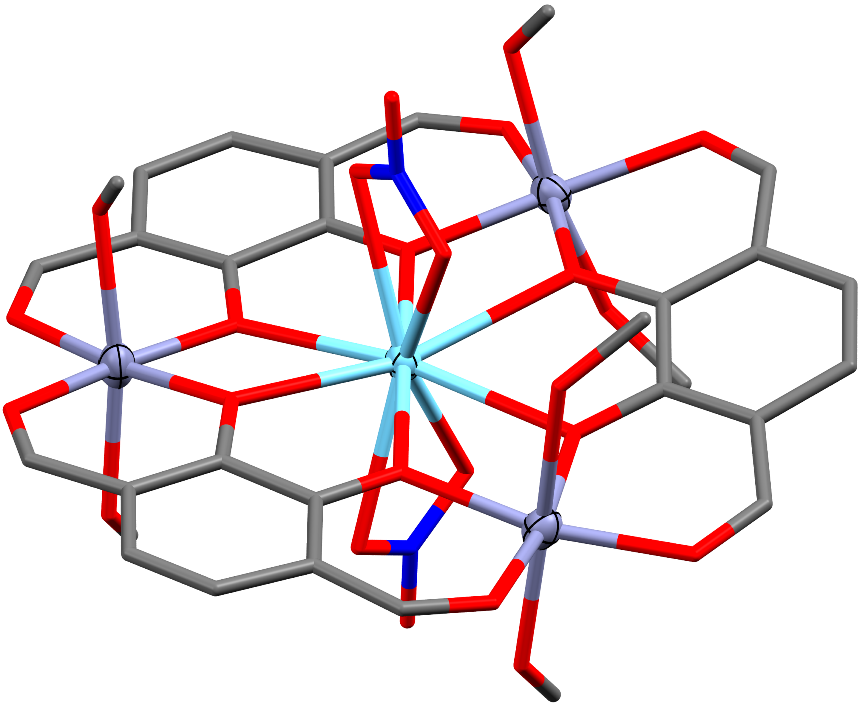

FIGURE 1.21: X-ray crystal structure of the first non-macrocyclic Zn_3La metallacycle complex reported by Nabeshima *et al.* Non-coordinated species and hydrogen atoms have been omitted for clarity. Thermal ellipsoids of metal atoms shown at 70%. C = grey, La = light blue, N = blue, O = red, Zn = purple.

The Plieger groups continued interest in the coordination chemistry of symmetric dialdehyde/diimine based ligand systems fuelled the direction of this research. We aimed to exploit the structural rigidity of a small symmetric ligand, namely 1,4-bisformyl-2,3-naphthalenediol (**H_2L1**), to investigate its coordination chemistry and examine the magnetic properties of the resulting complexes. The Plieger group has previously studied the magneto-structural correlation in a number of homometallic 3*d* complexes, with a growing interest in heterometallic 3*d*-4*f* complexes as functional SMMs. By incorporating both 3*d* and 4*f* metals in close proximity within a complex, the magnetic shortcomings of homometallic SMMs can often be overcome. By building on a family of macrocyclic complexes reported in the literature, we expected to be able to generate $\mathbf{L}_3X^{II}{}_3Y^{II/III}{}_1$ complexes as in Figure 1.18, where M is a first row transition metal, with approximate three fold symmetry about the Y (or Ln) centre.

The use of a small, stable, and symmetric dialdehyde ligand such as **H_2L1** also opens the possibility to extend and further functionalize the ligand system through a large number of reactions; with perhaps the most obvious being through Schiff base condensation to yield a symmetric diimine ligand, while also introducing another chelating group.

Throughout this PhD, the aim was to explore the coordination chemistry of related symmetric dialdehyde/diimine ligands through self-assembly with various homo- or heterometallic combinations of metals, with the overall goal of generating magnetically interesting compounds.

Chapter 2

A Fleeting Look at Synthesis

2.1 General Experimental Details

Reagents and Solvents

All starting materials, reagents, and solvents were obtained from commercial sources and used without purification, unless otherwise stated. All solvents used were of analytical reagent grade, if stated as dry they were subject to the following purification: MeOH and EtOH were distilled from their corresponding magnesium alkoxides and stored over activated molecular sieves. THF, toluene, and DCM were passed through alumina columns on an in-house solvent purification system and stored over activated molecular sieves.

Synthetic Methods

All reactions were carried out in acetone rinsed, oven-dried glassware, under ambient conditions unless otherwise stated. Reactions under an inert atmosphere were carried out under an argon atmosphere using standard Schlenk line techniques. Elevated reaction temperatures refer to the temperature of an external oil or sand bath. All organic extracts were dried over magnesium or sodium sulfate and filtered through glass wool. Solvents were removed under reduced pressure using a rotary evaporator, with the last traces of solvents being removed under high vacuum using an oil pump attached to a Schlenk line or freeze drier.

Characterization

All organic compounds were characterized by ^{1}H and ^{13}C NMR on a Bruker Avance 500 spectrometer. All chemical shifts are reported relative to residual solvent. Full NMR assignments were made using their ^{1}H and ^{13}C spectra, including NOESY, HMQC, and HMBC where necessary. Selected spectra can be found in Appendix B.

High resolution MS (HR-MS) were recorded on a ThermoScientific Q Exactive Focus Hybrid Quadrupole-Orbitrap Mass Spectrometer. Elemental analyses (C, H, and N) were provided by the Campbell Microanalytical Laboratory, University of Otago, New Zealand. ATR-FTIR spectra were collected on a Nicolett 5700 FTIR fitted with a diamond ATR module. Selected IR spectra can be found in Appendix B. Melting point measurements were collected on a Gallenkamp melting point apparatus, and are uncorrected.

Single crystal X-ray data were collected on a Bruker D8 Venture equipped with a IμS 3.0 Microfocus Cu-Kα source and PHOTON III detector. Samples were mounted on MiTeGen mylar loops using Fomblin Y perfluoro-ether oil and cooled to 100 K using an Oxford Cryostream 800. The reflection data was collected using the APEX3 software package.[116] Structures were solved by intrinsic phasing algorithms using SHELXT,[117] and unless otherwise stated, all non-hydrogen atoms were refined anisotropically using SHELXL,[118] as implemented in Olex2.[119] Hydrogen atoms were calculated at their ideal positions, and refined using the riding model with fixed U_{iso} values. Crystal structure and refinement details can be found in Appendix D. CIF files and CheckCif reports can be found in the enclosed digital appendix.

ConQuest 2.0.4 (Build 270014) was used to access the CSD library, version 5.41 (November 2019), when searching the literature.

Magnetic measurements were carried out by our collaborator, Prof. Takayuki Ishida, at Tokyo Univeristy of Electro-Communications, Chofugaoka, Japan. DC magnetization and magnetic susceptibility measurements were carried out with a Quantum Design MPMS-XL7 SQUID magnetometer using a static field of 0.05 T. A field of 0.5 T was used to measure the susceptibility of samples with small magnetic moments. Measurements were corrected with diamagnetic blank data from the empty sample holder and the diamagnetic contributions of the samples were estimated using Pascal's constants. The AC magnetic susceptibilities were recorded on a Quantum Design PPMS apparatus equipped with an AC/DC magnetic susceptibility option. The polycrystalline samples were fixed with a small amount of eicosane to avoid magnetic torquing of the sample.

2.2 Ligand Synthesis

1,4-Bisformyl-2,3-naphthalenediol
H_2L1

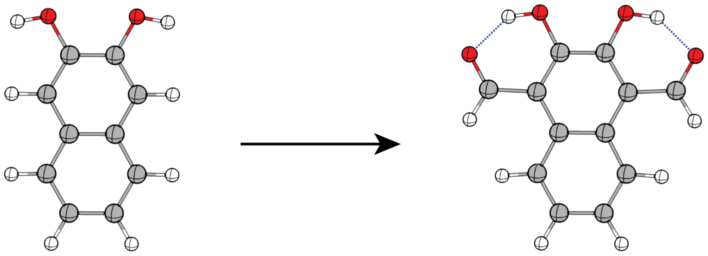

This synthesis of **H_2L1**[112] is based on a procedure originally published by MacLachlan *et al.*[120]

To a stirred suspension of formamidine acetate (15.6 g, 150 mmol) in dioxane (300 mL) at 95 °C was added acetic anhydride (28.4 mL, 300 mmol). After one hour, 2,3-naphthalenediol (3.00 g, 18.8 mmol) was added in one portion and stirred at 95 °C for 2 days, after which time the the mixture was concentrated under reduced pressure until a thick red paste remained. Water (400 mL) was then added and the mixture stirred at 60 °C for two hours, followed by the addition of HCl (1 M, 400 mL). A fine yellow-brown solid precipitated from solution upon stirring overnight and was isolated by filtration. The crude product was washed with water (3 x 100 mL) followed by hexane (3 x 100 mL), then purified by silica gel column chromatography, eluting with 100% DCM (R_f = 0.25), yielding 1,4-bisformyl-2,3-naphthalene-2,3-diol (3.82 g, 94%). The ^{1}H NMR spectrum agreed with literature values, (500 MHz, $CDCl_3$): δ 12.98 (2H, *s*, Ar-OH), 10.91 (2H, *s*, CH=O), 8.39 (2H, *dd*, J_1 = 6.4 Hz, J_2 = 3.1 Hz, Ar-H), 7.59 (2H, *dd*, J_1 = 6.4 Hz, J_2 = 3.1 Hz, Ar-H) ppm. ATR-IR $\bar{\nu}$: 3409, 1673, 1641, 1610, 1554, 1522, 1452, 1422, 1405, 1375, 1308, 1260, 1219, 1172, 1165, 1022, 1007, 929, 857, 745, 700 cm^{-1}. Decomposes above 190 °C.

H_2L1 can be purified by crystallization, with yields around 85%, from the slow evaporation of DCM or $CHCl_3$ to yield thin yellow plates suitable for single crystal X-ray diffraction, as reported by MacLachlan *et al.*[120]

2-(Aminomethyl)phenol

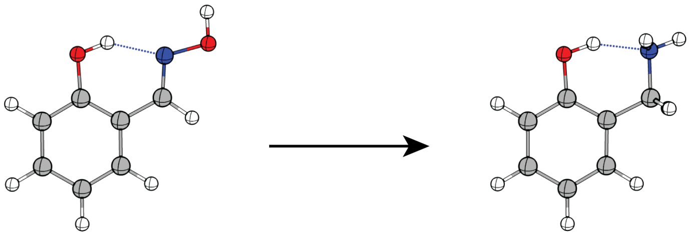

Due to limited reagents, ambient interference by humidity, and intermittently working equipment, two different syntheses have been used to generate crude 2-(aminomethyl) phenol with roughly equal effect: a Pd/C hydrogenation and a $LiAlH_4$ reduction.

Pd/C hydrogenation

Salicylaldoxime (1.50 g, 10.9 mmol) and 10% Pd/C (0.15 g) were mixed in MeOH (10 mL) in a Parr hydrogenation vessel. The vessel was evacuated then maintained under a hydrogen atmosphere at 40 psi, with vigorous shaking, for 16 hours. The reaction mixture was filtered through Celite and the filtrate was concentrated under reduced pressure to yield crude 2-(aminomethyl)phenol as a pale yellow-brown solid.

$LiAlH_4$ reduction

To a stirred suspension of salicylaldoxime (1.50 g, 10.9 mmol) in dry Et_2O (120 mL) at 0 °C under a positive pressure of Ar, was added $LiAlH_4$ (1.37 g , 36.00 mmol), in small portions. After complete addition, the mixture was allowed to warm to room temperature then refluxed for 4 hours. The reaction was then cooled to 0 °C and slowly quenched with 10% aqueous NaOH. The organic layer was separated and concentrated under reduced pressure to yield crude 2-(aminomethyl)phenol as a pale yellow solid.

Purification

Purification of crude 2-(aminomethyl)phenol was first attempted by silica gel column chromatography eluting with hexane/EtOAc in ratios from 19:1 to 1:1, however bis(2-hydroxybenzyl)amine was the primary product obtained. Purification by recrystallization of the crude product was successful by the slow evapouration of a concentrated solution in CCl_4. This method gave analytically pure 2-(aminomethyl)phenol as an off-white solid in yields from 0.42 g (31%) to 0.47 g (35%), independent of the preparation method. The ^1H NMR spectrum agreed with literature values, (500 MHz, D_2O): δ 7.19 - 7.25 (2H, *m*, Ar-H), 6.76 (1H, *d*, J_1 = 7.8 Hz, Ar-H), 6.71 (1H, *t*, J_1 = 7.4 Hz, Ar-H), 4.08 (2H, *s*, CH_2) ppm.

1,4-Bis((*E*)-((2′-hydroxybenzyl)imino)methyl)-2,3-naphthalenediol

H_4L2

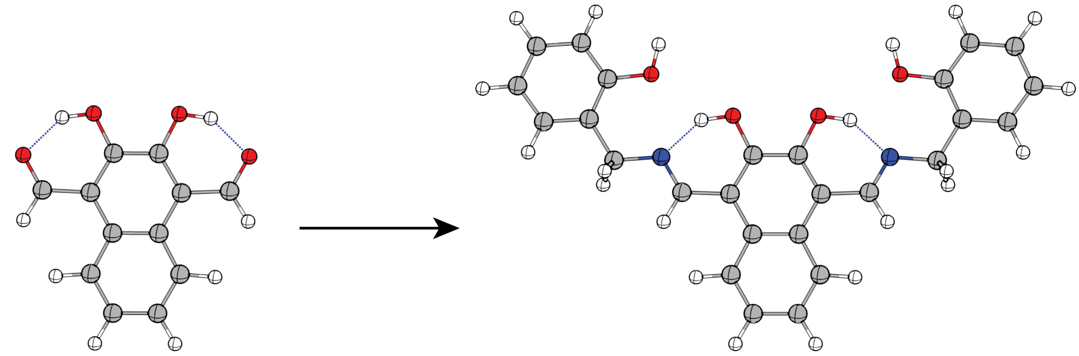

To a stirred suspension of 1,4-bisformyl-2,3-naphthalenediol (1.08 g, 5.00 mmol) in dry MeOH (40 mL) was slowly added a solution of 2-(aminomethyl)phenol (1.24 g, 10.0 mmol) in dry MeOH (10 mL). The reaction mixture was refluxed for 2 hours, then stood overnight to precipitate the product as a brown solid. The solid material was filtered off and the filtrate was concentrated to approximately 15 mL under reduced pressure and cooled to -4 °C to afford red crystals. The combined solids were hot recrystallized from dry MeOH or $CHCl_3$, affording pure 1,4-bis((*E*)-((2′-hydroxybenzyl)imino)methyl)-2,3-naphthalenediol (2.07 g, 97%) as bright red block crystals. ^1H NMR (500 MHz, DMSO-d_6): δ 13.39 (2H, *t*, J_1 = 5.4 Hz, Naphth-OH), 9.94 (2H, *s*, Ar-OH), 8.93 (2H, *d*, J_1 = 11.6 Hz), 7.71 (2H, *m*, Naphth-H), 7.26 (2H, *d*, J_1 = 7.4 Hz, Ar-H), 7.16 (2H, *t*, J_1 = 7.4 Hz, Ar-H), 7.06 (2H, *m*, Naphth-H), 6.86 (2H, *d*, J_1 = 8.0 Hz, Ar-H), 6.80 (2H, *t*, J_1 = 7.4 Hz, Ar-H), 4.72 (4H, *d*, J_1 = 4.4 Hz, CH_2) ppm. ^{13}C NMR (126 MHz, DMSO-d_6): δ 176.2, 158.6, 155.9, 129.9, 129.8, 127.0, 124.1, 123.4, 119.6, 119.0, 115.7, 106.6, 50.1 ppm. ATR-IR $\overline{\nu}$: 3063, 2940, 2705, 2614, 1631, 1603, 1532, 1459, 1444, 1387, 1360, 1328, 1282, 1243, 1213, 1186, 1138, 1108, 1041, 987, 936, 874, 834, 766, 756, 740 cm^{-1}. HR-MS: 427.1652 (calculated for $C_{26}H_{22}N_2O_4 + H^+$). Microanalytical data found(calc) for **H_4L2** (calculated for $C_{26}H_{22}N_2O_4$, M_r = 426.46 g mol^{-1}) C: 72.98(73.23), H: 5.14(5.20), N: 6.81(6.57). MP: 178.6 – 184.1 °C.

1,4-Bis((*E*)-((2-(pyridin-2-yl)ethyl)imino)methyl)-2,3-naphthalenediol
H_2L3

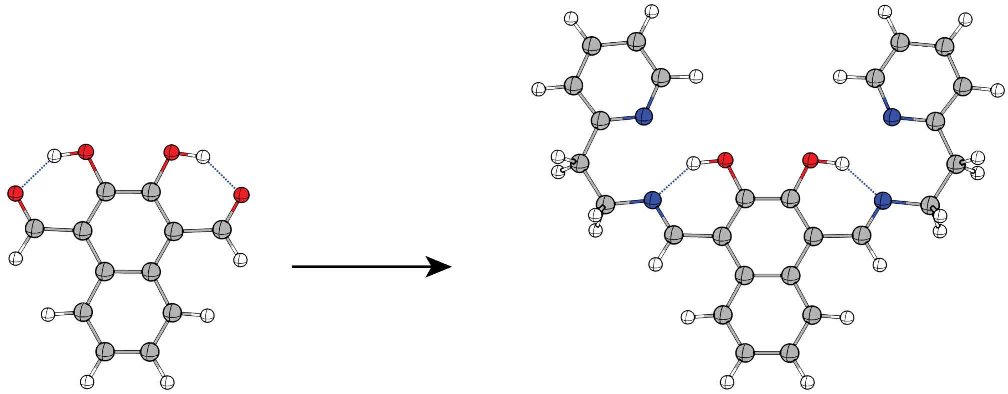

To a stirred suspension of 1,4-bisformyl-2,3-naphthalenediol (1.08 g, 5.00 mmol) in dry MeOH (40 mL) was slowly added a solution of 2-(2-aminoethyl)pyridine (1.23 g, 10.0 mmol) in dry MeOH (10 mL). The reaction mixture was refluxed for 2 hours, then stood overnight to precipitate the product as an orange solid. The solid material was filtered and the filtrate was concentrated to approximately 10 mL under reduced pressure and cooled to -4 °C to afford dark red crystals. The combined solids were hot recrystallized from dry MeOH, affording pure 1,4-bis((*E*)-((2-(pyridin-2-yl)ethyl)imino)methyl)-2,3-naphthalenediol (1.99 g, 94%) as dark red block crystals. ^{1}H NMR (500 MHz, DMSO-d_6): δ 13.12 (2H, *br s*, Naphth-OH), 8.766 (2H, *s*, CHN), 8.55 (2H, *d*, J_1 = 4.7 Hz, Ar-H), 7.73 (2H, *t*, J_1 = 7.6 Hz, Ar-H), 7.65 (2H, *m*, Naphth-H), 7.32 (2H, d, J_1 = 7.6 Hz, Ar-H), 7.24 (2H, *t*, J_1 = 6.4 Hz, Ar-H), 7.02 (2H, *m*, Naphth-H), 4.01 (4H, *t*, J_1 = 6.7 Hz, CH_2), 3.16 (4H, *t*, J_1 = 6.7 Hz, CH_2) ppm. ^{13}C NMR (126 MHz, DMSO-d_6): δ 175.5, 158.1, 158.0, 149.1, 136.6, 126.4, 123.5, 122.8, 121.7, 118.6, 106.1, 48.9, 38.0 ppm. ATR-IR $\bar{\nu}$: 3585, 3256, 2976, 1627, 1603, 1594, 1569, 1538, 1479, 1439, 1362, 1331, 1285, 1244, 1152, 1102, 1002, 851, 777, 750, 676, 657, 629 cm^{-1}. HR-MS: 425.1967 (calculated for $C_{26}H_{24}N_4O_2 + H^+$). Microanalytical data found(calc) for **H_2L3** (calculated for $C_{26}H_{22}N_2O_4$, M_r = 424.49 g mol^{-1}) C: 73.55(73.56), H: 5.63(5.70), N: 13.51(13.20). MP: 148.3 – 151.0 °C.

2-Hydroxy-3-(aminomethyl)-5-(*tert*-butyl)benzaldehyde hydrochloride aminoSal

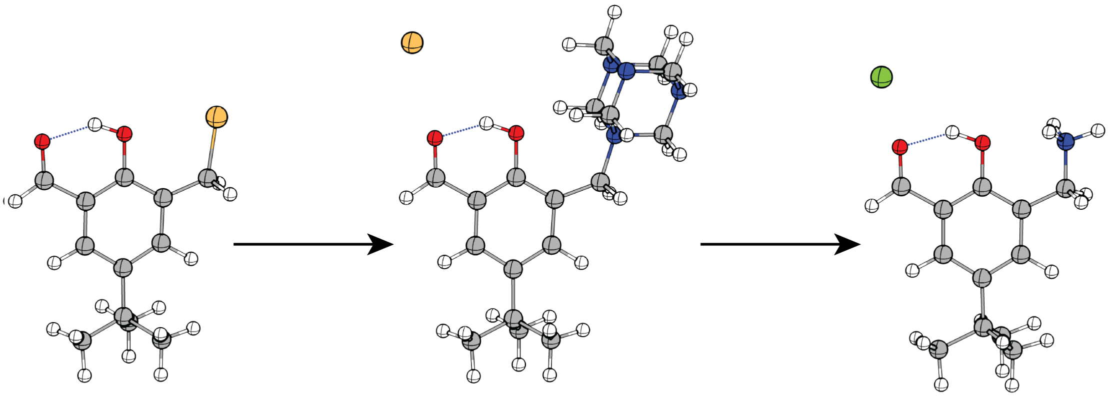

The starting material for this reaction is readily available in the Plieger lab, and its synthesis starting from 4-(*tert*-butyl)phenol has been well documented.[121–124]

To a stirred solution of 2-hydroxy-3-(bromomethyl)-5-(*tert*-butyl)benzaldehyde (5.00 g, 18.5 mmol) in warm $CHCl_3$ (50 mL) was added a solution of 1,3,5,7-tetraazaadamantane (3.48 g, 25.0 mmol) in $CHCl_3$ (100 mL). The reaction was vigorously stirred and after three minutes the intermediate product, 1-(2-hydroxy-3-formyl-5-(*tert*-butyl)benzyl)-1,3,5,7-tetraazaadamantium bromide (**hexamineSal**), rapidly precipitated as a flaky pale yellow crystalline solid (6.91 g), which could be redissolved in hot chloroform (300 mL) and crystallized in the freezer (6.42 g, 17.5 mmol, 95%). Once filtered and dried, **hexamineSal** (5.00 g, 12.2 mmol) was suspended in hot EtOH (250 mL) to which concentrated HCl (37%, 100 mL) was added dropwise until the suspension became a bright yellow solution and refluxed overnight. Upon cooling in a freezer the product, 2-hydroxy-3-(aminomethyl)-5-(*tert*-butyl)benzaldehyde hydrochloride (**aminoSal**), precipitated as a hygroscopic yellow powder (2.91 g, 12 mmol, 98%). ^1H NMR (500 MHz, DMSO-d_6): δ 11.10 (1H, *s*, Ar-OH), 10.12 (1H, *s*, CHO), 8.33 (3H, br *s*, NH_3^+), 7.90 (1H, *d*, J_1 = 2.3 Hz, Ar-H), 7.81 (1H, *d*, J_1 = 2.3 Hz, Ar-H), 7.27 (3H, 1:1:1 *t*, ^{14}N–^1H coupling, NH_3^+, J_1 = 50 Hz), 4.06 (2H, *s*, CH_2), 1.30 (9H, *s*, ^{t}Bu) ppm. ^1H NMR (500 MHz, DMSO-d_6): δ 197.1, 156.7, 142.7, 135.8, 129.9, 122.3, 121.2, 36.9, 34.6, 31.5 ppm. ATR-IR $\overline{\nu}$: 3382, 3116, 2962, 2868, 1654, 1614, 1463, 1308, 1267, 1218, 1118, 1081, 1002, 951, 900, 893, 883, 829, 767, 752, 713 cm^{-1}. HR-MS: 208.1331 (calculated for $C_{12}H_{18}NO_2Cl - Cl^-$). Microanalytical data found(calc) for **aminoSal** (calculated for $C_{12}H_{18}NO_2Cl$, M_r = 243.73 g mol^{-1}) C: 59.41(59.13), H: 7.72(7.44), N: 5.81(5.75). Decomposes above 168.5 °C.

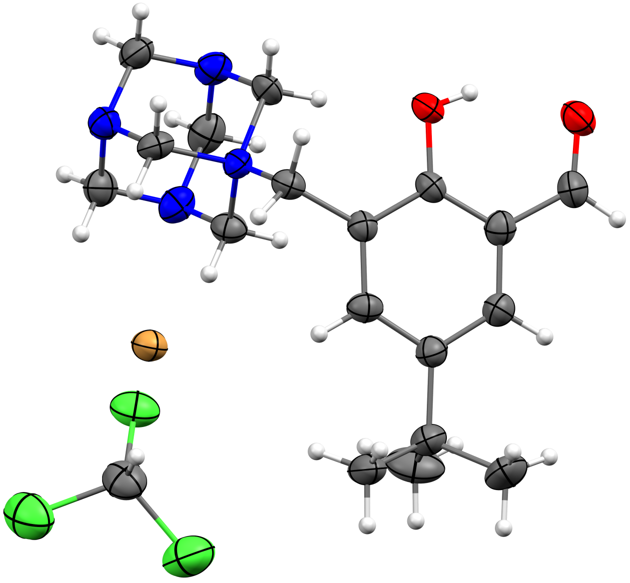

FIGURE 2.1: X-ray crystal structure of the **hexamineSal** chloroform solvate. Thermal ellipsoids shown at the 30% probability level. C = grey, O = red, N = blue, Br = orange, Cl = green.

2.3 Complexes of H_2L1

M_3Ln Triangle complexes

All M_3Ln triangle complexes, including **[Ni_3Gd]**$_{acid}$ and the polymeric **[Ni_3Tb]**$_n$, featured in Chapters 3 – 5 were prepared by the same method.

To a stirred suspension of **H_2L1** (108 mg, 0.5 mmol) in methanol (5 mL) was added a methanolic solution of the appropriate transition metal nitrate (0.5 mmol, 5 mL), causing the ligand suspension to rapidly dissolve. Methanolic solutions of the appropriate lanthanide salt (0.167 mmol, 2 mL) were then added, and no further colour changes were observed. Certain reaction mixtures, particularly those involving cobalt, produced an intermediate precipitate which redissolved upon further stirring, thus all complexations were stirred overnight to ensure complete dissolution of all components. Solutions were then filtered into the inner of a double vial setup, with Et_2O in the outer vial for crystallization by vapour diffusion. IR spectroscopy confirmed the presence of coordinated aldehyde groups in the 1610 – 1620 cm^{-1} region with the complete disappearance of the stretches corresponding to unreacted aldehyde (1673 and 1641 cm^{-1}).

Subsequent recrystallizations were performed in the same manner, by filtering the crystalline material and redissolving in a minimal amount of methanol before vapour diffusing with Et_2O, to yield high-quality crystals which were characterized by FT-IR and single crystal XRD, with bulk purity established by elemental analysis.

2.4 Molecular Structures

H_4L2

The red block shaped crystals of **H_4L2** produced upon cooling or by hot recrystallization were of sufficient quality for single crystal X-ray diffraction. **H_4L2** typically crystallized in the triclinic space group $P\bar{1}$ as the dimethanol solvate with $Z' = 1$ (Figure 2.2), however plate-like crystals of the same material were sometimes observed which crystallized in the centrosymmetric monoclinic space group $P2_1/n$, also as the dimethanol solvate with $Z' = 1$. Both the triclinic and monoclinic phases pack with considerable naphthalene – naphthalene $\pi - \pi$ interactions as well as intermolecular $COH_{benzyl} \cdots CO_{naphth}$ hydrogen bonds, the triclinic phase also features $\pi - \pi$ stacking interactions between the benzyl side-arms of neighbouring molecules.

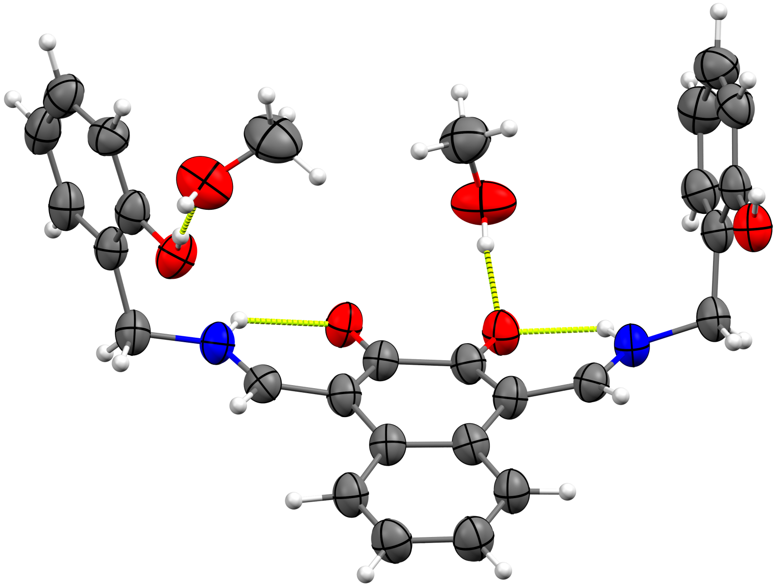

FIGURE 2.2: X-ray crystal structure of the **H_4L2** dimethanol solvate. Thermal ellipsoids shown at the 70% probability level. C = grey, O = red, N = blue.

H_2L3

The dark red block crystals of **H_2L3** were also of sufficient quality for single crystal X-ray diffraction. **H_2L3** crystallized in the base centred monoclinic space group $C2/c$ ($Z' = 0.5$) as the chloroform solvate (Figure 2.3). All aromatic rings are significantly offset resulting in no appreciable $\pi - \pi$ stacking interactions, nor are there any notable intermolecular hydrogen bonds or CH – π interactions.

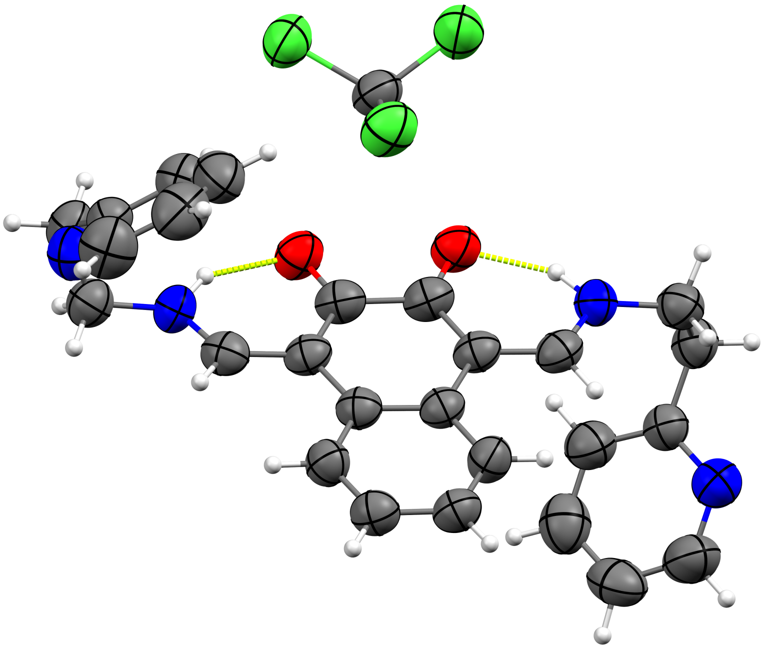

FIGURE 2.3: X-ray crystal structure of the **H_2L3** chloroform solvate. Thermal ellipsoids shown at the 70% probability level. C = grey, O = red, N = blue, Cl = green.

Tautomerism

Of particular note in the crystal structures of **H_4L2** and **H_2L3** is the protonation of the nitrogen atoms either side of the naphthalene ring, and consequent shortening of the $C_{naphth} - O$ bond (1.274(2) Å and 1.274(4) Å, respectively), indicating significant double bond character. The unit cell parameters remain the same for both compounds at 293 K and 100 K, indicating this is phenomena is not a low temperature induced transition but simply occurs in the solid state. Figure 2.4 shows a proposed scheme for the keto-enol — imine-enamine like tautomerism occurring in both **H_4L2** and **H_2L3**. Bond lengths of interest for both of these ligands are tabulated in Table 2.1 along with the dialdehyde precursor (**H_2L1**) and **L2** bound in the complex **Ni_{16}** as the enol-imine form for comparison.

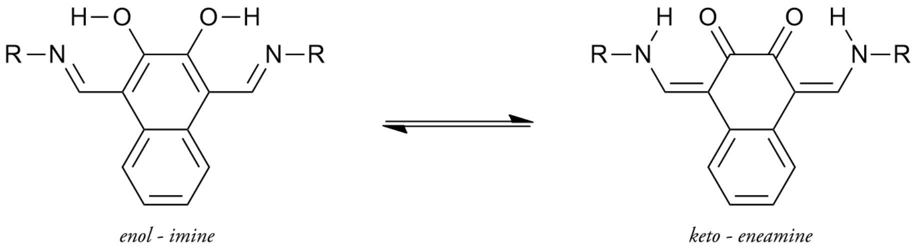

FIGURE 2.4: Schematic representation for the proposed keto-enol — imine-enamine like tautomerism.

TABLE 2.1: Selected average bond lengths (Å) for **H_4L2**, **H_2L3**, **H_2L1** and **$L2^{Ni_{16}}$**.

	enol-imine		*keto-eneamine*	
	H_2L1[a]	**$L2^{Ni_{16}}$**	**H_4L2**	**H_2L3**
$C_{naphth} - O$	1.350(3)	1.356(9)	1.274(2)	1.274(4)
$C_{naphth} - CN$	1.458(3)	1.462(9)	1.418(3)	1.404(5)
OC – CO	1.421(3)	1.482(9)	1.501(3)	1.495(5)
C – N	1.234(3)	1.258(9)	1.305(3)	1.316(5)

[a] Lengths given correspond to aldehyde group rather than imine/eneamine group.

DFT calculations (Output 2.1) were performed to relax the geometries of both the keto-eneamine and enol-imine forms of **H_4L2**, with appropriate bond modifications made from the crystal structure. The B3LYP hybrid functional,[125] when paired with a relatively large basis set and Grimme's dispersion correction, has been shown to provide fast and accurate geometries for main group and organic systems.[126–128] The conductor-like polarizable continuum model, CPCM,[129] has also been included as a solvent model, which when used with an infinite dielectric constant is a common way to crudely model non-covalent interactions in a crystalline environment for small molecules,[130–132] however will not fully reproduce the effects of $\pi - \pi$ stacking between the benzyl arms of **H_4L2**.

OUTPUT 2.1: Input parameters used for the geometry optimization of **H_4L2** and **H_2L3**.

```
! B3LYP Def2-TZVP Def2/J RIJCOSX D3BJ CPCM Opt Freq
```

The enol-imine form of **H_4L2** optimized with near perfect C_s symmetry (RMSD = 0.039), and as a consequence of the fully aromatized ring system, the naphthalene backbone is perfectly planar (Figure 2.5). In contrast, the keto-eneamine form of **H_4L2** better represents the crystal structure with an RMSD value of 0.312 from the idealized C_s point group and a non-planar naphthalene backbone due to its naphthalene-2,3(1*H*,4*H*)-dione character. Consistent with the structural comparison, single point energy calculations indicate that the keto-eneamine form is more stable than the enol-imine form by 0.0142 Hartree (37.3 kJ mol^{-1}). Similar calculations using an infinite dielectric constant for both forms of **H_2L3** indicate that the keto-eneamine form is more stable than the corresponding enol-imine form by 0.0150 Hartree (39.4 kJ mol^{-1}). Gas phase calculations for each form of **H_4L2** also indicate that the keto-eneamine form is more stable, however the energy difference is much smaller at just over $2k_\mathrm{B}T$ (0.0022 Hartree, 5.76 kJ mol^{-1}).

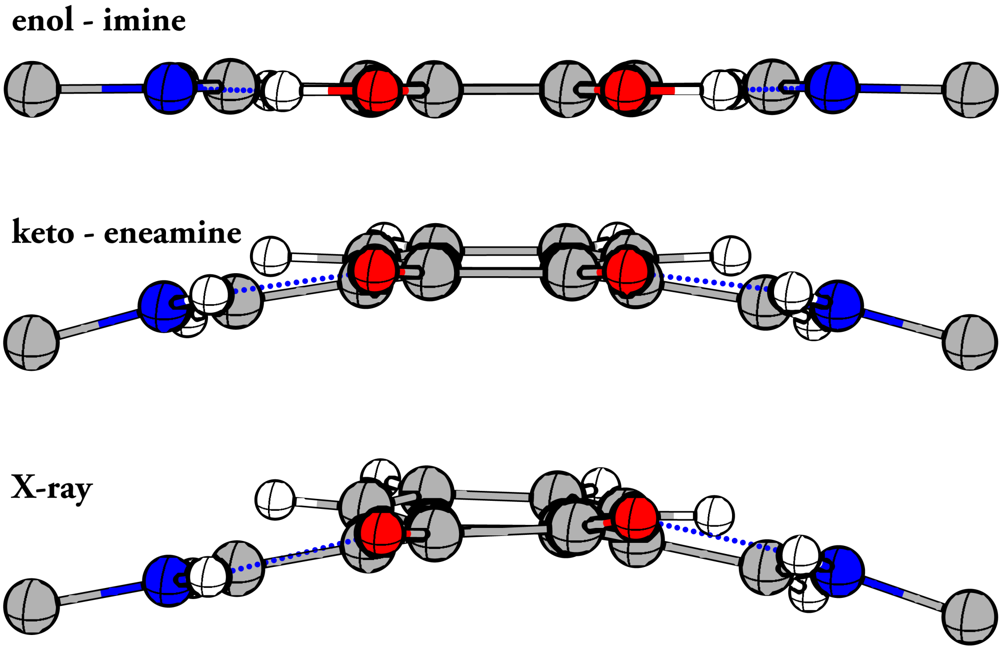

enol - imine

keto - eneamine

X-ray

FIGURE 2.5: Comparison of the enol-imine, keto-eneamine, and X-ray structures looking down the catechol-naphthalene plane aligning C2 and C3 with C5 and C10.

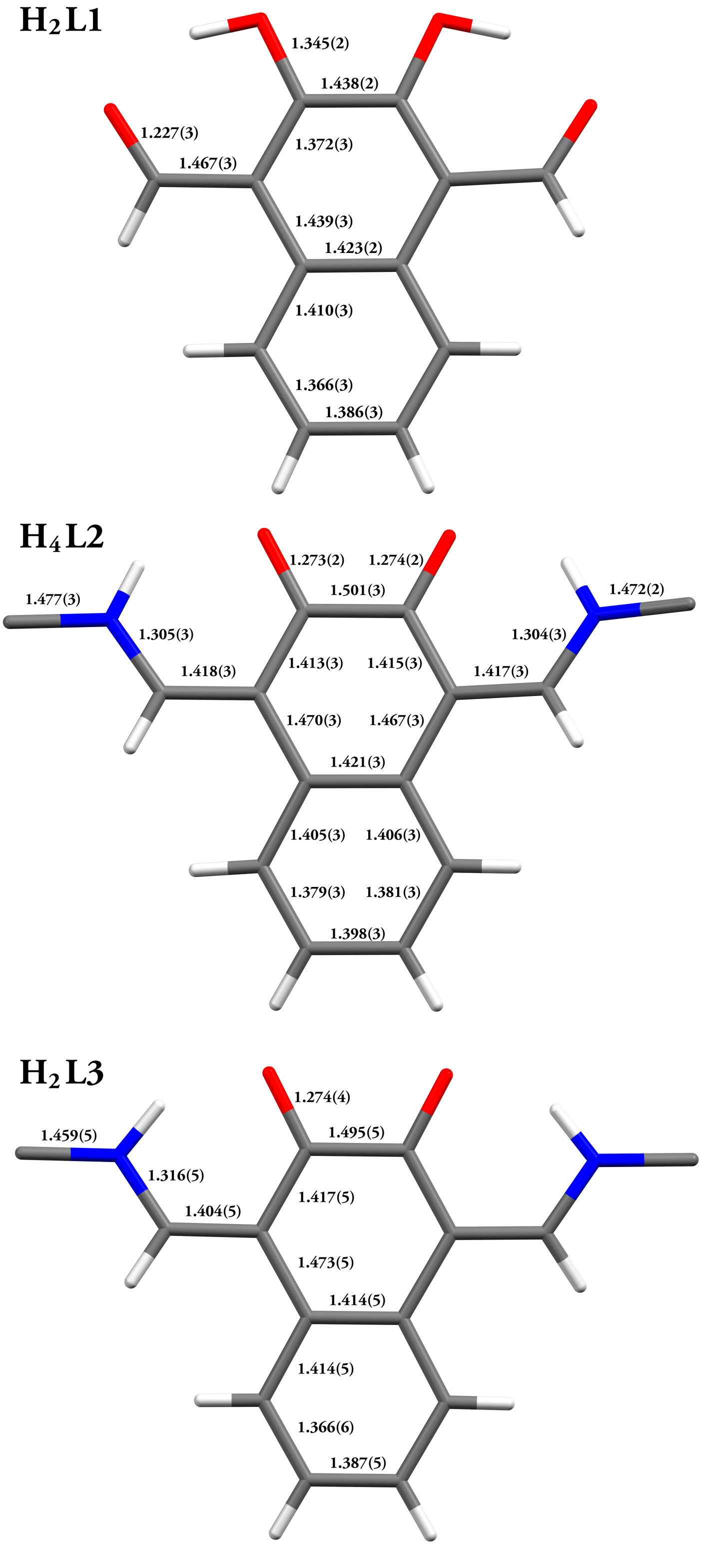

FIGURE 2.6: X-ray crystal structure of the naphthalene cores of **H_2L1**, **H_4L2**, and **H_2L3**, including bond lengths. Note: **H_2L1** and **H_2L3** crystallize with $Z' = 0.5$

A Brief Interlude

Non-macrocyclic Heterometallic M_3Ln Triangle Clusters

A series of structurally similar tetranuclear heterometallic $X^{II}{}_3Y^{II/III}{}_1$ complexes have been synthesized using the ligand 1,4-bisformyl-2,3-naphthalenediol (**H_2L1**), where X_3Y_1 represents various combinations with X = Co, Ni, or Cu; and Y = Ba, La, Eu, Gd, Tb, Dy, Ho, Er or Yb. The relatively planar arrangement of ligands and metals in these complexes can be seen schematically in Figure 2.7. The coordination of uncharged capping groups to the axial positions (in and out of the plane of Figure 2.7) of both the octahedrally and non-octahedrally bound metals is an indication of some Lewis acid character. The following three chapters discuss the structure and properties of these complexes.

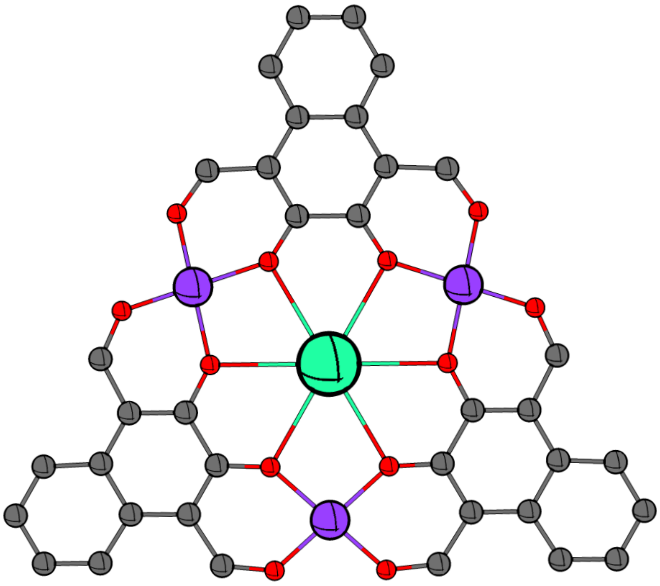

FIGURE 2.7: Generalized schematic showing the binding modes of the ligand to the lanthanide (light green) and transition metals (purple) in the heterometallic tetranuclear complexes.

Continuous shape measurement (CShM) calculations and octahedral distortion parameter calculations were performed using the SHAPE[133,134] and OctaDist[135] software packages, respectively, to better aid in the assessment of local coordination geometries. Cross-sectional molecular areas were calculated in ChemCraft[136] and non-covalent interactions were assessed in Olex2. Schematic representation of the selected 5-, 6-, 9-, 10-, and 11-coordinate geometries can be found in Appendix A Figures A.2 – A.5. SHAPE outputs for the 9-, 10- and 11-coordinate centres featured in Chapters 3 – 5 can also be found in Appendix A Output A.1.

Single crystal XRD data were collected in triplicate, from freshly prepared samples, to ensure consistency in the crystal form, axially coordinated groups, and non-coordinated lattice species. The crystal structures presented in this thesis correspond to the data set with the best refinement statistics, found in Appendix D. Lattice solvents have, in most cases, been confirmed by CHN microanalytical data. Full chemical formulations for each complex are based upon a combination of crystallographic and microanalytical data; which were only found to conflict for complexes containing diethyl ether in the crystal lattice, however, these same complexes were observed to crumble upon standing in air as one would expect from rapid desolvation of the crystal lattice.

Chapter 3

Ni3Ln Clusters

A family of six $Ni^{II}{}_3Y^{II/III}$ triangle type complexes, where Y = Ba^{II}, La^{III}, Eu^{III}, Gd^{III}, or Tb^{III}, have been synthesized and characterized. Single crystal X-ray diffraction studies revealed the expected [**L1**$_3Ni^{II}{}_3Ln^{III}$] structural motif was present for the four monomeric complexes, along with a fifth unexpected monomeric complex and a 1D polymeric complex. Each complex in the Ni^{II} series was prepared by the simple 3:3:1 reaction of H_2**L1** suspended in methanol with methanolic solutions of $Ni(NO_3)_2 \cdot 6H_2O$ and the appropriate heavy metal salt. Complexes **Ni3La**, **Ni3Gd**, and **Ni3Eu** also underwent magnetic characterization to explore the nature of the Ni – Ni coupling across the four-atom bridges and direct Ni – Ln coupling for **Ni3Eu** and **Ni3Gd**. Complex **Ni3Ba** was generated in an attempt to further extend this structural motif to include alkaline earth centred analogues. Similar preparative methods were also carried out with Sr^{II} and Y^{III} salts, however no crystalline materials were forthcoming.

3.1 Molecular Structure

The lanthanum containing complex, **Ni3La** (Figure 3.1), and gadolinium containing complex, **Ni3Gd** (Figure 3.2), both crystallized in the primitive monoclinic space group $P2_1/n$, while the remaining monomeric lanthanide containing complex, **Ni3Eu** (Figure 3.3), crystallized in the base centred monoclinic space group $C2/c$ and the alkaline earth containing complex, **Ni3Ba** (Figure 3.4), crystallized in the triclinic space group $P\bar{1}$.

All Ni^{II} centres are 6-coordinate with the equatorial sites occupied by the phenolate and aldehyde groups of **L1** and a mixture of methanol and water groups coordinating axially, in regular octahedral geometries with CShM `OC-6` values of 0.284 – 0.290 (**Ni3La**), 0.318 – 0.685 (**Ni3Gd**), 0.295 – 0.447 (**Ni3Eu**), and 0.090 – 0.130 (**Ni3Ba**).

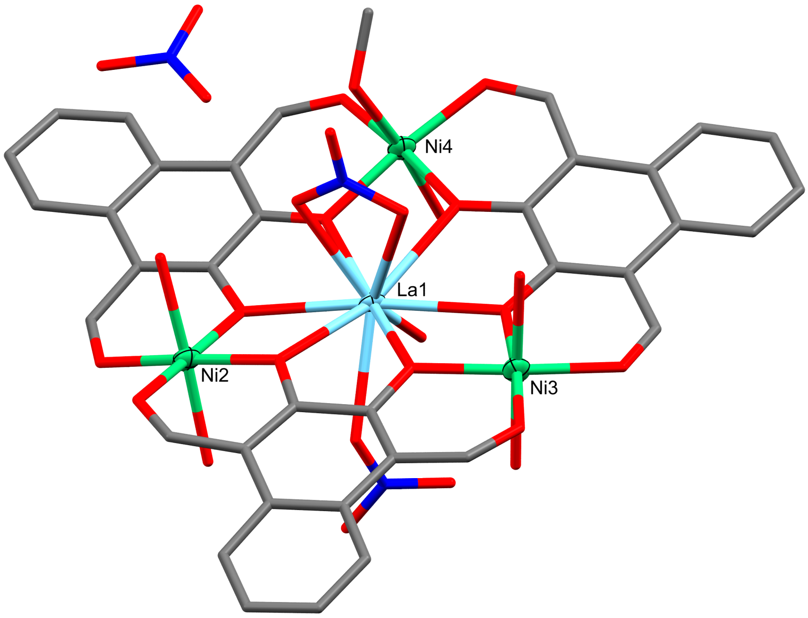

FIGURE 3.1: X-ray crystal structure of **Ni_3La**. Non-coordinated solvate species and hydrogen atoms are omitted for clarity. Thermal ellipsoids of metal atoms shown at the 70% probability level.
C = grey, O = red, N = blue.

While the central metal ions of **Ni_3La**, **Ni_3Gd**, and **Ni_3Eu** are all 10-coordinate, only the Gd^{III} and Eu^{III} centres feature two axially coordinated η_2-NO_3 groups, whereas the La^{III} centre has one bidentate nitrate, a monodentate nitrate, and a coordinated water molecule. Finally, complex **Ni_3Ba**, containing the much larger divalent alkaline earth metal, features an 11-coordinate Ba^{II} centre with two bidentate η_2-NO_3 anions and a coordinated methanol. The lanthanide containing complexes all require an additional monoanionic counterion to be present, which was crystallographically identified as a non-coordinated nitrate ion in all cases. Complex **Ni_3La** has six water caps, two on each Ni2 and Ni3 and one on each Ni4 and La1, with the remaining axial Ni4 site being occupied by a methanol molecule. Despite the difference in space group symmetries, **Ni_3Gd** and **Ni_3Eu** are very similar in core structure; with the former having only axial water caps on all three Ni^{II} centres and the later having only axial methanol caps on each Ni^{II}.

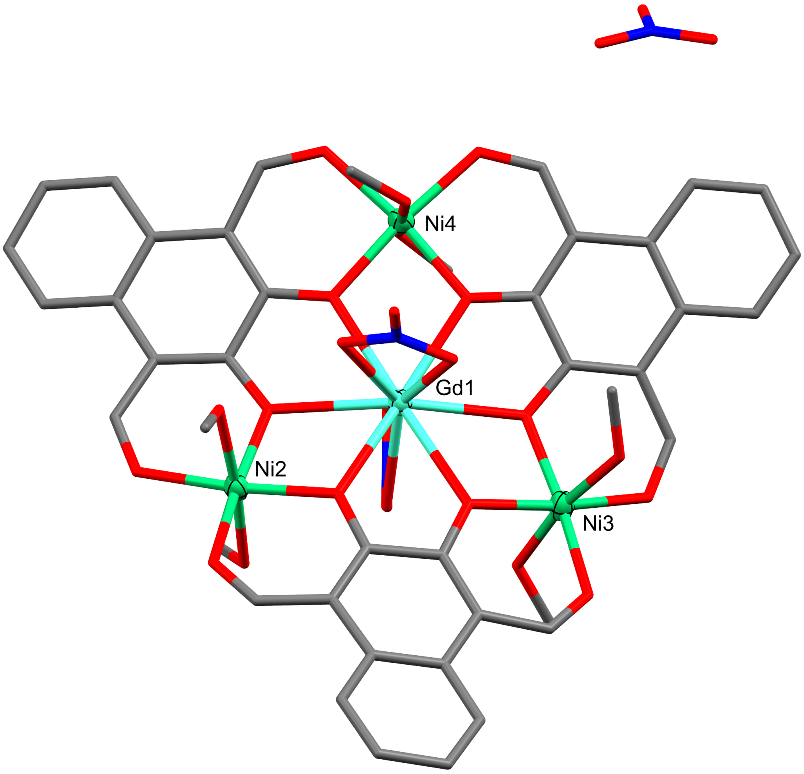

FIGURE 3.2: X-ray crystal structure of **Ni_3Gd**. Non-coordinated solvate species and hydrogen atoms are omitted for clarity. Thermal ellipsoids of metal atoms shown at the 70% probability level.
C = grey, O = red, N = blue.

Crystallographic analysis showed **Ni_3Ba** contains a mixture of axial water and methanol capping groups, with Ni4 being symmetrically capped by two water molecules, whereas Ni2 and Ni3 have crystallographically disordered axial sites formulated as $(H_2O)_{1.5}(MeOH)_{0.5}$ and $(H_2O)_{0.5}(MeOH)_{1.5}$, respectively. The eleventh, non-nitrate, coordination site of the Ba^{II} centre was also found to be present as a crystallographically disordered 1:1 mixture, $(H_2O)_{0.5}(MeOH)_{0.5}$. The crystal lattice was also found to contain heavily disordered solvate species which have been included within a solvent mask consisting of 33 electrons per asymmetric unit in a 136 Å^3 void, corresponding to two methanol molecules totalling 36 electrons, which is consistent with the CHN analysis.

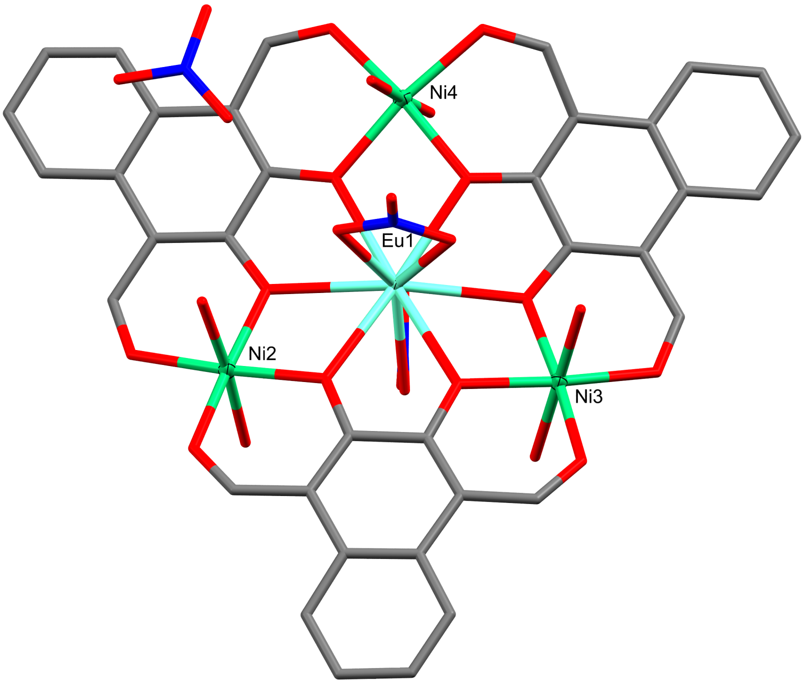

FIGURE 3.3: X-ray crystal structure of **Ni$_3$Eu**. Non-coordinated solvate species and hydrogen atoms are omitted for clarity. Thermal ellipsoids of metal atoms shown at the 70% probability level.
C = grey, O = red, N = blue.

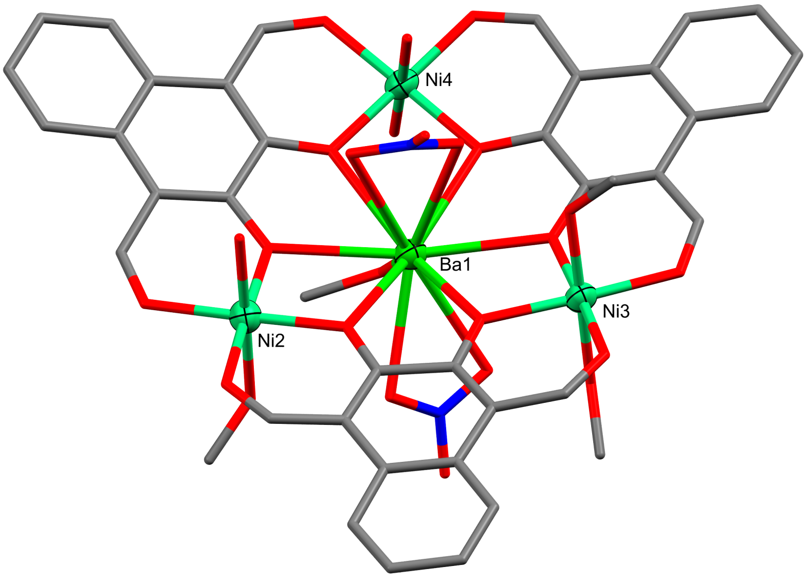

FIGURE 3.4: X-ray crystal structure of **Ni_3Ba**. Non-coordinated solvate species, disordered species, and hydrogen atoms are omitted for clarity. Thermal ellipsoids of metal atoms shown at the 70% probability level. C = grey, O = red, N = blue.

The Ni^{II} series contains a further two complexes, $\mathbf{[Ni_3Tb]}_n$ and $\mathbf{[Ni_3Gd]}_{acid}$ which are somewhat different in structure and formulation to the other triangle clusters. The complex $\mathbf{[Ni_3Tb]}_n$, as the name implies, is a polymeric analogue of the system one might expect to be formed from the reaction of $\mathbf{H_2L1}$ with nickel and terbium salts. This complex crystallized in the enantiomorphic orthorhombic space group $P2_12_12_1$, forming a 1D polymer along a 2-fold screw axis running parallel to the crystallographic *a*-axis.

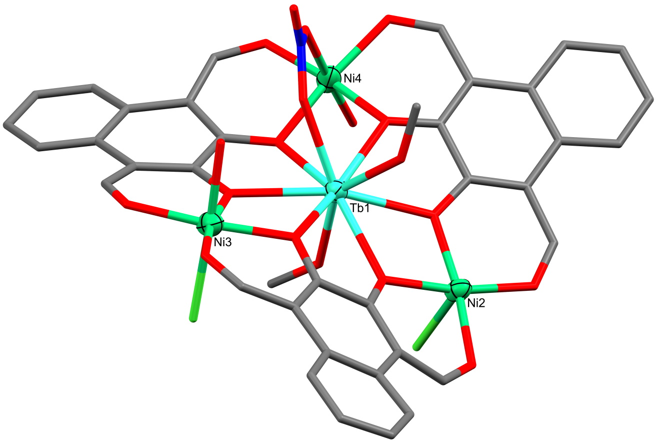

FIGURE 3.5: X-ray crystal structure showing the asymmetric unit of $\mathbf{[Ni_3Tb]}_n$. Disordered species and hydrogen atoms are omitted for clarity. Thermal ellipsoids of metal atoms shown at the 70% probability level. C = grey, O = red, N = blue, Cl = green.

The asymmetric unit of $\mathbf{[Ni_3Tb]}_n$ contains the expected $\mathbf{L1}_3Ni_3Tb$ unit in a very non-planar arrangement. Ni2 and Ni3 each feature an axially coordinated chloride cap, with the required third negative charge being provided by a μ_2-NO_3 anion bridging the Tb1 and Ni4 centres on the opposite side of the Ni_3 plane to the chlorides. Ni3 and Ni4 also each have a crystallographically disordered water/methanol cap (both present in a 1:1 ratio). The remainder of the Tb^{III} coordination sphere consists of a methanol molecule proximal to the nitrate, for which the carbon is spatially disordered (1:1) over two sites, and a well-ordered methanol molecule which hydrogen bonds to the Cl1 cap of Ni2. Through symmetry generation (denoted by *) along a 2-fold screw axis $((-1/2+X, 3/2-Y, 1-Z)$ and $(1/2+X, 3/2-Y, 1-Z))$, the polymeric nature of $\mathbf{[Ni_3Tb]}_n$ can be seen (Figure 3.6). The Cl2* cap of Ni3* fills the sixth and final coordination site of Ni2 with a slightly longer bond length (Ni2 – Cl1 = 2.442(4) Å and Ni2 – Cl2* = 2.475(3) Å). This longer Ni – Cl bond increases the `OC-6` value of Ni2 to 1.454, which is significantly higher than the values for Ni3 (0.382) and Ni4 (0.841), describing a 6-coordinate centre that is less octahedral and more orthorhombic in nature, i.e. three pairs of similar lengths rather than all six similar lengths.

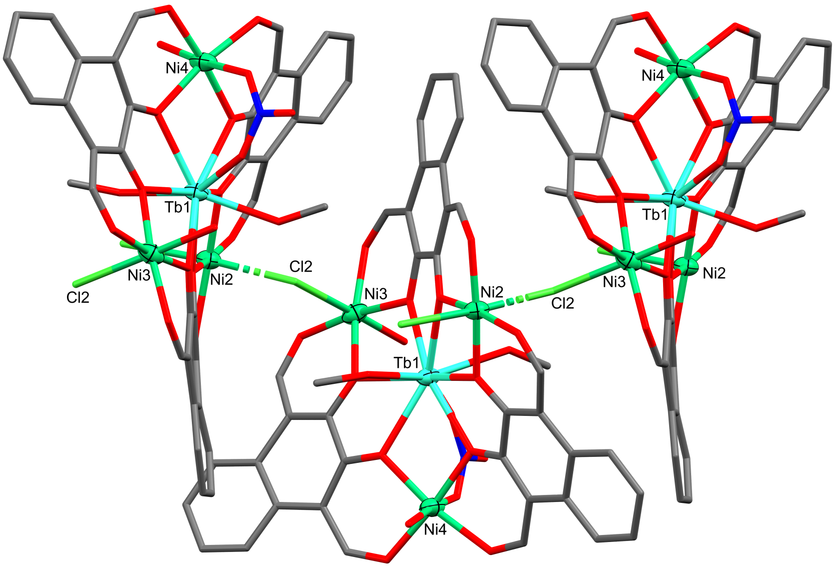

FIGURE 3.6: X-ray crystal structure showing a 3-mer of $[\mathbf{Ni_3Tb}]_n$.
Thermal ellipsoids of metal atoms shown at the 70% probability level.
C = grey, O = red, N = blue, Cl = green.

While $[\mathbf{Ni_3Tb}]_n$ isn't the first example of an $\mathrm{M^{II}}_3$Ln triangle complex forming a 1D polymeric chain; it is, at the time of writing, the only example where the bridging group originates from what would be the monomeric complex rather than an added co-ligand, and one of a limited number of examples of μ_2-Cl bridged $\mathrm{Ni^{II}}$ complexes reported in the literature. Furthermore, there are only 13 structurally characterized heterometallic complexes reported which feature a single-atom Ni – Cl – Ni bridging motif, one of which is a perfectly linear bridge (180°) and the rest of which all have bridging angles less than 90°. The Brooker group have reported six polymeric variants of their macrocyclic $\mathrm{LCu_3Tb}$ complex, one where the amine linker is 1,2-ethylenediamine and bridging co-ligand is terephthalic acid;[108] and all others were derived from the 1,3-diaminopropane linked macrocycles, with metal cyanides providing the bridging moieties in various configurations.[107,109] The terephthalate containing complex has a mixture of η_1 and η_2 binding modes attached directly to the $\mathrm{Tb^{III}}$ centre, whereas the metal cyanide containing complexes bridge only the transition metal centres like in $[\mathbf{Ni_3Tb}]_n$.

The single atom bridging in $[\mathbf{Ni_3Tb}]_n$ dramatically decreases the intra-chain $\mathrm{M^{II}}$ – $\mathrm{M^{II}}$ and $\mathrm{Tb^{III}}$ – $\mathrm{Tb^{III}}$ separations in comparison with the larger molecular bridging species reported by Brooker *et al.* (Table 3.1). The Ni2 – Ni3 separation in $[\mathbf{Ni_3Tb}]_n$ (4.352(3) Å) via the bridging Cl2 (where Ni2 – Cl2 – Ni3 = 125.8(1)°) is far shorter than any Cu – Cu separation observed in the literature analogues. While initially this might be seen as a good magnetic superexchange pathway connecting two high spin d^8 centres, the literature suggests that chloride mediated exchange between Ni^{II} centres with similar M – M distances and M – Cl – M angles are in fact strongly antiferromagnetic in nature.[137–139]

TABLE 3.1: Smallest M^{II} – M^{II} and Tb^{III} – Tb^{III} separations (Å) in **$[Ni_3Tb]_n$** and similar literature complexes.

Complex	**M^{II} – M^{II}** complex	**M^{II} – M^{II}** intra-chain	**M^{II} – M^{II}** inter-chain	**Tb^{III} – Tb^{III}** intra-chain	**Tb^{III} – Tb^{III}** inter-chain
$[Ni_3Tb]_n$	6.150(3)	4.352(3)	6.126(3)	8.229(1)	11.914(1)
$CuTb^{\text{terephthalate}}$	6.114(2)	6.962(2)	6.084(2)	10.059(1)	9.783(1)
$CuTb^{\text{stepped W(CN)}_8}$	6.315(2)	10.489(3)	6.403(2)	14.894(3)	10.385(3)
$CuTb^{\text{square wave W(CN)}_8}$	6.189(1)	10.928(2)	6.596(1)	15.154(1)	9.420(1)
$CuTb^{trans\text{-Fe(CN)}_6}$	6.123(1)	10.202(1)	7.696(1)	14.463(1)	9.836(1)
$CuTb^{cis\text{-Fe(CN)}_6}$	6.142(1)	7.529(1)	6.128(1)	12.713(1)	8.416(1)
$CuTb^{cis\text{-Co(CN)}_6}$	6.156(1)	7.533(1)	6.162(1)	12.755(1)	8.419(1)

$CuTb^{\text{terephthalate}}$[108]
$CuTb^{\text{stepped W(CN)}_8}$ and **$CuTb^{\text{square wave W(CN)}_8}$**[107]
$CuTb^{trans\text{-Fe(CN)}_6}$, **$CuTb^{cis\text{-Fe(CN)}_6}$**, and **$CuTb^{cis\text{-Co(CN)}_6}$**[109]

The other structural oddity, **$[Ni_3Gd]_{acid}$** (Figure 3.7), was found in an aged sample thought to be **Ni_3Gd**. This complex also crystallized in the monoclinic space group $P2_1/n$, however, X-ray crystallographic analysis showed that in place of the nitrate anion or solvent molecule expected to be axially coordinated to the Gd^{III} centre, there was an oxidized form of **H_2L1**, 2,3-dihydroxynaphthalene-1,4-dicarboxylic acid (**H_4L1'**). It is worth noting that no other discrete complexes featuring a 2,3-dihydroxyterephthalate type moiety, or related ether/ester derivatives, have been structurally reported throughout the literature making this 'accidental co-ligand' a potentially interesting synthetic pathway to investigate, if large scale polymerization and/or MOF formation can be avoided. With the inevitable presence of water in the reaction mixture, transition metal mediated oxidation of **H_2L1** to **H_4L1'** is likely to have occurred through the initial formation of a *gem*-diol species. This fourth ligand unit was found to bind Gd1 through its fully deprotonated catechol moiety in an η_2 fashion, with the ninth and final coordination site of Gd1 being occupied by an η_1-NO_3. Each Ni^{II} centre in **$[Ni_3Gd]_{acid}$** is capped by either methanol or water molecules, maintaining its octahedral coordination sphere and having `OC-6` values (0.298 – 0.491) comparable to those calculated for **Ni_3Gd** (0.318 – 0.685, Table 3.1).

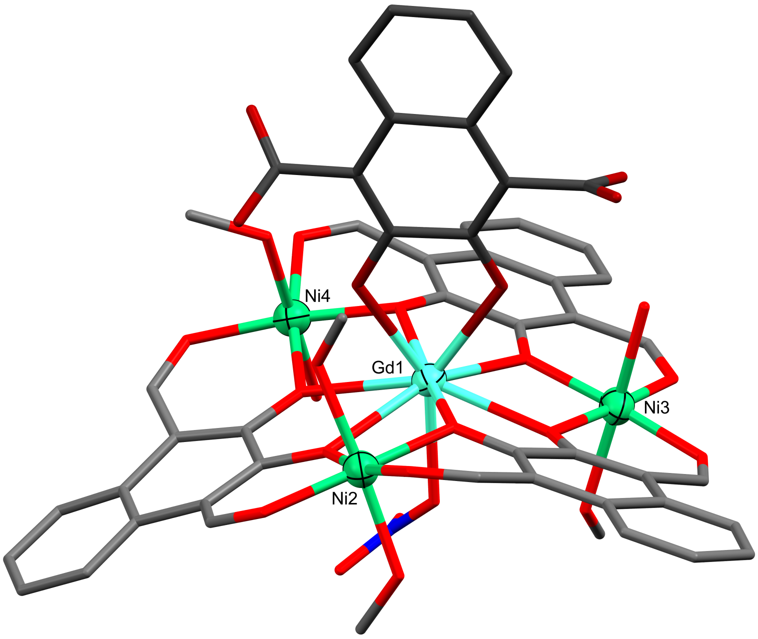

FIGURE 3.7: X-ray crystal structure of **[Ni$_3$Gd]**$_{acid}$. Non-coordinated solvate species and hydrogen atoms are omitted for clarity. Thermal ellipsoids of metal atoms shown at the 70% probability level. **L1′** shown in a darker colour scheme. C = grey, O = red, N = blue.

In the crystal structure of **[Ni$_3$Gd]**$_{acid}$ the carboxylic acid groups of **L1′** are not protonated as all four acid C – O bond lengths sit in the range of 1.204(11) to 1.243(11) Å, putting them in the range of a deprotonated carboxylate group in its resonance form. However, the nickel and gadolinium based bond lengths are consistent with those observed in **Ni$_3$Gd**, thus are in the expected +2 and +3 oxidation states, respectively. The C – C and C – O$_{\text{phenol}}$ bond lengths of **H$_4$L1′** are also consistent with those of **H$_2$L1**. Further, the low min/max residual electron densities (-1.0/+1.8) and lack of major peaks within the difference map indicate that there are no other cationic species present – such as alkali, alkali earth, or transition metals – which is also consistent with the elemental analysis. This allows us to conclude that despite the ambiguous bond lengths in the crystal structure, the acid groups are in fact protonated.

OUTPUT 3.1: SHAPE output for 6-coordinate Ni^{II} centres of **Ni3La**, **Ni3Gd**, **Ni3Eu**, **Ni3Ba**, **Ni3Tb**, and **[Ni3Gd]**$_{acid}$ (labeled as Ni3Gd′).

```
Structure       PPY-6      OC-6     TPR-6     JPPY-6
Ni3La-Ni2,     27.185,    0.284,   13.953,   30.571
Ni3La-Ni3,     27.852,    0.286,   14.672,   31.441
Ni3La-Ni4,     27.643,    0.290,   15.497,   31.336

Ni3Gd-Ni2,     27.109,    0.318,   14.008,   30.650
Ni3Gd-Ni3,     25.783,    0.685,   12.330,   29.415
Ni3Gd-Ni4,     27.148,    0.403,   14.174,   30.718

Ni3Eu-Ni2,     27.870,    0.335,   14.935,   31.352
Ni3Eu-Ni3,     26.764,    0.295,   14.256,   30.468
Ni3Eu-Ni4,     26.179,    0.447,   13.838,   29.848

Ni3Ba-Ni2,     28.612,    0.113,   15.315,   31.986
Ni3Ba-Ni3,     29.286,    0.090,   16.033,   32.618
Ni3Ba-Ni4,     28.942,    0.130,   15.535,   32.370

Ni3Tb-Ni2,     26.847,    1.454,   14.688,   30.069
Ni3Tb-Ni3,     27.275,    0.382,   13.756,   30.967
Ni3Tb-Ni4,     27.494,    0.841,   14.651,   30.772

Ni3Gd'-Ni2,    25.860,    0.491,   13.405,   29.688
Ni3Gd'-Ni3,    26.966,    0.299,   15.282,   30.447
Ni3Gd'-Ni4,    27.316,    0.371,   14.212,   31.068
```

3.2 Supramolecular Interactions

The five monomeric Ni_3Ln complexes feature extensive intermolecular hydrogen bonding networks involving the axially coordinated solvate and nitrate groups, as well as non-coordinated nitrate and solvate species. The packing of these monomeric Ni_3Ln complexes is further stabilized by a considerable number of supramolecular $\pi - \pi$ interactions ranging from 3.519 Å in **Ni3La** to 3.960 Å in **Ni3Eu** (Table 3.2), with centroid – centroid separations of up to 3.8 Å and angles up to 20° considered to be strong $\pi - \pi$ interactions.[140] With the presence of *pseudo*-C_{3h} symmetry in the M_4**L1**$_3$ plane, selected distances and angles are given in Table 3.3 as ranges over similar atom groups, e.g. Ni^{II}– O_{phenol}, for each complex.

Complexes **Ni3La** and **Ni3Eu** both feature notably shorter minimum Ln^{III} – Ln^{III} separations (9.160(1) and 9.767(1) Å, respectively) than the two non-macrocyclic Ni_3Ln complexes reported by Brooker *et al.* (9.912(2) Å for the Ni_3Dy complex and 9.900(2) Å for the Ni_3Yb complex),[111] and indeed complexes **Ni3Gd**, **[Ni3Gd]**$_{acid}$, and **Ni3Ba** – see Table 3.3 for further details. An even shorter 'intra-chain' Ln^{III} – Ln^{III} separation of 8.229(1) Å is observed for **[Ni3Tb]**$_n$ due to the conformational restrictions imposed by its polymeric nature, while these same constraints result in a much longer 'inter-chain' Ln^{III} – Ln^{III} separation of 12.733(1) Å. A consequence of the increased intermolecular Ln^{III} – Ln^{III} separations is a reduction of spin-dipole interactions, which can act as a QTM pathway, and a subsequent decrease in the mixing of Ln^{III} wave functions.[141–143]

Complexes **Ni3La**, **Ni3Eu**, **Ni3Ba**, and **[Ni3Gd]**$_{acid}$ also feature a number of direct inter-complex hydrogen bonds, some of which may help in the stabilization of deviations in the ligands planarity (e.g. the formyl carbon being skewed from the naphthalene plane as in Figure 3.8). Notably, **Ni3Gd** does not form any direct inter-complex hydrogen bonds nor are there any inter-chain hydrogen bonds present in **[Ni3Tb]**$_n$.

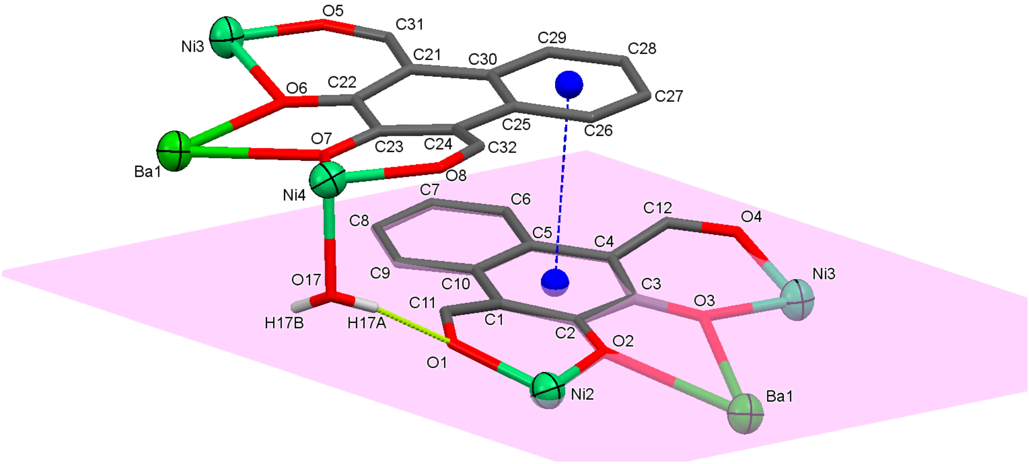

FIGURE 3.8: X-ray crystal structure highlighting the inter-complex interactions between two partial units of **Ni_3Ba**. The pink plane was calculated for the C1 – C10 naphthalene plane. The dashed yellow bond represents a hydrogen bond, while the dashed blue line joining the blue centroids represents the $\pi - \pi$ stacking interaction occurring between the respective rings.

TABLE 3.2: List of $\pi - \pi$ stacking interactions with centroid-centroid distances and angles, as calculated by Olex2. The second plane in each row corresponds to a symmetry generated molecule.

Complex	Planes	Distance (Å)	Angle (°)
Ni3La	⟨C1, C2, C3, C4, C5, C6⟩ ⟨C25, C26, C27, C28, C29, C30⟩	3.519	5.130
	⟨C41, C42, C43, C44, C45, C46⟩ ⟨C25, C26, C27, C28, C29, C30⟩	3.597	4.422
Ni3Gd	⟨C1, C2, C3, C4, C5, C10⟩ ⟨C5, C6, C7, C8, C9, C10⟩	3.606	5.855
	⟨C5, C6, C7, C8, C9, C10⟩ ⟨C5, C6, C7, C8, C9, C10⟩	3.723	0.000
Ni3Eu	⟨C41, C42, C43, C44, C45, C46⟩ ⟨C45, C46, C47, C48, C49, C50⟩	3.668	8.272
	⟨C21, C22, C23, C24, C25, C30⟩ ⟨C25, C26, C27, C28, C29, C30⟩	3.820	3.426
	⟨C1, C2, C3, C4, C5, C10⟩ ⟨C25, C26, C27, C28, C29, C30⟩	3.885	18.729
	⟨C41, C42, C43, C44, C45, C46⟩ ⟨C41, C42, C43, C44, C45, C46⟩	3.960	8.900
Ni3La	⟨C1, C2, C3, C4, C5, C10⟩ ⟨C25, C26, C27, C28, C29, C30⟩	3.580	3.674
	⟨C21, C22, C23, C24, C25, C30⟩ ⟨C25, C26, C27, C28, C29, C30⟩	3.714	4.300

TABLE 3.3: Selected structural parameters for the Ni^{II} series.

Bond (Å)	**Ni3La**	**Ni3Eu**	**Ni3Gd**	**Ni3Ba**	**[Ni3Tb]**$_n$	**[Ni3Gd]**$_{acid}$
Ni – O_{phenol}[a]	1.978(4) - 2.003(4)	1.962(2) - 1.993(2)	1.963(2) - 1.999(2)	1.990(6) - 2.015(6)	1.961(7) - 1.995(8)	1.957(7) - 1.990(6)
Ni – $O_{aldehyde}$[b]	1.983(4) - 2.016(4)	1.981(2) - 2.008(2)	1.975(2) - 2.023(2)	1.990(6) - 2.013(6)	1.985(9) - 2.015(9)	1.962(7) - 2.015(7)
Ni – O_{H_2O}	2.073(4) - 2.169(4)	2.076(2) - 2.167(1)		2.067(6) - 2.112(6)	2.081(9) - 2.094(2)	2.072(7) - 2.084(8)
Ni – O_{MeOH}	2.098(4)		2.061(2) - 2.120(2)	2.068(7) - 2.099(7)	2.081(9) - 2.094(2)	2.083(8) - 2.115(7)
Ni – Anion[c]					2.098(9) - 2.474(3)	
Ln – O_{phenol}	2.544(4) - 2.597(4)	2.473(2) - 2.543(2)	2.493(2) - 2.525(2)	2.686(6) - 2.752(6)	2.411(8) - 2.490(8)	2.361(7) - 2.567(6)[d]
Ln – O_{NO_3}	2.614(4) - 2.658(4)	2.487(2) - 2.555(2)	2.455(2) - 2.516(2)	2.824(8) - 3.306(7)	2.410(9)	2.424(7)
Ln – $O_{solvent}$[e]	2.515(4)			2.881(9)	2.360(9) - 2.390(8)	
Ni – Ni	6.339(2)	6.276(1)	6.296(1)	6.404(3)	6.150(3) - 6.287(3)	6.262(2) - 6.268(2)
Ni – Ln	3.670(2)	3.625(1)	3.636(1)	3.761(2)	3.536(2) - 3.656(2)	3.588(2) - 3.670(2)
Min. Ln – Ln	10.221(2)	10.625(2)	9.598(1)	10.430(1)	8.229(1)	10.496(1)
Ln – Ni3 plane	0.139(2)	0.091(1)	0.333(1)	0.143(1)	0.237(2)	0.376(2)
Angle (°)						
Ni – O_{phenol} – Ln	105.6(2) - 107.3(2)	106.2(1) - 108.7(1)	106.1(1) - 108.9(1)	102.6(2) - 105.4(2)	103.8(3) - 109.6(3)	106.9(3) - 109.4(3)

[a] O_{phenol} corresponds to O2, O3, O6, O7, O10, and O11.

[b] $O_{aldehyde}$ corresponds to O1, O4, O5, O8, O9, and O12.

[c] Anion is μ_1-NO_3 for lower range of **[Ni3Tb]**$_n$ and μ_1-Cl for upper range.

[d] The lower range corresponds to the axially coordinated **L1′**.

[e] Solvent is MeOH for **Ni3Ba** and **[Ni3Tb]**$_n$, and H_2O for **Ni3La** and **Ni3Ba**.

Complex **Ni3La** has three unique inter-complex hydrogen bonds (Figure 3.9a) each of which indicates an interaction between the proton of a nickel bound water capping group to an aldehyde moiety of a neighbouring unit complex (O1 ··· H15A = 2.851(5) Å, O5 ··· H13B = 2.456(6) Å, and O12 ··· H18B = 2.825(5) Å). Thus each complex is connected to four other complex units. **Ni3Eu**, however, contains four unique inter-complex hydrogen bonds (Figure 3.9b), all of which are water-cap donors with a mixture of water, aldehyde, and nitrate acceptors. Each unit complex of **Ni3Eu** interacts with five neighbouring molecules, with a notably short hydrogen bond between the H15A proton of a water cap and the O21 oxygen of a nitrate group (O8 ··· H16B = 2.492(7) Å, O13 ··· H18A = 2.242(6) Å, O16 ··· H17B = 2.049(6) Å, and O21 ··· H15A = 1.965(8) Å). The alkaline earth metal containing complex, **Ni3Ba**, forms three unique inter-complex hydrogen bonds (Figure 3.9c) between the water capping groups of the Ni^{II} centres and both nitrate anions bound to Ba1 as well the O1 formyl oxygen (O1 ··· H17A = 2.722(8) Å, O21 ··· H1AA = 2.738(13) Å, and O25 ··· H18A = 2.827(9) Å). Interestingly, the mixed ligand Ni3Gd based complex, **[Ni3Gd]**$_{acid}$, features two unique inter-complex hydrogen bonds linking each unit complex with four neighbours. Each unit complex forms a strong hydrogen bond between a formyl oxygen and a methanolic proton (O8 ··· H14 = 1.923(9) Å) and a relatively weaker hydrogen bond between a different formyl group and a water cap (O12 ··· H15A = 2.093(8) Å). Note that these hydrogen bonds are either in the ’moderate’ or ’weak’ category defined by Jeffrey[144] and Steiner[145] as being mostly electrostatic with H ··· A separations of 1.5 – 2.2 Å, or being a mixture of electrostatic and dispersive with H ··· A separations $>$ 2.2 Å, respectively.

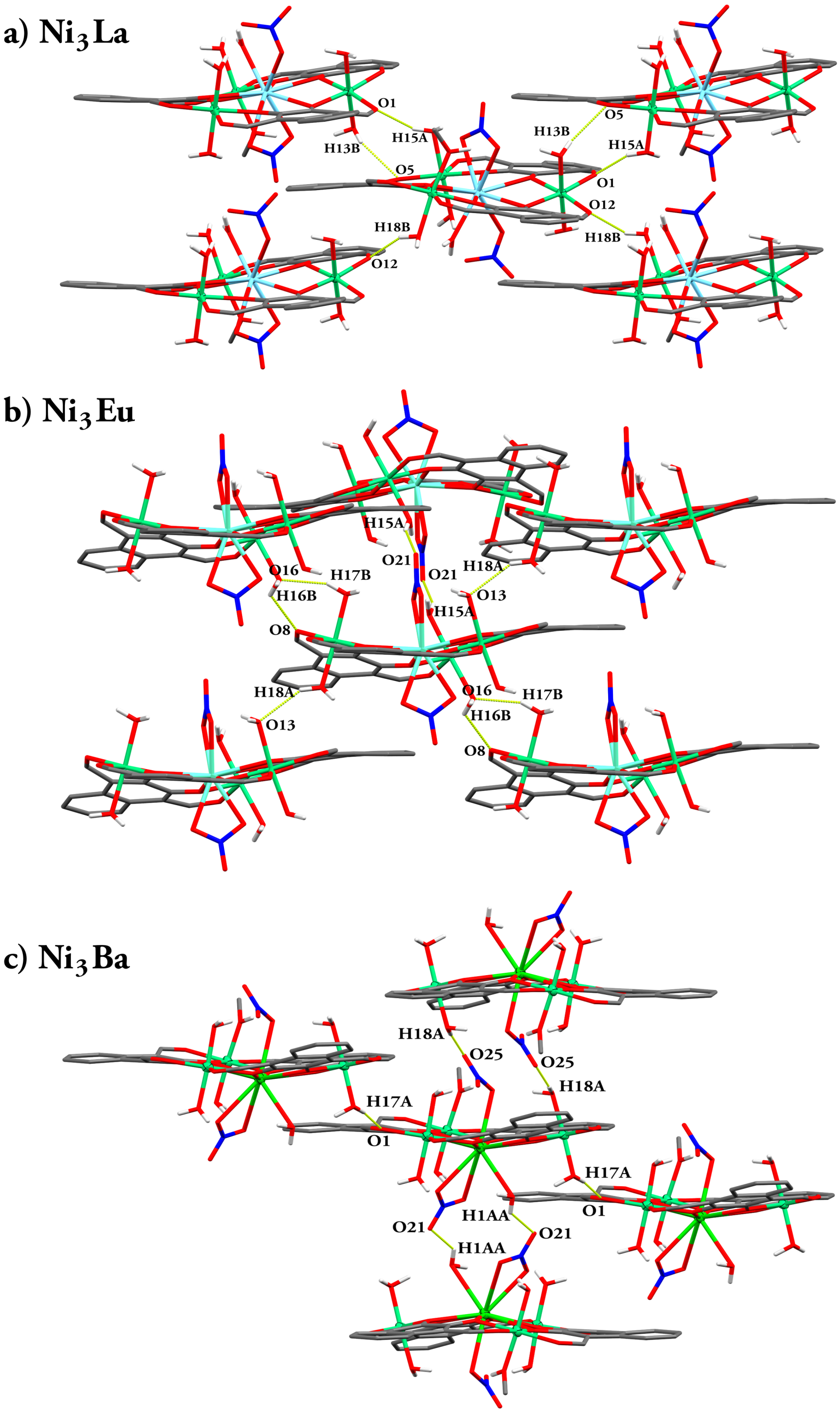

FIGURE 3.9: X-ray crystal structures of **Ni$_3$La** (a), **Ni$_3$Eu** (b), and **Ni$_3$Ba** (c) highlighting inter-complex hydrogen bonds from the central unit complex. All non-coordinated species, disordered species, and non-acidic hydrogen atoms omitted for clarity. Thermal ellipsoids of metal atoms shown at the 70% probability level. C = grey, O = red, N = blue, hydrogen bonds = yellow.

3.3 Magnetic Characterization

The absence of magnetic characterization within the literature for Ni^{II} based non-macrocyclic M_3Ln triangle complexes fuelled our interest in investigating these systems as potential SMM candidates. Due to complexes **Ni3La** and **Ni3Ba** being structurally and electronically similar, with both Ba^{II} and La^{III} being diamagnetic, both complexes are representative of a $Ni^{II}{}_3$-only spin system. Therefore, only **Ni3La** was chosen to undergo magnetic characterization as it presented crystals of a higher metric symmetry and more readily crystallized without the presence of other crystalline impurities.

DC magnetic susceptibility and magnetization measurements of **Ni3La** clarified the presence of three $S_{Ni^{II}} = 1$ centres with $g = 2.3$. A wide plateau of 4.0 cm^3 K mol^{-1} can be observed in the $\chi_m T$ vs T plot (Figure 3.10) at 300 K, which exceeds the theoretical spin-only value ($g_{Ni^{II}} = 2.0$) of 3.00 cm^3 K mol^{-1} for three non-coupled Ni^{II} ions. The magnetization at 1.8 K (Figure 3.11) was observed to be proportional to the g-factor, furthermore, the experimental magnetization reached 5.9 μ_B at 7 T with a positive slope, which is consistent with the susceptibility measurement. A decrease of $\chi_m T$ at low temperature was observed, which can be attributed to the zero field splitting of the Ni^{II} centres.[146] A mixture of intramolecular Ni – Ni superexchange and non-covalent intermolecular interactions may be operative, contributing to the drop. Unfortunately these contributions could not be quantitatively separated due to the small and monotonic

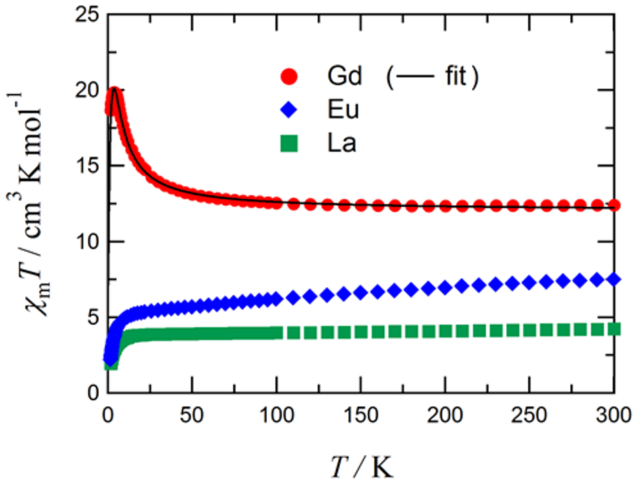

FIGURE 3.10: Plot of DC magnetic susceptibility ($\chi_m T$ vs T) for polycrystalline **Ni3La**, **Ni3Eu**, and **Ni3Gd**. The solid black line represents the fit for the susceptibility data of **Ni3Gd**. Samples **Ni3Eu** and **Ni3Gd** were fixed in a small amount of eicosane prior to measurement. Data for **Ni3La** was collected in a 5000 Oe applied field, while **Ni3Eu** and **Ni3Gd** were collected in a 500 Oe applied field.

decrease of the $\chi_m T$ value. The $\chi_m T$ value of **Ni3Eu** (Figure 3.10) was found to be 7.49 cm^3 K mol^{-1} at 300 K. Since the ground state of Eu^{III} has $J = L + S = 0$, the magnetic susceptibility arising from the Eu^{III} centre must be assigned to excited state moments and temperature independent paramagnetism. In the low temperature regime the spin projection is dominated by S_{Ni}, and extrapolating the $\chi_m T$ product to 0 K gives a value of approximately 5.0 cm^3 K mol^{-1} resulting in a Ni^{II} g-factor ($g_{Ni^{II}}$) of 2.5 – 2.6. The final drop in the $\chi_m T$ vs T plot is attributed to the ZFS of the nickel centres, similar to **Ni3La**. The magnetization measurement of **Ni3Eu** at 1.8 K (Figure 3.11) reached 8.07 μ_B however there was a considerable residual slope at 7 T – the majority of which is assigned to the Ni^{II} moments.

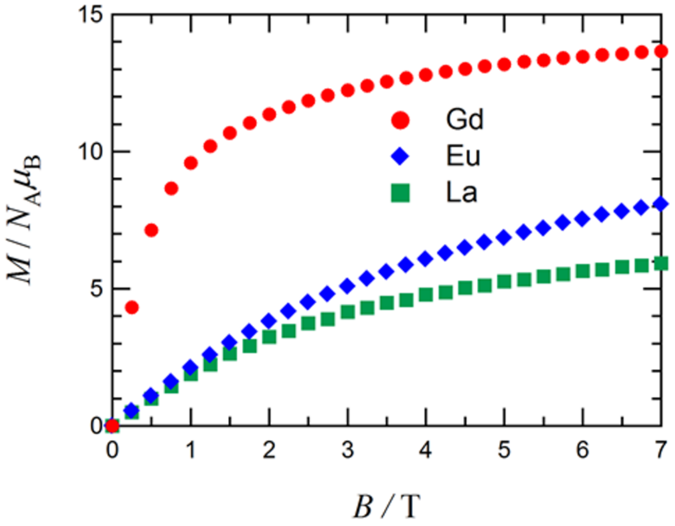

FIGURE 3.11: Plot of DC magnetization data (M vs H) for polycrystalline **Ni3La**, **Ni3Eu**, and **Ni3Gd** at 1.8 K, where **Ni3Eu** and **Ni3Gd** were fixed in a small amount of eicosane.

Figure 3.10 also shows the $\chi_m T$ vs T data and fit for **Ni3Gd**. The $\chi_m T$ value for this complex was found to be 12.4 cm^3 K mol^{-1} at 300 K, which is greater than the theoretical spin-only value of 10.9 cm^3 K mol^{-1}. This discrepancy can be attributed to the g-factor of the Ni^{II} centres which was estimated to be 2.46. There is a sharp increase in the $\chi_m T$ product upon cooling below 50 K, indicating the presence of ferromagnetic interactions and reaching a maximum of 19.8 cm^3 K mol^{-1} at 3.6 K. The magnetization measurements of **Ni3Gd** at 1.8 K (Figure 3.11) reached 13.7 μ_B at 7 T, which is near the saturation point as indicated by the small residual slope in the plotted data. Assuming the experimental value of $g_{Ni^{II}} = 2.46$ and a ground state spin projection of $S_{total} = {}^{13}/_{2}$ (corresponding to a $M_{spin\text{-}only}$ value of 13 μ_B), the calculated M_{sat} is 14.4 μ_B – where $M_{sat} = g_{Gd^{III}} S_{Gd^{III}} + g_{Ni^{II}} S_{Ni^{II}}$.

The Ni – Gd exchange coupling has been estimated using the van Vleck equation (Eq. 3.1) based on the spin Hamiltonian $\mathscr{H} = -2J(\mathbf{S}_1 \cdot \mathbf{S}_2 + \mathbf{S}_1 \cdot \mathbf{S}_3 + \mathbf{S}_1 \cdot \mathbf{S}_4)$, and including the Weiss mean field parameter, θ, to account for intermolecular interactions. To avoid over-parameterization, only a single J-coupling term is calculated, as quantitative separation of the $J_{\text{Gd1-Ni2}}$, $J_{\text{Gd1-Ni3}}$, and $J_{\text{Gd1-Ni4}}$ terms becomes difficult in the presence of local C_{3h} symmetry within the M_4O_6 plane.

$$\chi_{\mathrm{m}}T = \frac{2N_{\mathrm{A}}^2 g_{\mathrm{ave}}^2 \mu_{\mathrm{B}}^2}{k_{\mathrm{B}}} \frac{T}{T-\theta} \frac{A}{B} \tag{3.1}$$

where

$$\begin{aligned} A = {} & 3\exp(-48J/k_{\mathrm{B}}) + 30\exp(-45J/k_{\mathrm{B}}) + 105\exp(-40J/k_{\mathrm{B}}) + 60\exp(-39J/k_{\mathrm{B}}) \\ & + 210\exp(-34J/k_{\mathrm{B}}) + 252\exp(-33J/k_{\mathrm{B}}) + 315\exp(-30J/k_{\mathrm{B}}) + 504\exp(-27J/k_{\mathrm{B}}) \\ & + 495\exp(-24J/k_{\mathrm{B}}) + 756\exp(-23J/k_{\mathrm{B}}) + 252\exp(-21J/k_{\mathrm{B}}) + 990\exp(-18J/k_{\mathrm{B}}) \\ & + 1485\exp(-14J/k_{\mathrm{B}}) + 858\exp(-13J/k_{\mathrm{B}}) + 1716\exp(-7J/k_{\mathrm{B}}) + 1365 \end{aligned}$$

$$\begin{aligned} B = {} & \exp(-48J/k_{\mathrm{B}}) + 2\exp(-45J/k_{\mathrm{B}}) + 3\exp(-40J/k_{\mathrm{B}}) + 4\exp(-39J/k_{\mathrm{B}}) \\ & + 6\exp(-34J/k_{\mathrm{B}}) + 4\exp(-33J/k_{\mathrm{B}}) + 9\exp(-30J/k_{\mathrm{B}}) + 8\exp(-27J/k_{\mathrm{B}}) \\ & + 5\exp(-24J/k_{\mathrm{B}}) + 12\exp(-23J/k_{\mathrm{B}}) + 4\exp(-21J/k_{\mathrm{B}}) + 10\exp(-18J/k_{\mathrm{B}}) \\ & + 15\exp(-14J/k_{\mathrm{B}}) + 6\exp(-13J/k_{\mathrm{B}}) + 12\exp(-7J/k_{\mathrm{B}}) + 7 \end{aligned}$$

Optimization of Eq. 3.1 gave $2J/k_{\mathrm{B}} = 1.95(2)$ K, $g_{\mathrm{ave}} = 2.103(2)$, and $\theta = 0.832(9)$ K to produce the fit (solid black line) in Figure 3.10. In general, complexes containing paramagnetic Ni$^{\mathrm{II}}$ centres involve the zero field splitting effect, which can lead to a drop in the $\chi_{\mathrm{m}}T$ product upon cooling.[146] Although it can be difficult to separate the ZFS D parameter from the intramolecular Ni – Ni superexchange coupling (j) and the intermolecular mean field (θ). An attempt was made to evaluate D and j simultaneously. A simulation of **Ni$_3$La** run using the MagPack software package[147,148] to evaluate only D gave $D/k_{\mathrm{B}} = 9$ K (Figure 3.12). A simulation of j based on the spin Hamiltonian $\mathscr{H} = -2j(\mathbf{S}_2 \cdot \mathbf{S}_3 + \mathbf{S}_2 \cdot \mathbf{S}_4 + \mathbf{S}_3 \cdot \mathbf{S}_4)$, where j represents coupling between Ni$^{\mathrm{II}}$ centres, was completed resulting in $2j/k_{\mathrm{B}} = -0.8$ K (Figure 3.13), the optimization of j reproduced the experimental $\chi_{\mathrm{m}}T$ vs T profile well, however the fit for the M vs H data was unsatisfactory. This result implies that the contribution from j is minor.

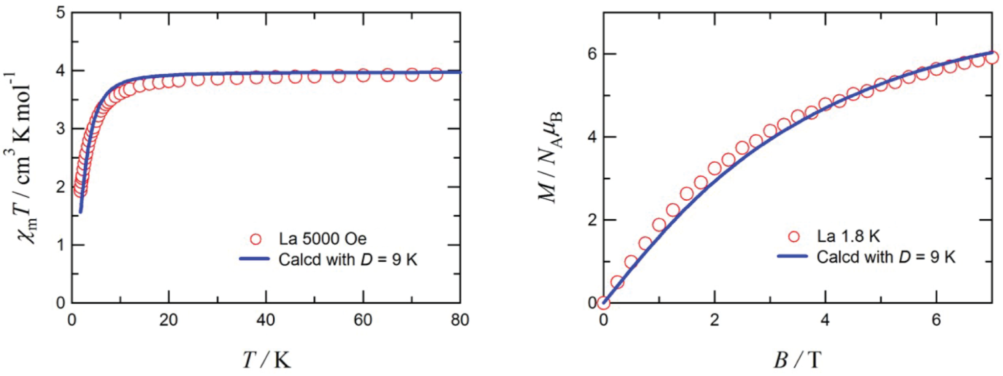

FIGURE 3.12: Plots of $\chi_m T$ vs T and M vs H for **Ni$_3$La** and fit with the optimized value of D.

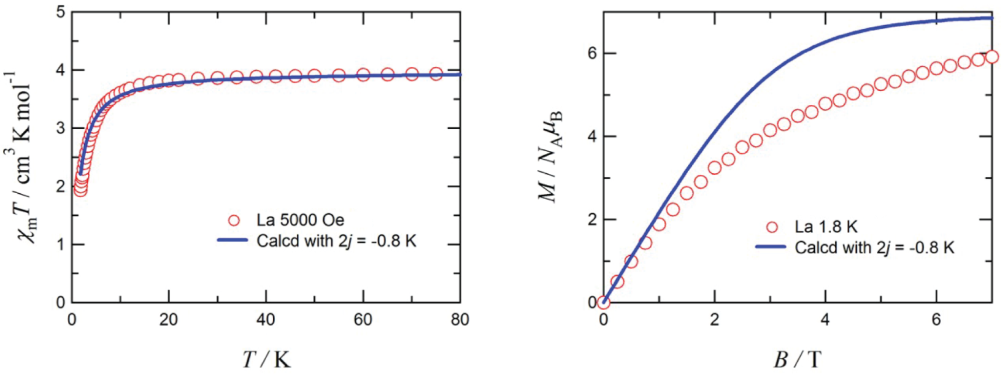

FIGURE 3.13: Plots of $\chi_m T$ vs T and M vs H for **Ni$_3$La** and fit with the optimized value of j.

When simulating the data using both D and j, the $|2j|$ value is indicated to be less than 0.6 K (Figure 3.14), which is consistent with a long super exchange pathway across the four atom O – C – C – O bridge. Furthermore, it can be concluded that the experimental value of D would be smaller than or equal to 9 K for **Ni$_3$La**. In light of the results found for **Ni$_3$La**, further calculations were performed for **Ni$_3$Gd**. A simulation of **Ni$_3$Gd** evaluating J and D resulted in values of $2J/k_B = 1.6$ K and $D/k_B = 11$ K (Figure 3.15). A different simulation using J and j for **Ni$_3$Gd** led to $2J/k_B = 2.0$ to 2.4 K and $2j/k_B = -2.4$ to -3.4 K (Figure 3.16). When simultaneously accounting for D and j, we found $|2j| < 0.8$ K (Figure 3.17). The AC magnetic susceptibility of **Ni$_3$Gd** was also investigated (Figure 3.18), however, no appreciable frequency dependent signals were observed. The magnetically isotropic nature of Gd^{III} means that this observation is not surprising; and although Gd^{III} complexes do not generally behave as SMMs, related heavier lanthanide ions could be prepared by means of the present synthetic strategy.

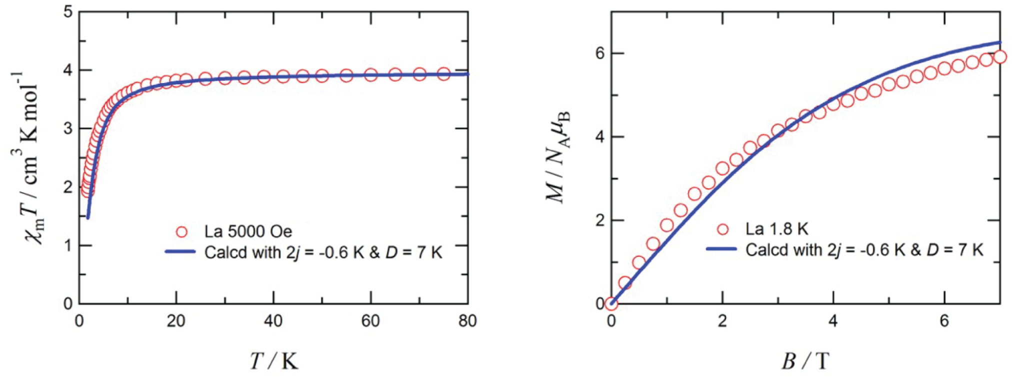

FIGURE 3.14: Plots of $\chi_m T$ vs T and M vs H for **Ni3La** and fit with the optimized values of D and j.

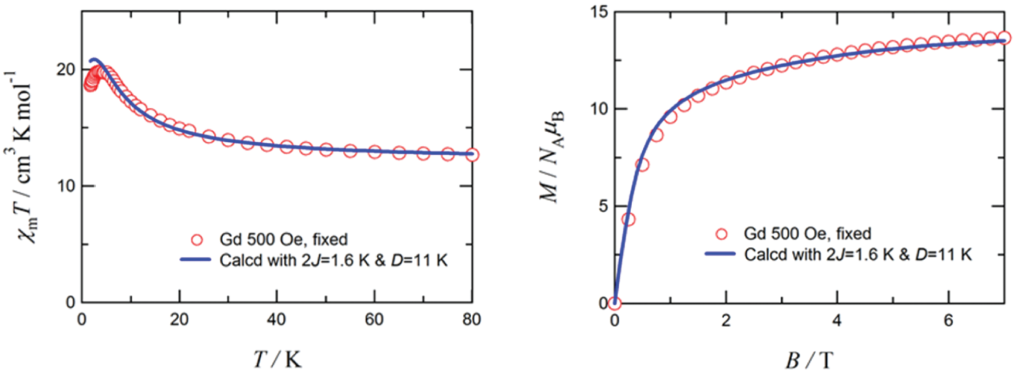

FIGURE 3.15: Plots of $\chi_m T$ vs T and M vs H for **Ni3Gd** and fit with the optimized values of D and J.

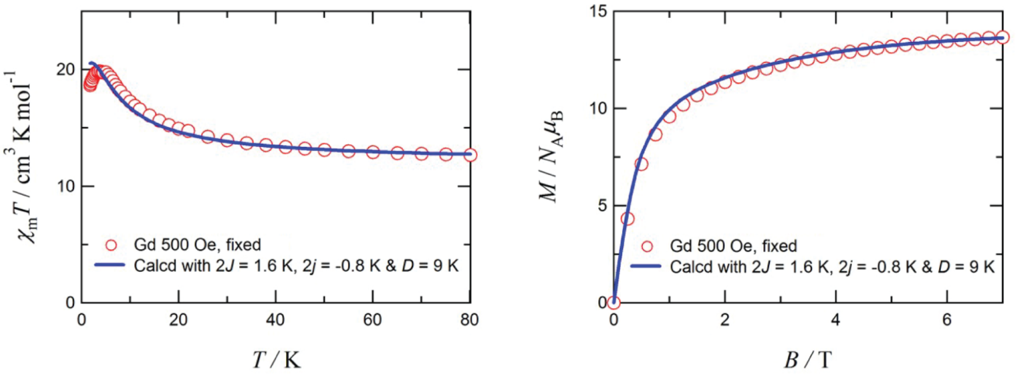

FIGURE 3.16: Plots of $\chi_m T$ vs T and M vs H for **Ni3Gd** and fit with the optimized values of D, J, and j.

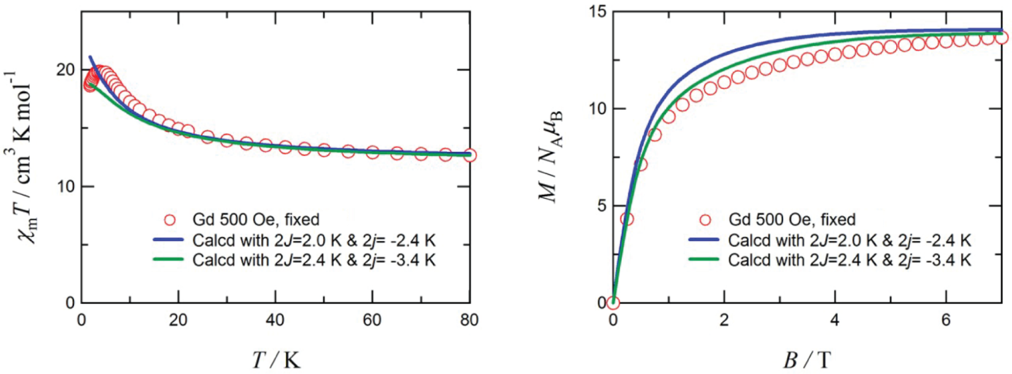

FIGURE 3.17: Plots of $\chi_m T$ vs T and M vs H for **Ni3Gd** and fit with the optimized values of J and j.

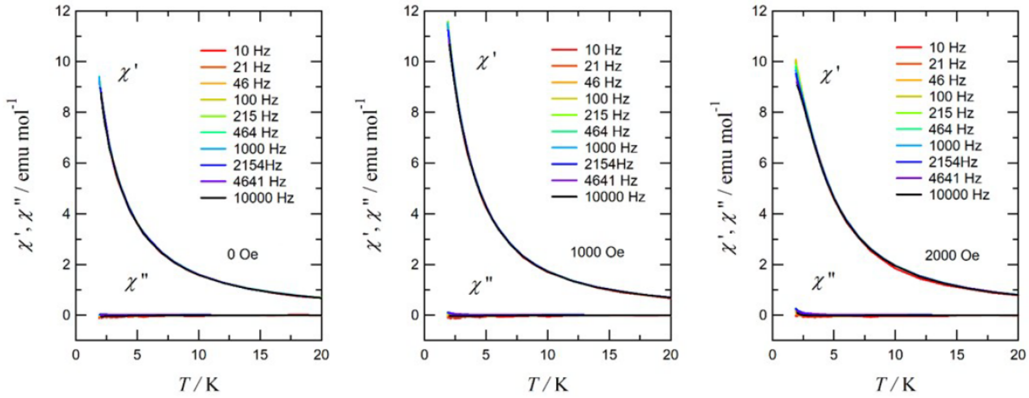

FIGURE 3.18: Plots of AC magnetic susceptibilities (in phase, χ', and out of phase, χ'') for **Ni3Gd**. The applied DC bias fields are indicated for each plot. Lines are shown as a guide to the eye only.

Conclusions

Six new non-macrocyclic heterometallic triangular tetranuclear clusters have been generated from the methanolic reaction of **H_2L1** and $Ni(NO_3)_2 \cdot 6\,H_2O$ with hydrated nitrate salts of La^{III}, Eu^{III}, Gd^{III}, and Ba^{II} or $TbCl_3 \cdot 6\,H_2O$. These complexes have been characterized by single crystal X-ray diffraction, confirming their relatively planar Ni_3LnO_6 cores. The successful isolation of the Ba^{II} centred complex, **Ni_3Ba**, shows the potential for other non-lanthanide metals to be introduced into the centre of this type of complex while maintaining the same general formulation and structure. The Tb^{III} containing complex, **$[Ni_3Tb]_n$**, also provides the first polymeric example of this type of complex to contain single-atom bridges between the monomeric units. Complexes **Ni_3La**, **Ni_3Eu**, and **Ni_3Gd** underwent magnetic characterization to examine possible ferromagnetic Ni – Ln couplings that have not been observed in the previously reported macrocyclic hexa-imine/oxime analogues. The three Ni^{II} centres in **Ni_3Gd** were observed to be ferromagnetically coupled to the central Gd^{III} ion with a calculated coupling constant of $2J/k_B = 1.6 – 2.0$ K. The Ni^{II} ZFS leads to a decrease of the magnetic susceptibility, which is particularly evident in the low-temperature regime. AC magnetic susceptibility experiments were carried out, but no frequency dependent signals were observed and thus the slow relaxation of magnetization which is characteristic of SMMs was not observed for these complexes. The results reported here show that utilizing a somewhat overlooked non-macrocyclic class of ligands to generate these triangular metal clusters can yield interesting results.

Preparation

Ni_3La formulated as [**L1**$_3$Ni$_3$La(NO$_3$)$_2$(H$_2$O)$_6$(MeOH)](NO$_3$)(H$_2$O)$_4$(MeOH) was obtained as orange plate crystals in 81% yield (based on La(NO$_3$)$_3 \cdot 6\,H_2O$). ATR-IR $\overline{\nu}$: 1616, 1566, 1484, 1449, 1429, 1379, 1354, 1307, 1261, 1127, 1027, 997, 970, 955, 753, 712, 689, 646 cm^{-1}. Microanalytical data found(calc) for **Ni_3La** (calculated for $C_{37}H_{42}Ni_3LaN_3O_{32}$, M_r = 1355.72 g mol^{-1}) C: 32.63(32.78), H: 2.92(3.12), N: 3.23(3.10).

Ni_3Eu formulated as [**L1**$_3$Ni$_3$Eu(NO$_3$)$_2$(H$_2$O)$_6$](NO$_3$)(MeOH)$_2$ was obtained as orange block crystals in 68% yield (based on Eu(NO$_3$)$_3 \cdot 6\,H_2O$). ATR-IR $\overline{\nu}$: 1620, 1569, 1489, 1450, 1436, 1383, 1353, 1312, 1262, 1131, 1025, 969, 955, 747, 714, 690, 649 cm^{-1}. Microanalytical data found(calc) for **Ni_3Eu** (calculated for $C_{38}H_{38}Ni_3EuN_3O_{29}$, M_r = 1328.76 g mol^{-1}) C: 34.69(34.35), H: 2.72(2.88), N: 2.99(3.16).

Ni_3Gd formulated as [**L1**$_3$Ni$_3$Gd(NO$_3$)$_2$(MeOH)$_6$](NO$_3$)(MeOH)$_3$ was obtained as orange plate crystals in 72% yield (based on Gd(NO$_3$)$_3 \cdot 6\,H_2O$). ATR-IR $\overline{\nu}$: 1620, 1569, 1489, 1450, 1436, 1383, 1353, 1312, 1262, 1131, 1025, 969, 955, 747, 714, 690, 649 cm^{-1}. Microanalytical data found(calc) for **Ni_3Gd** (calculated for $C_{45}H_{54}Ni_3GdN_3O_{30}$, M_r = 1450.24 g mol^{-1}) C: 37.17(37.27), H: 3.55(3.75), N: 3.01(2.90).

Ni_3Ba formulated as [**L1**$_3$Ni$_3$Ba(NO$_3$)$_2$(H$_2$O)4.5(MeOH)2.5](MeOH) $\cdot$ 2 [MeOH] was obtained as orange block crystals in 47% yield (based on Ba(NO$_3$)$_2 \cdot 6\,H_2O$). ATR-IR $\overline{\nu}$: 1620, 1563, 1492, 1427, 1377, 1346, 1310, 1260, 1239, 1130, 1029, 1001, 970, 957, 755, 711, 688, 661 cm^{-1}. Microanalytical data found(calc) for **Ni_3Ba** (calculated for C41.5$H_{49}Ni_3BaN_2O_{28}$, M_r = 1337.24 g mol^{-1}) C: 37.45(37.27), H: 3.55(3.69), N: 2.32(2.09).

[Ni_3Tb]$_n$ formulated as [**L1**$_3$Ni$_3$TbCl$_2$(NO$_3$)(H$_2$O)(MeOH)$_3$] was obtained as orange block crystals in 30% yield (based on TbCl$_3 \cdot 6\,H_2O$). ATR-IR $\overline{\nu}$: 1624, 1561, 1492, 1428, 1378, 1347, 1311, 1258, 1235, 1129, 1030, 999, 964, 958, 758, 712, 687, 660 cm^{-1}. Microanalytical data found(calc) for **[Ni_3Tb]$_n$** (calculated for $C_{39}H_{42}Ni_3TbCl_2NO_{24}$, M_r = 1314.65 g mol^{-1}) C: 36.01(35.63), H: 3.56(3.22), N: 1.21(1.07).

[Ni_3Gd]$_{acid}$ formulated as [**L1**$_3$(**H$_2$L1′**)Ni$_3$Gd(NO$_3$)(H$_2$O)$_2$(MeOH)$_3$](Et$_2$O) was obtained as large orange block crystals in 22% yield (based on Gd(NO$_3$)$_3 \cdot 6\,H_2O$). ATR-IR $\overline{\nu}$: 1623, 1567, 1520, 1486, 1456, 1425, 1380, 1357, 1312, 1264, 1243, 1166, 1126, 1028, 969, 954, 795, 739, 713, 690, 649 cm^{-1}. Microanalytical data found(calc) for **[Ni_3Tb]$_n$** (calculated for $C_{52}H_{44}Ni_3GdNO_{27}$, M_r = 1448.23 g mol^{-1}) C: 42.83(43.13), H: 2.81(3.06), N: 0.75(0.97).

Chapter 4

Cu_3Ln Clusters

A family of seven [**L1**$_3$Cu$^{II}_3$Ln^{III}] complexes, where Ln = La, Gd, Tb, Dy, Ho, Er, or Yb, have been synthesized and characterized. The entire family of Cu_3Ln complexes crystallized in either monoclinic or orthorhombic space groups, and contain only 5-coordinate copper centres. Complexes **Cu$_3$Gd**, **Cu$_3$Tb**, **Cu$_3$Dy**, **Cu$_3$Ho**, and **Cu$_3$Yb** were prepared in sufficient quantities to undergo magnetic characterization.

4.1 Molecular Structure

Complexes Cu_3La, Cu_3Gd, Cu_3Dy, and Cu_3Yb

Complexes **Cu$_3$La**, **Cu$_3$Gd**, **Cu$_3$Dy**, and **Cu$_3$Yb** are isomorphous and crystallize in the centrosymmetric monoclinic space group $C2/c$ (Figure 4.1). They form a set of relatively planar complexes, with only minor deviations of the Ln^{III} centre and ligands from the Cu_3 plane. Each Ln^{III} centre is 10-coordinate, with an axially bound η_2-NO_3 anion either side of the plane in a *pseudo*-hexagonal bipyramidal coordination geometry. All copper atoms are 5-coordinate with square pyramidal coordination geometries, where the axial cap of each copper is on the same side of the Cu_3 plane. Gd1 is displaced from its respective Cu_3 plane the least among these four complexes (0.050(2) Å) while Yb1 is displaced by the most (0.060(2) Å), with the Dy1 and Yb1 displacements sitting between these two values, both at 0.053(2) Å. Each complex contains two water caps (on their respective Cu2 and Cu3 centres) and a methanol cap on Cu4. Unfortunately, the axial sites of each copper centre in **Cu$_3$Yb** were poorly ordered, thus were modelled with only 50% chemical occupancy, however, the microanalytical data for **Cu$_3$Yb** is consistent with full occupancy of these axial donors. All four of these complexes exhibited further crystallographic disorder with one non-coordinated nitrate per unit complex, required to achieve charge balance, being spatially disordered over at least two sites. This nitrate group was identified to occupy a special position on a two-fold rotation axis in **Cu_3Gd**, **Cu_3Dy**, and **Cu_3Yb**, with 50% occupancy per unit complex. A second disordered nitrate fragment was located for **Cu_3Gd**, but was only stable to refinement at 25% occupancy – with the remaining quarter equivalent of nitrate being contained within a solvent mask. The remaining half occupancy nitrate anion in **Cu_3Dy** was located vicinal to the methanol cap of Cu4, and was stable to refinement only with very hard isotropic restraints. Finally, the remaining half occupancy nitrate for **Cu_3Yb** and full nitrate anion for **Cu_3La** could not be located in the difference map, and thus were included in a solvent mask. The presence of a non-coordinate nitrate anion per unit complex is consistent with the CHN microanalysis for each complex.

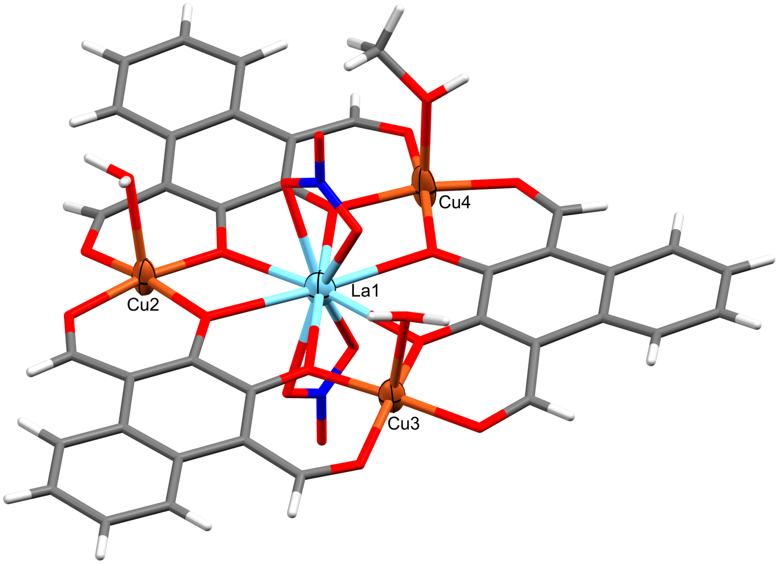

FIGURE 4.1: X-ray crystal structure of **Cu_3La**. Thermal ellipsoids of metal atoms shown at the 50% probability level. C = grey, H = white, O = red, N = blue.

Cu_3Ho and Cu_3Er

Two isomorphous complexes, **Cu_3Ho** (Figure 4.2) and **Cu_3Er**, crystallized in the centrosymmetric orthorhombic space group *Pbcn* and exclusively feature chloride anions from the heavy metal salts used in preparation. The Ln^{III} centre in each of these complexes is displaced above the Cu_3 plane by 0.245(1) Å, and the ligand unit which bridges Cu2 and Cu3 in each sits well below the plane. These two copper centres are axially coordinated by chloride anions on one side of the plane, while Cu4 is axially coordinated on the opposite side of the Cu_3 plane. This Cu4 cap is the only structural difference between **Cu_3Ho** and **Cu_3Er**, with **Cu_3Er** containing a crystallographically disordered water/methanol cap (in a 1:1 ratio) in place of the well ordered methanol cap of

Cu_3Ho. Holmium and erbium, being amongst the smaller lanthanide metals, occupy 9-coordinate sites in their respective complexes, each with two water molecules bound above the plane and one water molecule below. Considering the charge balance of the species present in each crystal structure, an additional negative charge per unit complex is required. A third, non-coordinated, chloride anion was crystallographically observed in both **Cu_3Ho** and **Cu_3Er**, but was heavily disordered across no less than three sites (one of which occupies a special position on a two-fold rotation axis) but was unstable, even to anisotropic refinement. As such, these chlorides have been included within a solvent mask for each complex. The lack of nitrogen in the microanalytical data helped further evidence the presence of a third chloride anion being present, as opposed to a nitrate anion which would have originated from the copper salt. The solvent mask for each complex was the same, consisting of 38 electrons in approximately 100 Å^3, which is consistent with the presence of one chloride and two water molecules per unit complex.

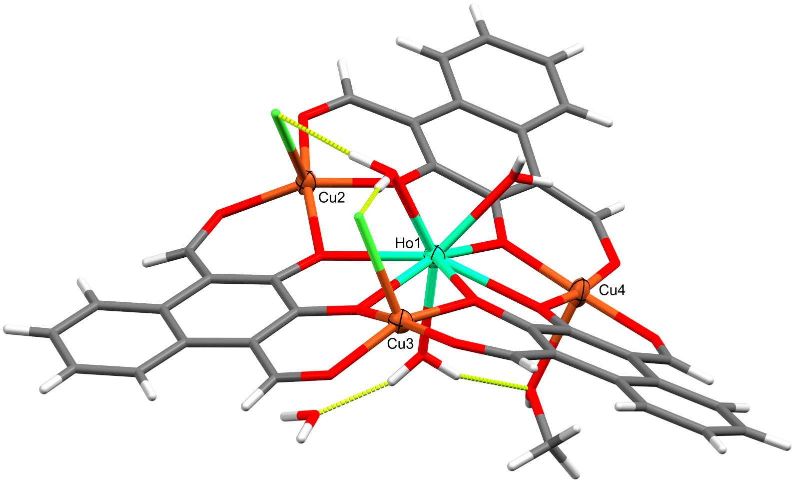

FIGURE 4.2: X-ray crystal structure of **Cu_3Ho**. Thermal ellipsoids of metal atoms shown at the 50% probability level. C = grey, Cl = green, H = white, O = red.

Cu_3Tb

Much like the two orthorhombic Cu_3Ln complexes, the crystal structure of **Cu_3Tb** revealed a relatively non-planar complex (Figure 4.3) which crystallized in the enantiomorphic monoclinic space group $P2_1$. Although **Cu_3Tb** was not the only Cu_3Ln type complex prepared using a $LnCl_3{\cdot}xH_2O$ and $Cu(NO_3)_2{\cdot}3H_2O$ combination, it is the only complex in this family to feature both chloride and nitrate capping groups – as confirmed by single crystal X-ray diffraction and elemental analyses. As expected, the large Tb$^{\mathrm{III}}$ ion sits in the middle of the O_6 equatorial binding environment formed by the ligands, with its axial coordination sites occupied by two water molecules above the Cu$_3$ plane, and an η_2-NO$_3$ anion below the plane. Similar to **Cu$_3$Ho**, Cu2 and Cu3 each have an axially coordinated chloride and Cu4 is capped by a methanol molecule, which for **Cu$_3$Tb** is on the same side as the chlorides. The entire ligand unit which bridges Cu2 and Cu3 sits below the Cu$_3$ plane, while Tb1 is displaced above the plane by 0.162(3) Å. The curvature of **Cu$_3$Tb** relative to the chloride caps is quite different to the curvature of **Cu$_3$Ho** and **Cu$_3$Er**, and can be quantified by examining the angle at which the chlorides are either converging or diverging from the centroid of the bridging catechol unit ($\overline{\mathrm{O2}\cdots\mathrm{O3}}$). The chlorides of **Cu$_3$Tb** can be seen to diverge away from the centre of the complex, with an angle of 129.6° and a Cl – Cl separation of 8.327(8) Å, allowing for a parallel arrangement of the water caps on Tb1. The two chloride caps each accept a hydrogen-bond from a different water molecule (O14 – H14A $\cdots$ Cl1 = 2.494 Å and O15 – H15A $\cdots$ Cl2 = 2.407 Å). In contrast, the Cu – Cl bonds in **Cu$_3$Ho** and **Cu$_3$Er** converge relative to their respective $\overline{\mathrm{O2}\cdots\mathrm{O3}}$ centroids, forming 77.1° and 76.9° angles, respectively. These angles imply a much smaller Cl – Cl separation (4.826(1) Å for **Cu$_3$Ho** and 4.814(2) Å for **Cu$_3$Er**) meaning the two water caps on Ho1 and Er1 must run perpendicular to Cl – Cl, with only a single water molecule forming hydrogen bonds to both Cl1 and Cl2 in each complex (average hydrogen bond length of 2.029 Å in **Cu$_3$Ho** and 2.122 Å in **Cu$_3$Er**).

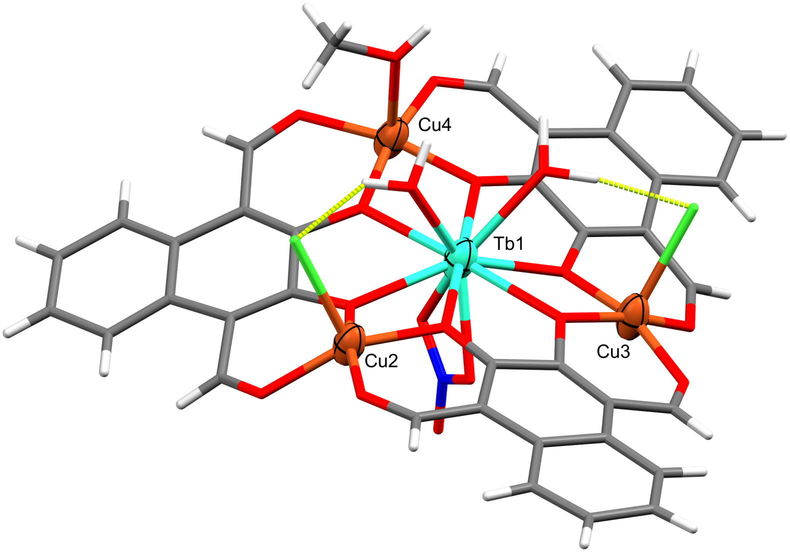

FIGURE 4.3: X-ray crystal structure of **Cu$_3$Tb**. Thermal ellipsoids of metal atoms shown at the 50% probability level. C = grey, Cl = green, H = white, O = red, N = blue.

4.2 Supramolecular Interactions

Throughout the entire Cu$_3$Ln series there is an absence of inter-complex hydrogen bonding, with complexes **Cu$_3$La** and **Cu$_3$Yb** featuring no hydrogen bonding at all. Complexes **Cu$_3$Gd** and **Cu$_3$Dy** each feature an intermolecular hydrogen bond between their non-coordinated nitrate and the methanol cap of Cu4 (O22 $\cdots$ H15 = 1.949(18) and 2.193(19) Å, respectively). The two coordinated chloride caps in **Cu$_3$Ho** (Figure 4.4) and **Cu$_3$Er** each form intermolecular hydrogen bonds to symmetry generated water solvates (Cl1 $\cdots$ H17A* = 2.190(8) and 2.188(7) Å, and Cl2 $\cdots$ H17B* = 2.271(7) and 2.298(9) Å, respectively). Each chloride cap in the Cu^{II} series is also involved in intramolecular hydrogen bonding with water capping groups on each of the respective Ln^{III} centres in **Cu$_3$Ho** (Cl1 $\cdots$ H14A = 2.014(9) Å and Cl2 $\cdots$ H14B = 2.044(9) Å), **Cu$_3$Er** (Cl1 $\cdots$ H15A = 2.108(9) Å and Cl2 $\cdots$ H15B 2.136(9) Å), and **Cu$_3$Tb** (Cl1 $\cdots$ H14A = 2.494(7) Å and Cl2 $\cdots$ H15A = 2.046(7) Å).

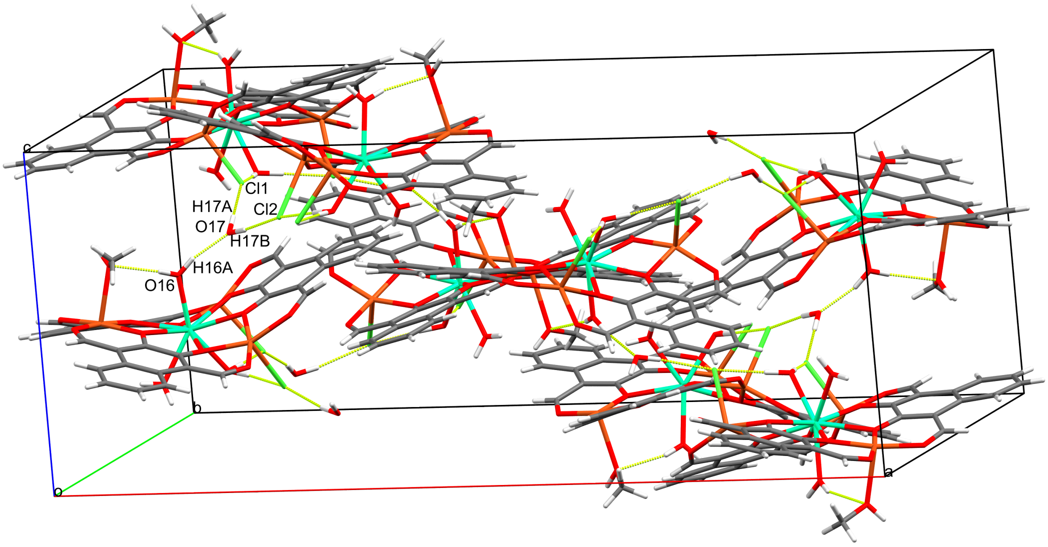

FIGURE 4.4: X-ray crystal packing of **Cu$_3$Ho** within the unit cell with hydrogen bonds (in yellow) shown to highlight the intermolecular hydrogen bonds stabilizing the position of the non-coordinated water molecule (O17).

In contrast to the large hydrogen bonding networks present in the Ni$_3$Ln complexes discussed in Chapter 3, the inter-complex interactions of the Cu$_3$Ln series are largely dominated by $\pi-\pi$ stacking interactions (Figure 4.5). Although **Cu$_3$Tb**, notably, features only a single $\pi-\pi$ interaction with a distance of 3.825 Å (Figure 4.6, Table 4.1).

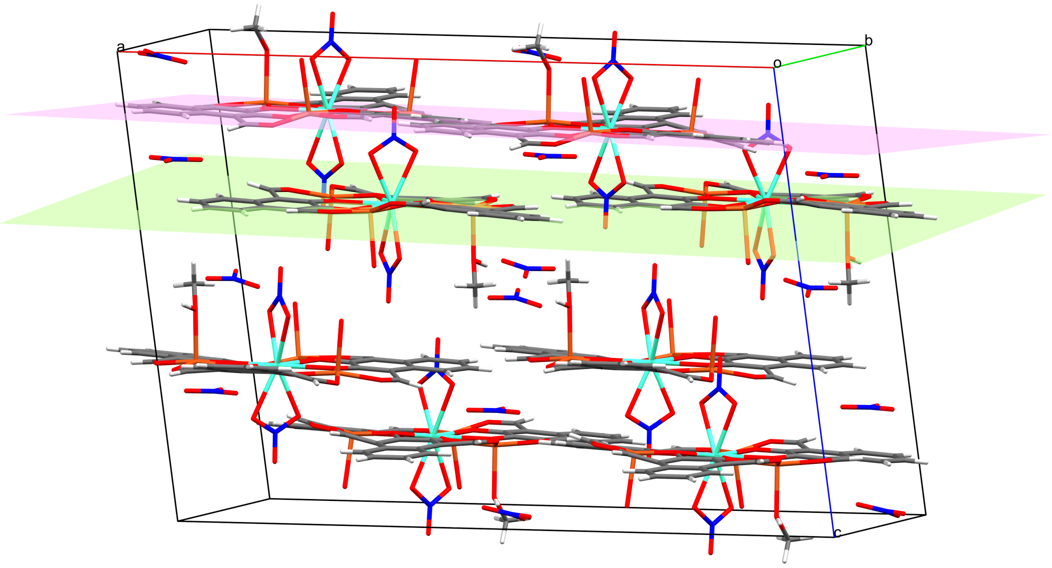

FIGURE 4.5: Packing of the unit cell of **Cu3Dy**. Least-squares planes visualized for the Cu3 planes of neighbouring unit complexes to show the relative planarity of the crystal packing within **Cu3Dy**, **Cu3Gd**, **Cu3Yb**, and **Cu3La**.

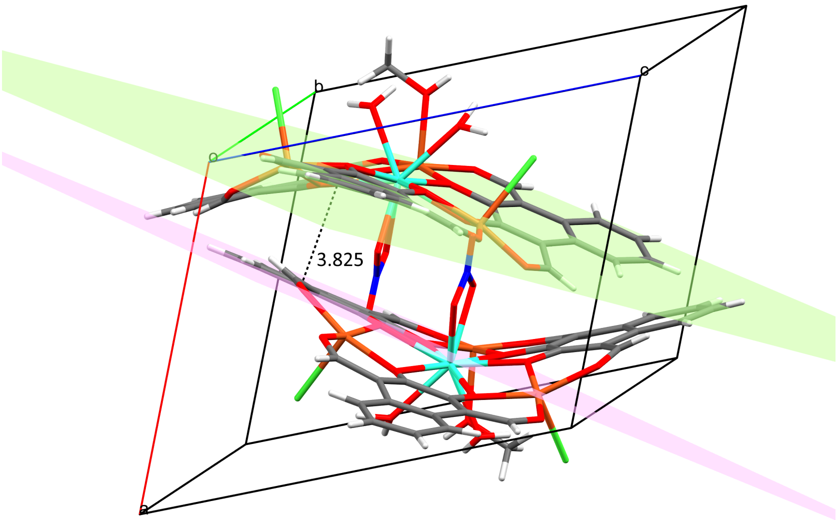

FIGURE 4.6: Packing of two molecules of **Cu3Tb** within the unit cell. Least-squares planes visualized for each Cu3 plane. The distance given corresponds to the $\pi - \pi$ stacking separation of the naphthalene backbone sitting in the Cu3 plane.

TABLE 4.1: Calculated $\pi - \pi$ stacking distances and cross-sectional areas.

Complex	**$\pi - \pi$ stacking (Å)**	**Molecular area (Å^3)**
Cu$_3$La	3.763 – 3.824	210.0
Cu$_3$Gd	3.632 – 3.898	219.1
Cu$_3$Dy	3.642 – 3.935	218.7
Cu$_3$Yb	3.622 – 3.892	223.5
Cu$_3$Ho	3.644 – 3.914	203.1
Cu$_3$Er	3.614 – 3.987	203.0
Cu$_3$Tb	3.825	203.6

4.3 Magnetic Characterization

Five of the seven Cu$_3$Ln complexes have been characterized with DC susceptibility and magnetization measurements, with AC measurements completed for the three most promising complexes: **Cu$_3$Tb**, **Cu$_3$Dy**, and **Cu$_3$Gd**. Unfortunately, the **Cu$_3$Er** and **Cu$_3$La** complexes could not be prepared in the required quantity to facilitate magnetic characterization.

DC Magnetic Measurements

Complexes **Cu$_3$Ho** and **Cu$_3$Yb** both exhibited room temperature $\chi_m T$ products (13.79 and 3.63 cm^3 K mol^{-1}) below their expected spin-only values of 15.2 and 3.70 cm^3 K mol^{-1}, respectively. It was found that upon decreasing temperature, both **Cu$_3$Ho** and **Cu$_3$Yb** exhibited a monotonic decrease in the $\chi_m T$ product (Figure 4.7, top) which may be associated with the progressive depopulation of the Stark sub-levels of each lanthanide ion. This suggests an apparent weak antiferromagnetic coupling between the Cu^{II} and Ln^{III} ions, which is further evidenced by the experimental M vs H data (*vide infra*). Complexes **Cu$_3$Dy** and **Cu$_3$Tb** both exhibited room temperature $\chi_m T$ products (14.06 and 11.70 cm^3 K mol^{-1}) below their expected spin-only values of 15.3 and 12.9 cm^3 K mol^{-1}, respectively. **Cu$_3$Gd** had an experimental room temperature $\chi_m T$ product of 9.06 cm^3 K mol^{-1} which slightly exceeded the calculated spin-only value of 9.00 cm^3 K mol^{-1}. These three complexes exhibited a sharp increase in their respective $\chi_m T$ products when cooled below ca. 50 K, with **Cu$_3$Tb** reaching a peak of 14.6 cm^3 K mol^{-1} at 2.2 K and **Cu$_3$Gd** reaching a peak of 12.5 cm^3 K mol^{-1} at 7.5 K (Figure 4.7, bottom). These peaks strongly suggest ferromagnetic coupling between the Ln^{III} and Cu^{II} centres.

The M vs H magnetization plots for each complex is shown in Figure 4.8. The magnetization of **Cu$_3$Gd** nearly reached its theoretical saturation magnetization (M_{sat} =

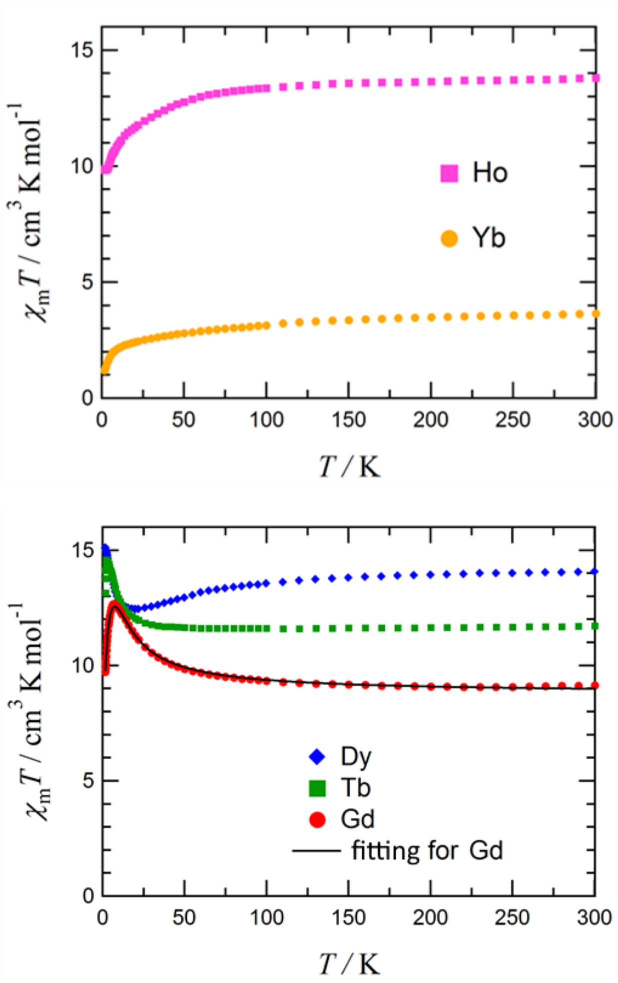

FIGURE 4.7: Plot of $\chi_m T$ vs T for **Cu$_3$Ho** and **Cu$_3$Yb** (top), and **Cu$_3$Dy**, **Cu$_3$Gd**, and **Cu$_3$Tb** (bottom), measured at 5000 Oe above 100 K and 500 Oe below 100 K.

$g_{\mathrm{Ln^{III}}} S_{\mathrm{Ln^{III}}} + g_{\mathrm{Cu^{II}}} S_{\mathrm{Cu^{II}}}$) of 10 $N_A \mu_B$, while **Cu$_3$Tb** and **Cu$_3$Dy** did not reach their theoretical M_{sat} values even at 7 T (Table 4.2), owing to the presence of strong magnetic anisotropy. However, these values exceeded the antiferromagnetic limit, supporting the presence of a ferromagnetic ground state. The magnetization data of **Cu$_3$Ho** and **Cu$_3$Yb** similarly exceeded the antiferromagnetic limit, however, practically non-coupled systems would also show a similar behaviour due to the additive property of magnetic susceptibility, i.e. $\chi_m T(\mathrm{Cu_3Ho}) \approx 3 \times \chi_m T(\mathrm{Cu^{II}}) + \chi_m T(\mathrm{Ho^{III}})$ for a non-coupled Cu$_3$Ho complex. Combining the susceptibility results, we can cautiously conclude that the Ln – Cu exchange couplings in **Cu$_3$Ho** and **Cu$_3$Yb** are ferromagnetic in nature.

The M vs H data for **Cu$_3$Gd** reached 9.84 μ_B, very near its spin only M_{sat} of 10μ_B, which unequivocally evidences a high spin ground state with $S_{\mathrm{total}} = 10/2$. The $\chi_m T$ vs T plot

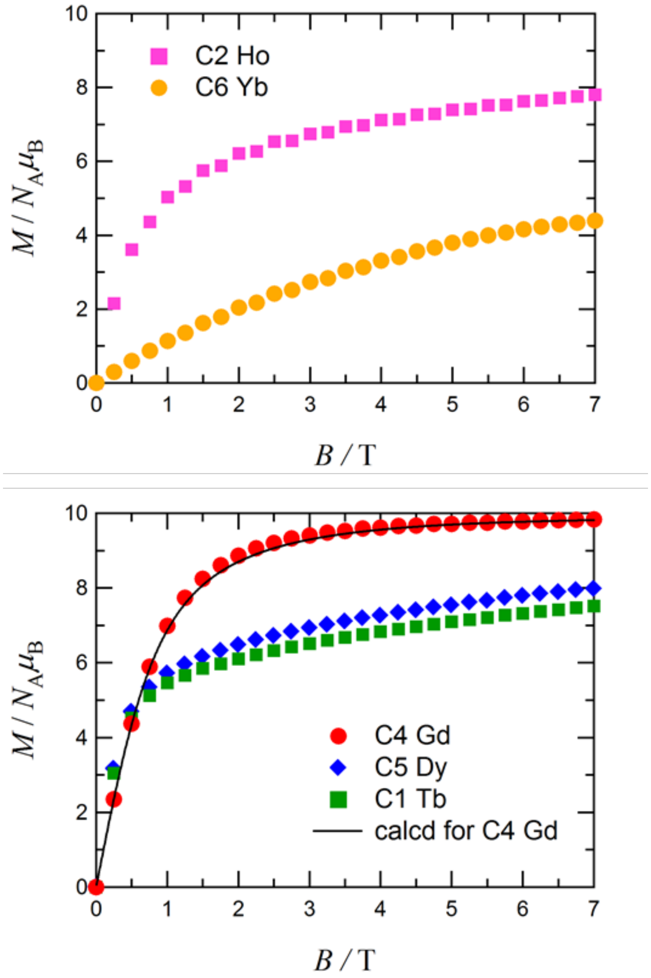

FIGURE 4.8: Plot of M vs H for **Cu$_3$Ho** and **Cu$_3$Yb** (top), and **Cu$_3$Dy**, **Cu$_3$Gd**, and **Cu$_3$Tb** (bottom), measured at 1.8 K.

for **Cu$_3$Gd** shows a monotonic increase down to 7.5 K, originating from the three Cu$^{\mathrm{II}}$ – Gd$^{\mathrm{III}}$ interactions. However, the quantitative separation of the J-coupling terms is difficult from an experimental standpoint due to the approximate local C_{3h} symmetry about Gd1. Thus, to avoid over-parameterization **Cu$_3$Gd** has been approximated to feature only a single Cu$^{\mathrm{II}}$ – Gd$^{\mathrm{III}}$ coupling term; i.e. $J_{12} = J_{13} = J_{14} = J$, where J can be estimated with the following van Vleck equation (Eq. 4.1) based on the spin Hamiltonian $\mathcal{H} = -2J(S_1 \cdot S_2 + S_1 \cdot S_3 + S_1 \cdot S_4)$:

$$\chi_\mathrm{m} T = \frac{2N_\mathrm{A}^2 g_\mathrm{ave}^2 \mu_\mathrm{B}^2}{k_\mathrm{B}} \frac{T}{T-\theta} \frac{A}{B} \tag{4.1}$$

where

$$\begin{aligned}
A &= 5\exp(-24J/k_\mathrm{B}) + 14\exp(-18J/k_\mathrm{B}) + 28\exp(-15J/k_\mathrm{B}) + 30\exp(-10J/k_\mathrm{B}) \\
&\quad + 60\exp(-7J/k_\mathrm{B}) + 55 \\
B &= 5\exp(-24J/k_\mathrm{B}) + 7\exp(-18J/k_\mathrm{B}) + 14\exp(-15J/k_\mathrm{B}) + 9\exp(-10J/k_\mathrm{B}) \\
&\quad + 18\exp(-7J/k_\mathrm{B}) + 11
\end{aligned}$$

The Weiss mean field parameter, θ, has also been included to account for intermolecular interactions. Optimization of Eq. 4.1 gave $2J/k_\mathrm{B} = +5.78(6)$ K, $g_\mathrm{ave} = 1.976(2)$, and $\theta = -0.898(7)$ K. The calculated fitting parameters reproduced the trend of the experimental data well (Figures 4.7 and 4.8, bottom).

Fitting of the experimental DC susceptibility and magnetization data of **Cu3Gd** was attempted using a $2j$ model based on a modified spin Hamiltonian, Eq. 4.2. However, the final decrease in the $\chi_\mathrm{m}T$ product below 7 K could not be properly reproduced (Figure 4.9) when modelling the Cu – Cu interactions (J_{23}, J_{24}, and J_{34}) with MAGPACK.[147,148]

$$\mathcal{H} = -2J(S_1 \cdot S_2 + S_1 \cdot S_3 + S_1 \cdot S_4) - 2j(S_2 \cdot S_3 + S_2 \cdot S_4 + S_3 \cdot S_4) \tag{4.2}$$

where $2J/k_\mathrm{B} = +5.78$ K and $2j_\mathrm{Cu—Cu}/k_\mathrm{B} = 8.0$ or 16.0 K.

TABLE 4.2: Calculated and experimental values for the magnetic properties of complexes **Cu3Tb**, **Cu3Ho**, **Cu3Gd**, **Cu3Dy**, and **Cu3Yb**.

Complex	g_J **of Ln**$^\mathrm{III}$	$\chi_\mathrm{m}T$ **/ cm^3 K mol^{-1} (exp. at 300 K)[a]**	$\chi_\mathrm{m}T$ **/ cm^3 K mol^{-1} (calc.)**	M **/ $N_\mathrm{A}\mu_\mathrm{B}$ (exp. at 7 T)[b]**	M_sat **/ $N_\mathrm{A}\mu_\mathrm{B}$ (calc)[c]**
Cu3Tb	3/2	11.70	12.9	7.52	12
Cu3Ho	5/4	13.79	15.2	7.81	13
Cu3Gd	2	9.06	9.00	9.84	10
Cu3Dy	4/3	14.06	15.3	7.98	13
Cu3Yb	8/7	3.63	3.70	4.39	7

[a] Measured at 500 Oe, fixed with eicosane

[b] Measured at 1.8 K, fixed with eicosane

[c] Calculated for strongly anisotropic Ln$^\mathrm{III}$ ions where $|J_z| \approx J$

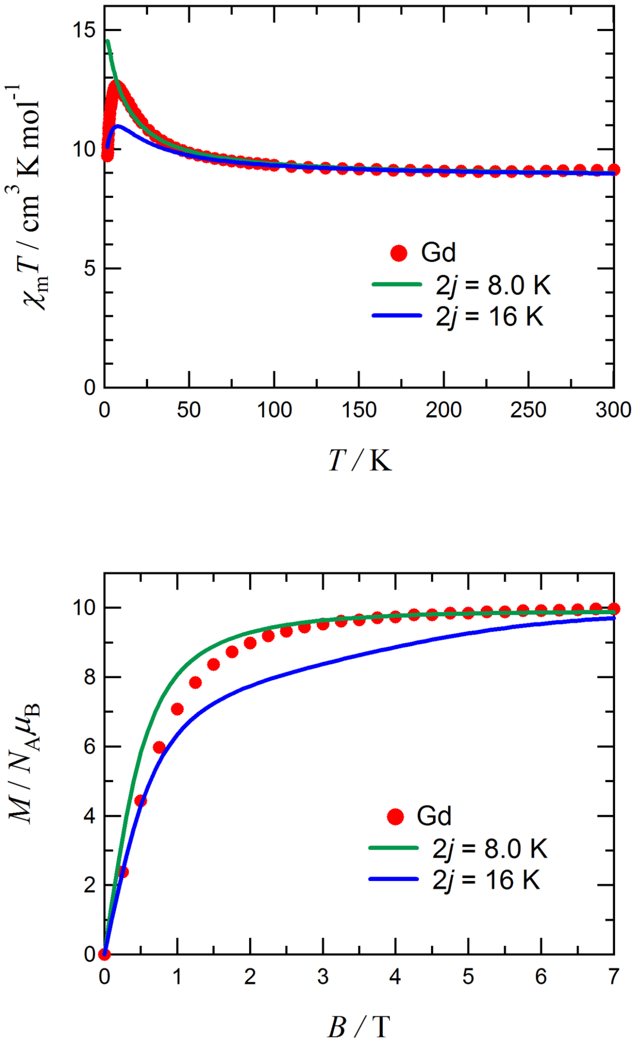

FIGURE 4.9: Plots of $\chi_m T$ vs T (top) and M vs H (bottom) for **Cu3Gd** and their simulated fits using a 2j model based on the below spin Hamiltonian.

AC Magnetic Measurements

As expected from the profile of the DC magnetic susceptibility measurements, only **Cu3Dy**, **Cu3Gd**, and **Cu3Tb** exhibited meaningful frequency dependence in the AC susceptibility measurements. Complexes **Cu3Gd** (Figure 4.10) and **Cu3Dy** (Figure 4.11) showed appreciable frequency-dependent AC susceptibilities below 5 K with applied DC bias fields of 2000 and 1000 Oe, respectively.

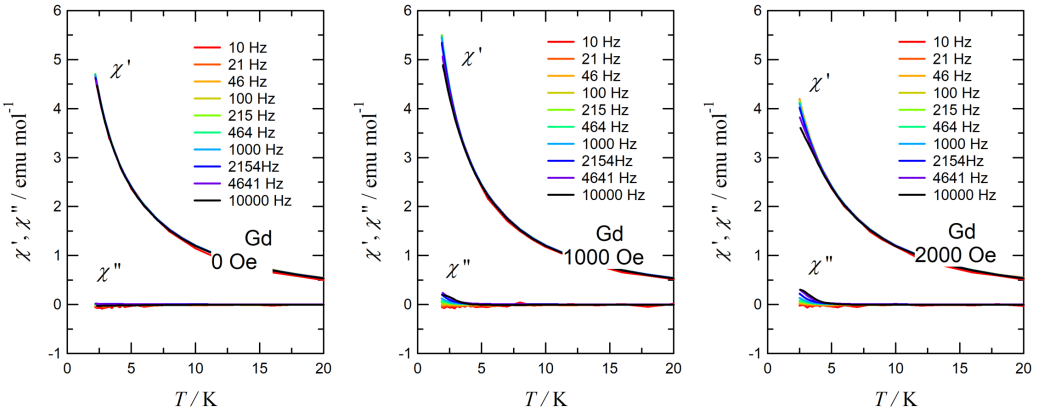

FIGURE 4.10: Temperature and frequency dependence of the AC susceptibilities in various applied DC fields for **Cu3Gd**.

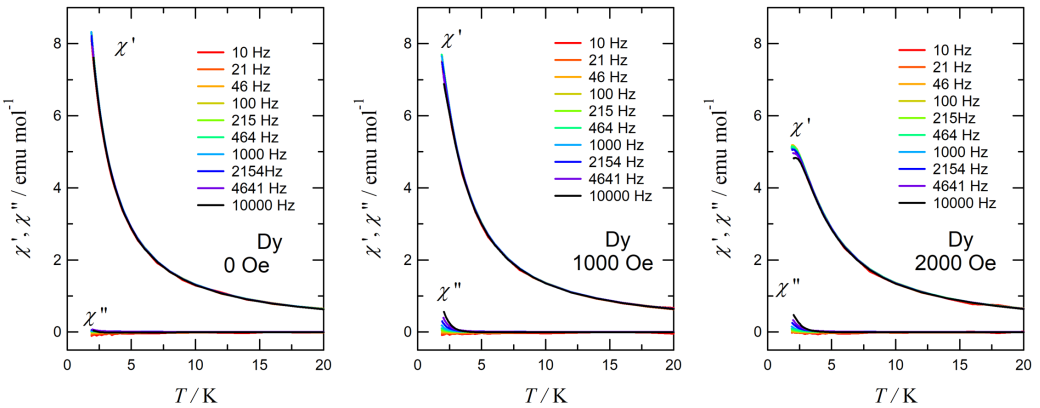

FIGURE 4.11: Temperature and frequency dependence of the AC susceptibilities in various applied DC fields for **Cu3Dy**.

Similarly, **Cu_3Tb** exhibited slow relaxation of magnetization as indicated by the appreciable frequency dependence of the AC susceptibility below ca. 5 K (Figure 4.12). The effective barrier for the reversal of magnetization, U_{eff}, for **Cu_3Tb** was estimated using a modified Arrhenius plot (Figure 4.13) based on Eq. 4.3:[149]

$$\ln\left(\frac{\chi''}{\chi'}\right) = \ln(2\pi\nu\tau_0) + \frac{U_{\mathrm{eff}}}{k_{\mathrm{B}}T} \tag{4.3}$$

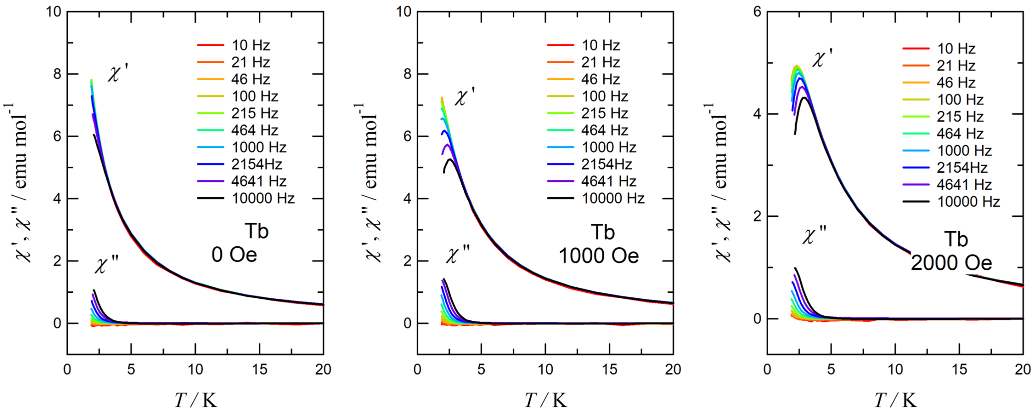

FIGURE 4.12: Temperature and frequency dependence of the AC susceptibilities in various applied DC fields for **Cu_3Tb**.

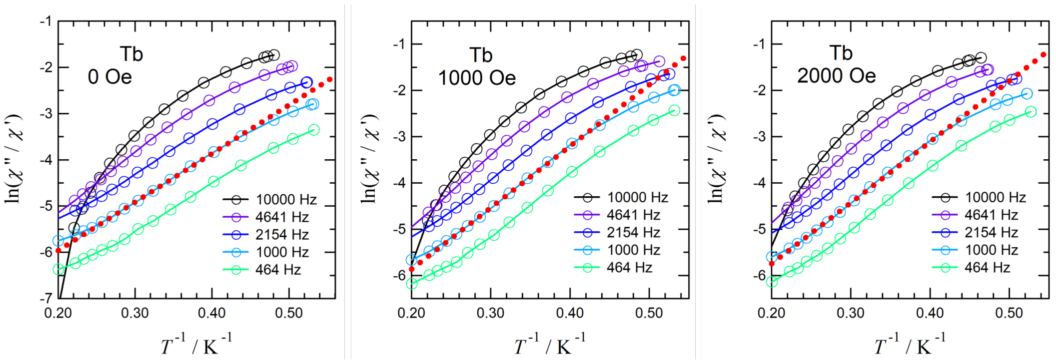

FIGURE 4.13: Modified Arrhenius plots for **Cu_3Tb** at various frequencies and static fields. The dotted red line is drawn for the estimation of U_{eff} and τ_0.

Based on Figure 4.13 and Eq. 4.3, the U_{eff} values for **Cu_3Tb** are 10.5(1) K (in zero applied field) and 13.3(2) K (in a 1000 Oe applied bias), with τ_0 values of 5.02×10^{-8} and 3.10×10^{-8} s, respectively. Similarly, based on the plots in Figure 4.14, Eq. 4.3 can be optimized for **Cu_3Gd** (in a 2000 Oe applied bias) and **Cu_3Dy** (in a 1000 Oe applied bias), to give U_{eff} values are 10.8(2) and 7.82(4) K and τ_0 values of 8.80×10^{-8} and 6.05×10^{-8} s, respectively. Figure 4.15 shows the modified Arrhenius plots for the 1000 Hz data of each complex.

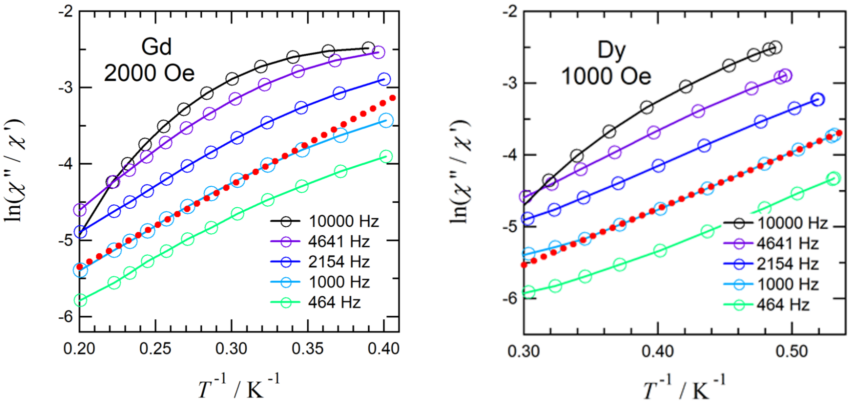

FIGURE 4.14: Modified Arrhenius plots for **Cu_3Gd** (left) and **Cu_3Dy** (right) at various frequencies with the stated applied biases. The dotted red line is drawn for the estimation of U_{eff} and τ_0.

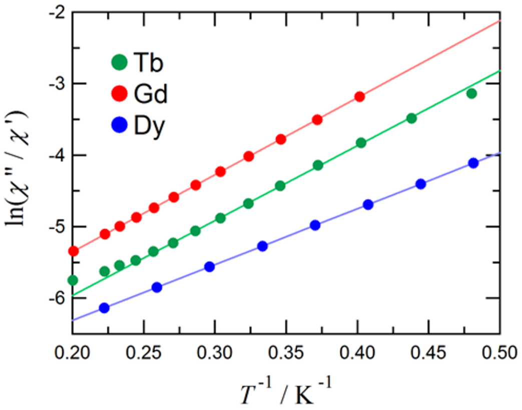

FIGURE 4.15: Modified Arrhenius plots for the 1000 Hz data of **Cu_3Tb** in zero applied DC field, **Cu_3Gd** in a 2000 Oe static field, and **Cu_3Dy** in a 1000 Oe static field.

Based on the AC susceptibility data of **Cu_3Tb** in a 1000 Oe static field, a Cole-Cole plot can be drawn (Figure 4.16) to show the relationship between the in-phase data (χ') and the out-of-phase data (χ''). The solid lines drawn for data sets at 2.0, 2.1, and 2.3 K represent the best fit obtained at the given temperature when considering the generalized Debye model, as in Eq. 4.4:[150]

$$\chi(\omega) = \chi_S + \frac{\chi_T - \chi_S}{1 + (i\omega\tau)^{1-\alpha}} \tag{4.4}$$

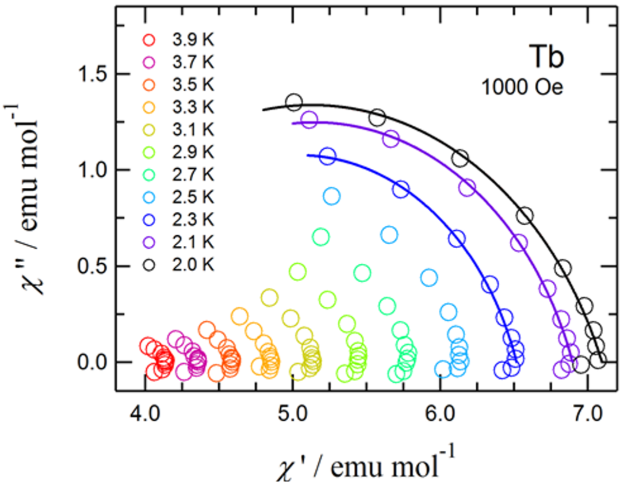

FIGURE 4.16: Cole-Cole plot for **Cu_3Tb** in 1000 Oe static field, with traces drawn for data sets recorded at 2.0, 2.1, and 2.3 K.

where χ_S is the adiabatic susceptibility, χ_T is the isothermal susceptibility, ω is the frequency, τ is the relaxation time, and α is the Cole-Cole parameter which is related to the distribution of relaxation times.[151] The best line fits at 2.0, 2.1, and 2.3 K almost trace quarter circles where α = 0.24(2), 0.21(2), and 0.19(5), respectively. In this low temperature regime, the thermal energy is of the order of the exchange coupled excited states, thus allowing thermal population of these states and serving as a potential magnetization relaxation pathway, where the Orbach process may be operative. Unfortunately, a normal Arrhenius plot cannot be drawn from the data, and based on the collected data the exact relaxation mechanisms at play in this system cannot be determined with accuracy. However, the relatively small Cole-Cole parameter values do indicate the there is only likely to be one relaxation process occurring.

Table 4.3 summarizes the results of the AC magnetic susceptibility measurements. In general, superexchange between the $3d_{x^2-y^2}$ orbitals of the transition metals and the $4f$ spins of the heavy lanthanide metals depends on the geometry of the Cu – O – Ln – O four-membered chelate ring – where more planar MO_2 and LnO_2 dihedral angles lead to stronger ferromagnetic couplings.[152–155] Based on macrocyclic Cu_3Ln analogues previously prepared by Brooker *et al.*; **Cu_3Tb**, containing the Cu_3TbO_6 core, was expected to show the greatest potential as an SMM. The Cu_3TbL^{Bu} complex[106] (L^{Bu} = [3 + 3] Schiff base of 1,4-diaminobutane and 1,4-diformyl-2,3-dihydroxybenzene) containing a 10-coordinate Tb ion was reported to have a barrier of 19.5(5) K. A smaller Cu_3TbL^{Pr} analogue[104] (L^{Pr} = 3 + 3 Schiff base of 1,3-diaminopropane and 1,4-diformyl-2,3-dihydroxybenzene), which contained a 9-coordinate Tb ion, was also determined to be an SMM although a barrier height could not be extracted. **Cu_3Tb**, being a Kramer's type molecule, showed the most promise as an SMM as indicated by the magnitude of χ' and its frequency dependence. **Cu_3Gd** and **Cu_3Dy** also showed appreciable frequency dependence in an applied field, but had lower effective barriers, which may be related to the fact they are not Kramer's type molecules.[156,157] Since Gd^{III} itself is an isotropic ion, the origin of the slow relaxation of magnetization for **Cu_3Gd** is unclear. There are many literature examples of Gd^{III} containing complexes, and indeed CuGd type systems, which exhibit slow relaxation of magnetization. In the case of **Cu_3Gd** it is thought that the observed anisotropy could arise from an asymmetric crystal field environment where J_z is not equal to J_x and J_y.[158]

TABLE 4.3: Summary of the key parameters extracted from the AC susceptibility measurements.

Complex	**H / Oe**	**τ_0 / 10^{-8} s**	**U_{eff} / k_B K**
Cu_3Tb	0	5.0(1)	10.5(1)
	1000	3.1(2)	13.3(2)
	2000	3.6(3)	13.2(3)
Cu_3Gd	2000	8.8(6)	10.8(2)
Cu_3Dy	1000	6.0(1)	7.82(4)

Conclusions

The reaction between **H_2L1** and $Cu(NO_3)_2 \cdot 3\,H_2O$ in the presence of various lanthanide salts has yielded seven new complexes, all of which have been structurally characterized. This class of self-assembled metallacyclic complexes has previously been overlooked in favour of macrocyclic analogues where peripheral diimine chelators are typically used to stabilize complexes involving a transition metal ion with five- or six-membered chelation rings. Formation of a macrocyclic scaffold was found to be unnecessary in the successful construction of tetranuclear clusters with SMM properties. Five of the complexes were prepared in sufficient quantity and purity to elicit magnetic characterization. DC susceptibility measurements indicated a ferromagnetic ground state was present for **Cu_3Gd**, **Cu_3Dy**, and **Cu_3Tb**, furthermore, all three of these complexes exhibited appreciable frequency dependence in their AC magnetic measurements. Macrocyclic analogues indicated that the Cu_3Tb complex was likely to exhibit SMM properties; however, observation of the slow relaxation of magnetization in monomeric Cu_3Ln (Ln = Gd or Dy) complexes of this type have not previously been reported. Fitting of the AC data yielded small values for the Cole-Cole parameter, α, implying that there is most likely only a single relaxation pathway present in these complexes. **Cu_3Tb**, containing Tb^{III}, is a Kramers-type molecule and had an observable barrier to relaxation in the absence of an applied field, with its maximum barrier determined to be 13.3(2) K in a 1000 Oe applied bias. Complexes **Cu_3Gd** and **Cu_3Dy** are not Kramers-type molecules but still yielded meaningful frequency dependent data in their AC susceptibility measurements. The Gd-containing complex, **Cu_3Gd**, was found to have a barrier height of 10.8(2) K in a 2000 Oe applied bias, while **Cu_3Dy** showed a lower barrier of 7.82(4) K in a 1000 Oe applied bias. This chapter represents the first reported observation of the slow relaxation of magnetization in this type of Cu_3Ln complex utilizing an acyclic ligand system.

Preparation

Cu$_3$Dy formulated as [**L1**$_3$Cu$_3$Dy(NO$_3$)$_2$(H$_2$O)$_2$(MeOH)](NO$_3$) was obtained as orange plate crystals in 47% yield (based on Dy(NO$_3$)$_3 \cdot 6\,$H$_2$O). ATR-IR $\bar{\nu}$: 1611, 1568, 1486, 1432, 1382, 1351, 1313, 1259, 1141, 1030, 974, 755, 711 cm^{-1}. Microanalytical data found(calc) for **Cu$_3$Dy** (calculated for C$_{37}$H$_{26}$Cu$_3$DyN$_3$O$_{24}$, M_r = 1249.75 g mol^{-1}) C: 35.72(35.56), H: 1.97(2.10), N: 3.31(3.36).

Cu$_3$Er formulated as [**L1**$_3$Cu$_3$ErCl$_3$(H$_2$O)3.5(MeOH)0.5](H$_2$O) was obtained as orange plate crystals in 84% yield (based on ErCl$_3 \cdot 6\,$H$_2$O). ATR-IR $\bar{\nu}$: 1612, 1567, 1484, 1428, 1381, 3152, 1310, 1264, 1143, 1027, 981, 756, 710 cm^{-1}. Microanalytical data found(calc) for **Cu$_3$Er** (calculated for C$_{36.5}$H$_{29}$Cu$_3$ErCl$_3$O$_{17}$, M_r = 1203.87 g mol^{-1}) C: 36.70(36.42), H: 2.48(2.43).

Cu$_3$Gd formulated as [**L1**$_3$Cu$_3$Gd(NO$_3$)$_2$(H$_2$O)$_2$(MeOH)](NO$_3$) was obtained as orange plate crystals in 88% yield (based on Gd(NO$_3$)$_3 \cdot 6\,$H$_2$O). ATR-IR $\bar{\nu}$: 1616, 1566, 1485, 1429, 1382, 1351, 1314, 1258, 1140, 1029, 975, 756, 718 cm^{-1}. Microanalytical data found(calc) for **Cu$_3$Gd** (calculated for C$_{37}$H$_{26}$Cu$_3$GdN$_3$O$_{24}$, M_r = 1244.50 g mol^{-1}) C: 36.07(35.71), H: 1.97(2.11), N: 3.59(3.38).

Cu$_3$Ho formulated as [**L1**$_3$Cu$_3$HoCl$_3$(H$_2$O)$_4$(MeOH)](H$_2$O) was obtained as orange block crystals in 56% yield (based on HoCl$_3 \cdot 6\,$H$_2$O). ATR-IR $\bar{\nu}$: 1611, 1568, 1486, 1433, 1382, 1352, 1313, 1259, 1141, 1029, 975, 755, 717 cm^{-1}. Microanalytical data found(calc) for **Cu$_3$Ho** (calculated for C$_{37}$H$_{30}$Cu$_3$HoCl$_3$O$_{17}$, M_r = 1208.55 g mol^{-1}) C: 36.47(36.77), H: 2.38(2.50).

Cu$_3$La formulated as [**L1**$_3$Cu$_3$La(NO$_3$)$_2$(H$_2$O)$_2$(MeOH)](NO$_3$) was obtained as orange plate crystals in 28% yield (based on La(OAc)$_3 \cdot 6\,$H$_2$O). ATR-IR $\bar{\nu}$: 1614, 1566, 1488, 1434, 1387, 1351, 1317, 1261, 1144, 1030, 975, 751, 710 cm^{-1}. Microanalytical data found(calc) for **Cu$_3$Ho** (calculated for C$_{37}$H$_{26}$Cu$_3$LaN$_3$O$_{24}$, M_r = 1226.15 g mol^{-1}) C: 36.40(36.24), H: 1.80(2.14), N: 3.41(3.43).

Cu$_3$Tb formulated as [**L1**$_3$Cu$_3$TbCl$_2$(NO$_3$)(H$_2$O)$_2$] was obtained as orange block crystals in 77% yield (based on TbCl$_3 \cdot 6\,$H$_2$O). ATR-IR $\bar{\nu}$: 1612, 1569, 1485, 1450, 1432, 1382, 1351, 1314, 1259, 1141, 1030, 975, 756, 718 cm^{-1}. Microanalytical data found(calc) for **Cu$_3$Tb** (calculated for C$_{36}$Cu$_3$TbCl$_2$NO$_{17}$, M_r = 1161.03 g mol^{-1}) C: 37.19(37.24), H: 1.71(1.91), N: 1.22(1.21).

Cu$_3$Yb formulated as [**L1**$_3$Cu$_3$Yb(NO$_3$)$_2$(H$_2$O)$_2$(MeOH)](NO$_3$) was obtained as orange block crystals in 44% yield (based on Yb(OAc)$_3 \cdot 6\,$H$_2$O). ATR-IR $\bar{\nu}$: 1610, 1567, 1488, 1434, 1383, 1355, 1316, 1260, 1143, 1032, 975, 752, 699 cm^{-1}. Microanalytical data found(calc) for **Cu$_3$Yb** (calculated for C$_{37}$H$_{26}$Cu$_3$YbN$_3$O$_{24}$, M_r = 1260.30 g mol^{-1}) C: 36.40(36.24), H: 1.80(2.14), N: 3.41(3.43).

Chapter 5

Co_3Ln Clusters

This chapter discusses the preparation, structural elucidation, and some further characterization for the four Co^{II} based triangle clusters (**Co_3Dy**, **Co_3Gd**, **Co_3La**, and **Co_3Tb**). This modest series of complexes features variations in the coordination geometry of one cobalt centre within each of the complexes **Co_3Gd**, **Co_3La**, and **Co_3Tb**. Aside from these three exceptions, all of the Co^{II} centres in this series are octahedrally coordinated. The lanthanum bearing complex, **Co_3La**, was prepared in sufficient quantity and purity to undergo magnetic characterization. The [Xe]$4f^0$ electronic configuration of La^{III} makes the **Co_3La** complex a model compound for cyclic triangular Co^{II} – Co^{II} – Co^{II} interactions in the absence of another paramagnetic ion.

A literature search revealed only a single publication to date which featured complexes with a $Co^{II}{}_3Ln^{III}O_6$ core (Figure 5.1). This report by Mashima *et al.* detailed the synthesis of seven macrocyclic triangle complexes, four of which ([Co_3La], [Co_3Ce], [Co_3Sm], and [Co_3Eu]) were structurally characterized.[113] As with a majority of other analogous systems within the literature, a single [3 + 3] macrocyclic ligand was present in these complexes, providing an N_2O_2 equatorial environment for the Co^{II} centres – the ligand in this case was prepared from the Zn_3La templated [3 + 3] condensation of 1,4-diformylbenzene-2,3-diol with 1,2-bis(aminooxy)ethane, prior to metal abstraction with HCl. The focus of this paper was not on magneto-structural correlations, but rather the catalytic properties of the complexes for the co-polymerization of CO_2 and cyclohexene oxide. Notably, the Co1 centre of Mashima's [Co_3Ce] complex exhibits a square pyramidal coordination geometry (`SPY-5 = 0.645`).[113]

5.1 Molecular Structure

Complex **Co_3Dy** has the formula $[Co_3Dy\mathbf{L1}_3(H_2O)(MeOH)_5(NO_3)_2](NO_3)$ and crystallizes in the triclinic space group $P\bar{1}$ with the asymmetric unit containing a full complex.

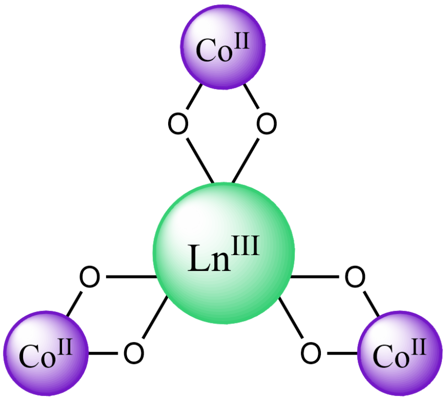

FIGURE 5.1: Schematic of the relatively unseen Co_3LnO_6 core.

This complex is relatively non-planar, as seen in Figure 5.2, with each cobalt centre being axially capped by two methanol molecules (Co2), a methanol and a water (Co3), or a methanol and an η_1-NO_3^- anion (Co4). The Dy^{III} ion sits in a 9-coordinate environment being equatorially bound by the six phenol groups and capped on one side of the Co_3 plane by an η_2-NO_3^- anion and on the other side by a methanol molecule. Charge balance considerations require all methanol and water caps to be fully protonated (*i.e.* charge neutral), with the metals contributing a total charge of +9 (Dy^{+3} and 3 × Co^{+2}) which is balanced by the three ligands with a −2 charge each and three nitrate anions.

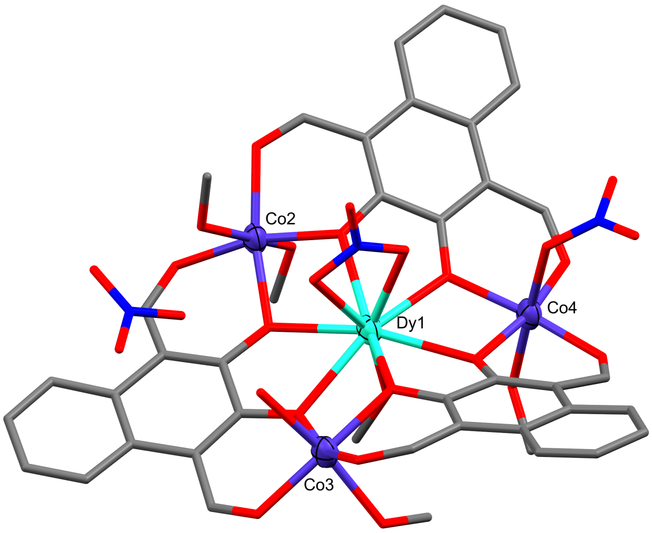

FIGURE 5.2: X-ray crystal structure of **Co3Dy**. Hydrogen atoms omitted for clarity. Thermal ellipsoids of metal atoms shown at the 70% probability level. C = grey, O = red, N = blue.

Co_3Dy features extensive intermolecular and intra-complex hydrogen bonding (Figure 5.3). The non-coordinated nitrate group forms strong hydrogen bonds from its O26 oxygen with a methanol cap of Co2 and the water cap of Co3 (O26 · · · H13 = 1.989(10) Å and O26 · · · H15A = 1.904(10) Å, respectively). A symmetry generated unit of complex provides a further two hydrogen bonds, stemming from the H14* proton of a Co2* bound methanol cap (O27 · · · H14* = 2.496(9) Å and O28 · · · H14* = 2.100(8) Å). There are another two strong hydrogen bonds formed directly between the two complex units by the methanol cap of Co4* with the water cap of Co3 (O15 · · · H17* = 2.008(7) Å) and the proton of the Co3 water cap acting as a hydrogen bond donor to the aldehyde binding Co4* in a symmetry generated molecule (O9* · · · H15B = 2.078(8) Å).

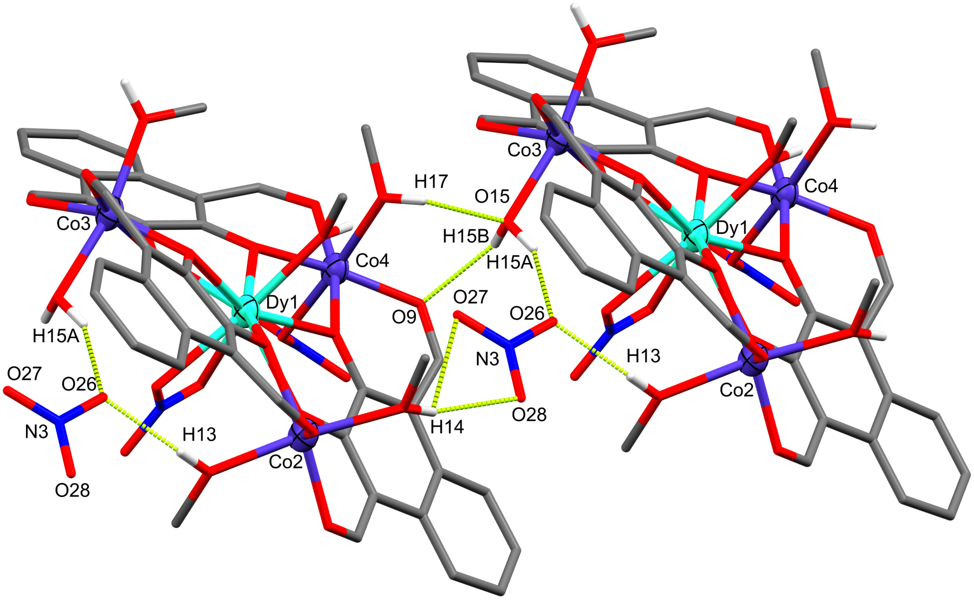

FIGURE 5.3: X-ray crystal structure showing the intermolecular hydrogen bonding between two unit complexes of **Co_3Dy** and the non-coordinated nitrate. C = grey, O = red, N = blue.

The **Co_3Gd** complex crystallizes in the triclinic space group $P\bar{1}$ ($Z' = 1$) with the formula [Co_3Gd**L1**$_3(MeOH)_4(NO_3)_3$] (Figure 5.4). **Co_3Gd** is significantly more planar than **Co_3Dy** and features two near octahedral cobalt centres (Co2 and Co3) each capped with two methanol molecules and one cobalt centre (Co4) in a strongly distorted octahedral environment (`OC-6 = 4.914`, Output 5.1). Co4 features an η_2-NO_3^- cap which leads to the aldehyde groups binding in a relatively distorted manner. The gadolinium centre of **Co_3Gd** sits in a 10-coordinate *pseudo*-hexagonal bipyramidal site with an η_2-NO_3^- cap either side of the Co_3 plane. With the three nitrate ions bound to metals, this complex is overall charge neutral. The absence of non-coordinated lattice species greatly reduces the number of intermolecular hydrogen bonds present in **Co_3Gd**.

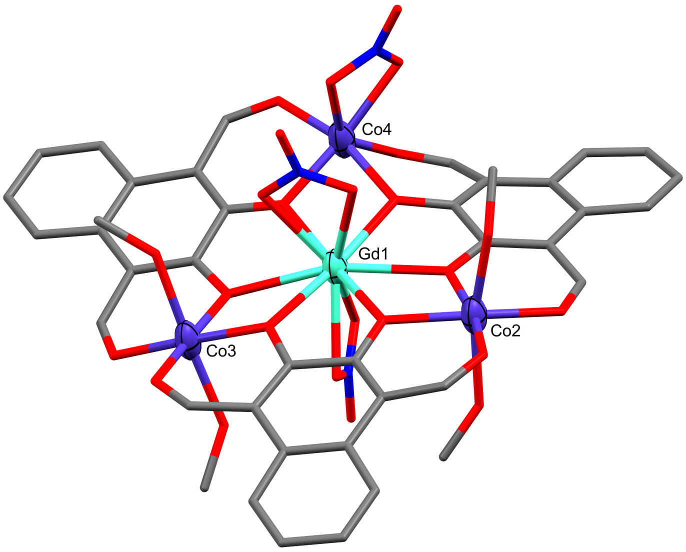

FIGURE 5.4: X-ray crystal structure of **Co_3Gd**. Hydrogen atoms omitted for clarity. Thermal ellipsoids of metal atoms shown at the 70% probability level. C = grey, O = red, N = blue.

Similar to **Co_3Dy** and **Co_3Gd**, the **Co_3La** complex (Figure 5.5) also crystallizes in the triclinic space group $P\bar{1}$ ($Z' = 1$), with only two near octahedral cobalt centres (Co2 and Co3). The other cobalt centre in this complex, Co4, sits in a distorted 5-coordinate trigonal bipyramidal environment (`TBPY-5 = 1.678`, Output 5.2). Water caps are present on both axial sites on Co2 and Co3, as well as the remaining equatorial coordination site on Co4. With two $\eta_2NO_3^-$ caps and one water cap, La1 has a coordination number of 11. Complex **Co_3La** has the formula $[Co_3La\mathbf{L1}_3(H_2O)_6(NO_3)_2]NO_3{\cdot}H_2O{\cdot}[1.5\,Et_2O]$, where the solvent contained within the square brackets corresponds to the contents of the solvent mask, with the non-coordinated nitrate being almost equally disordered over two spatially close sites with freely refined occupancies of 0.47(2) and 0.53(2).

Complex **Co_3La** packs with extensive inter- and intra-molecular hydrogen bonding (Figure 5.6). All but one of these hydrogen bonding interactions (O15 $\cdots$ H18A = 2.054 Å) occur with a nitrate being the hydrogen bond acceptor, with all three nitrates per unit complex forming two hydrogen bonds, and all hydrogen bond donors stemming from water caps. Inversion symmetry forms a small hydrogen bonding network between the N1 nitrate cap of La1 and an O13 water cap of Co2 with those of the inverted unit complex (O19 $\cdots$ H13A = 1.936 Å, and O21 $\cdots$ H13B* = 1.951 Å). The non-coordinated nitrate species shown in Figures 5.5 and 5.6 has the slightly higher occupancy (0.53(2)), and is stabilized by two hydrogen bonds to H15A (O31B $\cdots$ H15A = 1.848 Å and

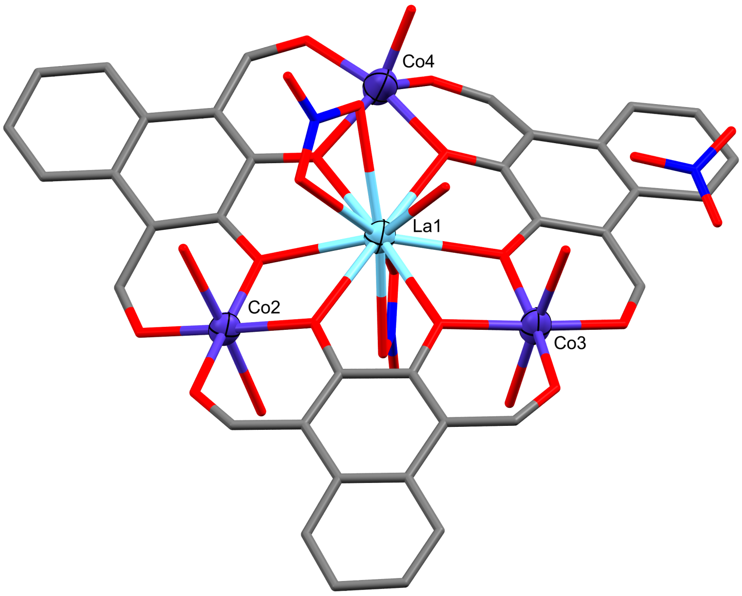

FIGURE 5.5: X-ray crystal structure of **Co_3La**. Hydrogen atoms, solvated, and disordered species are omitted for clarity. Thermal ellipsoids of metal atoms shown at the 70% probability level. C = grey, O = red, N = blue.

O33B ··· H15A = 2.281 Å), whereas, the nitrate site with occupancy 0.47(2) forms weaker hydrogen bonds (O31A ··· H15A = 2.905 Å and O33A ··· H15A = 2.154 Å). The remaining nitrate cap forms a strong hydrogen bond to the H14A water cap (O22 ··· H14A = 1.931 Å) of Co2 and a relatively weaker bond to the H16B water cap (O22 ··· H16B = 2.307 Å) of Co3. The crystal data for **Co_3La** shows a solvent accessible void of 192 $Å^3$, however there are no obvious structures present in the difference map, thus has been modelled with a solvent mask which accounts for 127 electrons per unit cell, this fits well for three diethyl ether molecules per unit cell (which equates to 126 electrons). The presence of diethyl ether in the crystal lattice, while not seen in the elemental analysis, is consistent with the observation of crystalline **Co_3La** samples rapidly crumbling when removed from the mother liquor and sat in air.

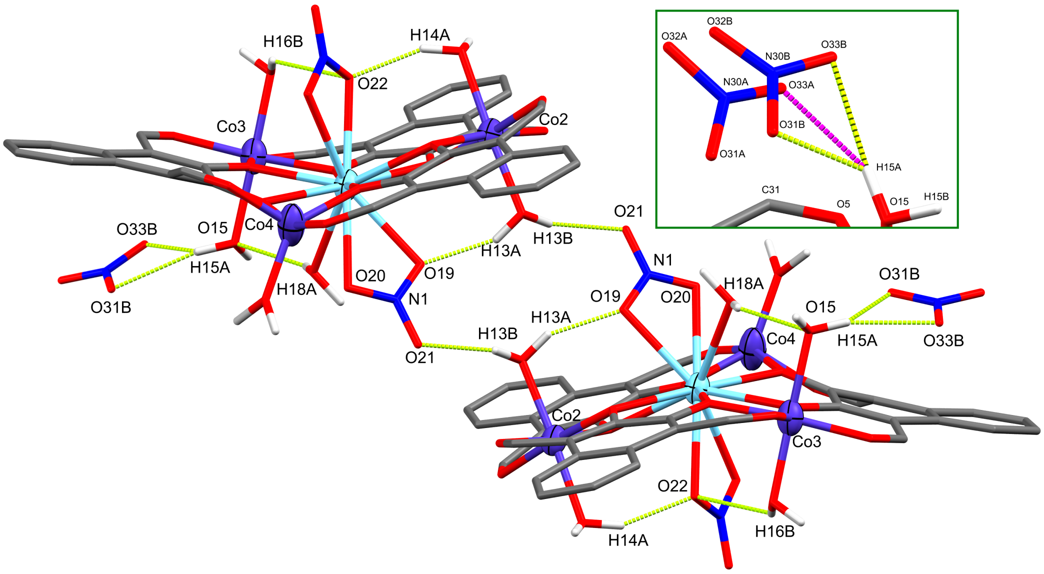

FIGURE 5.6: X-ray crystal structure of **Co_3La** showing the intermolecular hydrogen bonding between two complex units and the non-coordinated nitrate. The inset shows the two partially occupied nitrate sites. Thermal ellipsoids of metal atoms shown at 70% probability. Non-acidic hydrogen atoms have been omitted for clarity. H bonds shown as segmented yellow/pink bonds. C = grey, O = red, N = blue.

OUTPUT 5.1: SHAPE output for 6-coordinate Co^{II} centres of **Co_3Dy** **Co_3Gd** **Co_3La** and **Co_3Tb**.

```
Structure       PPY-6       OC-6     TPR-6     JPPY-6
Co3Dy-Co2,     23.460,     1.586,     9.247,    26.862
Co3Dy-Co3,     23.511,     1.634,     9.167,    27.141
Co3Dy-Co4,     26.314,     0.733,    13.479,    30.101

Co3Gd-Co2,     24.208,     1.263,    10.607,    28.554
Co3Gd-Co3,     27.422,     0.301,    14.711,    31.137
Co3Gd-Co4,     18.605,     4.914,     9.173,    22.831

Co3La-Co2,     26.572,     0.355,    13.673,    30.169
Co3La-Co3,     25.998,     0.605,    12.287,    29.345

Co3Tb-Co2,     25.058,     0.738,    11.901,    28.808
Co3Tb-Co4,     24.589,     0.947,    12.115,    28.466
```

OUTPUT 5.2: SHAPE output for 5-coordinate Co^{II} centres of **Co_3La** **Co_3Tb** and Mashima's [Co_3Ce] complex.

```
Structure       vOC-5     TBPY-5      SPY-5    JTBPY-5
Co3La-Co4,      5.623,     1.678,     3.334,     4.048
Co3Tb-Co3,      4.736,     3.221,     1.734,     6.781
Co3Ce-Co1,      1.884,     3.944,     0.645,     6.061
```

Complex **Co_3Tb** (Figure 5.7) is a charge neutral mixed anion complex with the formula [Co_3Tb**L1**$_3Cl(H_2O)_{0.5}(MeOH)_{4.5}(NO_3)_2$]·[1.5 H_2O] which crystallizes in the centrosymmetric monoclinic space group *C2/c* ($Z' = 1$). Similar to **Co_3La**, **Co_3Tb** has two near octahedral cobalt centres (Co2 and Co4) and a square pyramidal Co3 (`SPY-5 = 1.734`, Output 5.2). Although **Co_3Tb** was not the only Co_3Ln complex prepared using a non-nitrate salt (see the preparation of **Co_3La**), the square pyramidal cobalt centre, Co3, is unambiguously capped by a single chloride anion originating from the $TbCl_3 \cdot 6H_2O$ salt used in the complex preparation. Both Co2 and Co4 are octahedral but Co2 is capped equally by two methanol molecules, whereas one cap of Co4 is methanol and the other is crystallographically present as both water and methanol occupying the same site (in a 1:1 ratio).

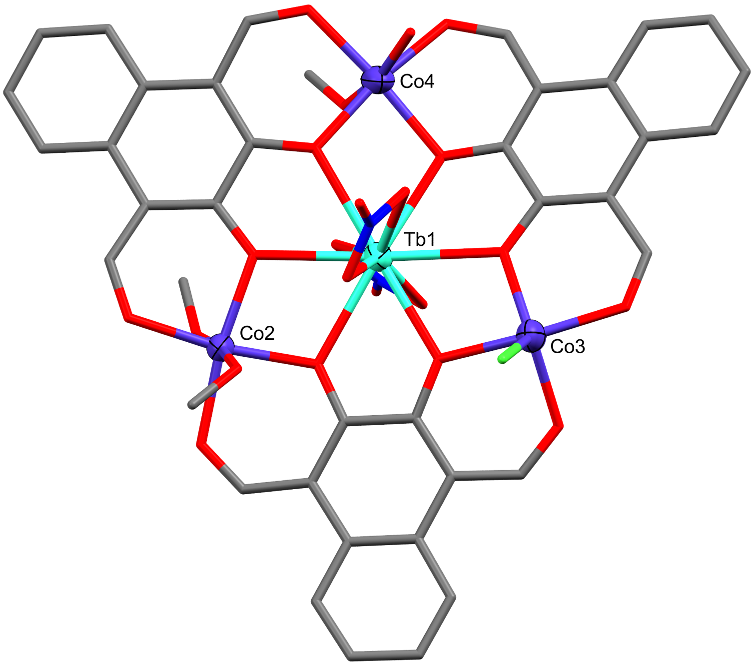

FIGURE 5.7: X-ray crystal structure of **Co_3Tb**. Hydrogen atoms, and disordered species are omitted for clarity. Thermal ellipsoids of metal atoms shown at the 70% probability level. C = grey, O = red, N = blue.

Of the four Co_3Ln type complexes structurally characterized by Mashima *et al.*, the two most important complexes, for the purposes of comparison, are [Co_3Ce] with its non-octahedral Co1, and [Co_3La] for a more direct analogy with **Co_3La**. As expected, both complexes have longer Co – N_{imine} bonds than the analogous Co – $O_{aldehyde}$ bonds, while the square pyramidal Co1 of the cerium containing complex (with a Co1 – O_4 plane separation of 0.459(2) Å) shows similarities to the **Co_3Tb** complex, its metal – metal related separations make it more comparable to **Co_3La**. Selected distances and angles for **Co_3Dy**, **Co_3Gd**, **Co_3La**, and **Co_3Tb** are listed in Table 5.1. The [Co_3Ce] complex has a small minimum intermolecular Ln^{III} – Ln^{III} separation (9.441(1) Å) while also having longer Co^{II} – Co^{II} and Co^{II} – Ln^{III} separations in the range of **Co_3La**; 6.225(1) - 6.448(1) Å and 3.603(1) - 3.760(1) Å for [Co_3Ce], respectively. Putting aside the absence of a non-octahedral cobalt centre, the [Co_3La] complex is very similar in structure to [Co_3Ce] and thus **Co_3La**, with similar metal – metal separations (minimum Ln^{III} – Ln^{III} = 9.308(1) Å, Co^{II} – Co^{II} = 6.289(1) - 6.436(1) Å, and Co^{II} – Ln^{III} = 3.635(1) - 3.736(1) Å).

TABLE 5.1: Selected structural parameters for **Co$_3$Dy**, **Co$_3$Gd**, **Co$_3$La**, and **Co$_3$Tb**.

Bond (Å)	**Co$_3$Dy**	**Co$_3$Gd**	**Co$_3$La**	**Co$_3$Tb**
Co – O_{phenol}[a]	1.979(9) - 2.036(9)	1.989(5) - 2.011(5)	1.984(8) - 2.046(8)	1.984(5) - 2.045(5)
Co – $O_{aldehyde}$[b]	1.996(9) - 2.044(10)	1.990(8) - 2.046(5)	1.982(9) - 2.044(10)	1.998(5) - 2.025(4)
Co – O_{H_2O}	2.148(9)		1.922(9) - 2.177(8)	2.195(15)
Co – O_{MeOH}	2.133(8) - 2.191(8)	2.108(6) - 2.178(6)		2.133(6) - 2.204(10)
Co – Anion[c]	2.166(8)	2.130(5) - 2.206(6)		2.292(2)
Ln – O_{phenol}	2.394(9) - 2.460(10)	2.410(5) - 2.552(6)	2.567(9) - 2.657(8)	2.439(5) - 2.546(5)
Ln – O_{NO_3}	2.450(8) - 2.459(7)	2.455(6) - 2.498(5)	2.625(8) - 2.801(9)	2.438(6) - 2.494(5)
Ln – $O_{solvent}$[d]	2.339(7)		2.576(9)	
Co – Co	6.228(4) - 6.269(3)	6.335(2) - 6.393(2)	6.324(2) - 6.469(3)	6.345(2) - 6.366(1)
Co – Ln	3.594(2) - 3.623(3)	3.647(2) - 3.710(2)	3.682(2) - 3.733(2)	3.663(1) - 3.678(1)
Min. Ln – Ln	10.221(2)	10.625(2)	9.598(1)	10.540(1)
Ln – Co_3 plane	0.139(2)	0.091(1)	0.333(1)	0.143(1)
Co4 – O_4 plane[e]	0.015(5)	0.648(3)	0.609(5)	0.581(3)
Angle (°)				
Co – O_{phenol} – Ln	106.2(4) - 109.3(4)	106.2(2) - 111.1(2)	104.1(3) - 108.5(3)	107.0(2) - 109.2(2)

[a] O_{phenol} corresponds to O2, O3, O6, O7, O10, and O11.
[b] $O_{aldehyde}$ correspdonds to O1, O4, O5, O8, O9, and O12.
[c] Anion is μ_1-NO_3 for **Co$_3$Dy**, μ_2-NO_3 for **Co$_3$Gd**, and μ_1-Cl for **Co$_3$Tb**.
[d] Solvent is MeOH for **Co$_3$Dy** and H_2O for **Co$_3$La**.
[e] The O_4 plane corresponds to the least-squares plane of the four equatorial ligand based donors in the idealized octahedral binding environment.

5.2 Supramolecular Interactions

Co$_3$Dy contains the smallest trivalent lanthanide ion discussed in this section, with an effective ionic radius of 91.2 pm,[159] which affords each cobalt centre the steric freedom to dominate their own coordination geometry. The cross-sectional molecular area, in the Co$_3$**L1**$_3$ plane, was calculated using the inbuilt ChemCraft utility; and $\pi - \pi$ stacking interactions were analyzed in Olex2 with the aromatic centroid-centroid distances listed in Table 5.2. Complex **Co$_3$La**, containing the largest trivalent lanthanide ion (La^{III}), has the largest calculated molecular area as well as the longest range $\pi - \pi$ stacking interaction. It also features the longest average Co^{II} – Ln^{III} and Co^{II} – Co^{II} distances, however it interestingly also has the shortest Ln^{III} – Ln^{III} distance (Table 5.1). The same trend in ionic radii vs cross-sectional molecular area is not followed for the other three complexes. Complex **Co$_3$Tb** contains Tb^{III} which is smaller than Gd^{III} but larger than Dy^{III}, however **Co$_3$Tb** has the second largest calculated molecular area which may be attributed to the way in which the chloride cap of Co3 influences the planarity and shape of the complex and hence the crystal packing.

TABLE 5.2: Calculated $\pi - \pi$ stacking distances and cross-sectional areas.

Complex	**$\pi - \pi$ stacking (Å)**	**Molecular area (Å^3)**
Co3Dy	3.763 – 3.824	206.5
Co3Gd	3.731 – 3.740	208.9
Co3La	3.586 – 3.955	213.1
Co3Tb	3.551 – 3.791	212.1

At the mesoscale, the crystal packing of **Co3Gd** resembles that of **Co3Dy** (Figure 5.8). When viewed along the crystallographic *a*-axis, both complexes pack similar to two-dimensional layered systems along the *ab*-plane with clear inter-layer separations along the *c*-axis. Although **Co3La** has the same metric symmetry and is in the same space group as **Co3Dy** and **Co3Gd**, the geometry of the unit cell is considerably different. Where **Co3Dy** and **Co3Gd** have similar *a* and *b* lengths and both α and β angles are near 90°, **Co3La** has similar *b* and *c* lengths with the corresponding α and γ angles being near 90°. The shorter length of *c* in **Co3La** relative to the other two triclinic structures results in a greater proportion of a third molecule, whose centre of mass sits outside of the unit cell, occupying the space to ensure $Z = 2$ when $Z' = 1$, resulting in an apparent overlap of aromatic rings when viewed along the crystallographic *a*-axis.

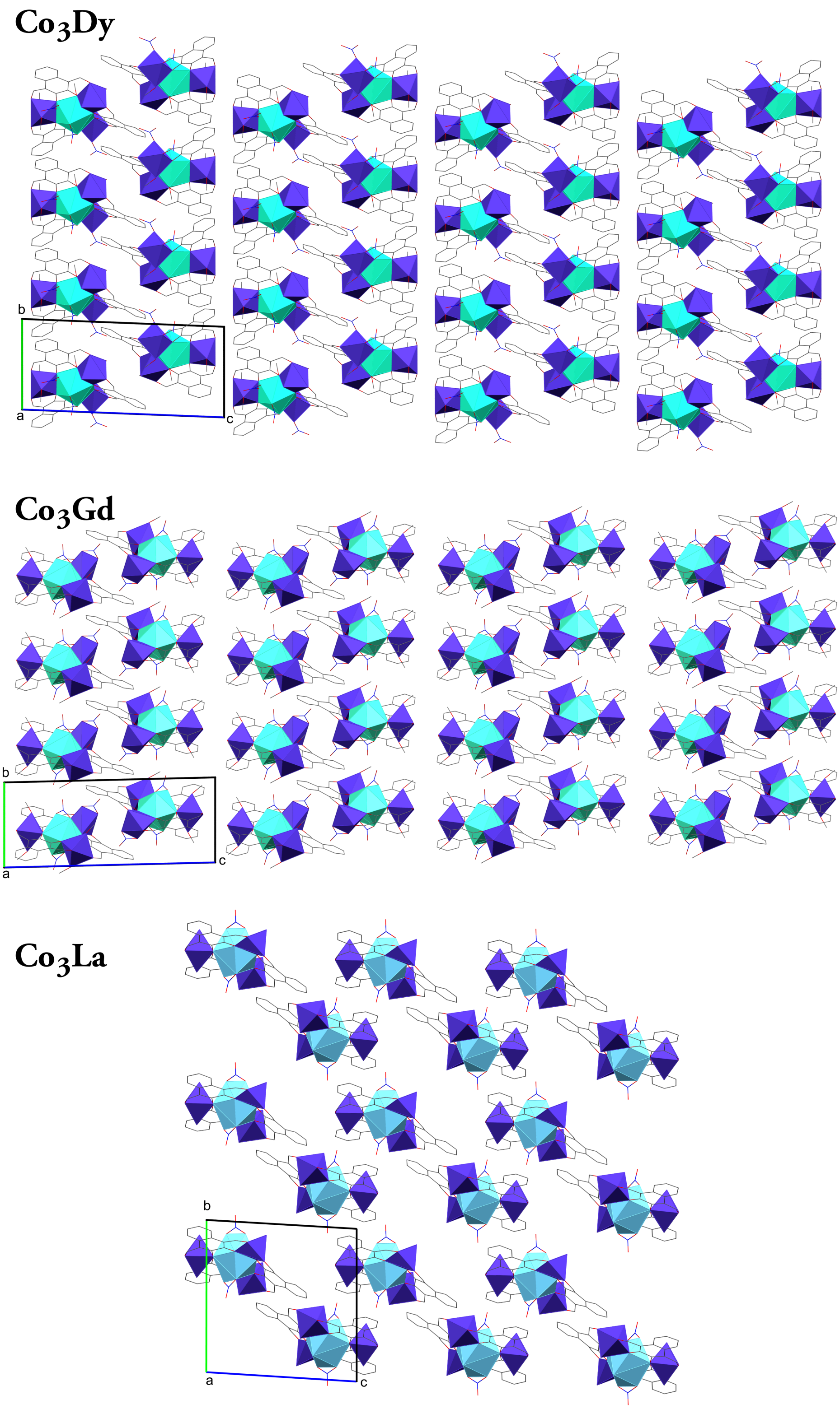

FIGURE 5.8: Simplified X-ray crystal structure packing diagrams of **Co3Dy**, **Co3Gd**, and **Co3La** viewed alone the crystallographic *a*-axis.

5.3 Magnetic Analysis of Co3La

DC magnetic susceptibility and magnetization measurements have been performed to examine the potential Co^{II} – Co^{II} interactions and/or zero field splitting effects present in the **Co3La** complex. As the other complexes within the Co3Ln family each feature different Co^{II} coordination geometries, this initial study of **Co3La** cannot be considered representative of the other complexes.

The $\chi_m T$ vs T product of **Co3La** (Figure 5.9) reached 9.4 cm^3 K mol^{-1} at 300 K, which exceeded the expected spin-only value for three isolated Co^{II} ions of 5.63 cm^3 K mol^{-1}, and clarified the presence of three $S_{\mathrm{Co^{II}}} = 3/2$ spins with $g = 2.59$. The experimental magnetization at 7 T was 7.1 μ_B, which corresponds to ca. 60% of the theoretical limit (11.7 μ_B). If antiferromagnetic interactions were dominant, the experimentally measured magnetization would be approximately one third of the theoretical value and the $\chi_m T$ product at 1.8 K would approach one third of the value at 300 K. Hence, the measured value of 7.1 μ_B indicates the antiferromagnetic interactions are relatively small for this system. Part of the gradual decrease in the profile of the $\chi_m T$ vs T data is likely to originate from the single-ion nature of the spatially separated Co^{II} centres. To evaluate the ZFS of the Co^{II} ions and further comprehend the magnetic properties of **Co3La**, simulations were performed using MAGPACK.[147,148]

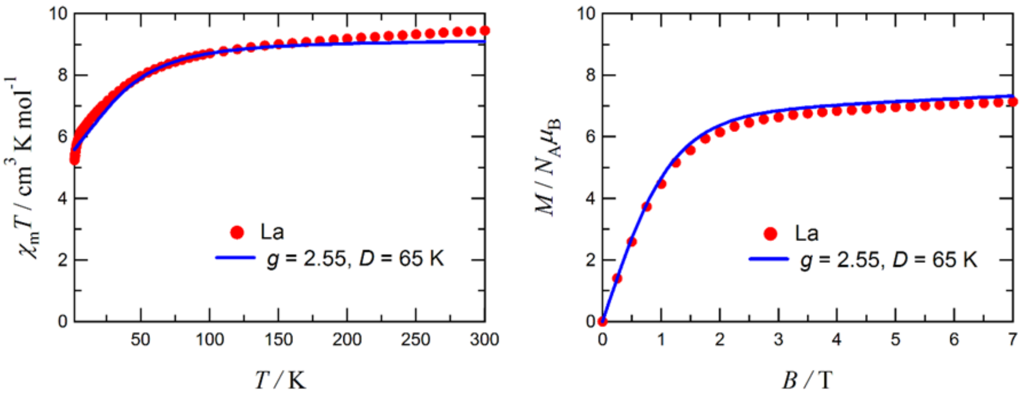

FIGURE 5.9: Plot of $\chi_m T$ vs T measured at 0.5 T (left) and M vs H plot measured at 1.8 K (right) for **Co3La**. Solid line traces the simulated fit, with parameters as noted on the figure. Measurements were performed on a polycrystalline sample fixed in a small amount of eicosane.

Using an approximation based on three-fold symmetry, optimization of the ZFS parameter D for each Co^{II} gave $D/k_B = 65$ K with $g_{ave} = 2.55$, neglecting any E value. Using these values of D and g, the calculated $\chi_m T$ vs T and M vs H profiles were reproduced nicely with this effectively 1J model. This value of D is relatively large, but is comparable with values reported in the literature.[160–165]

The large D value is likely related to the 5-coordinate cobalt centre (Co4), however, when considering the exchange coupling model using a spin Hamiltonian based on an antiferromagnetic triangular model, $\mathcal{H} = -2J(S_1 \cdot S_2 + S_1 \cdot S_3 + S_2 \cdot S_3)$, the experimental data cannot be reproduced (Figure 5.10). At low temperatures and under a small applied field the ground state of **Co_3La** will have a residual $S = 3/2$ moment stemming from only one Co^{II} centre, while in stronger applied fields the ground state becomes ferromagnetic ($S = 9/2$). The calculated $M - H$ profiles show a small curvature between 3 and 6 T which can be assigned to a gradual transition from the $S = 3/2$ state to the $S = 9/2$ state, however the experimental M vs H data in this region has a monotonically increasing profile.

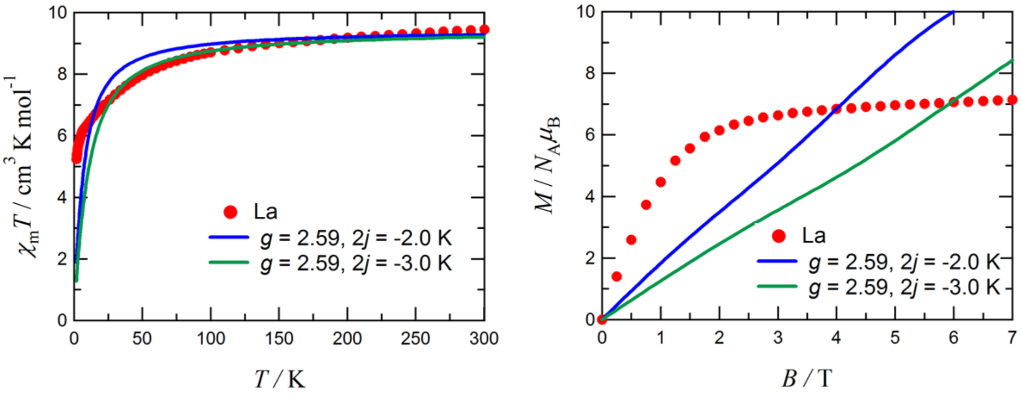

FIGURE 5.10: Simulation of the $\chi_m T$ vs T (left) and M vs H data (right) for **Co_3La** based on the above spin Hamiltonian. Using values of g_{ave} = 2.59 and $2j_{Co^{II}\text{-}Co^{II}} = -2.0$ and -3.0 K.

Conclusions

Four new non-macrocyclic heterometallic $Co^{II}{}_3Ln^{III}$ clusters have been prepared following the general method, and structurally characterized. The coordination geometry of each metal centre was examined by continuous shape measurements (CShM) using the SHAPE software package. While **Co_3Dy** was found to contain three near-perfectly octahedral Co^{II} centres, the remaining three complexes each contained one non-octahedral Co^{II} ion. This non-octahedral site was found to be strongly distorted towards trigonal prismatic in **Co_3Gd**, with 5-coordinate geometries observed for **Co_3La**, trigonal bipyramidal, and **Co_3Tb**, square pyramidal. DC magnetic measurements of **Co_3La** clarified a ground state spin projection of $S_{tot} = 3/2$, with weak antiferromagnetic contributions from the Co – Co interaction, and a relatively large ZFS parameter, $D/k_B = 65$ K. The large D value is likely associated with the trigonal bipyramidal Co^{II} centre (Co4). This work comprises only the second set of examples of Co_3Ln complexes with planar M_3LnO_3 cores within the literature, and also represents the first methodical structural study as well as the first magnetic investigation into these complexes.

Preparation

Co3Dy formulated as [**L1**$_3$Co$_3$Dy(NO$_3$)$_2$(H$_2$O)(MeOH)$_5$](NO$_3$) was obtained as orange block crystals in 58% yield (based on Dy(NO$_3$)$_3 \cdot 6\,$H$_2$O). ATR-IR $\overline{\nu}$: 1614, 1566, 1483, 1435, 1378, 1351, 1310, 1260, 1124, 1027, 969, 753, 682 cm^{-1}. Microanalytical data found(calc) for **Co3Dy** (calculated for $C_{41}H_{40}Co_3DyN_3O_{27}$, M_r = 1346.06 g mol^{-1}) C: 36.30(36.58), H: 3.32(3.00), N: 3.22(3.12).

Co3Gd formulated as [**L1**$_3$Co$_3$Gd(NO$_3$)$_3$(MeOH)$_4$] was obtained as orange block crystals in 51% yield (based on Gd(NO$_3$)$_3 \cdot 6\,$H$_2$O). ATR-IR $\overline{\nu}$: 1611, 1567, 1486, 1432, 1382, 1351, 1313, 1259, 1141, 1029, 975, 753, 697 cm^{-1}. Microanalytical data found(calc) for **Co3Gd** (calculated for $C_{40}H_{34}Co_3GdN_3O_{25}$, M_r = 1290.75 g mol^{-1}) C: 36.99(37.22), H: 2.92(2.66), N: 3.31(3.26).

Co3La formulated as [**L1**$_3$Co$_3$La(NO$_3$)$_2$(H$_2$O)$_6$](NO$_3$) $\cdot$ (H$_2$O) $\cdot$ 1.5[Et$_2$O] was obtained as orange plate crystals in 57% yield (based on La(OAc)$_3 \cdot 6\,$H$_2$O). ATR-IR $\overline{\nu}$: 1615, 1566, 1482, 1435, 1378, 1351, 1311, 1261, 1128, 1027, 969, 753, 682 cm^{-1}. Microanalytical data found(calc) for **Co3Ho** (calculated for $C_{36}H_{32}Co_3LaN_3O_{28}$, M_r = 1270.35 g mol^{-1}) C: 34.30(34.04), H: 2.32(2.54), N: 3.32(3.31).

Co3Tb formulated as [**L1**$_3$Cu$_3$TbCl(NO$_3$)$_2$(H$_2$O)0.5(MeOH)4.5] $\cdot$ 1.5[H$_2$O] orange block crystals in 66% yield (based on TbCl$_3 \cdot 6\,$H$_2$O). ATR-IR $\overline{\nu}$: 1611, 1568, 1486, 1432, 1382, 1352, 1313, 1259, 1141, 1030, 974, 755, 711 cm^{-1}. Microanalytical data found(calc) for **Co3Tb** (calculated for C39.5Co$_3$TbClN$_2$O24.5, M_r = 1303.90 g mol^{-1}) C: 36.15(36.38), H: 2.60(2.94), N: 2.00(2.15).

Chapter 6

A Descent Through the Nuclearities

Throughout this research a large number of complexes with nuclearities ranging from one to 16, with polymers being the exception, have been isolated. Some complexes presented multiple crystal polymorphs, which in turn, related to the physical morphology of the crystal — the cause of this was rudimentally explored for the complex Ni_{16}. Some, but not all, of the complexes discussed here were obtained using the symmetric dialdehyde ligand discussed in Chapter 2 or a simple Schiff base derivative of $\mathbf{H_2L1}$. Homometallic complexes with nuclearities ranging from eight to sixteen were isolated, one containing copper, two hexadecanuclear nickel complexes, and one octanuclear manganese complex. A heterometallic heptanuclear complex containing a $Mn^{II}La_6$ core was also obtained. Where possible there complexes have been structurally identified by single crystal X-ray diffraction experiments, with formulations confirmed by CHN microanalysis, and had the presence of their expected functional groups confirmed by IR. Of these five complexes only the largest, $\mathbf{Ni_{16}}$, could be reliably reproduced at larger scales. Synthetic methods for the preparation of each complex discussed here can be found at the end of the chapter.

6.1 $\mathbf{Ni_{16}}$

The largest complex in this set, the hexadecanuclear Ni_{16} complex (Figure 6.1) formed with the general formula $\mathbf{L2}_4Ni_{16}(OAc)_{16}(MeOH)_x(H_2O)_{12-x}$, in the form of a supramolecular ring with an almost bowl or cone like topology similar to that of calixarenes. As mentioned, this complex presented three distinct crystal morphologies (needles, plates, and blocks), each with its own unique unit cell. The complex, initially obtained as needles, featured an unwieldy monoclinic unit cell with a volume of approximately 52,000 Å^3 in the centrosymmetric space group $C2/c$ with $Z' = 1$ and $x = 2$. Attempts to synthesize more of the complex yielded larger plate-like crystals with a similarly large unit cell volume of almost 44,000 Å^3, this time in the monoclinic space group $P2_1/n$ with Z' = 2 and $x = 8$ on one of the molecules within the asymmetric unit and $x = 9$ on the other. Finally, a block-like crystal form presented itself, which was found to have a smaller unit cell volume of 23,700 Å^3 of polar tetragonal symmetry, in the space group $P4nc$ with Z' = 0.25, hereafter simply referred to **Ni$_{16}$**. All forms of this complex were obtained from the 1:4 reaction of **H$_4$L2** with $Ni(OAc)_2 \cdot 6\,H_2O$, refluxing in 10% water in methanol. It was observed that vapour diffusion after three days of refluxing resulted in primarily needle and plate crystals, however, if the mixture was refluxed for five to seven days, the crystalline product was almost exclusively blocks. The asymmetric unit of **Ni$_{16}$** contained two distinct fragments, both fitting the $x = 8$ formulation, albeit with the water caps in different positions. In all cases, the ligand (**H$_2$L2**) binds in a $5.2_{12}2_{23}2_{34}2_{45}1_21_4$ fashion. The 5.222211 Harris notation binding mode[82] indicates each ligand is bound to five metal centres with four μ_2-sites (all oxygen donors in this case) and two μ_1-sites (both imine groups). The central catechol group binds a nickel in its centre to form a five-membered chelate ring whilst also bridging to another Ni$^{\text{II}}$ ion on each side which are in turn meridionally bound by their nearest imine and phenol groups. These phenol groups each bridge to another Ni$^{\text{II}}$ ion either side which is shared with the phenol moiety of the neighbouring ligand unit. Every nickel centre is further bridged to at least two others through acetate groups which bind in both 2.11 and 3.21 modes. See Appendix A for illustrative examples of these binding modes.

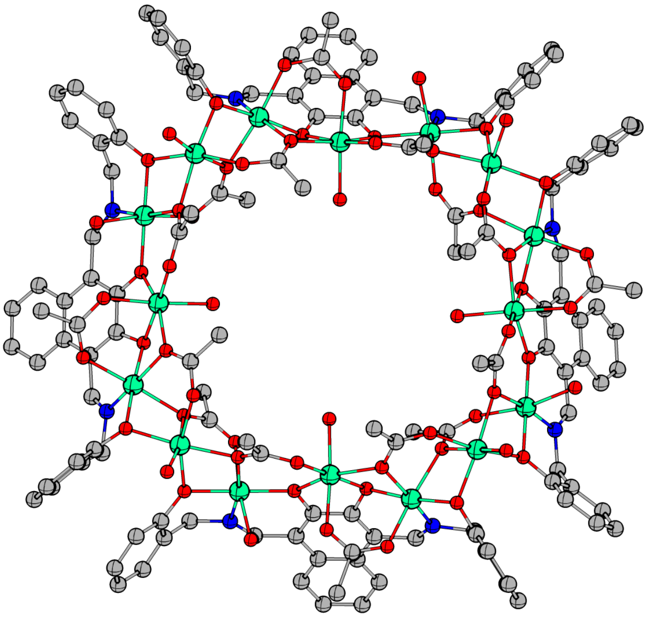

FIGURE 6.1: A cartoon schematic showing the generalized structure of the Ni$_{16}$ complex (represented with $x = 0$). Hydrogen atoms omitted for clarity. C = grey, N = blue, Ni = green, O = red.

By careful inspection of the two fragments within the asymmetric unit of the tetragonal **Ni$_{16}$** solution (Figure 6.2) it can be seen that the bridging direction of the 2.11 acetate bound to the central Ni^{II} (bound within the catechol group) changes and the axial water cap switches which side of the plane it is on. These fragments are almost isostructural by inversion, with an RMSD value of 0.320 Å when overlaid (based on the Ni^{II} connectivity), and can each be grown by 4-fold rotation to produce a unit of Ni$_{16}$ with different handedness, i.e. the connectivity pattern of two rings are reversed relative to each other. The presence of Ni$_{16}$ units with both handedness is also observed in the monoclinic solutions; in the case of the $C2/c$ solution, a Ni$_{16}$ unit of opposite handedness is generated by inversion symmetry. Ni$_{16}$ units of both handedness are present within the asymmetric unit of the $P2_1/n$ solution, however because the two units have formulations with different values of x there exists four distinct molecules.

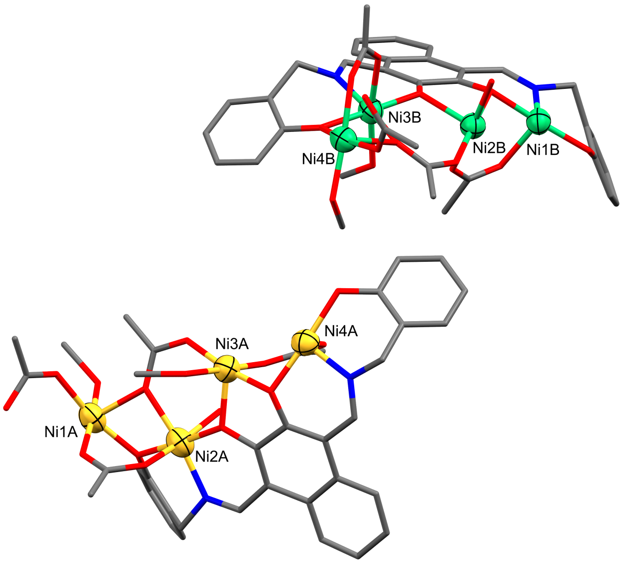

FIGURE 6.2: X-ray crystal structure showing the asymmetric unit of **Ni$_{16}$**. Thermal ellipsoids of metal atoms shown at 70%. Non-coordinated species and hydrogen atoms omitted for clarity. C = grey, N = blue, O = red.

While the established connectivities for each of the Ni$_{16}$ polymorphs are essentially the same, the data collected from the plate and needle samples were much weaker. Attempts were made with all three polymorphs to model as many of the non-coordinated solvent molecules as possible. However, even in the tetragonal **Ni$_{16}$**, solvents assigned based on the difference maps were unstable, with only one water molecule and two methanol molecules of half occupancy each (per asymmetric unit) being stable to refinement. The remainder of the electron density was modelled in a solvent mask containing 343 electrons occupying $\sim$ 1200 Å^3 per asymmetric unit, corresponding to 34 water molecules which is consistent with the presence of 32 to 36 water molecules estimated by CHN microanalysis. The lower quality data of the monoclinic solutions made the assignment of non-coordinated solvate species even more difficult, thus solvent masks with comparable contents were applied.

The three different solutions show good regularity with the exterior dimensions of the monomeric Ni_{16} units, with the monoclinic solutions differing from $\mathbf{Ni_{16}}$ by less than 3% in each dimension. The size of monomeric Ni_{16} units were calculated using an inbuilt ChemCraft utility. Figure 6.3 shows the dimensions of a single Ni_{16} complex from $\mathbf{Ni_{16}}$ (a and c) as well as the dimeric Ni_{16} capsule (b and d), note that the four-fold symmetry means the side lengths in the top down views (bottom) are equal in both dimensions. The total height of the dimeric capsule is $\sim$ 0.5 Å less than double the height of the monomeric unit, showing the considerable overlap between complexes which nestle together with a nearly 30° rotation along the same four-fold axis (Figure 6.3b) which generates each complex from its asymmetric unit.

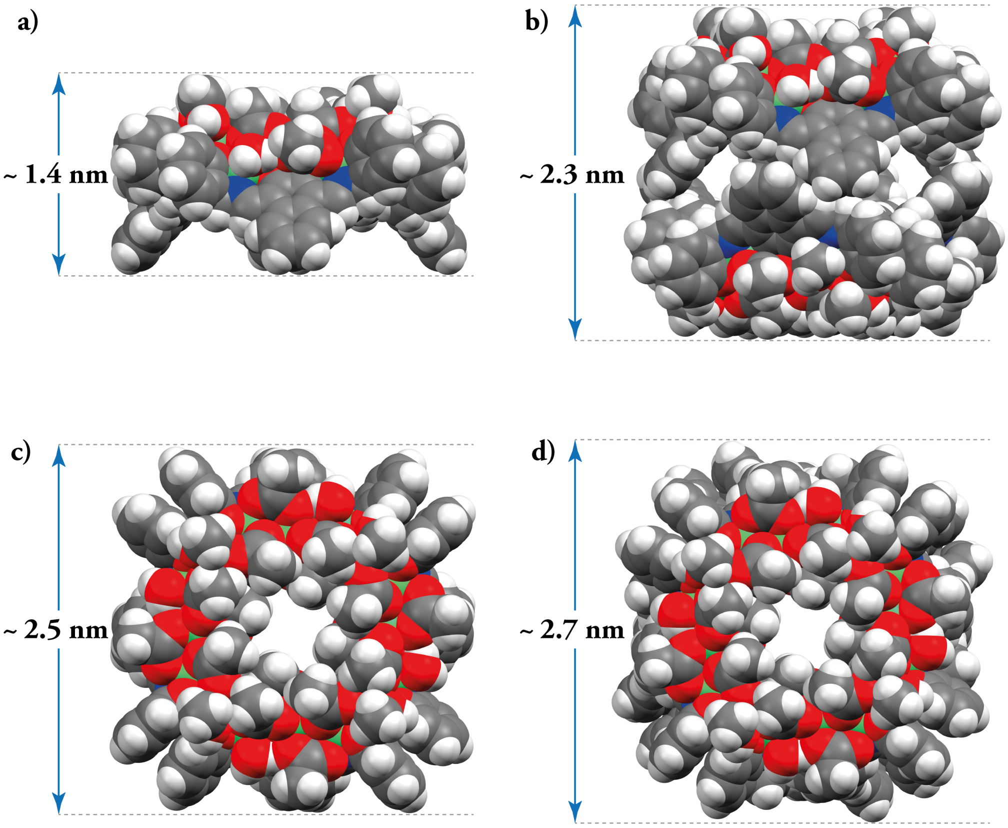

FIGURE 6.3: Space filling diagrams of $\mathbf{Ni_{16}}$ viewed parallel (a and b) and perpendicular (c and d) to the plane, showing the dimensions of the monomeric unit (a and c) and dimeric capsule (b and d).

As is expected from solutions in different space groups, the crystal packing of each solution is vastly different. Looking at the arrangement of molecules in the unit cell alone, it can be seen that the highest symmetry species packs as a molecular capsule where a Ni_{16} unit of each handedness dimerizes to form a closed capsule (Figures 6.4 and 6.5). The primitive monoclinic solution packs in the opposite manner with the two smaller rims of the complexes coming together to form the shape of an elliptic hyperboloid (Figure 6.6) where a Ni_{16} unit of each handedness and different formulations of x dimerize (i.e. an $x = 8$ and an $x = 9$ molecule of opposite handedness). No such open- or closed-capsule geometry is observed in the unit cell packing of the base-centred monoclinic species (Figure 6.7).

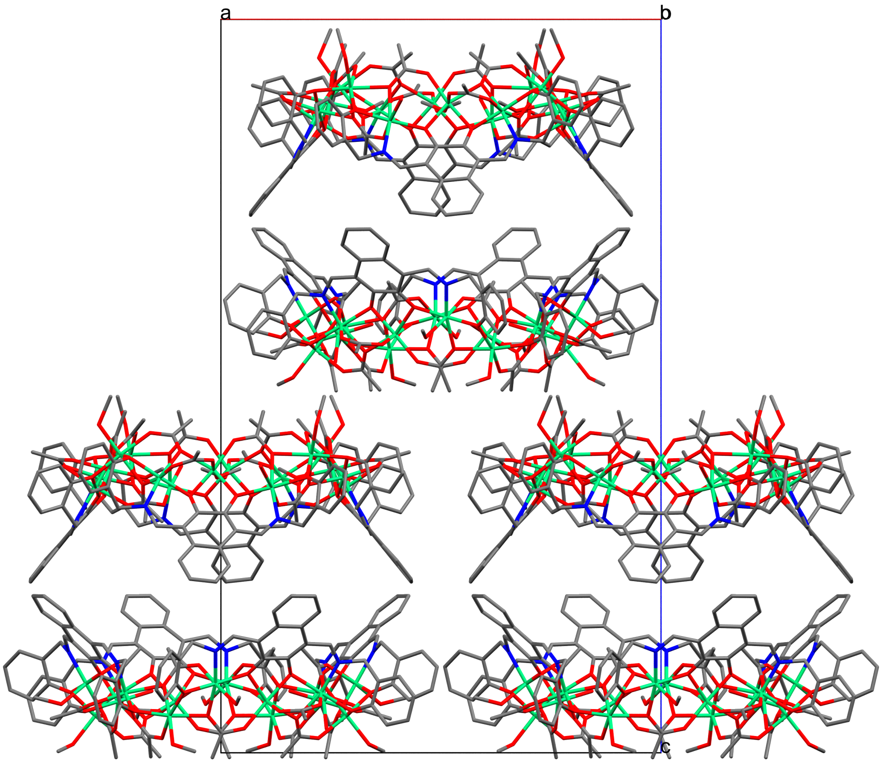

FIGURE 6.4: X-ray crystal packing of $\mathbf{Ni_{16}}$ within the unit cell, viewed along the crystallographic b-axis to highlight the capsule-like dimers. Non-coordinated species and hydrogen atoms omitted for clarity. C = grey, N = blue, Ni = green, O = red.

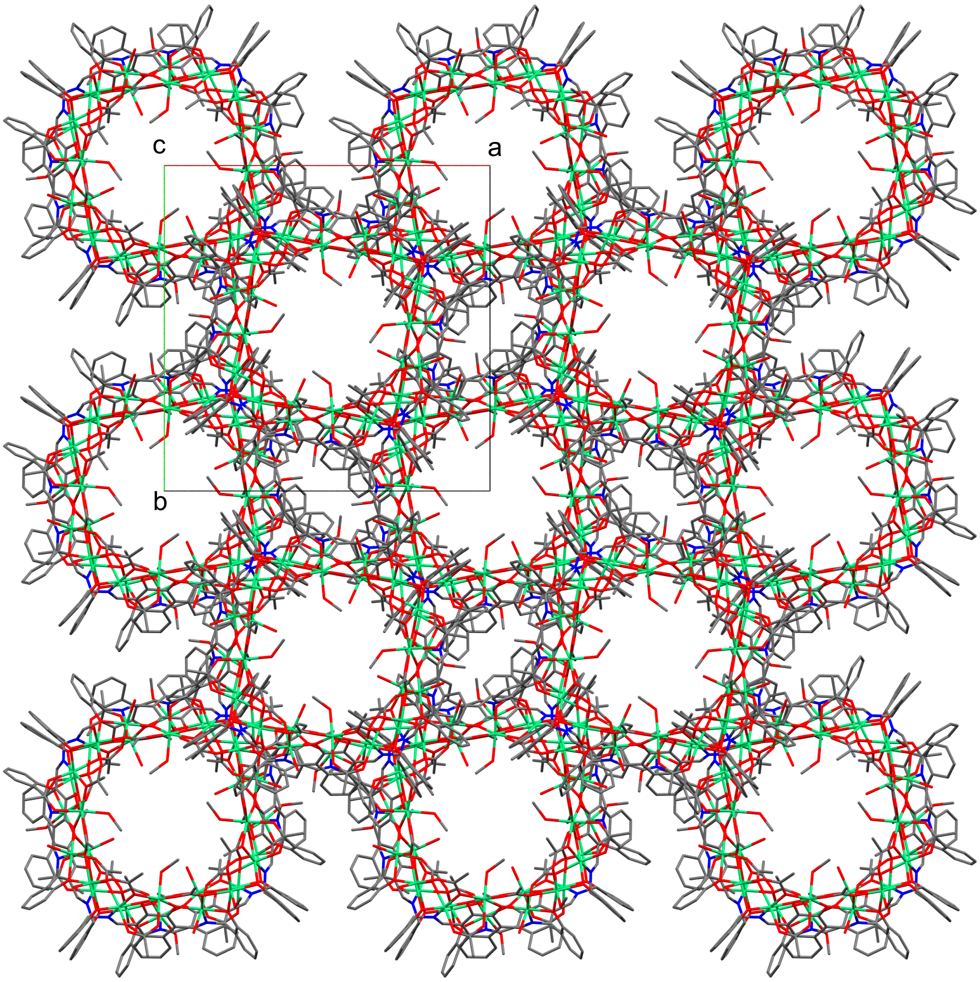

FIGURE 6.5: X-ray crystal packing of **Ni$_{16}$**, viewed along the crystallographic *c*-axis highlighting the off-set tubular stacking. Non-coordinated species and hydrogen atoms omitted for clarity. C = grey, N = blue, Ni = green, O = red.

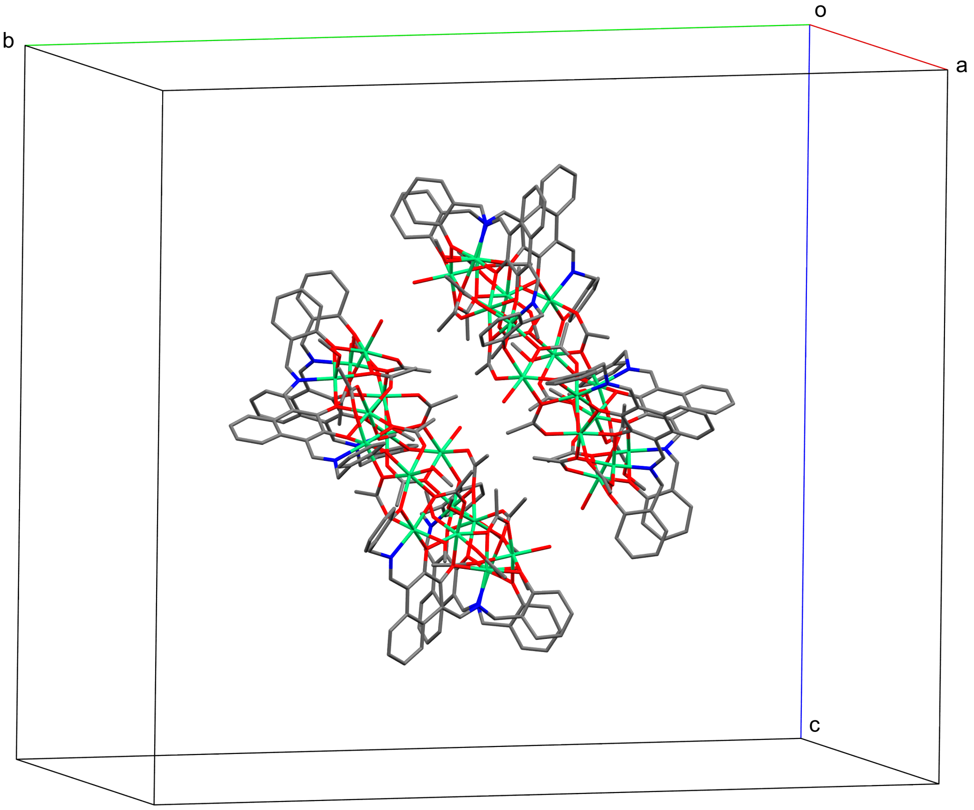

FIGURE 6.6: X-ray crystal structure of the $P2_1/c$ Ni$_{16}$ complex showing two molecules packed together as an elliptic hyperboloid. Non-coordinated species and hydrogen atoms omitted for clarity. C = grey, N = blue, Ni = green, O = red.

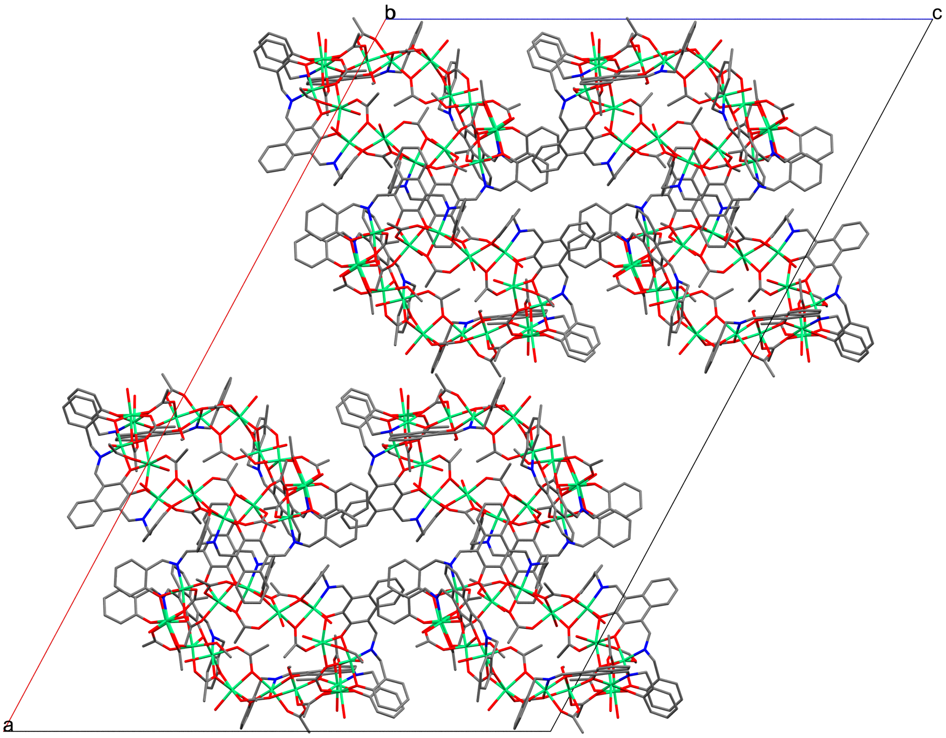

FIGURE 6.7: X-ray crystal packing of the $C2/c$ Ni_{16} complex within the unit cell, viewed along the crystallographic *b*-axis. Non-coordinated species and hydrogen atoms omitted for clarity. C = grey, N = blue, Ni = green, O = red.

6.1.1 The Call of the Void

The dimerization of **Ni_{16}** units into a non-covalently bound capsule presents an interesting void, which, under the right conditions, could encapsulate another species either non-covalently, as the system stands, or electrostatically by first altering the chemical environment within the void. The maximum possible guest diameter can be found by inspecting the distances across the inner ($H_2O \cdots H_2O$) and outer (naphthalene based centroids shown in pink in Figure 6.8) rims of a Ni_{16} unit, note that these distances must be corrected for the Van der Waals radii of the relevant atoms. When considering the full capsule of **Ni_{16}**, the naphthalene backbones encircling the widest point of the capsule makes $\pi - \pi$ stacking the obvious potential driving force to exploit. As such, attempts were made to encapsulate fullerene molecules within the capsule, similar to work previously reported by Truhler *et al.* for C_{60}[166] and Yamago *et al.* for C_{70}.[167] An initial model was developed to ensure there was a good size match between the host (**Ni_{16}** dimer) and guest molecules (C_{60} or C_{70}). It was thought that due to the prolate shape of the void and relatively large separation between the two Ni_{16} planes in the capsule (7.898 Å), C_{70} would be a better candidate (Figure 6.9).

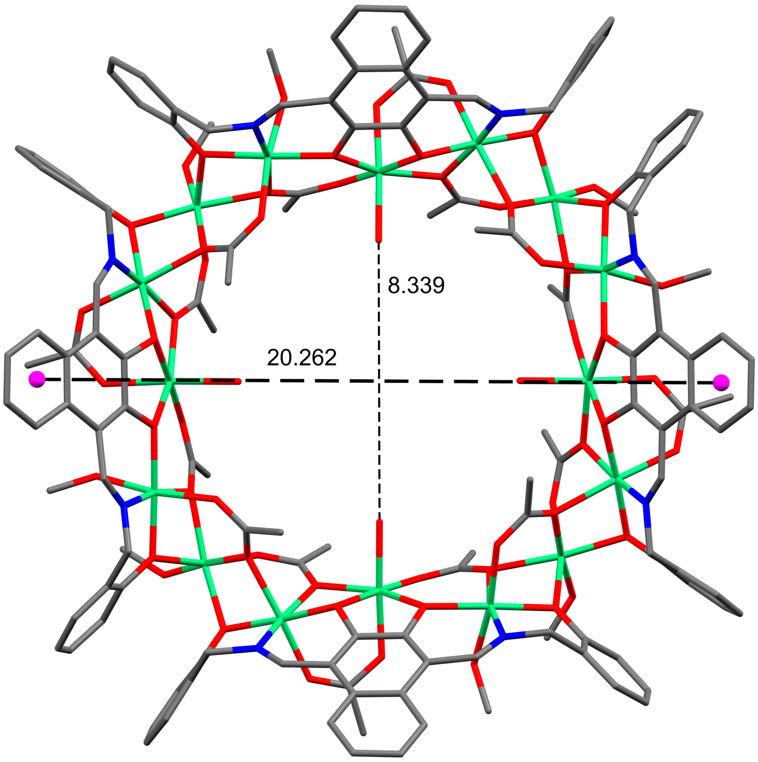

FIGURE 6.8: X-ray crystal structure of **Ni_{16}** showing the inner and outer rim distances. Hydrogen atoms omitted for clarity. C = grey, N = blue, Ni = green, O = red. Centroids in pink.

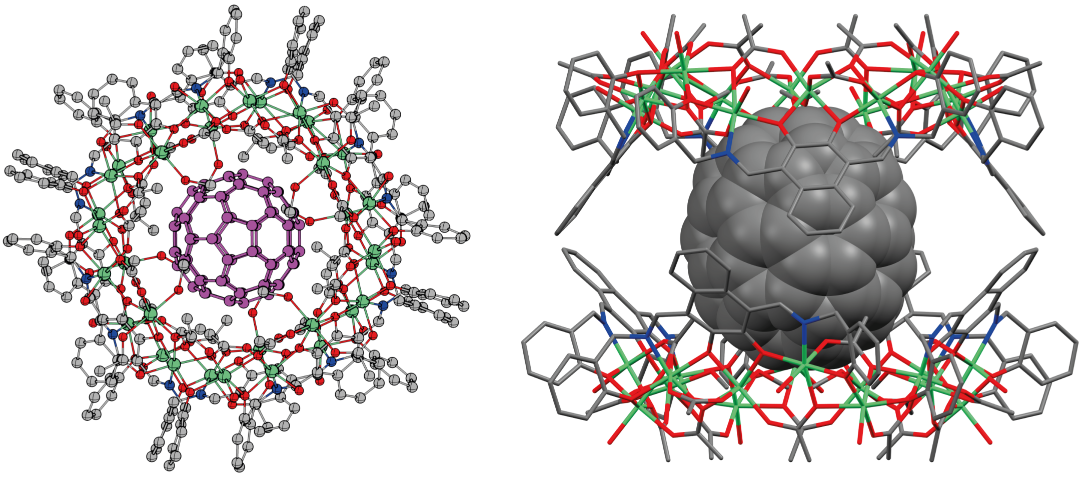

FIGURE 6.9: Schematic representations of a potential C_{70}@2Ni_{16} host-guest complex, from two perpendicular views, based on the original crystal structure coordinates of **Ni_{16}**. Hydrogen atoms omitted for clarity. C = grey, N = blue, Ni = green, O = red. C_{70} in purple (left) and space-filling (right).

Formation of the host-guest complex was attempted synthetically for both C_{60} and C_{70}, through various methods. Initial attempts involved layering a solution of Ni_{16} (in aqueous methanol, or a 1:1 methanol toluene/1,2-dichlorobenzene mix) with each fullerene dissolved in 1,2-dichlorobenzene, toluene, *p*-xylene, or mesitylene. After weeks of sitting undisturbed, both in light and out of light, no solids were observed. The same combinations of reactants and solvents were brought to reflux then cooled and allowed to slowly evaporate, with a black amorphous solid precipitating on cooling which IR identified as the fullerene starting material and small black crystals of the respective fullerene, crystallized on slow evapouration of the solvents. C_{70} was also introduced to the initial **Ni_{16}** reaction mixture in its final 24 hours of reflux, but upon cooling the same black precipitate was observed. A further polymorph of Ni_{16} was observed to crystallize from an encapsulation attempt in a purely 1,2-dichlorobenzene solution; however the data was only good enough to establish the connectivity, presence of two molecules of 1,2-dichlorobenzene in the asymmetric unit, and absence of any fullerene. Encapsulation experiments were also carried out, attempting to encapsulate *trans*-dichlorotetrakispyridine ruthenium(II) within a **Ni_{16}** capsule. These attempts followed the same methods of layering, mixing, or adding to the reaction mixture; with less success than the fullerene attempts.

6.1.2 A Formate Analogue

During the writing of this thesis, another analogue of Ni_{16} was isolated and structurally characterized. The complex $\mathbf{Ni_{16}}^{\mathbf{formate}}$ (Figure 6.10) was prepared in the same manner as $\mathbf{Ni_{16}}$, using $Ni(HCOO)_2 \cdot 2\,H_2O$ in place of $Ni(OAc)_2 \cdot 6\,H_2O$, and crystallized in the enantiomorphic trigonal space group $P3_121$ ($Z' = 0.5$) as small green blocks with the formula $\mathbf{L2}_4Ni_{16}(HCOO)_{16}(H_2O)_{12}$ + *solvents*. The conditions used to crystallize this complex also leads to the crystallization ofunreacted $Ni(HCOO)_2 \cdot 2\,H_2O$ over the same time period, which could not be separated by solvent-solvent extraction. This complex has not yet been produced in larger quantities for purification, thus it has only been structurally characterized. The asymmetric unit contains half of the $\mathbf{Ni_{16}}^{\mathbf{formate}}$ complex where the presence of two-fold symmetry, rather than four-fold rotational symmetry as in $\mathbf{Ni_{16}}$, results in a slightly less symmetrical complex with more ellipsoid character and asymmetric dimensions (Figure 6.11).

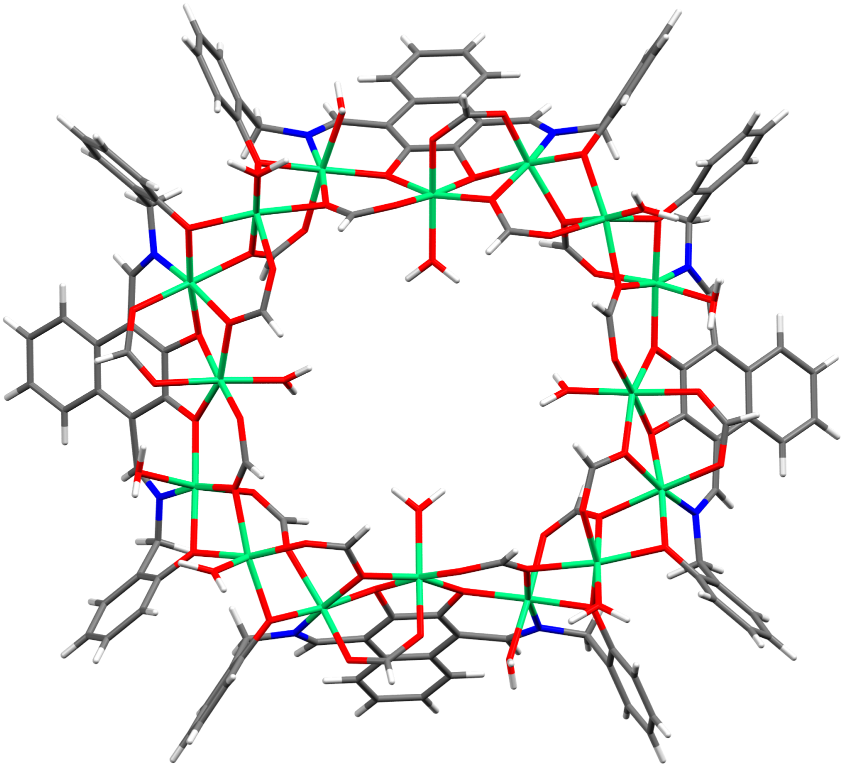

FIGURE 6.10: X-ray crystal structure of $\mathbf{Ni_{16}}^{\mathbf{formate}}$. Disordered species omitted for clarity. C = grey, N = blue, Ni = green, O = red.

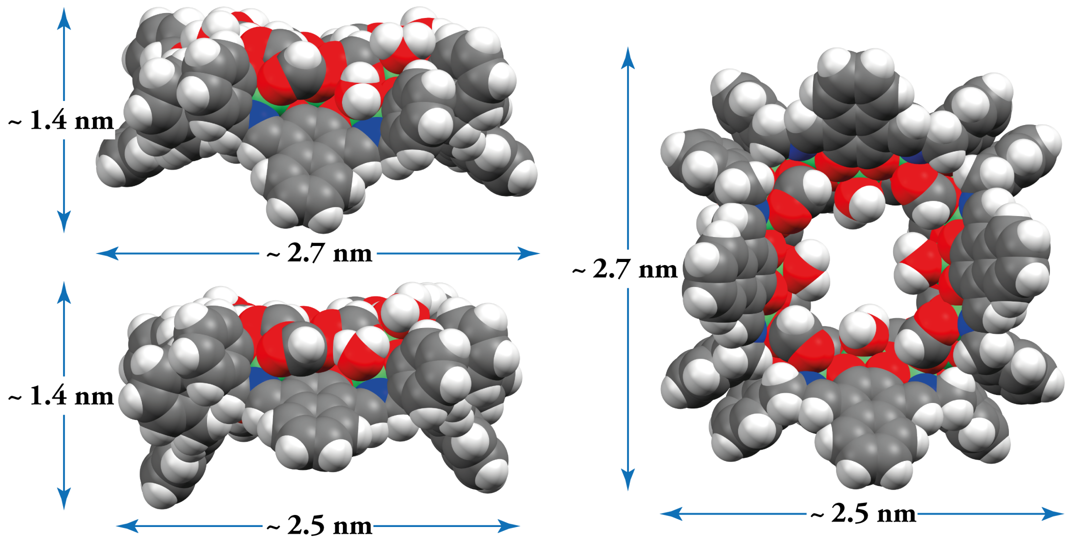

FIGURE 6.11: Space filling diagrams of $\mathbf{Ni_{16}}^{\mathbf{formate}}$ viewed parallel (left) and perpendicular (right) to the plane, including dimensions.

Although this complex has not yet been produced at larger scales and fully characterized, it indicates the possibility for this system to be further modified by other carboxylate anions, and potentially introduce additional functionality to the interior of each Ni_{16} bowl. Accordingly, synthetic efforts have been made to produce analogues containing trifluoroacetate, 2-hydroxyacetate, glycinate, or benzoate through the initial formation of their respective Ni^{II} salts, however, characterizable solids have not yet been obtained. The much lower pK_a of trifluoroacetic acid could potentially produce a smaller Ni_{16} bowl as a result of the larger O–C–O bridging angle, while the 2-hydroxyacetate and glycinate analogues would provide more hydrogen-bonding capabilities to the interior of the Ni_{16} bowl. Finally, a benzoate analogue would produce a smaller cavity space within the complex and provide more aromatic surfaces to help facilitate $\pi - \pi$ stacking interactions.

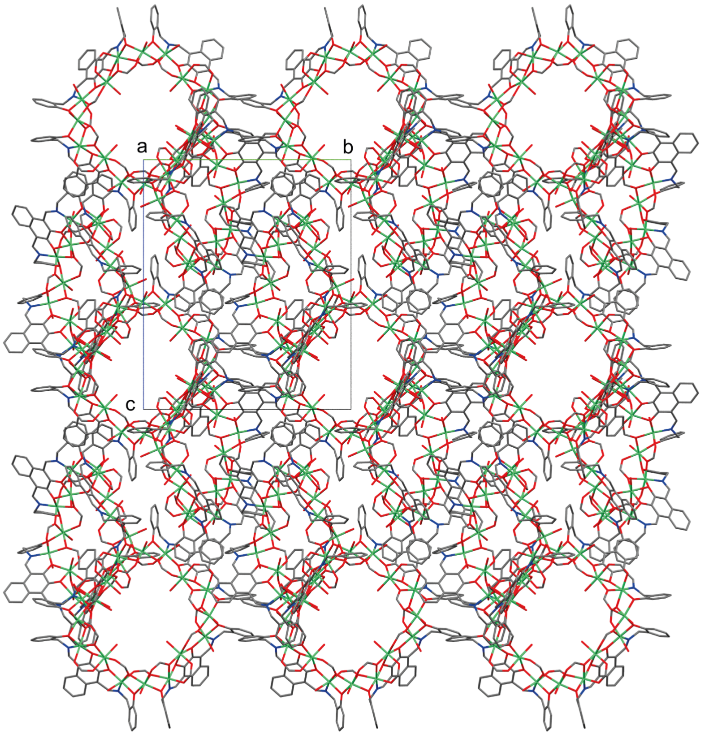

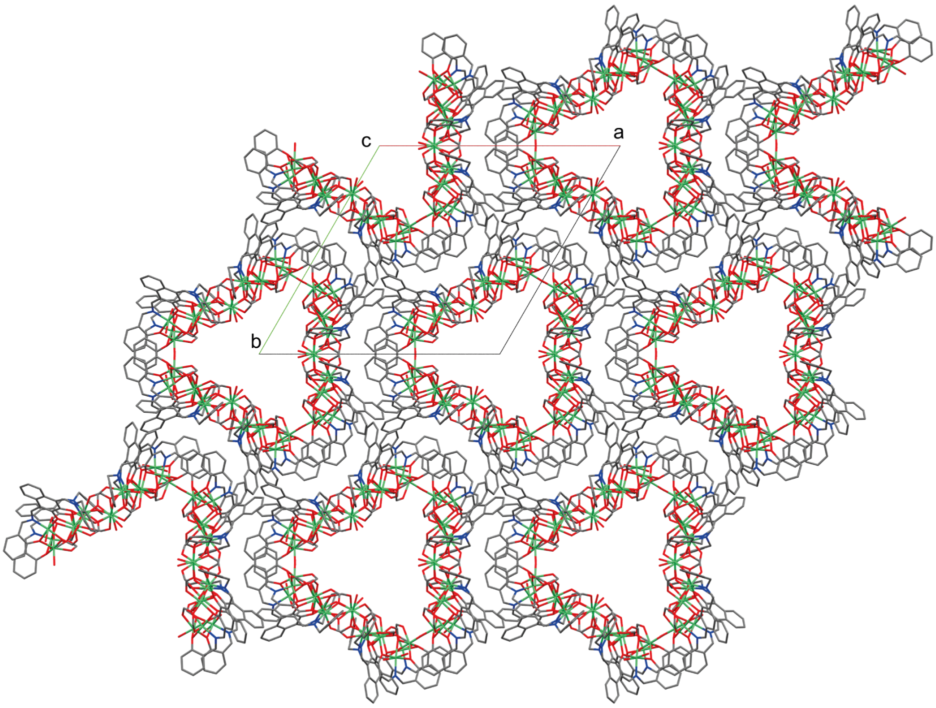

FIGURE 6.12: X-ray crystal packing of **Ni$_{16}$$^{\mathbf{formate}}$** viewed along the crystallographic *b*-axis (top) and *c*-axis (bottom). Disordered species and hydrogen atoms omitted for clarity. C = grey, N = blue, Ni = green, O = red.

Structural Parameters for Ni$_{16}$ Complexes

TABLE 6.1: Selected structural parameters for each Ni$_{16}$ complex.

Bond (Å)	**Ni$_{16}$**	Ni$_{16}$$^{P2_1/n}$	Ni$_{16}$$^{C2/c}$	**Ni$_{16}$$^{\text{formate}}$**
Ni – O$_{\text{phenol}}$	1.956(5) - 2.099(4)	1.969(4) - 2.077(4)	1.962(6) - 2.103(6)	1.991(6) - 2.108(9)
Ni – N$_{\text{imine}}$	1.924(6) - 2.058(5)	1.973(5) - 2.021(5)	1.912(9) - 2.033(9)	1.947(8) - 2.013(9)
Ni – O$_{H_2O}$	2.111(5) - 2.175(5)	2.053(4) - 2.145(6)	2.009(6) - 2.192(8)	2.016(8) - 2.139(7)
Ni – O$_{\text{MeOH}}$	2.016(5) - 2.120(4)	2.037(5) - 2.173(4)	2.092(6) - 2.107(9)	
Ni – COO$^-$	1.928(4) - 2.177(4)	1.957(5) - 2.213(4)	1.996(8) - 2.187(6)	1.894(9) - 2.131(8)
Ni – Ni[a]	3.039(1) - 3.458(1)	3.032(1) - 3.465(1)	3.021(2) - 3.445(2)	3.022(2) - 3.510(3)
Ni $\cdots$ Ni$_{16}$[b]	0.143 - 0.965	0.000 - 1.400	0.049 - 1.203	0.019 - 1.119
× Ni $\cdots$ Ni[c]	14.884(1)-14.949(1)	13.643(1)-15.910(2)	14.600(3)-15.030(2)	14.518(2)-14.603(2)
+ Ni $\cdots$ Ni[d]	12.317(1)-12.393(1)	11.845(1)-12.472(1)	12.066(3)-12.621(2)	11.357(2)-12.254(2)
Single-atom bridging angle (°)				
Ni – O$_{\text{phenol}}$ – Ni	97.8(2) - 119.4(2)	97.4(2) - 116.8(2)	97.8(2) - 117.2(3)	95.7(3) - 117.2(3)
Ni – O$^{COO^-}$ – Ni[e]	92.2(2) - 95.6(2)	92.2(1) - 96.4(2)	91.0(3) - 96.8(3)	91.8(4) - 98.2(3)

[a] for neighbouring Ni^{II} centres.
[b] deviation of Ni^{II} centres from the calculated Ni$_{16}$ plane.
[c] "corner-to-corner" distances between Ni^{II} centres bound by phenol side-arms of separate ligand units.
[d] "side-to-side" distances between Ni^{II} centres bound by catechol groups on opposite sides of the ring.
[e] this applies only to the μ_2-O of 3.21 type carboxylate groups.

Conclusions

Four related Ni$_{16}$ wheel complexes have been prepared, isolated, and structurally characterized. All complexes self-assemble into **L2**$_4$Ni$_{16}$ supramolecular wheels; with three acetate containing complexes being nearly isostructural, each presenting a unique crystal morphology corresponding to their crystallographic symmetry. A fourth formate containing analogue has also been obtained, which presents a strikingly different packing arrangement. While only structural data has been obtained so far for these complexes, they present an exciting opportunity for extension in magnetic analysis and host-guest chemistry.

6.2 Cu_{14}

During attempts to make a $\mathrm{Cu^{II}}$ analogue of $\mathbf{Ni_{16}}$, a single acetonitrile based sample presented crystals as bright green blocks after 3 months. X-ray crystallographic analysis revealed a tetradecanuclear copper complex, $\mathbf{Cu_{14}}$ (Figure 6.13). Formulated as $\mathbf{L2}_2\mathbf{L2'}_2\mathrm{Cu}_{14}(\mu_4{-}\mathrm{O})_2(\mu_2{-}\mathrm{OH})_2(\mu_3{-}\mathrm{OMe})_2(\mathrm{OAc})_6(\mathrm{H_2O})(\mathrm{MeCN})(\mathrm{MeOH})_2$, this complex contains **L2′**, an oxidized form of **L2** where one of the imine arms has cleaved and been oxidized to a nitrile (**L2′** = (*E*)-2,3-dihydroxy-4-(((2-hydroxybenzyl)imino)methyl)-1-naphthonitrile).

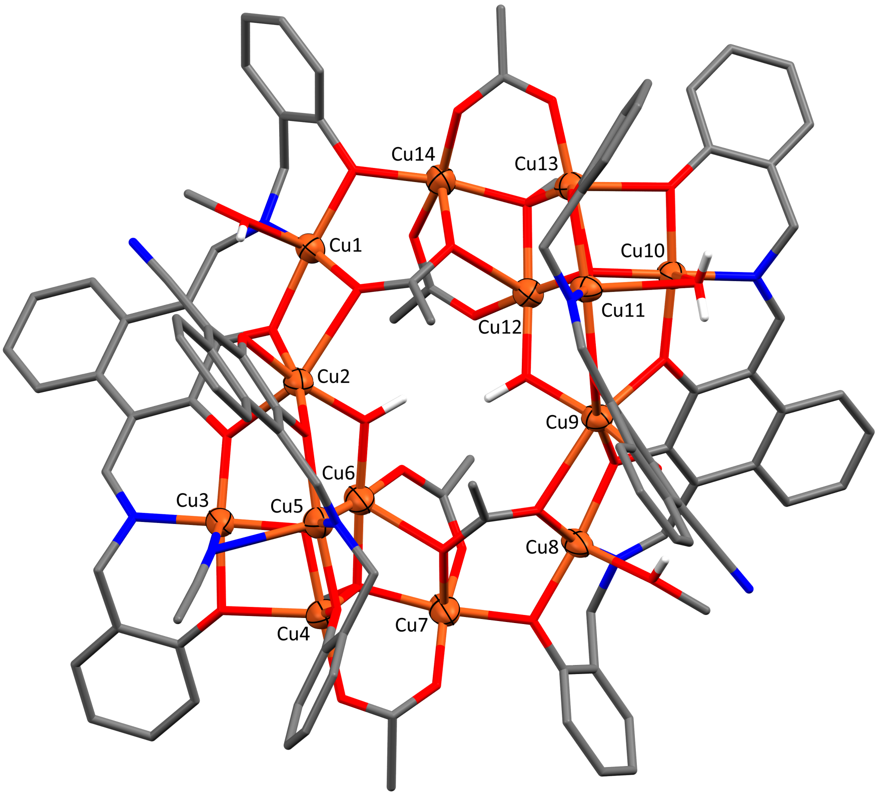

FIGURE 6.13: X-ray crystal structure of $\mathbf{Cu_{14}}$. Disordered species and non-acidic hydrogen atoms omitted for clarity. C = grey, Cu = orange, N = blue, O = red.

Both units of **L2** follow the same 5.222211 binding mode seen in the $\mathrm{Ni_{16}}$ complexes, whereas the oxidized **L2′** exhibits a 3.2211 binding mode. The $\mathbf{Cu_{14}}$ cluster features $\mathrm{Cu^{II}}$ centres in four different geometries: seven square pyramidal environments (note Cu2 is weakly coordinated by an acetate at 2.45(1) giving it octahedral character, `SPY-5 = 2.437` and `OC-6 = 4.282`), one trigonal bipyramidal centre (Cu4, `TBPY-5 = 2.254`), one distorted octehdral environment (Cu9, `OC-6 = 3.754`), and five square planar environments (Cu3, Cu5, Cu10, Cu11, and Cu12, `SP-4 = 0.181 – 0.489`) which each have a weakly coordinated axial site (MeCN, H_2O, or OAc) giving them some square pyramidal character. Without the weakly coordinated water and acetonitrile molecules, the complex exhibits near perfect C_2 symmetry, which can be seen by the symmetry of the inner binding groups. The presence of μ_2-OH groups was assigned on the basis of charge balance; the +28 charge from the 12 Cu^{+2} centres was partially balanced by two **L2** units (-8), two **L2′** units (-6), two μ_3-OMe anions (-2), six OAc anions (-6), and two μ_4-O^{-2} (-4), leaving a total charge of +2 to be balanced by the two μ_2-OH species bridging Cu2/Cu6 and Cu9/Cu12. The difference map indicates that there are a number of non-coordinated acetonitrile molecules present in the lattice, however, none were found to be stable to anisotropic refinement, even with freely refined occupancies. Due to the limited number of crystals of this compound being obtained, a solvent mask including 296 electrons in 1209 Å^3 has been applied to the data set, but without CHN microanalysis no reliable formulation which includes sufficient lattice solvent to satisfy the mask can be assigned. The axially coordinated methanol caps of Cu1 and Cu8 each form hydrogen bonds to the monodentate phenolic oxygen of the nearest **L2′** unit (O11 $\cdots$ H15 = 2.179(9) Å and O14 $\cdots$ H25 = 2.146(9) Å). No intermolecular hydrogen bonds are observed in the crystal packing (Figure 6.14), nor are any $\pi - \pi$ stacking interactions.

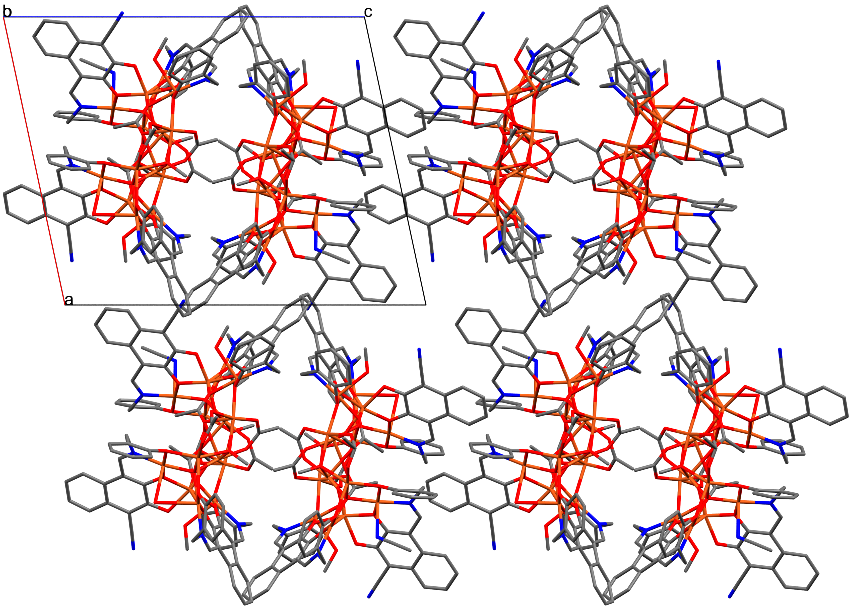

FIGURE 6.14: X-ray crystal packing of **Cu14**, viewed along the crystallographic *b*-axis. Disordered species and hydrogen atoms omitted for clarity. C = grey, Cu = orange, N = blue, O = red.

6.3 $Mn^{II}{}_8$

In the process of trying to synthesize paramagnetic homometallic clusters, using the dialdehyde ligand $\mathbf{H_2L1}$, the octanuclear complex $\mathbf{Mn_8}$ (Figure 6.15) was obtained as orange plate crystals. The complex exhibits the rare homometallic square-in-square topology, for which a $Mn_8L_8(PrOH)_4$ (L = diethyl ketipinate) analogue has been previously reported by Saalfrank *et al.*[168] Based on the crystal structure, $\mathbf{Mn_8}$ has the formulation $\mathbf{L1}_8Mn_8(H_2O)_2MeOH$, with the charge of each Mn^{II} centres being balanced by the -2 charge from each ligand. Each of the inner-square metals are bound by seven ligand based oxygen donors with molecular geometries somewhere between capped octahedra (`COC-7 = 1.958 – 2.246`) and capped trigonal prismatic (`CTPR-7 = 1.805 – 2.181`). The outer-square metal centres are only bound by six ligand based oxygen donors with a seventh coordination site occupied by water or methanol for Cu1, Cu2, and Cu4 resulting in the capped trigonal prismatic molecular geometries for all three (`CTPR-7 = 0.424 – 0.955`), with Cu3 remaining as a 6-coordinate distorted trigonal prism (`TPR-6 = 3.810`). The **L1** units can be split into two different groups; those in the Mn_8 plane, and those orthogonal to the plane. Each of the four in-plane **L2** units bind in a 3.1221 fashion where the salicylaldehyde-like binding mode forms a 6-membered ring with an outer-square Mn^{II} and the catechol group binds a Mn^{II} centre in the inner square. The four ligand units orthogonal to the plane bind in a 4.1321 mode, bridging each apex in the outer-square to the three nearest inner-square Mn^{II} centres.

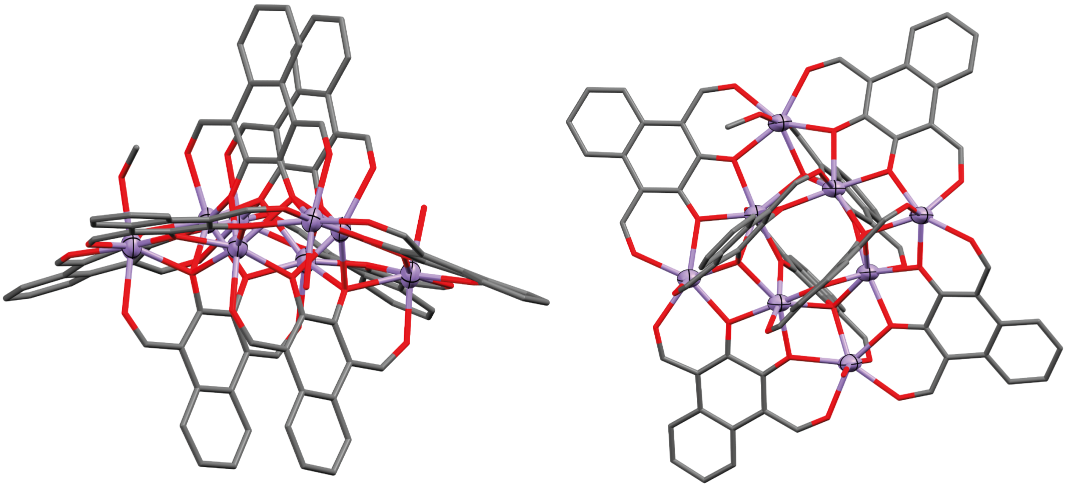

FIGURE 6.15: X-ray crystal structure of $\mathbf{Mn_8}$, viewed along the crystallographic *a*-axis (left) and *c*-axis (right). Thermal ellipsoids of metal atoms shown at 70%. Hydrogen atoms omitted for clarity. C = grey, Mn = light purple, O = red.

The large exposed naphthalene surfaces and the presence of three relatively small protic solvent caps allow the complex units to pack tightly together (Figure 6.16), with each complex forming three unique intermolecular hydrogen bonds (O4 $\cdots$ H35 = 1.829(9) Å, O12 $\cdots$ H34A = 1.951(8) Å, and O13 $\cdots$ H34A = 2.565(9) Å) forming hydrogen bonded 1D strands (Figure 6.17 note strands run along B). The intra-strand interactions are further enhanced by a $\pi - \pi$ interaction between in-plane ligand units ($\langle C5, C6, C7, C8, C9, C10\rangle \cdots \langle C24, C25, C26, C27, C28, C33\rangle$ = 3.811 Å) with an inter-strand interaction between $\langle C52, C53, C54, C55, C56, C57\rangle$ and $\langle C88, C89, C90, C91, C92, C93\rangle$ ensuring tight packing of the strands at 3.951 Å.

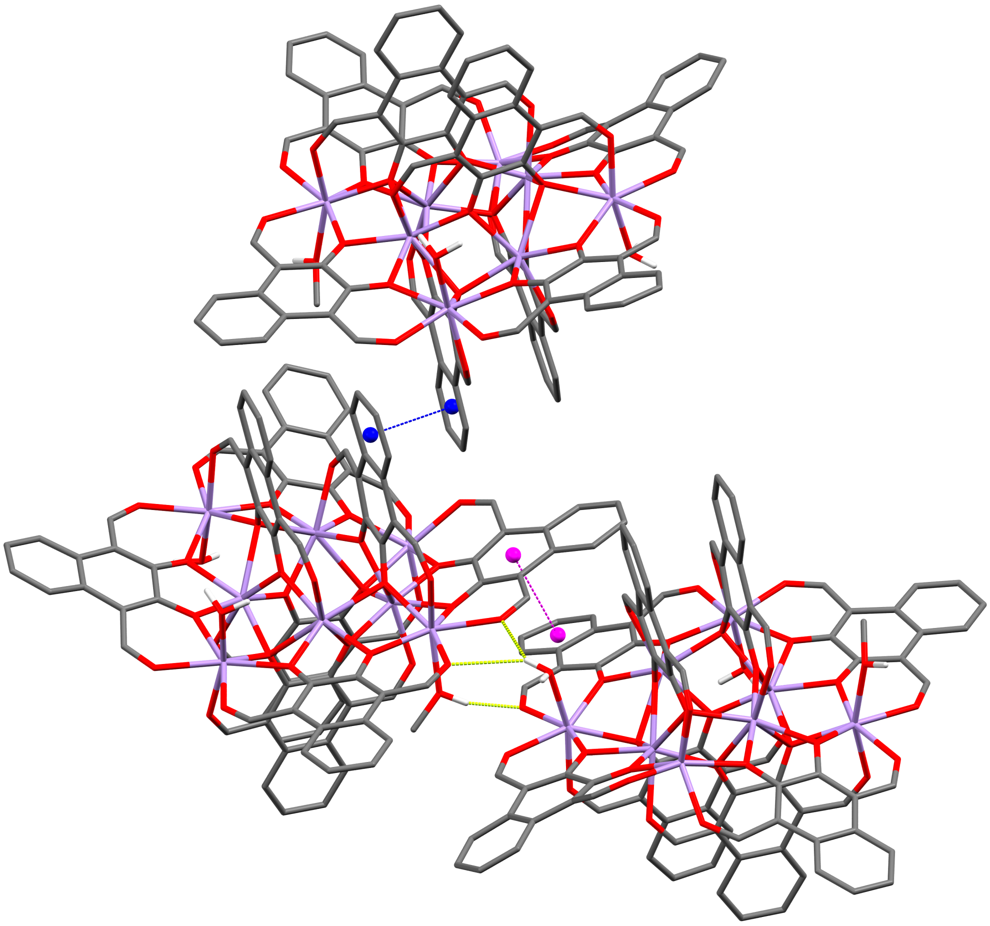

FIGURE 6.16: Crystal structure showing three interacting units of **Mn$_8$**. Hydrogen bonds shown as dashed yellow bond. Intra- and inter-strand $\pi - \pi$ interactions shown between the pink and blue centroids, respectively. Non-acidic hydrogen atoms omitted for clarity. C = grey, Mn = light purple, O = red.

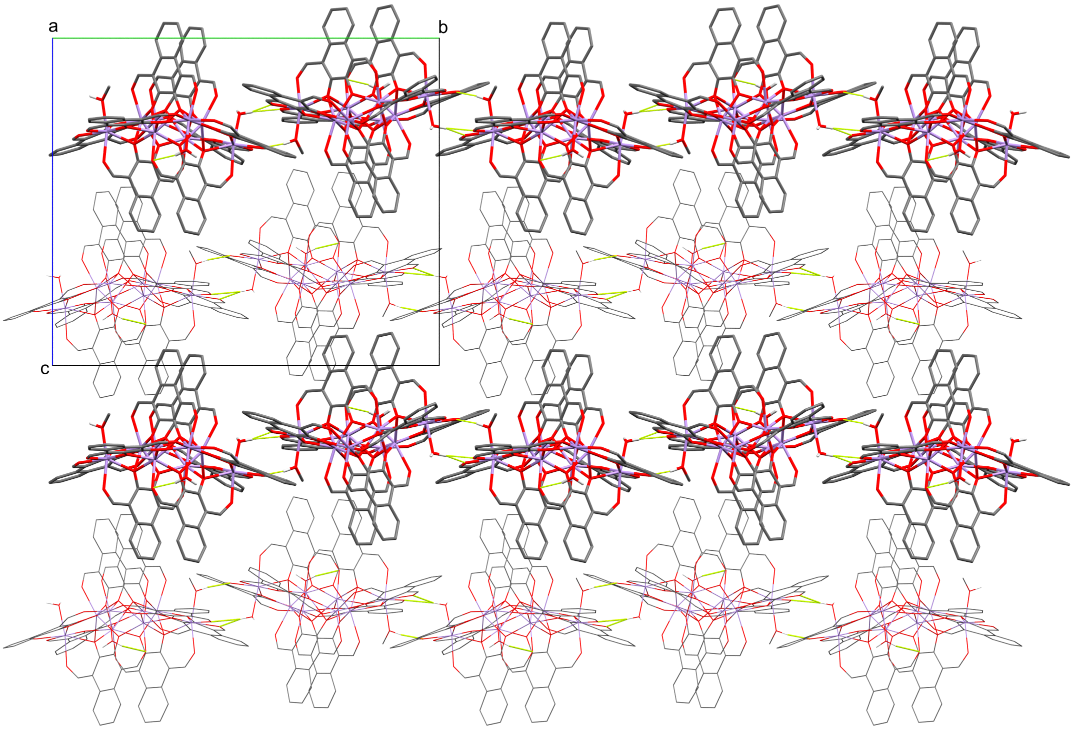

FIGURE 6.17: X-ray crystal packing of **Mn_8**, viewed along the crystallographic *a*-axis with two different styles to illustrate depth. Thermal ellipsoids of metal atoms shown at 70%. Non-acidic hydrogen atoms omitted for clarity. C = grey, Mn = light purple, O = red.

6.4 $\mathrm{Mn^{II}La^{III}_6}$

While attempting to produce manganese containing analogues of the M_3Ln triangles discussed in Chapters 3 – 5, only the sample containing lanthanum nitrate produced characterizable solids. The **$\mathbf{MnLa_6}$** complex formed from the same reaction stoichiometry as the M_3Ln triangles, and presented as bright orange plate crystals. Structural analysis however, showed that it was not the expected Mn_3La type complex but rather a heptanuclear complex which crystallized in the monoclinic space group $C2/c$ ($Z' = 0.5$) with the proposed formula $\mathbf{L1}_8\mathrm{Mn^{II}La^{III}_6(H_2O)_{12}(MeOH)_2(NO_3)_4}$, based on the crystal structure solution (Figure 6.18) and microanalytical data. Interestingly, this was the only structure of its type obtained from a large variety of transition metal/lanthanide combinations.

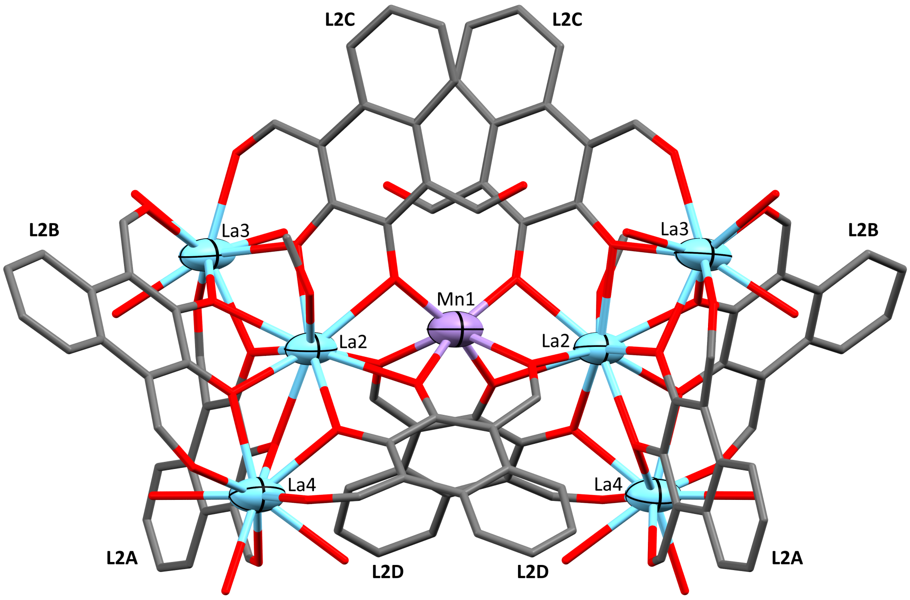

FIGURE 6.18: X-ray crystal structure of **$\mathbf{MnLa_6}$**, viewed along the crystallographic *c*-axis. Thermal ellipsoids of metal atoms shown at 70%. Non-coordinated species and hydrogen atoms omitted for clarity. C = grey, La = light blue, Mn = light purple, O = red.

The asymmetric unit consists of half of the full complex, with the remainder generated by two-fold rotation about the $\mathrm{Mn^{II}}$ centre. The ligands within the asymmetric unit have three unique binding modes: $3^{A/B}.1_{La2}2_{La2La3}2_{La3La4}1_{La4}$, $3^{C}.2_{Mn1La2}2_{La2La3}1_{La3}$, and $4^{D}.1_{La4}2_{La4La2}2_{La2Mn1}2_{Mn1La2^*}$ (see Figure 6.18 for labelling). The unbound aldehyde group of the ligand labelled **L2C** in Figure 6.18 was found to be crystallographically disordered over two sites in a freely refined ratio of 41:59. Figure 6.19 shows a reduced crystal structure with the other ligand units removed, both disordered aldehyde fragments of **L2C** are shown, with the primary component in yellow and the secondary component in red. The lower occupancy fragment (O1C) is weakly coordinated to the Mn1 centre at 2.64(3) Å. The central Mn^{II} ion ordinarily sits in a 6-coordinate distorted trigonal prismatic environment (`TPR-6 = 4.669`), but due to the weakly coordinated secondary fragment of O1C, there exists a possible 8-coordinate triangular dodecahedron geometry (`TDD-8 = 1.317`). The La2 centre methanol cap and is bound by the catechol groups of all four ligand units within the asymmetric unit as well as the O4D aldehyde of a symmetry generated **L2D** molecule, thus occupies a 10-coordinate site with approximate C_{2v} symmetry, best described as a sphenocorona (`JSPC-10 = 4.583`). The La3 and La4 centres are each bound by three of the four ligand units from within the asymmetric unit (through the salicyaldehyde-like binding mode), and are coordinated by three water caps per metal, resuling in a 9-coordinate muffin geometry (`MFF-9 = 0.692` and `0.599`, respectively). The total +20 charge of the metals (1 × Mn^{+2} and 6 × La^{+3}) is partially balanced by eight **L2** units (-16), with the remainder of the charge believed to be balanced by non-coordinated nitrate anions. The crystal structure

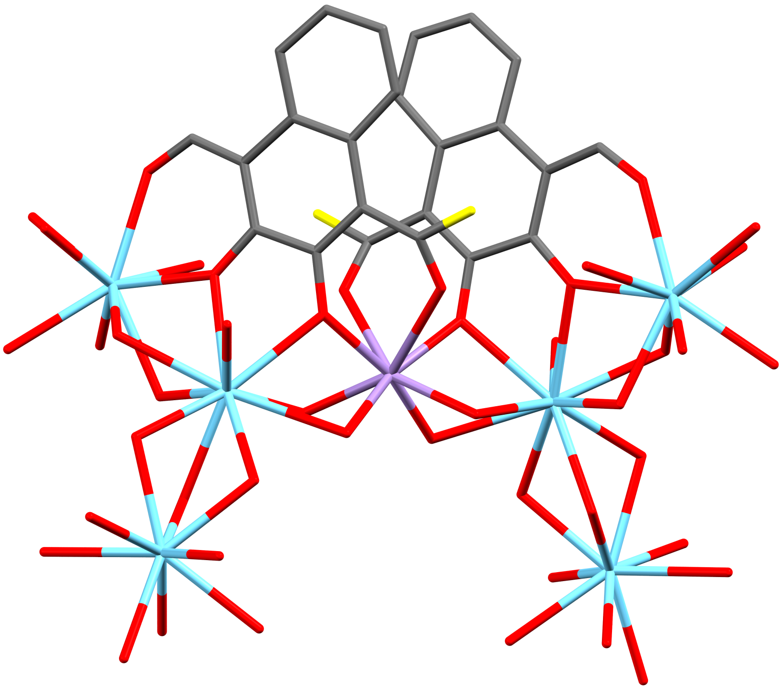

FIGURE 6.19: Reduced crystal structure of **MnLa$_6$**, highlighting the possible 8-coordinate Mn^{II} centre. Non-relevant carbons and all hydrogen atoms omitted for clarity. C = grey, La = light blue, Mn = light purple, O = red/yellow.

contains one nitrate per unit complex and has a solvent mask which contains 178 electrons in 632 Å^3 (per unit complex), which is consistent with three nitrate anions and eight water molecules (totalling 173 electrons). The nitrogen content found by CHN microanalysis supports the assignment of four nitrates per formula unit.

DC magnetic susceptibility and magnetization experiments have been completed for this complex (Figure 6.20) to confirm the oxidation and spin state of the manganese centre. The room temperature $\chi_\mathrm{m}T$ product of 5.0 cm^3 K mol^{-1} exceeded the theoretical spin-only value of 4.375 cm^3 K mol^{-1} at 300 K, which indicated the presence of a ⁵⁄₂ spin. The experimental magnetization at 7 T was almost 5 μ_B, which also agrees with the assignment of a single high-spin Mn$^\mathrm{II}$ centre, with $g = 2.0$. The slight residual slope in the $\chi_\mathrm{m}T$ vs T profile at high temperature could be assigned to some contribution from temperature independent paramagnetism.

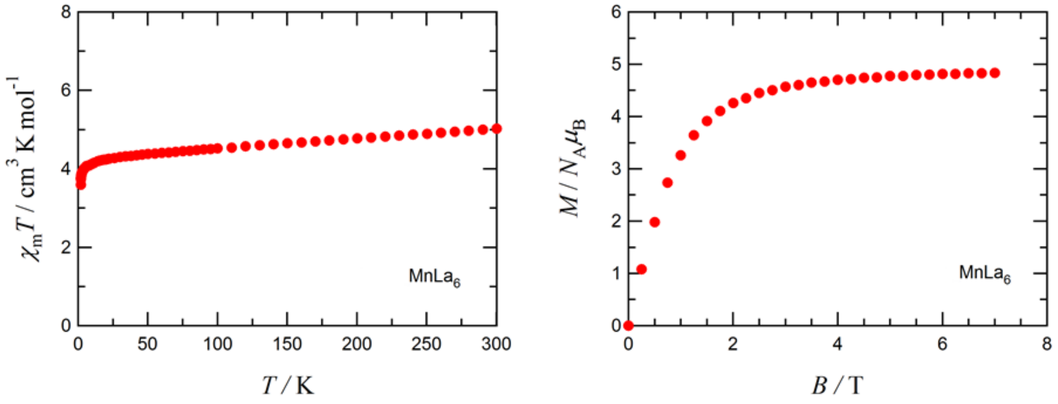

FIGURE 6.20: Plot of $\chi_\mathrm{m}T$ vs T measured at 0.5 T (left) and M vs H plot measured at 1.8 K (right) for **MnLa$_6$**. Measurements were performed on a polycrystalline sample fixed in a small amount of eicosane.

Structural Parameters for Cu_{14}, Mn_8, and $MnLa_6$

TABLE 6.2: Selected structural parameters for $\mathbf{Cu_{14}}$ and $\mathbf{Mn_8}$.

Bond (Å)	$\mathbf{Cu_{12}}$	$\mathbf{Mn_8}$
$M - O_{phenol}$	1.928(4) - 2.225(3)	2.091(3) - 2.459(3)
$M - X_{[a]}$	1.937(3) - 1.954(3)	2.137(3) - 2.279(3)
$M - O_{H_2O}$	2.452(3) - 2.584(3)	2.192(3) - 2.210(3)
$M - O_{MeOH}$	2.286(3) - 2.304(3)	2.234(3)
$M - O^{OAc^-}$	1.919(4) - 2.454(3)	
$M - M^{[b]}$	2.865(1) - 3.599(1)	3.473(1) - 3.534(1)
Single-atom bridging angle (°)		
$M - \mu_2\text{-}O_{phenol} - M$	93.2(1) - 123.6(1)	102.3(1) - 110.0(1)
$M - \mu_3\text{-}O^{phenol} - M$	94.8(1) - 103.6(1)	
$M - O^{OAc^-} - M^{[c]}$	85.4(1) - 97.6(1)	
$M - O^{H_2O} - M$	78.5(1)	
$M - N^{MeCN} - M$	73.1(1)	

[a] X is N^{imine} for $\mathbf{Cu_{14}}$ and $O^{aldehyde}$ for $\mathbf{Mn_8}$.
[b] for neighbouring metal centres connected by one-atom bridges.
[c] this applies only to the μ_2-O of 3.21 and 4.22 type acetate groups.

TABLE 6.3: Selected structural parameters for $\mathbf{MnLa_6}$.

Bond (Å)	$MnLa_2$ fragment[a]	La_3 fragment[b]
$M - O_{phenol}$	2.072(9) - 2.217(8)	2.432(6) - 2.648(7)
$M - O_{aldehyde}$	2.217(7)	2.483(7) - 2.685(9)
$M - O_{H_2O}$		2.535(4) - 2.638(3)
$M - O_{MeOH}$		2.511(9)
Single-atom bridging angle (°)		
M – O – La	93.7(3) - 100.5(2)	101.1(3) - 102.8(3)

[a] $M = Mn^{II}$.
[b] $M = La^{III}$.

Conclusions

While attempting to generate a Cu^{II} analogue to the cyclic Ni_{16} complexes reported at the start of this chapter, the large **$\mathbf{Cu_{14}}$** complex was isolated and structural analysis revealed a number of different coordination environments. During the assembly of this complex, two units of ligand were partially oxidized to form an asymmetric imine-nitrile ligand. Attempts to reproduce this complex have so far been unsuccessful. A further two polynuclear Mn^{II} containing complexes, **$\mathbf{Mn_8}$** and **$\mathbf{MnLa_6}$**, were also obtained while attempting to generate Mn^{II} analogues of the triangle complexes discussed in Chapters 3 – 5. X-ray crystallographic analysis revealed **$\mathbf{Mn_8}$** exhibited the relatively unseen homometallic square-in-square topology; the presence of a large number of single atom bridges between Mn^{II} centres could make it a magnetically interesting compound.

Preparative Methods

Ni_{16}

To a stirred suspension of $\mathbf{H_4L2}$ (0.426 g, 1 mmol) in MeOH (16 mL) was added $Ni(OAc)_2 \cdot 4\,H_2O$ (0.995 g, 4 mmol) in water (4 mL). The orange solution turned murky green on heating, and was refluxed for 7 days at 90°C before being concentrated to dryness under reduced pressure. The green-brown solid was then dissolved in a minimum amount of 5% water in MeOH and set up for vapour diffusion with diethyl ether, to yield green crystals. All three Ni_{16} polymorphs were prepared under the same synthetic conditions, however, it was observed that reduced reaction times resulted in increased formation of the monoclinic polymorphs (as needles and plates). The $\mathbf{Ni_{16}^{formate}}$ analogue was produced using the same general method, with $Ni(HCOO)_2 \cdot 2\,H_2O$ in place of $Ni(OAc)_2 \cdot 4\,H_2O$. Yield of the tetragonal species was approximately 15% based on $Ni(OAc)_2 \cdot 4\,H_2O$. ATR-IR $\overline{\nu}$: 3402, 1630, 1559, 1484, 1416, 1380, 1341, 1286, 1263, 1238, 1110, 1036, 928, 880, 754, 685 cm^{-1}. Microanalytical data found(calc) for $\mathbf{Ni_{16}}$ (calculated for $C_{140}H_{152}N_8Ni_{16}O_{60} \cdot 34\,H_2O$, M_r = 4458.34 g mol^{-1}) C: 37.70(37.72), H: 4.88(4.97), N: 2.32(2.51).

Cu_{14}

To a stirred suspension of $\mathbf{H_4L2}$ (0.426 g, 1 mmol) in MeCN (16 mL) was added $Cu(OAc)_2 \cdot H_2O$ (0.798 g, 4 mmol) in water (4 mL). The orange solution turned brown on heating, and was refluxed for 7 days at 100°C before being concentrated to dryness under reduced pressure. The brown solid was then dissolved in a minimum amount MeCN and set up for vapour diffusion with diethyl ether, producing bright green block crystals in very low yield.

Mn_8

To a stirred suspension of $\mathbf{H_2L1}$ (0.216 g, 1 mmol) in MeOH (15 mL) was added $Mn(NO_3)_2 \cdot 4\,H_2O$ (0.251 g, 1 mmol) in MeOH (15 mL), causing rapid dissolution to form a dark red solution which was stirred at 40°C for 3 days before being concentrated to dryness under reduced pressure. The red-brown solid was then dissolved in a minimum amount of MeOH and set up for vapour diffusion with diethyl ether, producing orange-red plate crystals in approximately 20% yield. ATR-IR $\overline{\nu}$: 3352, 2960, 1626, 1575, 1569, 15557, 1538, 1533, 1505, 1480, 1464, 1394, 1338, 1274, 1157, 1116, 754, 646 cm^{-1}. Microanalytical data found(calc) for $\mathbf{Mn_8}$ (calculated for $C_{98}H_{58}Mn_8O_{35}$, M_r = 2234.99 g mol^{-1}) C: 52.48(52.66), H: 2.30(2.62).

MnLa$_6$

The **MnLa$_6$** complex was prepared using the same general method for the triangular clusters discussed in Chapters 3 – 5. Varying the stoichiometry of starting materials to match the formulation of the crystal structure neither improved yield or time to crystallization. Using the general method, **MnLa$_6$** was obtained as bright orange-yellow plate crystals in 48% yield (based on $La(NO_3)_3 \cdot 6\,H_2O$). ATR-IR $\overline{\nu}$: 3382, 2361, 1620, 1564, 1521, 1471, 1427, 1377, 1355, 1335, 1262, 1243, 1112, 1031, 1000, 969, 948, 744, 679, 624, 512 cm^{-1}. Microanalytical data found(calc) for **MnLa$_6$** (calculated for $C_{98}H_{80}La_6MnN_4O_{58}$, M_r = 3130.05 g mol^{-1}) C: 37.49(37.60), H: 2.69(2.58), N: 2.00(1.79).

Chapter 7

Conclusions, Perspectives, and Outlooks

Throughout this research, the primary focus has been on two simple ligand systems and the metal clusters they (*do or do not*) produce. The dialdehyde ligand, **H_2L1**, was the organic focus for a majority of this work including all complexes in Chapters 3 – 5. Optimization of an effectively one-pot literature synthesis has led to an increase in yield from 52% for the literature method to $> 90\%$ as presented in this thesis, which is a four-fold improvement over multi-step syntheses of **H_2L1** and its monocyclic benzene analogue. The second ligand of focus, **H_4L2**, was a simple one-step transformation away from **H_2L1**. This diimine ligand was found to exhibit a tautomeric-like structure in the solid state corresponding to two symmetric [1,5]-proton shifts. **H_4L2** produced the high nuclearity complexes (M_x where $x > 10$) presented in Chapter 6.

The M_3Ln clusters discussed in Chapters 3 – 5 represent a class of under-represented structures, which previous to this work have only been isolated and structurally characterized as intermediate species on the way to larger macrocyclic systems. Exclusively featuring near-planar M_3LnO_{12} cores, the 15 standard monomeric complexes discussed in these chapters greatly expand this class of complex, and show promise for their potential as SMMs. While the magnetically characterized Ni_3Ln complexes in Chapter 3 did not display any meaningful frequency dependant AC data, the DC magnetic data did indicate the presence of dominant ferromagnetic interactions. Chapters 4 and 5 contain the first examples of non-macrocyclic Cu_3Ln and Co_3Ln complexes in this class, respectively. With the **Cu_3Tb** complex being the first in this class to exhibit SMM behaviour in zero applied field; with a barrier height, U_{eff}, of 10.5(1) K (7.30(7) cm^{-1}). The **Cu_3Gd** and **Cu_3Dy** complexes were also found to be field supported SMMs with $U_{\text{eff}} = 10.8(2)$ K and $U_{\text{eff}} = 7.8(1)$ K in 2 kOe and 1 kOe applied fields, respectively. Although Gd$^{\text{III}}$ is isotropic and hence should not exhibit slow relaxation of magnetization, the interesting magnetic responses of $\mathbf{Ni_3Gd}$ and $\mathbf{Cu_3Gd}$ can be attributed to an asymmetric crystal field where $J_z \neq J_x, J_y$. With only the $\mathbf{Co_3La}$ complex in Chapter 5 being produced in sufficient quantity for magnetic characterization, the potential magnetic properties of the Co_3Ln complex remains unclear. Based on structural characterization alone, it was clear that the size of the central lanthanide ion in the Co_3Ln complexes played an important role on influencing the coordination sphere of each Co^{II} centre, a study on the remainder of the lanthanide series and potentially on the reduction in size of the ligand to 1,4-diformylbenzene-2,3-diol would provide further insight.

The large bowl-shaped hexadecanuclear nickel complex formed using the $\mathbf{H_4L2}$ diimine ligand was found to crystallize as three distinct polymorphs with clear differences in crystal morphology, with perhaps the most interesting also being the most easily obtainable through extended reaction times. Obtained as block crystals, the tetragonal polymorph, $\mathbf{Ni_{16}}$, exhibits four-fold symmtery and packs each hexadecanuclear bowl together in the form a non-covalent dimerized molecular capsule. The ability for this capsule to act as the name suggest was explored through the introduction of C_{60} and C_{70} buckyballs; with the idea that given the reasonable size match of the capsule void with these buckyballs, $\pi - \pi$ interactions and the hydrophobic effect could potentially drive for formation of a $C_{70}@2Ni_{16}$ host-guest complex, however no evidence has been seen of a successful transformation. Although initial attempts have proven unsuccessful, other guest species such a InP magic-sized clusters or mono-disperse carbon dots could also be explored. At the time of writing, the $\mathbf{Ni_{16}}$ complex has not yet been magnetically characterized, but is awaiting further measurements with our collaborators, Prof. Annie Powell and Dr. Chris Anson, at Karlsruhe Institute of Technology, Germany. Modifications of the $\mathbf{Ni_{16}}$ complex have been explored in a limited capacity, with the successful isolation and structural characterization of a formate containing analogue, and further efforts put in to the incorporation of other carboxylate anions as well as other transition metal analogues.

A tetradecanuclear Cu^{II} complex was obtained in an effort to produce the Cu_{16} analogue. This $\mathbf{Cu_{14}}$ complex exhibits the same ligand-metal binding pattern as $\mathbf{Ni_{16}}$, showing promise that a Cu_{16} analogue could be obtained with different synthetic conditions, however the space has not yet been explored. Similarly, while attempting to generate manganese containing variations on the M_3Ln triangles and the $\mathbf{Ni_{16}}$ cluster, a variety of other unexpected complexes were obtained. In particular the $\mathbf{MnLa_6}$ complex presents an architecture rich for investigation. While an obvious variation is to incorporate paramagnetic lanthanide ions into the La^{III} sites, there also exsists the potential to substitute the central ion for other 3*d* metals, or potentially even a lanthanide given the ability of the weakly coordinated aldehyde arms to provide two additional donors.

Obviously, with positive signs of SMM properties found for some of the non-macrocyclic M_3Ln triangles, future synthetic efforts should be made to extend these; complete the available lanthanide families within each transition metal set, and magnetically characterize each for a more complete understanding. While initial attempts to produce a family of Mn_3Ln complexes were unsuccessful, there is still room to explore, and potentially further extend these systems to produce the as yet unreported Fe_3Ln triangles. Given the presence of SMM properties in **Cu_3Tb**, magnetic characterization of the **$[Ni_3Tb]_n$** polymer with synthetic efforts targeted at producing polymeric Co^{II} and Cu^{II} analogues could prove interesting.

Although this thesis has only studied some small portion of the possible non-macrocyclic M_3Ln triangle complexes and M_{16} bowl-shaped clusters, it has further demonstrated the versatility of simple ligand systems to produce wildly varied complexes.

Appendix A

A Geometric Appendix

This thesis makes use of the Harris method for ligand-metal binding notation; where the leading digit corresponds to the total number of metal centres the ligand is bound to, and each digit following the decimal place corresponds to the number of metal centres each donor is bound to. This notation works best for symmetric systems, where left-to-right or right-to-left orientations of the ligand do no change the binding pattern in Harris notation. Numbering of the donors is sequential per element, with O $>$ N $>$ S $>$ X, with no preference as to the type of donor. If the metal centres are labelled then a more explicit version of the notation can be used, where each of the digits corresponding to donors can be subscripted with the labels of the metals bound by that donor. For example, the 5.222211 notation used to describe the binding mode of **L2** in **Ni$_{16}$** can be more explicitly stated as $5.2_{12}2_{23}2_{34}2_{45}1_{2}1_{4}$, which implies the left hand phenolic side arm is bound to metals 1 and 2, the left oxygen of the catechol group is bound to metals 2 and 3, the right oxygen to metals 3 and 4, the right hand phenolic side arm to metals 4 and 5, with the left imine binding only to metal 2 and the right imine binding only to metal 4. Figure A.1 illustrates some common binding modes for the acetate anions, as well as the 5.222 binding mode of carbonate present in the Gd$_{140}$ complex discussed in Chapter 1.4.1.

The SHAPE software package has also been used extensively throughout this thesis for continuous shape measurement (CShM) calculations to aid in a more accurate determination of local coordination geometries. Figures A.2 – A.5 illustrates some of the more common 5-, 6-, 9-, 10-, and 11-coordinate geometries. SHAPE makes use of a number of non-standard 5- and 6-coordinate geometries, such as the vacant octahedron (`vOC-5`), Johnson trigonal bipyramidal (`JTBPY-5`), and Johnson pentagonl pyramidal (`JPPY-6`) geometries, which are axially compressed analogues of `SPY-5`, `TBPY-5`, and `PPY-6`, respectively. In the vacant octahedron and both Johnson solids, rather than having equal M – X distances, the distance between binding groups (X – X) is equal.

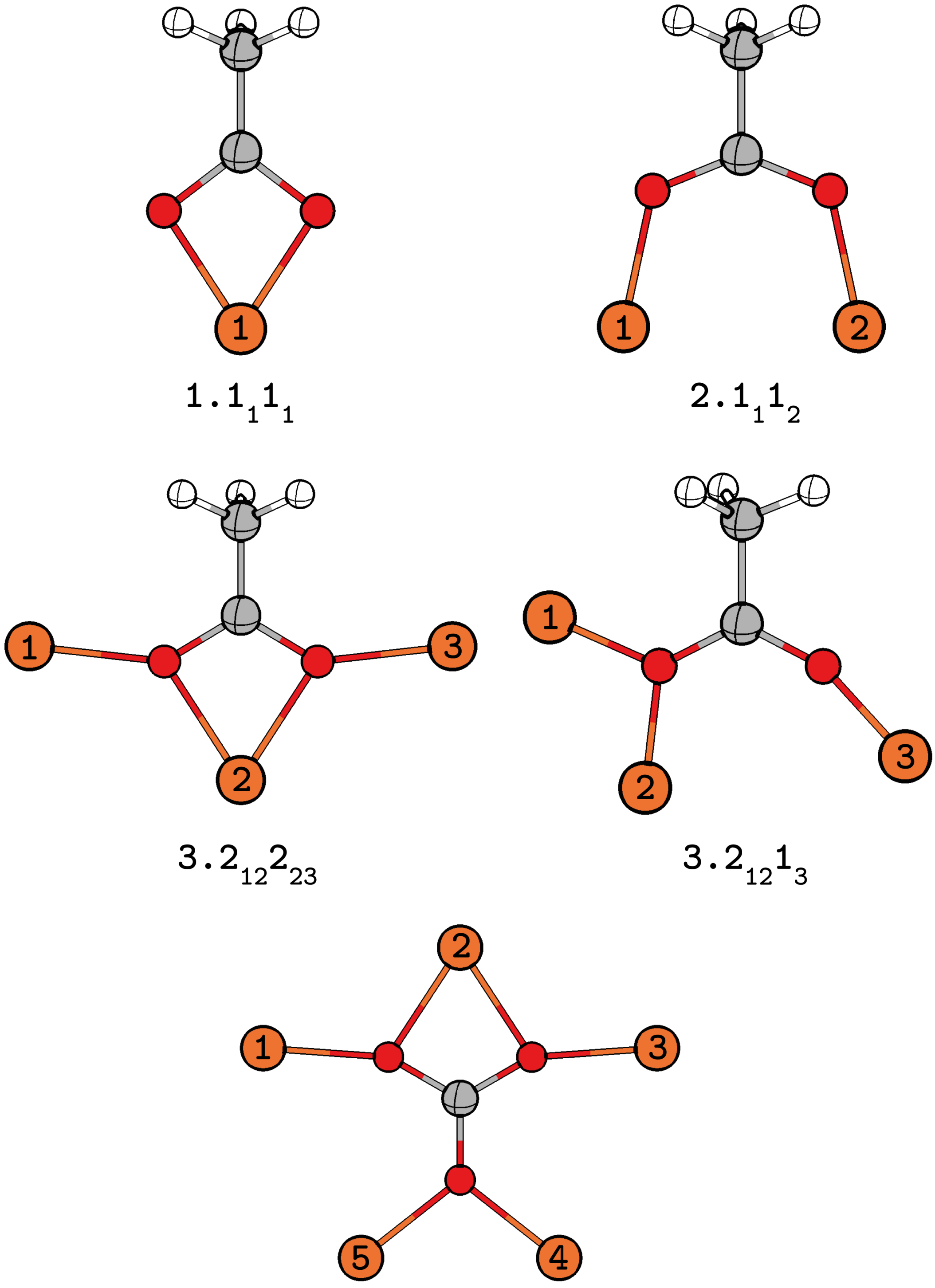

$1.1_1 1_1$

$2.1_1 1_2$

$3.2_{12} 2_{23}$

$3.2_{12} 1_3$

$5.2_{12} 2_{23} 2_{45}$

FIGURE A.1: Examples of Harris notation for selected binding modes of acetate and carbonate.

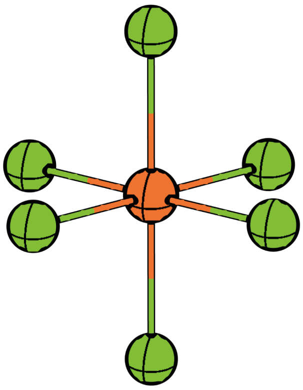

Octahedral
(OC-6, O_h)

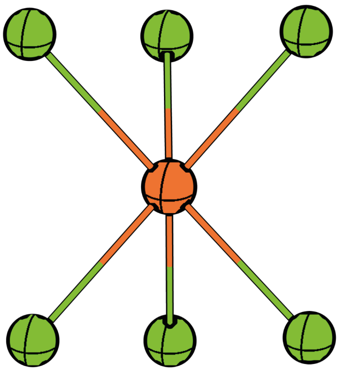

Trigonal Prismatic
(JPPY-6, C_{5v})

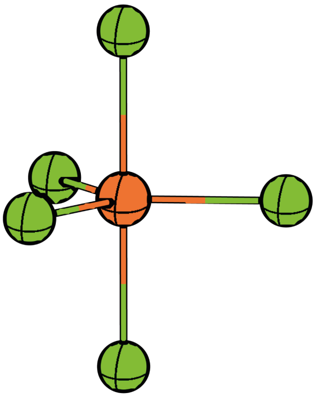

Trigonal Bipyramidal
(TBPY-5, D_{3h})

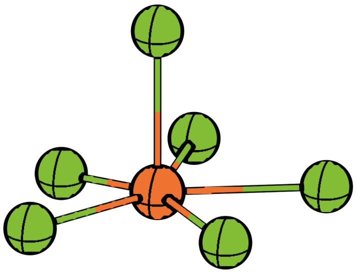

Pentagonal Pyramidal
(PPY-6, C_{5v})

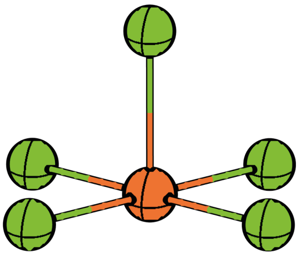

Square Pyramidal
(SPY-5, C_{4v})

FIGURE A.2: Schematic representation of some 5- and 6-coordinate geometries, with corresponding CShM labels.

OUTPUT A.1: SHAPE output for 9-, 10-, and 11-coordinate ions contained in the complexes reported in Chapters 3 – 5.

```
9-coordinate geometries
Structure      CSAPR-9      TCTPR-9         HH-9       MFF-9
Co3Dy,           4.391,       5.306,       4.561,      3.490
Cu3Er            4.373,       5.450,       3.928,      3.088
Cu3Ho            4.417,       5.524,       3.851,      3.110
Ni3Tb            4.217,       4.919,       3.848,      3.144
Ni3Gd_acid       5.501,       6.601,       2.757,      4.062

10-coordinate geometries
Structure      JSPC-10       SDD-10        TD-10       HD-10
Co3Gd            3.460,       2.094,       1.405,      5.768
Co3Tb            3.001,       2.078,       1.350,      6.553
Cu3Dy            4.181,       1.532,       0.608,      4.971
Cu3Yb            4.439,       1.565,       0.697,      4.683
Cu3La            4.341,       1.332,       0.637,      5.099
Cu3Gd            4.589,       1.477,       0.620,      4.970
Cu3Tb            2.052,       2.531,       1.665,      7.358
Ni3Gd            3.294,       2.725,       1.690,      5.659
Ni3Eu            3.173,       2.430,       1.596,      6.212
Ni3La            3.389,       1.724,       1.587,      6.731

11-coordinate geometries
Structure     JCPPR-11    JCPAPR-11     JAPPR-11    JASPC-11
Co3La            8.661,       4.655,      11.666,      5.964
Ni3Ba            9.993,       5.896,      12.313,      8.778
```

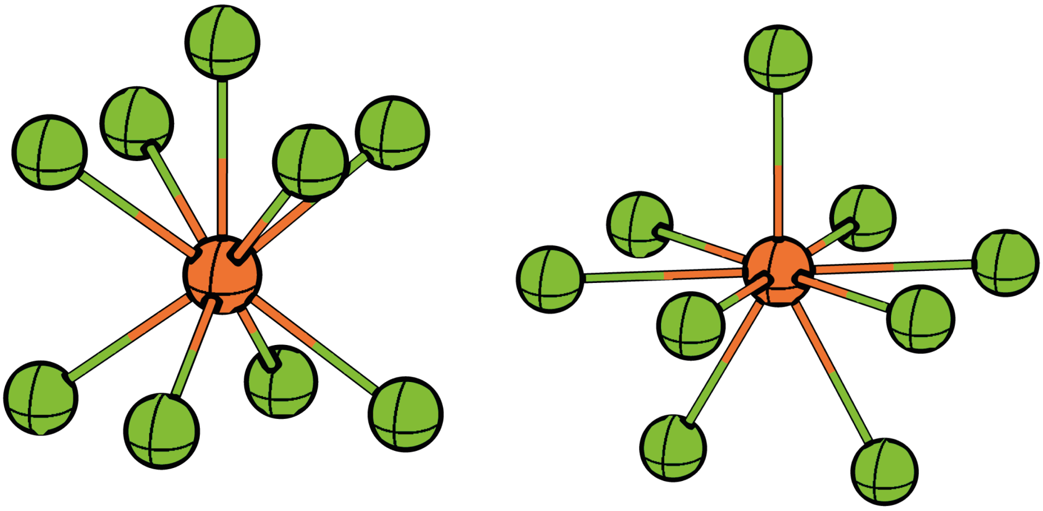

Capped Square Antiprism (CSAPR-9, C_{4v})

Hula-Hoop (HH-9, C_{2v})

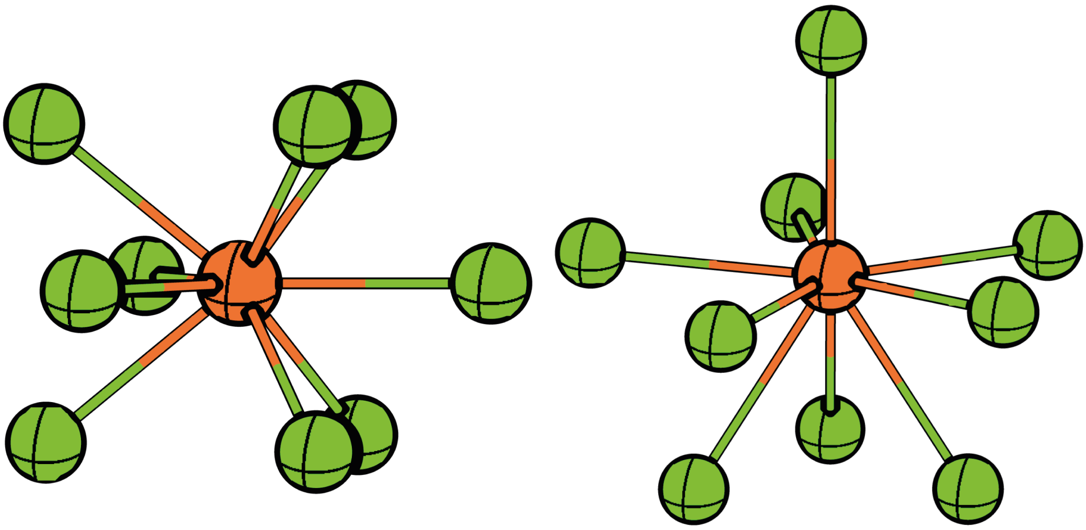

Tri-capped Trigonal Prism (TCTPR-9, D_{3h})

Muffin (MFF-9, C_s)

FIGURE A.3: Schematic representation of some 9-coordinate geometries, with corresponding CShM labels.

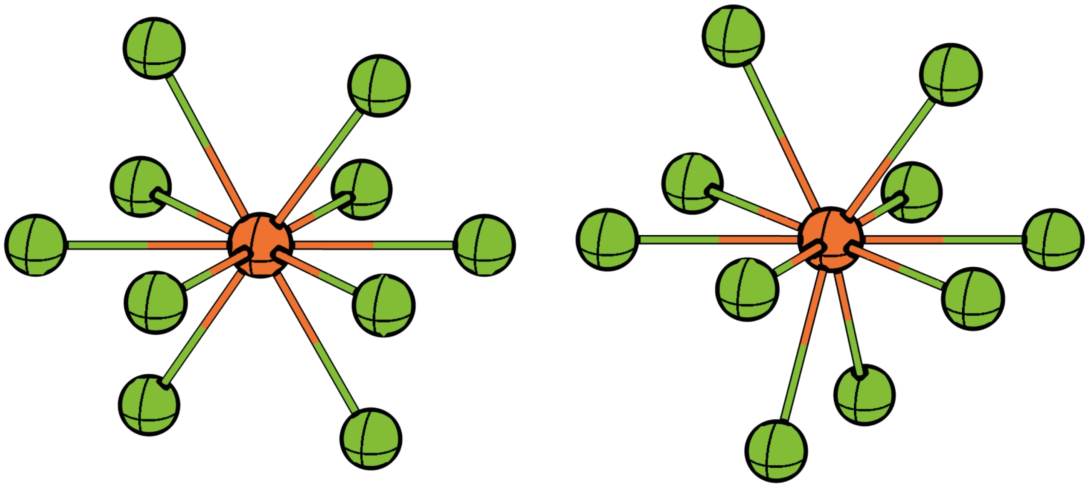

Hexadecahedron
(HD-10, D_{4h})

Tetradecahedron
(TDD-10, C_{2v})

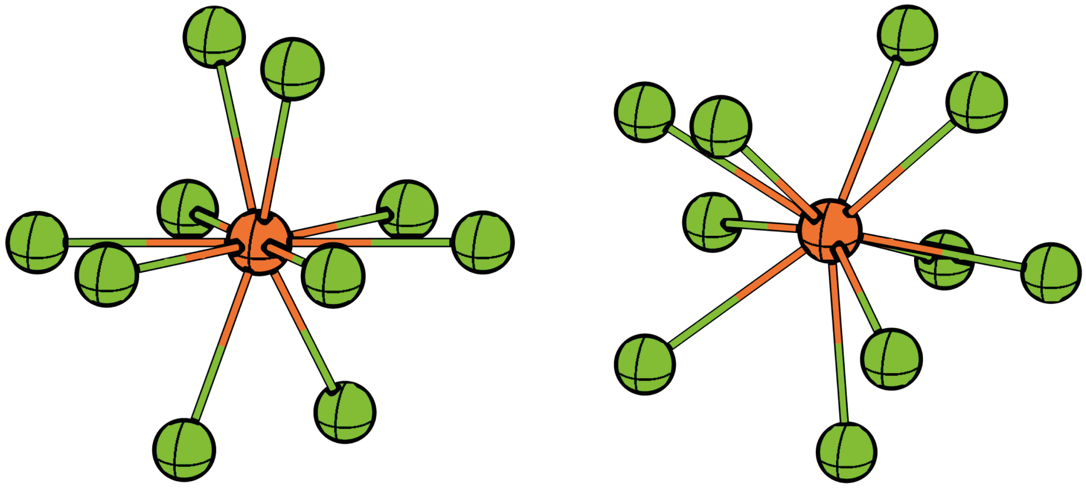

Staggered Dodecahedron
(SDD-10, D_2)

Sphenocorona
(JSPC-10, C_{2v})

FIGURE A.4: Schematic representation of some 10-coordinate geometries, with corresponding CShM labels.

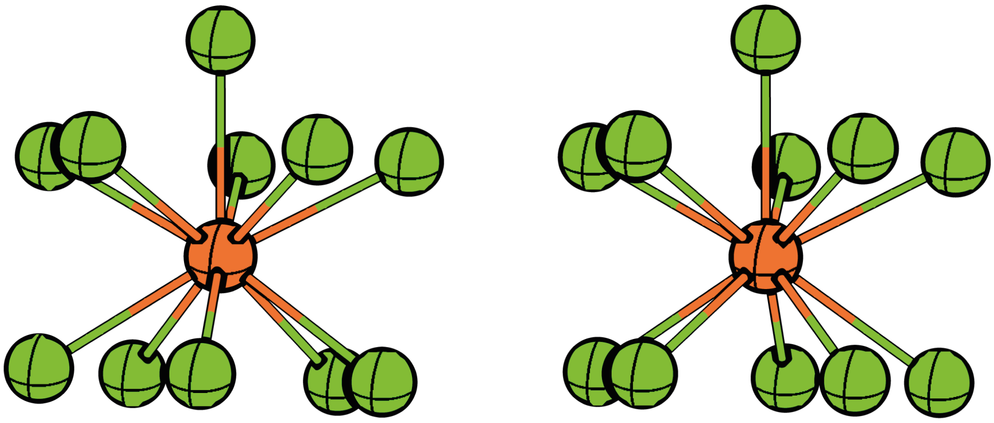

Capped Pentagonal Antiprism
(JCPAPR-11, C_{5v})

Capped Pentagonal Prism
(JCPPR-11, C_{5v})

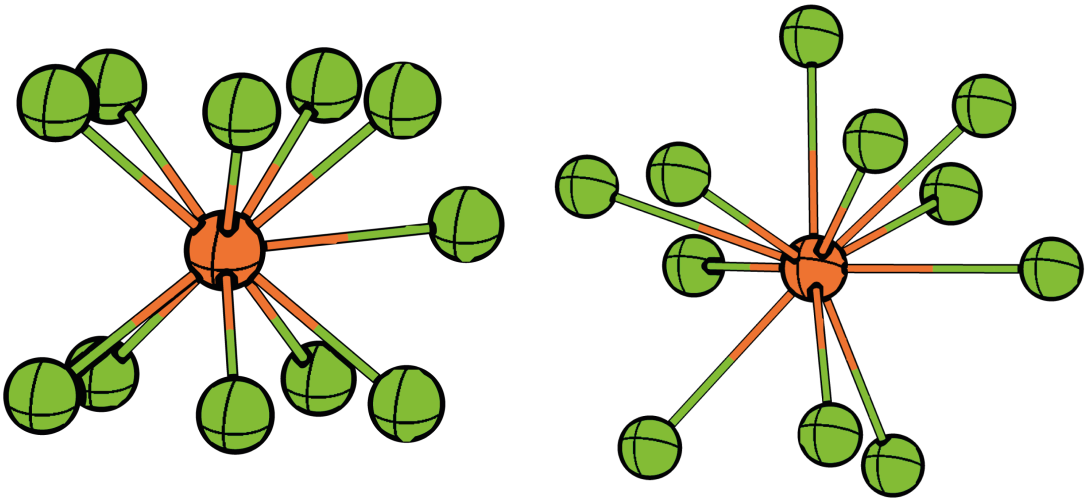

Augemented Pentagonl Prism
(JAPPR-11, C_{2v})

Augmented Sphenocorona
(JASPC-11, C_s)

FIGURE A.5: Schematic representation of some 11-coordinate geometries, with corresponding CShM labels.

Appendix B

Assorted Spectra

Assorted Spectra for Characterization

Figures B.1 – B.3 show labelled schematics of the three new organic compounds (**H_4L2**, **H_2L3**, and **aminoSal**) reported in this thesis and the accompanying spectra used for their characterization.

Selected ATR-IR spectra of metal complexes from Chapters 3 – 6 then follow in Figures B.4 – B.9.

H_4L2

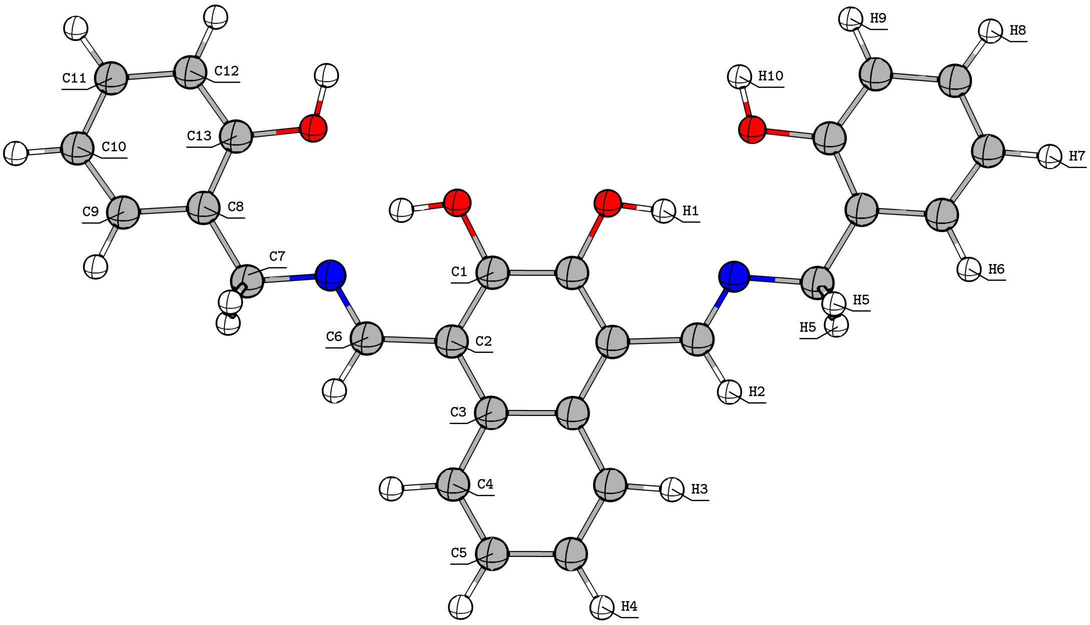

FIGURE B.1: Schematic of **H_4L2**, labelled for NMR assignment.

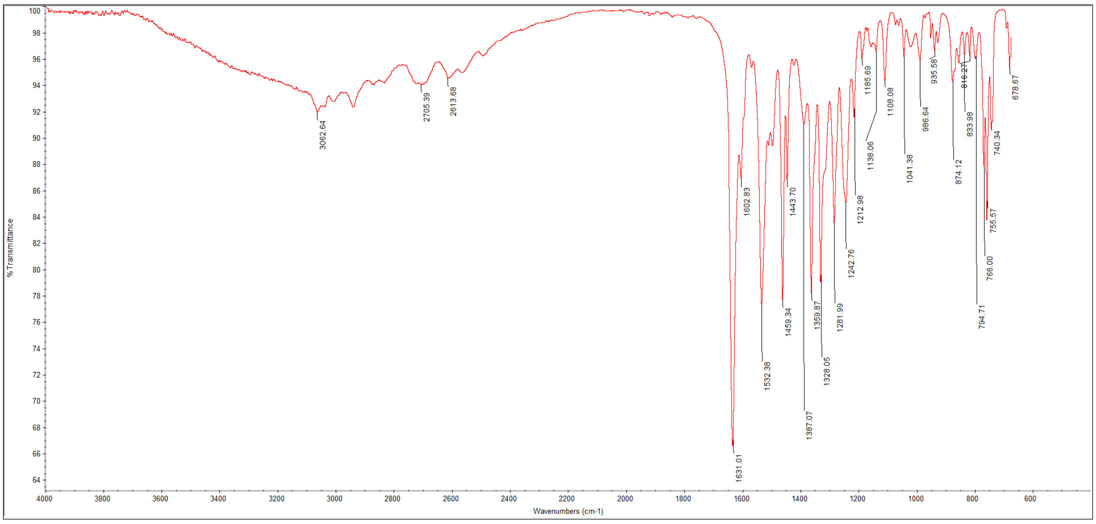

1,4-Bis((E)-((2'-hydroxybenzyl)imino)methyl)-2,3-naphthalenediol

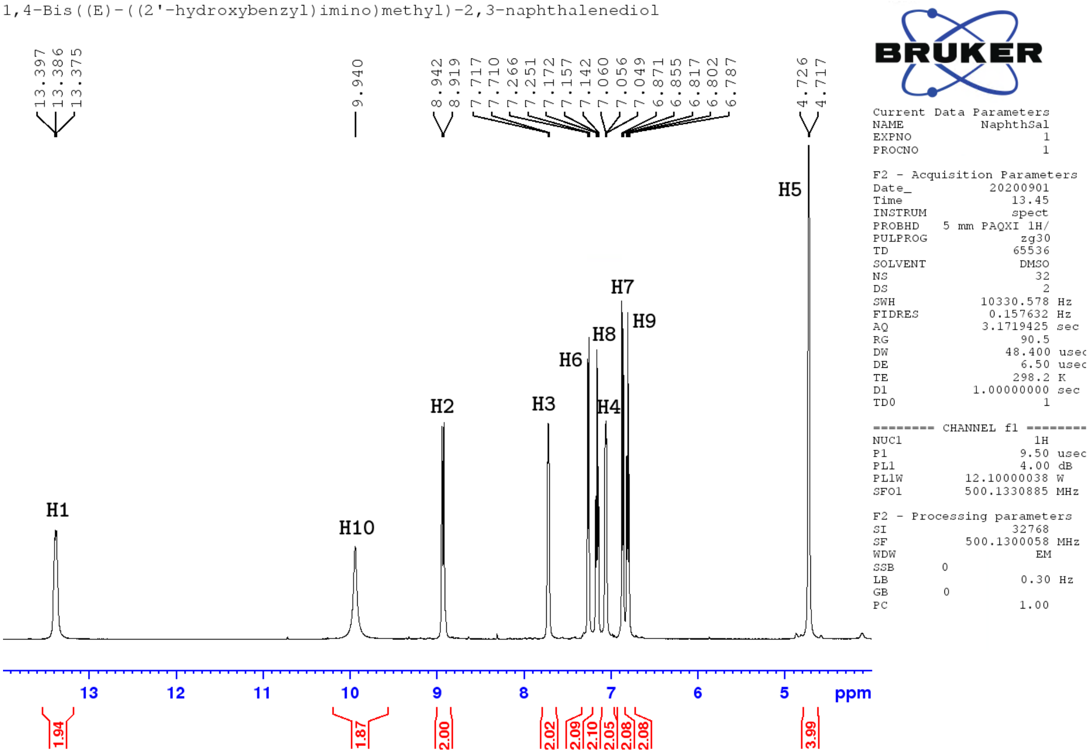

```
Current Data Parameters
NAME             NaphthSal
EXPNO                    1
PROCNO                   1

F2 - Acquisition Parameters
Date_             20200901
Time                 13.45
INSTRUM              spect
PROBHD   5 mm PAQXI 1H/
PULPROG               zg30
TD                   65536
SOLVENT               DMSO
NS                      32
DS                       2
SWH          10330.578 Hz
FIDRES        0.157632 Hz
AQ           3.1719425 sec
RG                    90.5
DW              48.400 usec
DE                6.50 usec
TE               298.2 K
D1          1.00000000 sec
TD0                      1

======== CHANNEL f1 ========
NUC1                    1H
P1                9.50 usec
PL1               4.00 dB
PL1W       12.10000038 W
SFO1       500.1330885 MHz

F2 - Processing parameters
SI                   32768
SF         500.1300058 MHz
WDW                     EM
SSB      0
LB                0.30 Hz
GB       0
PC                1.00
```

1,4-Bis((E)-((2'-hydroxybenzyl)imino)methyl)-2,3-naphthalenediol

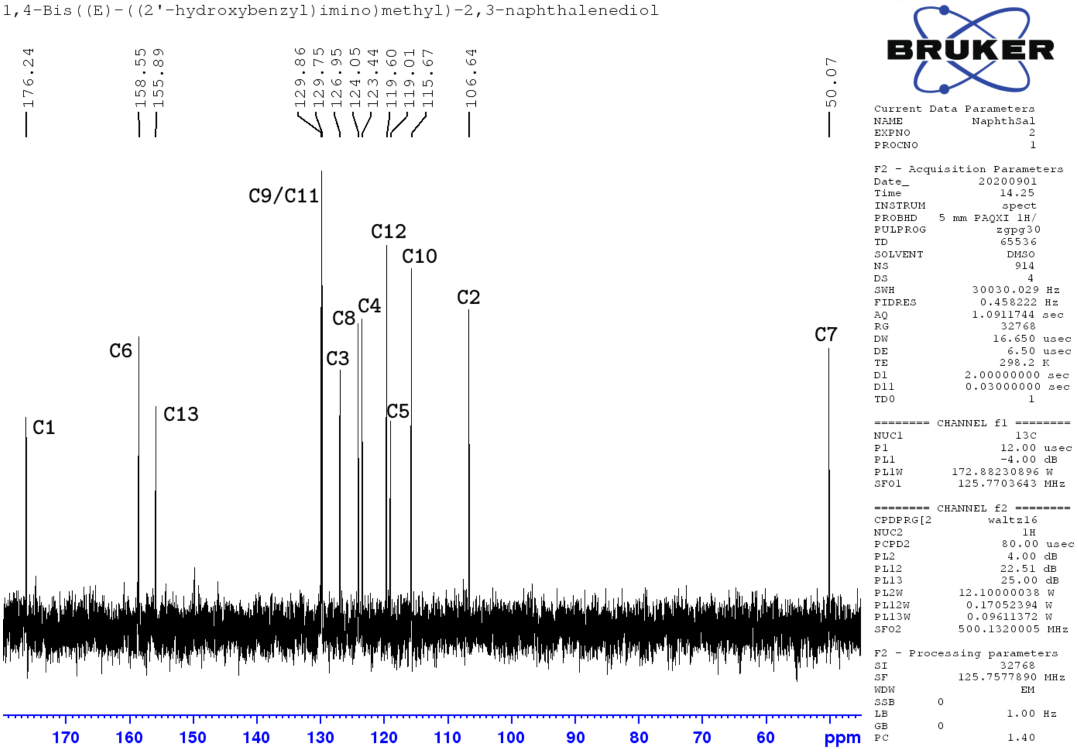

```
Current Data Parameters
NAME             NaphthSal
EXPNO                    2
PROCNO                   1

F2 - Acquisition Parameters
Date_             20200901
Time                 14.25
INSTRUM              spect
PROBHD   5 mm PAQXI 1H/
PULPROG             zgpg30
TD                   65536
SOLVENT               DMSO
NS                     914
DS                       4
SWH          30030.029 Hz
FIDRES        0.458222 Hz
AQ           1.0911744 sec
RG                   32768
DW              16.650 usec
DE                6.50 usec
TE               298.2 K
D1          2.00000000 sec
D11         0.03000000 sec
TD0                      1

======== CHANNEL f1 ========
NUC1                   13C
P1               12.00 usec
PL1              -4.00 dB
PL1W      172.88230896 W
SFO1       125.7703643 MHz

======== CHANNEL f2 ========
CPDPRG[2           waltz16
NUC2                    1H
PCPD2            80.00 usec
PL2               4.00 dB
PL12             22.51 dB
PL13             25.00 dB
PL2W       12.10000038 W
PL12W       0.17052394 W
PL13W       0.09611372 W
SFO2       500.1320005 MHz

F2 - Processing parameters
SI                   32768
SF         125.7577890 MHz
WDW                     EM
SSB      0
LB                1.00 Hz
GB       0
PC                1.40
```

H_2L3

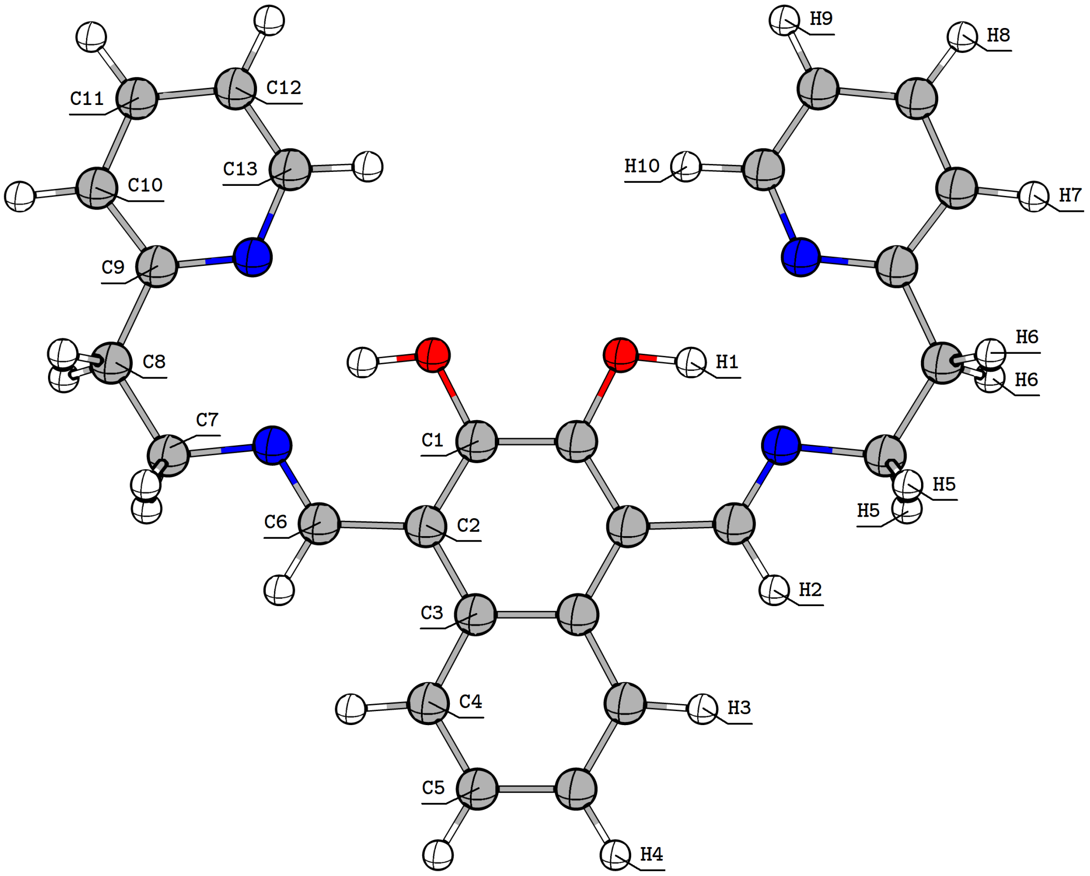

FIGURE B.2: Schematic of H_4L2, labelled for NMR assignment.

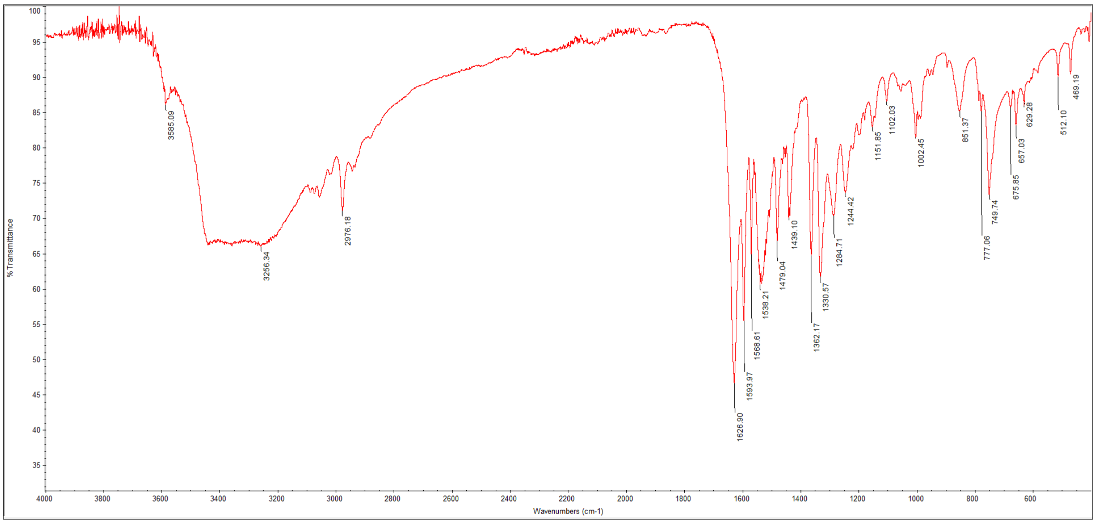

1,4-Bis((E)-((2-(pyridin-2-yl)ethyl)imino_methyl)-2,3-naphthalenediol

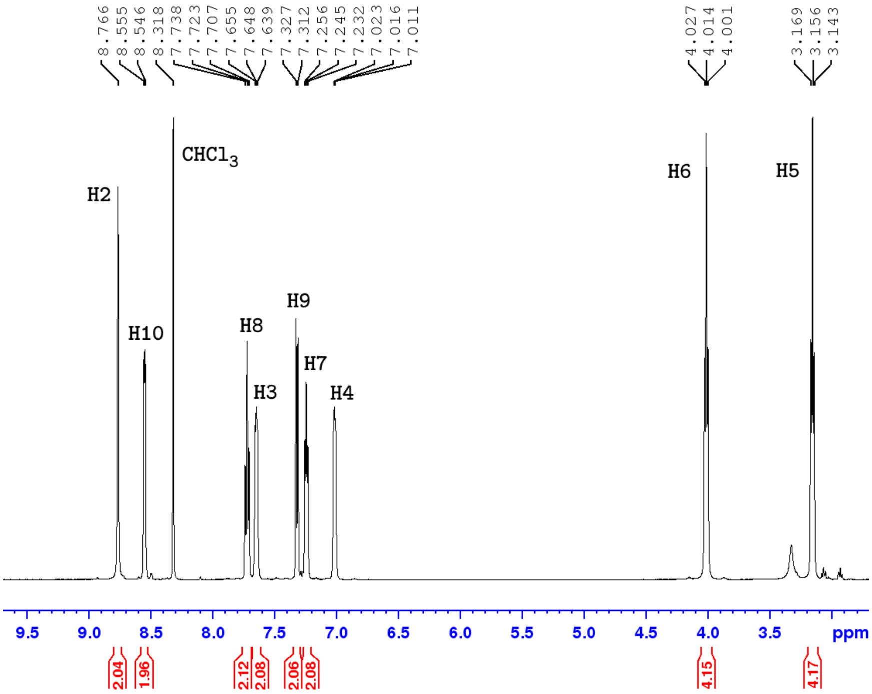

```
Current Data Parameters
NAME          NaphthEtPyr
EXPNO                   3
PROCNO                  1

F2 - Acquisition Parameters
Date_            20220215
Time                17.31
INSTRUM             spect
PROBHD   5 mm PAQXI 1H/
PULPROG              zg30
TD                  65536
SOLVENT              DMSO
NS                     32
DS                      2
SWH            10330.578 Hz
FIDRES          0.157632 Hz
AQ             3.1719425 sec
RG                   90.5
DW                 48.400 usec
DE                   6.50 usec
TE                  298.2 K
D1            1.00000000 sec
TD0                     1

======== CHANNEL f1 ========
NUC1                   1H
P1                   9.50 usec
PL1                  4.00 dB
PL1W          12.10000038 W
SFO1          500.1330885 MHz

F2 - Processing parameters
SI                  32768
SF            500.1300054 MHz
WDW                    EM
SSB      0
LB                   0.30 Hz
GB       0
PC                   1.00
```

1,4-Bis((E)-((2-(pyridin-2-yl)ethyl)imino)methyl)-2,3-naphthalenediol

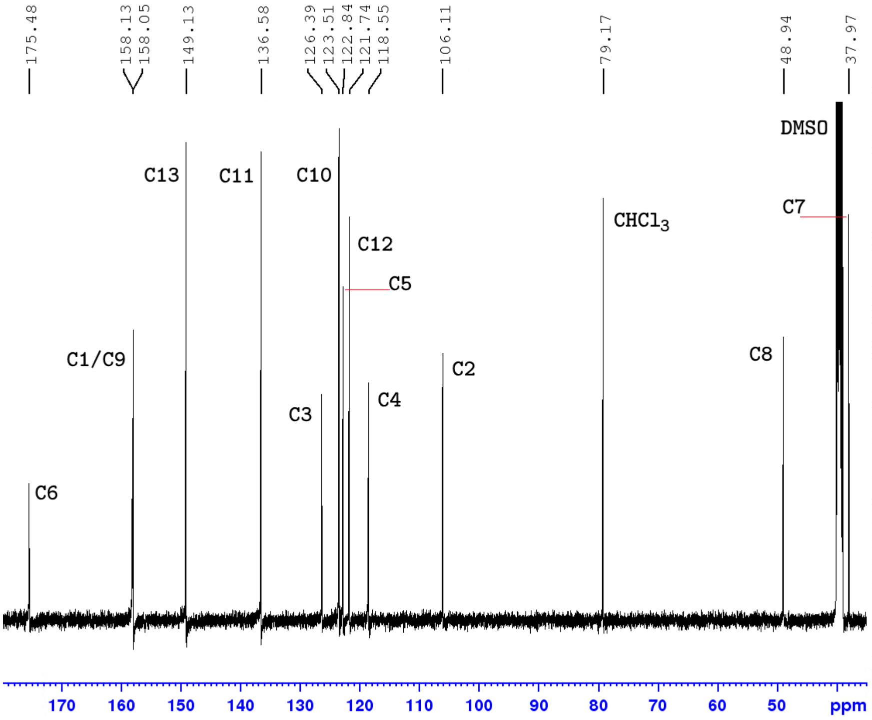

```
Current Data Parameters
NAME          NaphthEtPyr
EXPNO                   4
PROCNO                  1

F2 - Acquisition Parameters
Date_            20220215
Time                21.18
INSTRUM             spect
PROBHD   5 mm PAQXI 1H/
PULPROG            zgpg30
TD                  65536
SOLVENT              DMSO
NS                   4096
DS                      4
SWH            30030.029 Hz
FIDRES          0.458222 Hz
AQ             1.0911744 sec
RG                  32768
DW                 16.650 usec
DE                   6.50 usec
TE                  298.2 K
D1            2.00000000 sec
D11           0.03000000 sec
TD0                     1

======== CHANNEL f1 ========
NUC1                  13C
P1                  12.00 usec
PL1                 -4.00 dB
PL1W         172.88230896 W
SFO1          125.7703643 MHz

======== CHANNEL f2 ========
CPDPRG[2          waltz16
NUC2                   1H
PCPD2               80.00 usec
PL2                  4.00 dB
PL12                22.51 dB
PL13                25.00 dB
PL2W          12.10000038 W
PL12W          0.17052394 W
PL13W          0.09611372 W
SFO2          500.1320005 MHz

F2 - Processing parameters
SI                  32768
SF            125.7578510 MHz
WDW                    EM
SSB      0
LB                   1.00 Hz
GB       0
PC                   1.40
```

aminoSal

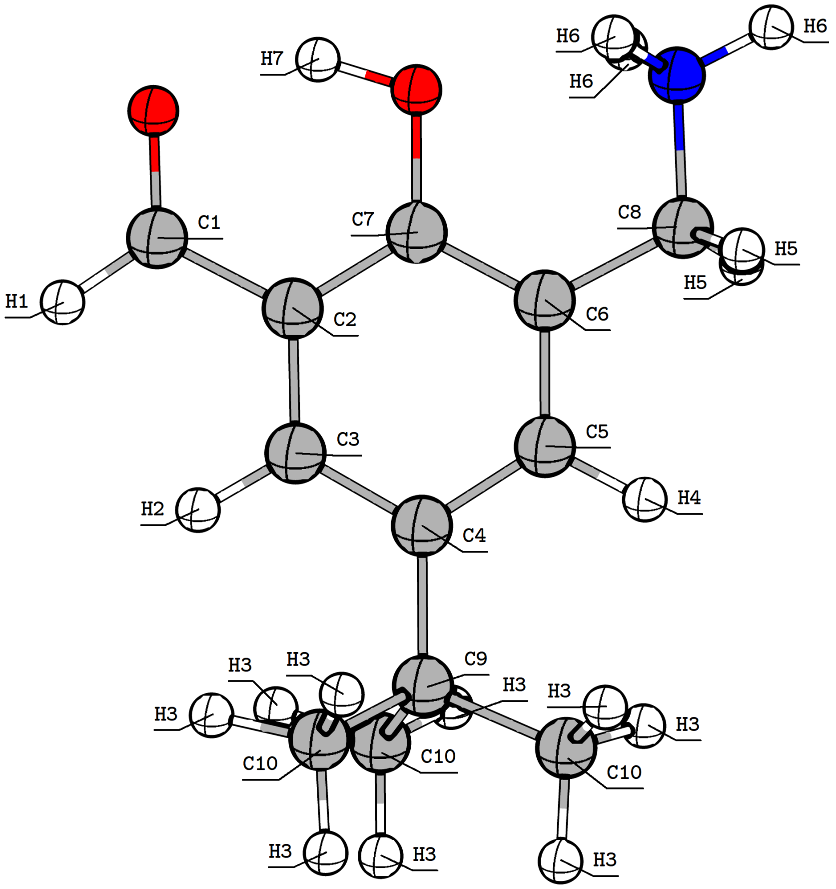

FIGURE B.3: Schematic of **aminoSal**, labelled for NMR assignment.

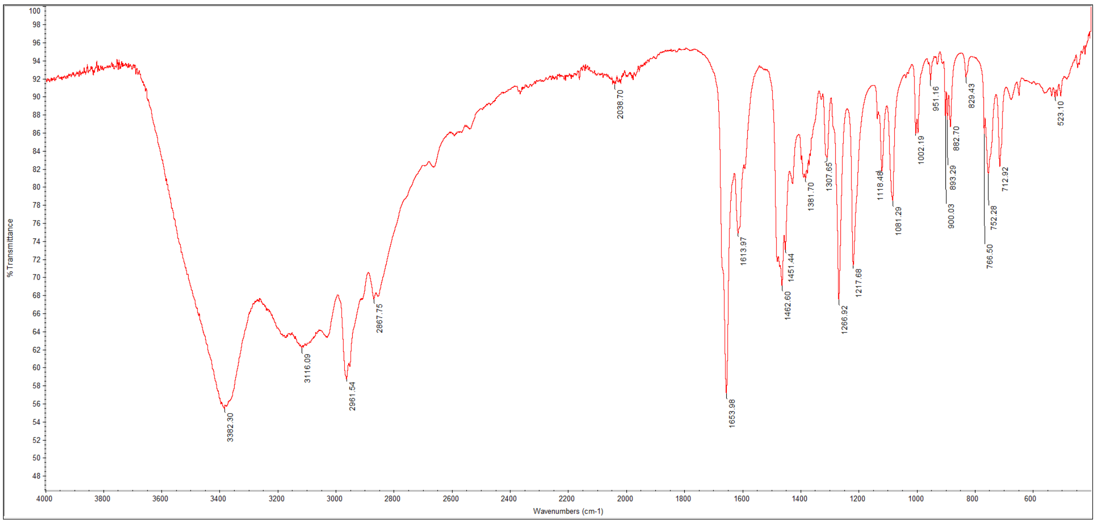

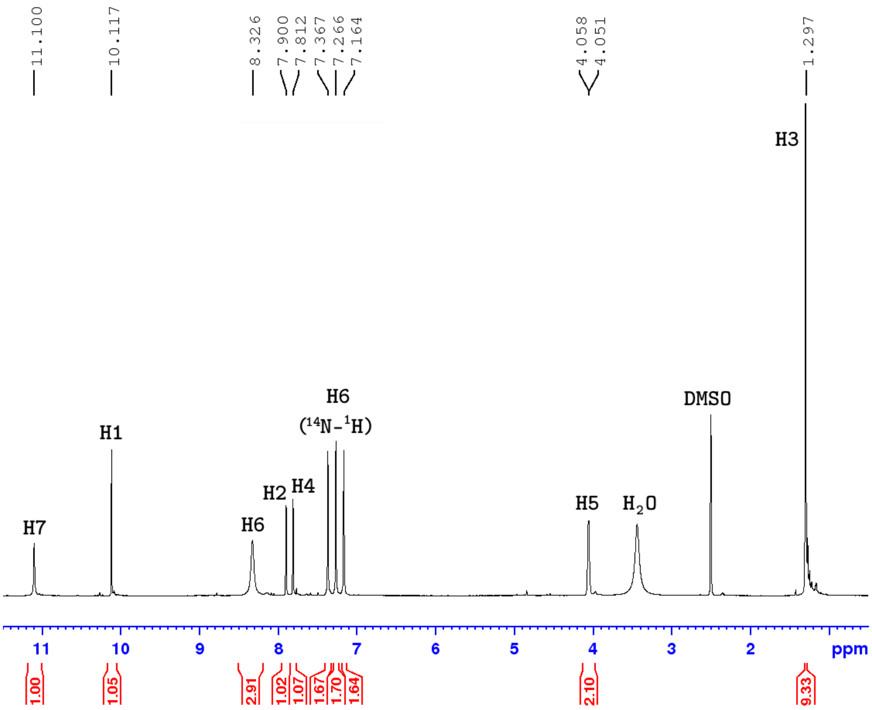

5-t-Bu-3-aminomethyl-2-hydroxybenzaldehyde HCl

```
Current Data Parameters
NAME       TND_SalAlAmHCl
EXPNO                   1
PROCNO                  1

F2 - Acquisition Parameters
Date_            20220201
Time                19.02
INSTRUM             spect
PROBHD    5 mm PAQXI 1H/
PULPROG              zg30
TD                  65536
SOLVENT              DMSO
NS                     16
DS                      2
SWH             10330.578 Hz
FIDRES           0.157632 Hz
AQ              3.1719425 sec
RG                   90.5
DW                 48.400 usec
DE                   6.50 usec
TE                  298.2 K
D1             1.00000000 sec
TD0                     1

======== CHANNEL f1 ========
NUC1                   1H
P1                   9.50 usec
PL1                  4.00 dB
PL1W          12.10000038 W
SFO1          500.1330885 MHz

F2 - Processing parameters
SI                  32768
SF            500.1300054 MHz
WDW                    EM
SSB       0
LB                   0.30 Hz
GB        0
PC                   1.00
```

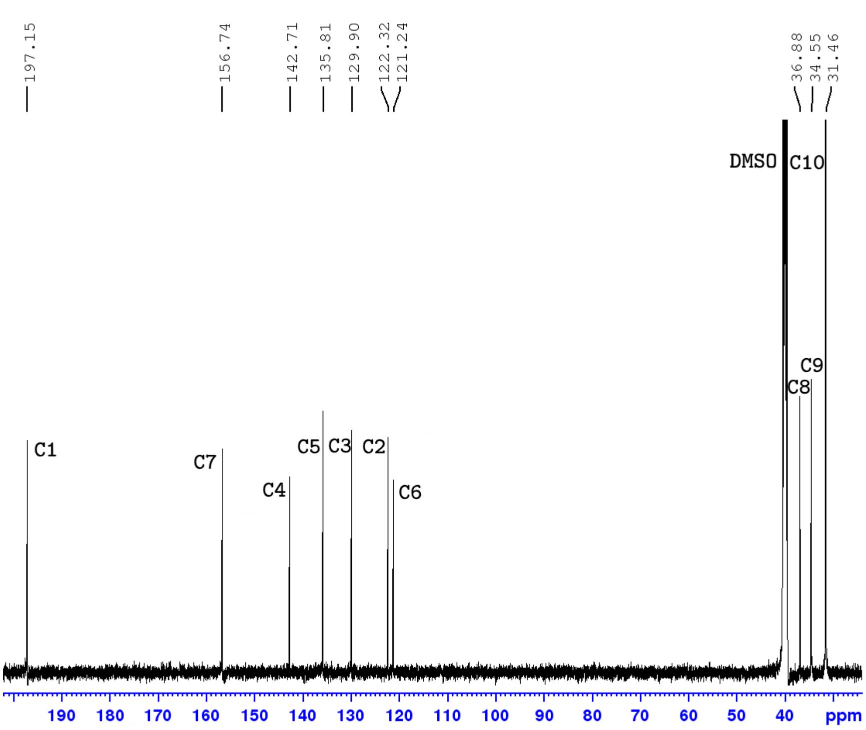

5-t-Bu-3-aminomethyl-2-hydroxybenzaldehyde HCl

```
Current Data Parameters
NAME       TND_SalAlAmHCl
EXPNO                   2
PROCNO                  1

F2 - Acquisition Parameters
Date_            20220201
Time                22.53
INSTRUM             spect
PROBHD    5 mm PAQXI 1H/
PULPROG            zgpg30
TD                  65536
SOLVENT              DMSO
NS                   4096
DS                      4
SWH             30030.029 Hz
FIDRES           0.458222 Hz
AQ              1.0911744 sec
RG                  32768
DW                 16.650 usec
DE                   6.50 usec
TE                  298.2 K
D1             2.00000000 sec
D11            0.03000000 sec
TD0                     1

======== CHANNEL f1 ========
NUC1                  13C
P1                  12.00 usec
PL1                 -4.00 dB
PL1W         172.88230896 W
SFO1          125.7703643 MHz

======== CHANNEL f2 ========
CPDPRG[2          waltz16
NUC2                   1H
PCPD2               80.00 usec
PL2                  4.00 dB
PL12                22.51 dB
PL13                25.00 dB
PL2W          12.10000038 W
PL12W          0.17052394 W
PL13W          0.09611372 W
SFO2          500.1320005 MHz

F2 - Processing parameters
SI                  32768
SF            125.7577890 MHz
WDW                    EM
SSB       0
LB                   1.00 Hz
GB        0
PC                   1.40
```

Selected ATR-IR of Metal Complexes

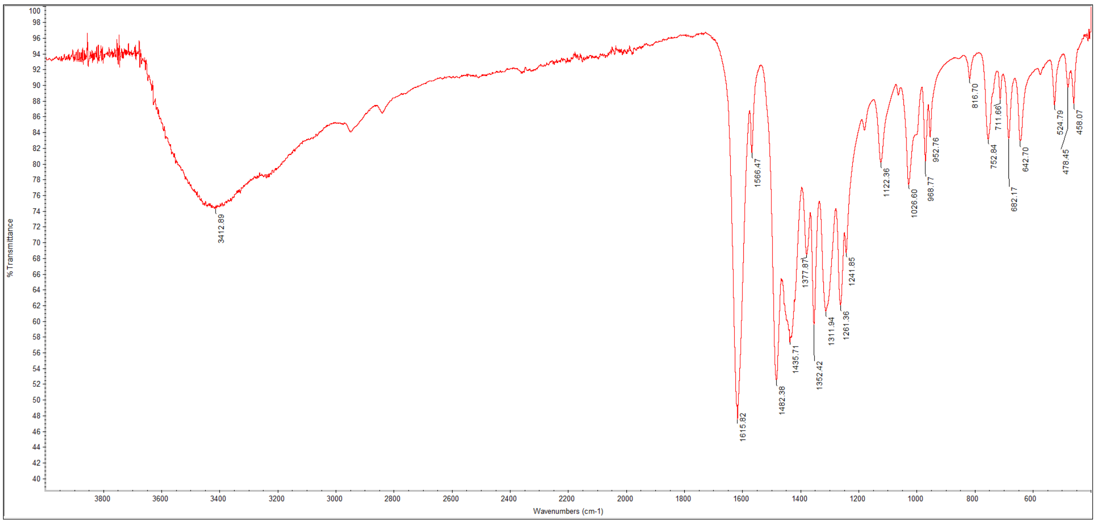

FIGURE B.4: Representative ATR-IR of the M_3Ln complexes.

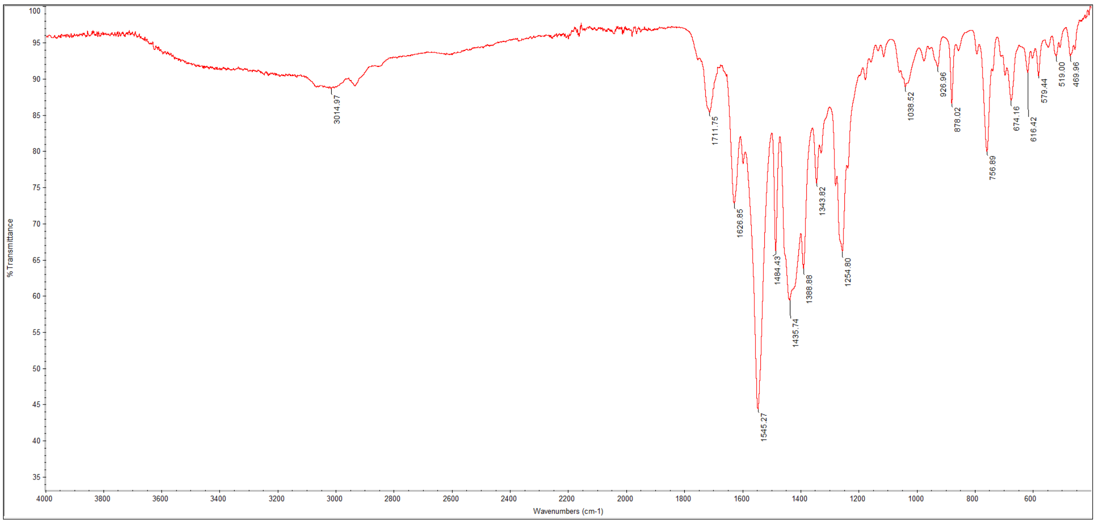

FIGURE B.5: ATR-IR of $[\mathbf{Ni_3Tb}]_n$.

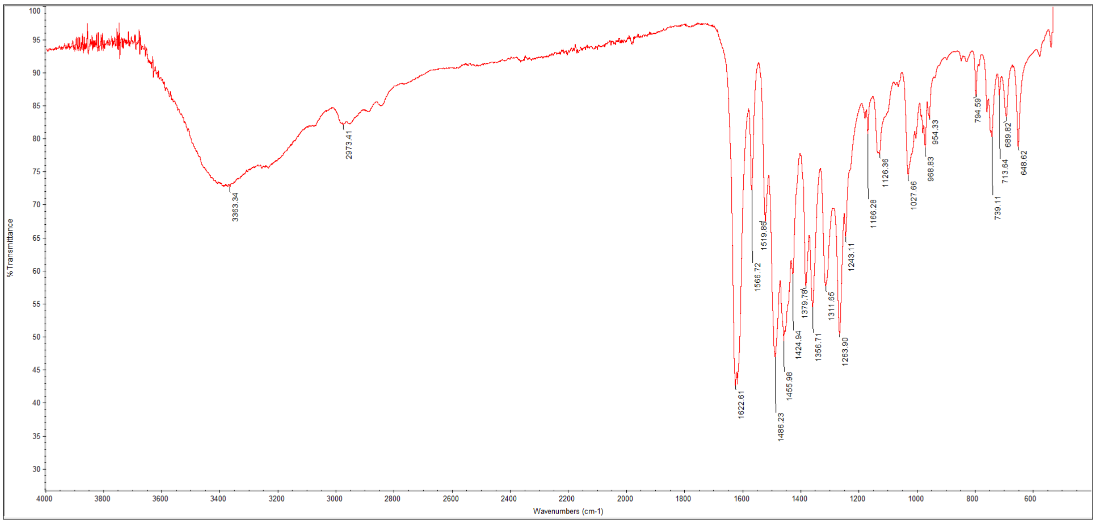

FIGURE B.6: ATR-IR of $\mathbf{[Ni_3Gd]}_{acid}$.

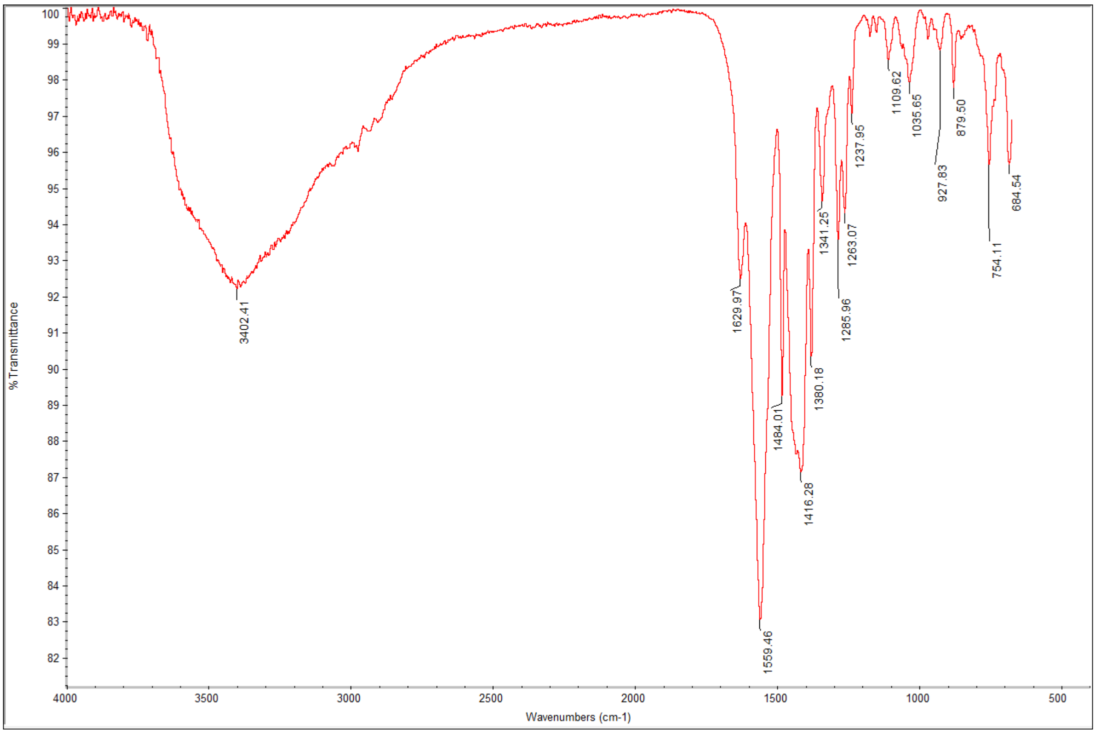

FIGURE B.7: ATR-IR of $\mathbf{Ni_{16}}$.

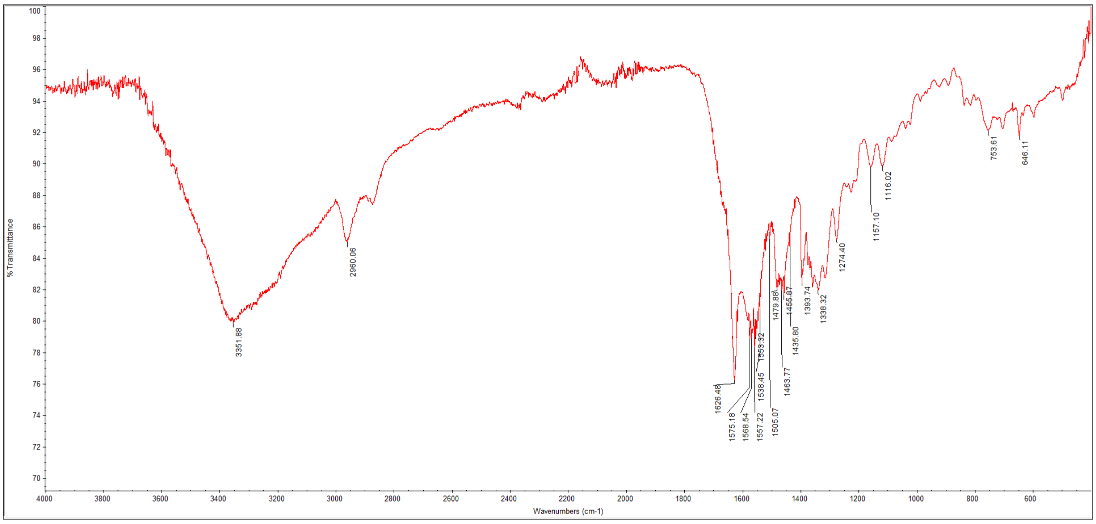

FIGURE B.8: ATR-IR of **Mn$_8$**.

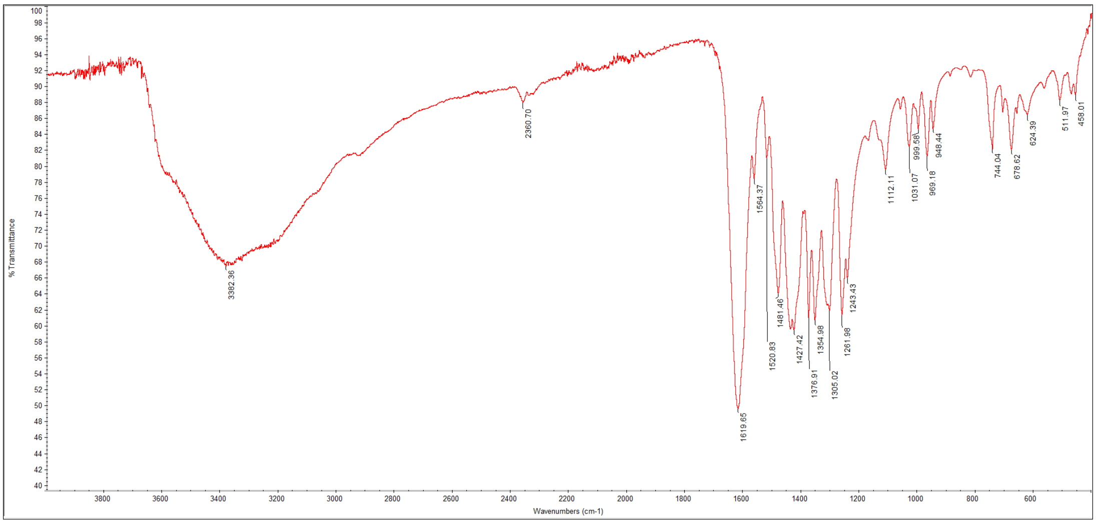

FIGURE B.9: ATR-IR of **MnLa$_6$**.

Appendix C

Miscellaneous Complexes

Synthetic Dribs and Drabs

Preparative notes and basic crystal data for a collection of complexes obtained throughout this PhD which, as yet, have little to no further characterization.

$L1_2Zn(H_2O)_2$

Attempts to produce Zn_3Ln analogues of the triangles reported in this thesis led to the isolation of a mononuclear Zn^{II} species, **$L1_2Zn(H_2O)_2$** (Figure C.1). Bound within the classic salicylaldehyde-like L_2M cavity, and axially coordinated by water molecules, this Zn^{II} complex crystallized in the centrosymmetric monoclinic space group $C2/c$ (Z' = 0.5) as yellow blocks. **$L1_2Zn(H_2O)_2$** was prepared using the general method for M_3Ln triangle complexes.

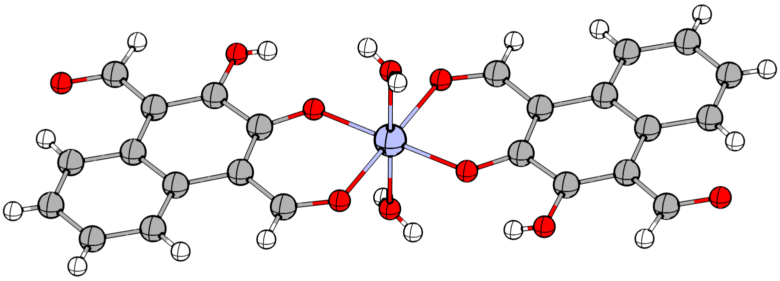

FIGURE C.1: X-ray crystal structure of **$L1_2Zn(H_2O)_2$**. C = grey, O = red, Zn = pale purple.

Crystal Data for $C_{24}H_{18}O_{10}Zn$ (M = 531.75 g mol^{-1}): monoclinic, space group $C2/c$ (no. 15), a = 19.8859(8) Å, b = 4.9509(2) Å, c = 22.2461(9) Å, β = 113.156(2)°, V = 2013.75(14) Å^3, Z = 4, T = 100.0 K, $\mu(\mathrm{CuK}_\alpha)$ = 2.284 mm^{-1}, D_{calc} = 1.754 g cm^{-3} 22952 reflections measured ($8.646° \leq 2\Theta \leq 136.468°$), 1829 unique ($R_{int}$ = 0.0493, R_{sigma} = 0.0233) which were used in all calculations. The final R_1 was 0.0329 ($I > 2\sigma(I)$) and wR_2 was 0.0942 (all data).

$\mathbf{L2_2Co_4(OTf)_3(OH)(H_2O)(MeOH)_2 \cdot 2\,Et_2O}$

The complex $\mathbf{L2_2Co_4(OTf)_3(OH)(H_2O)(MeOH)_2 \cdot 2\,Et_2O}$ (Figure C.2) was obtained as purple plates, which crystallized in the monoclinic space group $P2_1/n$ ($Z' = 1$), during attempts to produce a Co^{II} analogue to $\mathbf{Ni_{16}}$. Asymmetrically bound within two $\mathbf{H_2L2}$ ligands, there are four Co^{II} centres, with the ligands exhibiting a 3.012201 binding mode. One Co^{II} is bound within the centre of each catechol group with another in the ONO pocket and the third bridged by the phenol side-arms, resulting in a fragment of the complex which resembles the ligand-metal binding of $\mathbf{Ni_{16}}$. A μ_3-OH anion bridges the periphery metals, providing the fourth equatorial donor to each metal bound within the ONO pocket. The final equatorial site of the phenol bridged Co^{II} is provided by a water molecule, each metal centre is then axially coordinated by either a methanol molecule or a triflate anion, with one non-coordinated triflate and two diethyl ether solvates in the lattice, resulting in exclusively 5-coordinate square pyramidal Co^{II} centres. This complex was prepared at a reduced scale based on the preparation of $\mathbf{Ni_{16}}$ (see the end of Chapter 6), the triflate salt was used in this preparation as the acetate salt did not show signs of successful reaction.

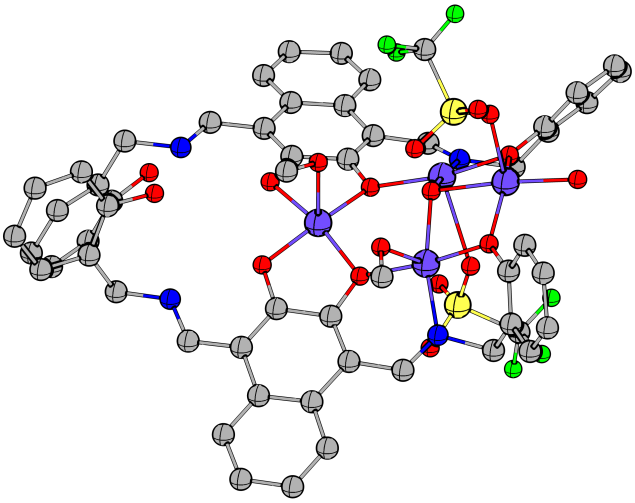

FIGURE C.2: X-ray crystal structure of $\mathbf{L2_2Co_4(OTf)_3(OH)(H_2O)(MeOH)_2 \cdot 2\,Et_2O}$. Non-coordinated species and hydrogen atoms omitted for clarity. C = grey, Co = purple, F = bright green, N = blue, O = red, S = yellow.

Crystal Data for $C_{65}H_{71}Co_4F_9N_4O_{23}S_3$ (M = 1779.15 g mol^{-1}): monoclinic, space group $P2_1/n$ (no. 14), $a = 18.901(3)$ Å, $b = 14.695(3)$ Å, $c = 28.391(5)$ Å, $\beta = 98.360(7)°$, V = 7802(2) Å^3, $Z = 4$, T = 100 K, $\mu(CuK_\alpha) = 8.130$ mm^{-1}, $D_{calc} = 1.515$ g cm^{-3} 143390 reflections measured ($5.282° \leq 2\Theta \leq 147.266°$), 15478 unique ($R_{int} = 0.1726$, $R_{sigma} = 0.1211$) which were used in all calculations. The final R_1 was 0.0896 ($I > 2\sigma(I)$) and wR_2 was 0.2987 (all data).

$\mathbf{L2_2Mn^{II}{}_2Mn^{III}{}_2(OAc)_2(MeOH)_6 \cdot 2\,MeOH}$

Attempts were made to produce a manganese based **$\mathbf{Ni_{16}}$** analogue, however the complex **$\mathbf{L2_2Mn^{II}{}_2Mn^{III}{}_2(OAc)_2(MeOH)_6 \cdot 2\,MeOH}$** (Figure C.3) was obtained as dark red, almost black, block crystals for all ligand:metal stoichiometries from 1:1 to 1:8, which crystallized in the monoclinic space group $C2/c$ ($Z' = 1$). This mixed valence manganese complex is analogous to a complex reported by Brooker *et al.*[86]

$\mathbf{L2_2Mn^{II}{}_2Mn^{III}{}_2(OAc)_2(MeOH)_6 \cdot 2\,MeOH}$ forms with two inner 7-coordinate Mn^{II} centres and two outer 6-coordinate Mn^{III} centres; symmetrically bound by a catechol group of one ligand and an ONO pocket of the second ligand, giving 5 equatorial donors, or the ONO pocket of one ligand and a phenol side-arm from the second ligand, respectively. Each Mn^{II} centre is axially coordinated by a μ_1, η_1-OAc anion and a methanol molecule, with the MnIII centres having their coordination sphere filled by a methanol donor on either side of the ligand plane. This complex was prepared following the general method for **$\mathbf{Ni_{16}}$**. It should be noted that while refluxing is not necessary for this complex, crystal formation was observed to be faster when the reaction was refluxed for a minimum of 3 days. This preparation can also be carried out with $Mn(NO_3)_2 \cdot 6\,H_2O$ to produce the nitrate analogue which features μ_1, η_1-NO_3 anions in place of the acetates, but is otherwise isostructural.

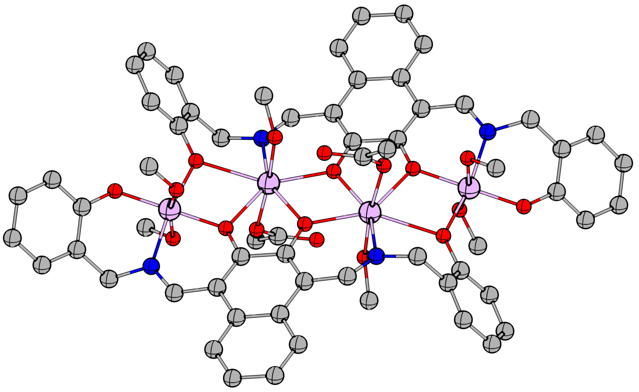

FIGURE C.3: X-ray crystal structure of **$\mathbf{L2_2Mn^{II}{}_2Mn^{III}{}_2(OAc)_2(MeOH)_6 \cdot 2\,MeOH}$**. Non-coordinated species and hydrogen atoms omitted for clarity. C = grey, Mn = light purple, N = blue, O = red.

Crystal Data for $C_{64}H_{74}Mn_4N_4O_{20}$ (M = 1439.03 g mol^{-1}): monoclinic, space group $C2/c$ (no. 15), a = 41.799(2) Å, b = 14.5983(8) Å, c = 25.1333(14) Å, β = 121.667(2)°, V = 13052.9(13) Å^3, Z = 8, T = 173.0 K, $\mu(\mathrm{CuK}_\alpha)$ = 6.801 mm^{-1}, D_{calc} = 1.465 g cm^{-3} 97491 reflections measured ($4.968° \leq 2\Theta \leq 130.164°$), 10612 unique ($R_{int}$ = 0.0781, R_{sigma} = 0.0540) which were used in all calculations. The final R_1 was 0.0567 ($I > 2\sigma(I)$) and wR_2 was 0.1246 (all data).

$[\mathbf{L2Zn_4(OAc)_4 \cdot 0.5H_2O \cdot 0.5DMF}]_n$

Synthetic efforts to produce a Zn^{II} analogue of **Ni$_{16}$** were similarly unsuccessful. The 1D polymer, $[\mathbf{L2Zn_4(OAc)_4 \cdot 0.5H_2O \cdot 0.5DMF}]_n$ (Figure C.4), was isolated as yellow blocks which crystallized in the triclinic space group $P\bar{1}$ ($Z' = 2$). This complex exhibits the same 5.222211 binding pattern seen in **Ni$_{16}$**, however, the mixture of 4- and 5-coordinate Zn^{II} centres doesn't allow for the nearly right-angled link between **L2**Zn_4 moieties necessary to make a wheel-shaped complex. Following the method for preparing **Ni$_{16}$**, this complex formed regardless of reaction temperature or time.

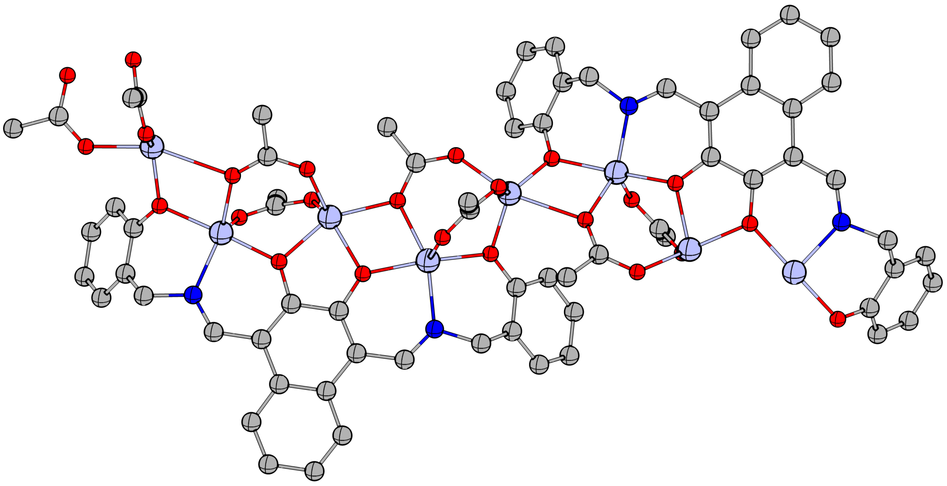

FIGURE C.4: X-ray crystal structure of the $[\mathbf{L2Zn_4(OAc)_4 \cdot 0.5H_2O \cdot 0.5DMF}]_n$ monomeric unit. Non-coordinated species and hydrogen atoms omitted for clarity. C = grey, N = blue, O = red, Zn = pale purple.

Crystal Data for $C_{35} \cdot 5\,H_{34} \cdot 5\,N_2 \cdot 5\,O_{13}Zn_4$ (M = 965.63 g mol^{-1}): triclinic, space group $P\bar{1}$ (no. 2), a = 13.9742(4) Å, b = 16.6949(5) Å, c = 17.3981(6) Å, α = 85.015(2)°, β = 80.164(2)°, γ = 86.080(2)°, V = 3978.2(2) Å^3, Z = 4, T = 100.0 K, μ(CuK$_\alpha$) = 3.294 mm^{-1}, D$_{\text{calc}}$ = 1.612 g cm^{-3} 75978 reflections measured (5.17° $\leq$ 2Θ $\leq$ 152.184°), 15408 unique (R_{int} = 0.0806, R_{sigma} = 0.0789) which were used in all calculations. The final R_1 was 0.0575 ($I > 2\sigma(I)$) and wR_2 was 0.1533 (all data).

$\mathbf{L3_2Ni_5F_4(H_2O)_4(MeOH)_2 \cdot 2\,BF_4}$

Replacement of the phenol side-arm of $\mathbf{H_4L2}$ with a pyridyl group (as in $\mathbf{H_2L3}$) was explored in an effort to provide a different ligand field for potential $\mathbf{Ni_{16}}$ analogues. The pentanuclear complex $\mathbf{L3_2Ni_5F_4(H_2O)_4(MeOH)_2 \cdot 2\,BF_4}$ (Figure C.5) was obtained from the 5:2 reaction of $Ni(BF_4)_2 \cdot 6\,H_2O$ and $\mathbf{H_2L3}$ in refluxing methanol. Vapour diffusion of diethyl ether into a concentrated methanolic solution of the complex yielded yellow block crystals, in the monoclinic space group $C2$ ($Z' = 1$). A Ni^{II} is centrally bound between the two catechol units, like in the $\mathbf{L2_2Co_4(OTf)_3(OH)(H_2O)(MeOH)_2 \cdot 2\,Et_2O}$ complex, and is axially capped either side of the ligand plane by water molecules. Each of the four ONO pockets bind a Ni^{II} centre, which are symmetrically bridged by two μ_2-F anions, which have been assigned as such on the basis of low-res mass spec. The charge of the complex is balanced by two non-coordinated BF_4 anions, which is also the proposed fluoride source for the μ_2-F bridges.

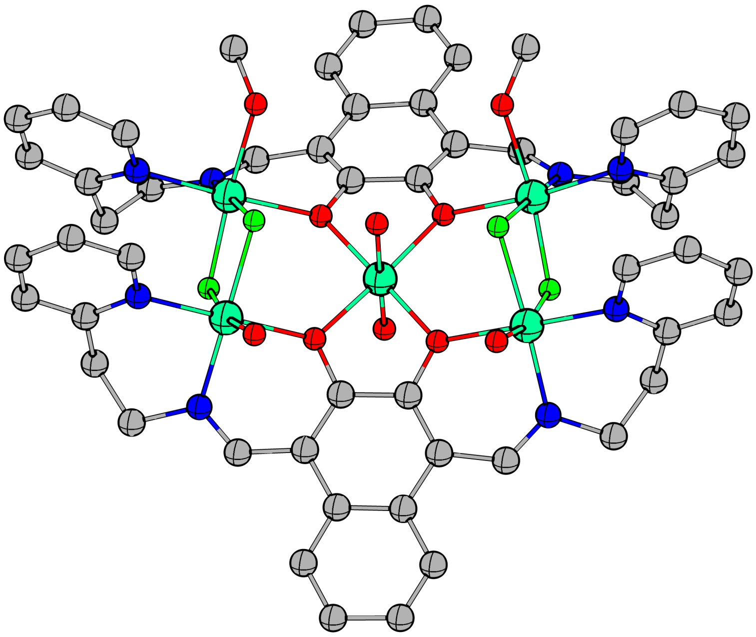

FIGURE C.5: X-ray crystal structure of $\mathbf{L3_2Ni_5F_4(H_2O)_4(MeOH)_2 \cdot 2\,BF_4}$. Non-coordinated species and hydrogen atoms omitted for clarity. C = grey, F = bright green, N = blue, Ni = pale green, O = red.

Crystal Data for $C_{54}H_{72}B_2F_{12}N_8Ni_5O_{16} \cdot 5$ (M = 1640.36 g mol^{-1}): monoclinic, space group $C2$ (no. 5), a = 31.5982(13) Å, b = 17.9409(7) Å, c = 17.3121(7) Å, β = 122.341(2)°, V = 8291.8(6) Å^3, Z = 4, T = 100.0 K, $\mu(CuK_\alpha)$ = 1.986 mm^{-1}, D_{calc} = 1.314 g cm^{-3} 203951 reflections measured ($6.042° \leq 2\Theta \leq 152.442°$), 15656 unique ($R_{int}$ = 0.0359, R_{sigma} = 0.0171) which were used in all calculations. The final R_1 was 0.0466 ($I > 2\sigma(I)$) and wR_2 was 0.1427 (all data).

$\mathbf{Cu_{12}}$

Formally called $\mathbf{Cu_{12}}$, reproducibility has been a struggle with this complex. Initially prepared by the 1:1:4 reaction of **aminoSal** with $Cu(ClO_4)_2 \cdot 6\,H_2O$ and KOH in refluxing 3:2 MeOH:water, the $\mathbf{Cu_{12}}$ complex indicated a potential impurity by means of the **aminoSal** ligand containing some traces of the bromide salt. The green-brown solid obtained upon drying was dissolved in acetonitrile to give a bright green solution, which formed large green block crystals when vapour diffused with diethyl ether. The samples were observed to rapidly desolvate and crumble upon removing from solution, and of those that survived transferring to oil, very few crystals proved of sufficient quality for single-crystal X-ray diffraction, with even the best data set obtained having less than desirable refinement statistics. With the generous input of Horst Puschmann and Oleg Dolomanov, a crystal structure solution was found in the monoclinic space group $P2_1/c$ with $Z' = 1$ (Figure C.6).

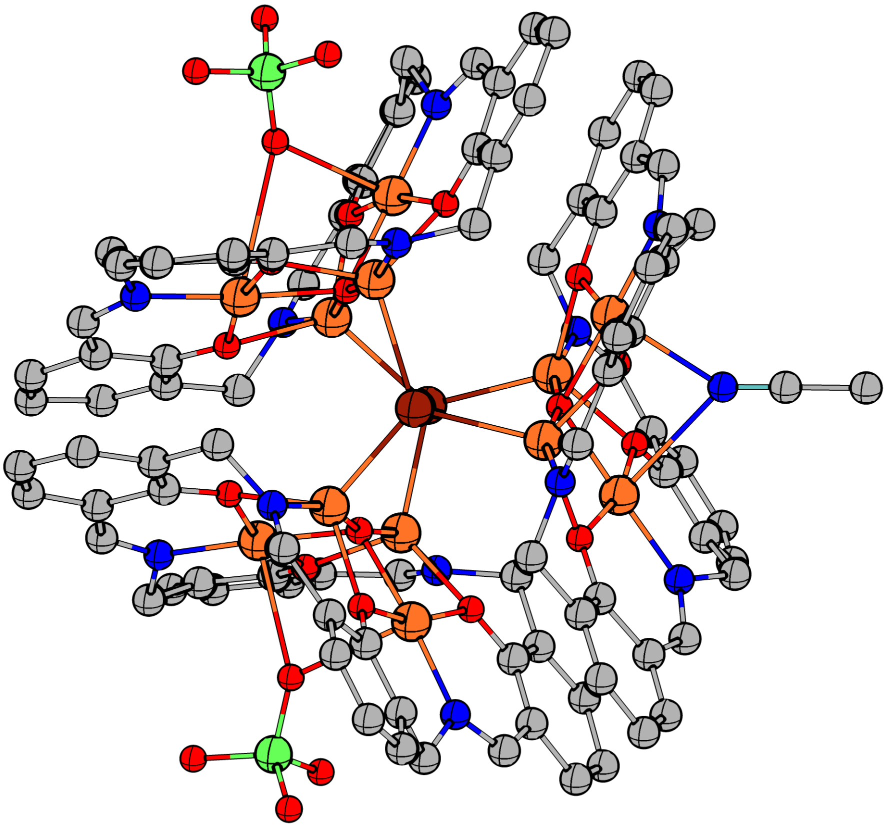

FIGURE C.6: X-ray crystal structure of $\mathbf{Cu_{12}}$. Non-coordinated species and hydrogen atoms omitted for clarity. Br = reddish-brown, C = grey, Cl = green, Cu = orange, N = blue, O = red.

Formulated as $[(\mathbf{L^4}Cu_4(\mu_4\text{-}O))_3(\mu_3\text{-}Br)_2]\cdot 4ClO_4\cdot 4MeCN$, where $\mathbf{L^4}$ is the tetrameric self-condensation product of four units of **aminoSal** which each bind four Cu^{II} centres within each ONO pocket. A μ_4-O^{-2} species is believed to bridge each copper ion within its respective ligand in a see-saw like geometry, with three of these tetrameric $\mathbf{L^4}Cu_4$ units (Figure C.7) folding slightly and coming together as a trimer bound by two μ_3-bromide anions bridging what are effectively the two *trans*-Cu^{II} centres along the 'folding-line' of the tetrameric units. Charge balance is afforded by two non-coordinated and two weakly coordinated perchlorate anions, with one weakly coordinated MeCN molecule identified and three other MeCN solvates which where stable to refinement. Although the data quality is poor, it was suggested by Horst and Oleg that the copper ions bridged by the bromide groups do not have 100% occupancy, but are rather five metals across six sites. The presence of bromine was confirmed by energy-dispersive X-ray spectroscopy. Unfortunately no sense could be made from the CHN microanalytical data.

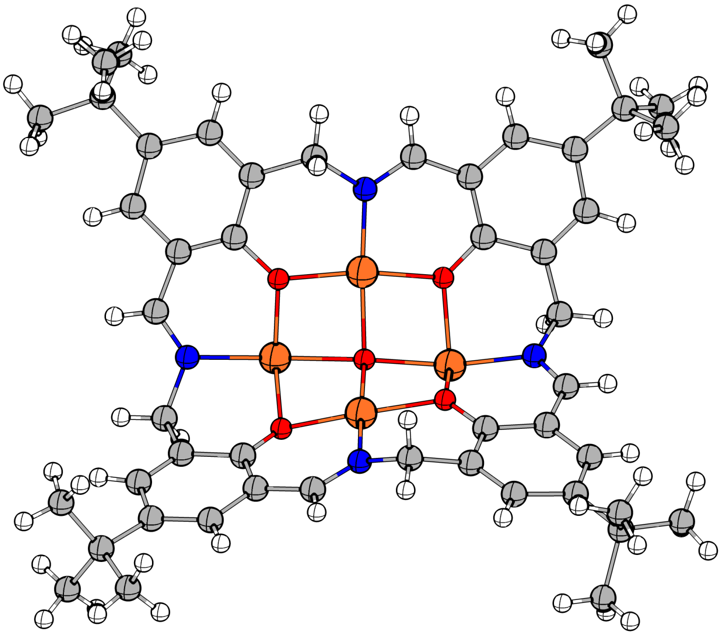

FIGURE C.7: Reduced X-ray crystal structure showing just one tetrameric unit of **Cu_{12}**. C = grey, Cu = orange, N = blue, O = red.

Crystal Data for $C_{152}H_{180}Br_2Cl_4Cu_{11}N_{16}O_{31}$ (M = 3727.67 g mol^{-1}): monoclinic, space group $P2_1/c$ (no. 14), a = 33.494(2) Å, b = 27.0856(18) Å, c = 20.0569(14) Å, β = 104.049(4)°, V = 17651(2) Å^3, Z = 4, T = 100.0 K, $\mu(CuK_\alpha)$ = 3.053 mm^{-1}, D_{calc} = 1.403 g cm^{-3}, 429619 reflections measured ($2.72° \leq 2\Theta \leq 136.488°$), 31915 unique ($R_{int}$ = 0.0714, R_{sigma} = 0.0348) which were used in all calculations. The final R_1 was 0.1738 ($I > 2\sigma(I)$) and wR_2 was 0.4839 (all data).

$[\mathbf{L^*_2Cu_2Br \cdot Br \cdot 2\,MeCN}]_n$

Given the evidence of a potential bromide impurity in **aminoSal**, the ligand was intentionally prepared as the HBr salt by using HBr in place of HCl in the cleavage of **hexamineSal** to **aminoSal**. However, attempts to prepare **Cu_{12}** in bulk using the bromide salt of **aminoSal** culminated in the unexpected isolation of **$[L^*_2Cu_2Br \cdot Br \cdot 2\,MeCN]_n$** (Figure C.8), where **L*** is 2-(aminomethyl)-4-(*tert*-butyl)-6-(iminomethyl)phenol. Appearing as green blocks which crystallized in the monoclinic space group $P2_1/c$ (Z' = 1). X-ray diffraction experiments revealed the sample to be a 1D polymer, containing the rarely seen primary imine (with just 29 hits for a search based on two 2-(iminomethyl)phenolates binding a metal within the N_2O_2 pocket). The presence of bromide anions remained, with two required to balance the overall charge of a monomeric unit of **$[L^*_2Cu_2Br \cdot Br \cdot 2\,MeCN]_n$**. One bromide remains uncoordinated, while the other axially coordinates to the amine bound Cu^{II} centre and acts to bridge it to the imine bound Cu^{II} centre of the next unit in the polymer.

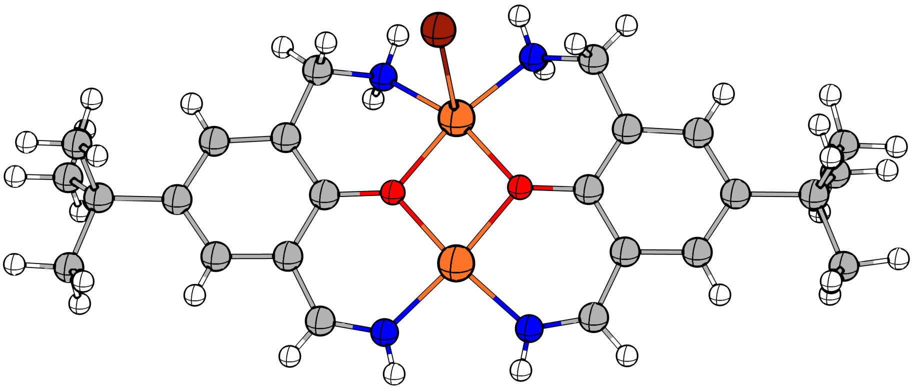

FIGURE C.8: X-ray crystal structure showing the asymmetric unit of **$[L^*_2Cu_2Br \cdot Br \cdot 2\,MeCN]_n$**. Non-coordinated species omitted for clarity. Br = reddish-brown, C = grey, Cu = orange, N = blue, O = red.

Crystal Data for $C_{28}H_{40}Br_2Cu_2N_6O_2$ (M = 779.56 g mol^{-1}): monoclinic, space group $P2_1/c$ (no. 14), a = 17.8293(13) Å, b = 20.7376(15) Å, c = 8.8396(6) Å, β = 102.187(2)°, V = 3194.7(4) Å^3, Z = 4, T = 100.0 K, $\mu(\mathrm{CuK}_\alpha)$ = 4.849 mm^{-1}, D$_{\mathrm{calc}}$ = 1.621 g cm^{-3} 64734 reflections measured (6.624° $\leq 2\Theta \leq$ 152.272°), 6187 unique (R_{int} = 0.0469, R_{sigma} = 0.0247) which were used in all calculations. The final R_1 was 0.0373 ($I > 2\sigma(I)$) and wR_2 was 0.1022 (all data).

The Ligands H_3SalAl^{Pr} and H_5SalOx^{Pr}

During the early stages of this PhD, the target ligand systems involved bridged salicylaldehyde derivatives using 2-hydroxy-3-(bromomethyl)-5-(*tert*-butyl)benzaldehyde (BrSal) as a starting point. The idea was to design amine or alcohol terminated bridging units, with additional donors near the centre of the bridge, such that they could undergo direct *N*-alkylation or Williamson ether formation with BrSal, resulting in a double headed aldehyde ligand. These dialdehyde ligands could then undergo Schiff base condensation or oximation to further functionalize them, with the intention of producing different types of binding pockets to better promote the formation of heterometallic 3*d*-4*f* complexes.

The dialdehyde ligand, **H_3SalAl^{Pr}**, was prepared by base-mediated direct *N*-alkylation of 1,3-bis(methylamino)propan-2-ol with BrSal, adapted from a method by Schröder *et al.*[169] commonly used by the Plieger group.[121–124] The dioxime ligand, **H_5SalOx^{Pr}**, was prepared by oximation of **H_3SalAl^{Pr}** using another method well known to the Plieger group.[121–124]

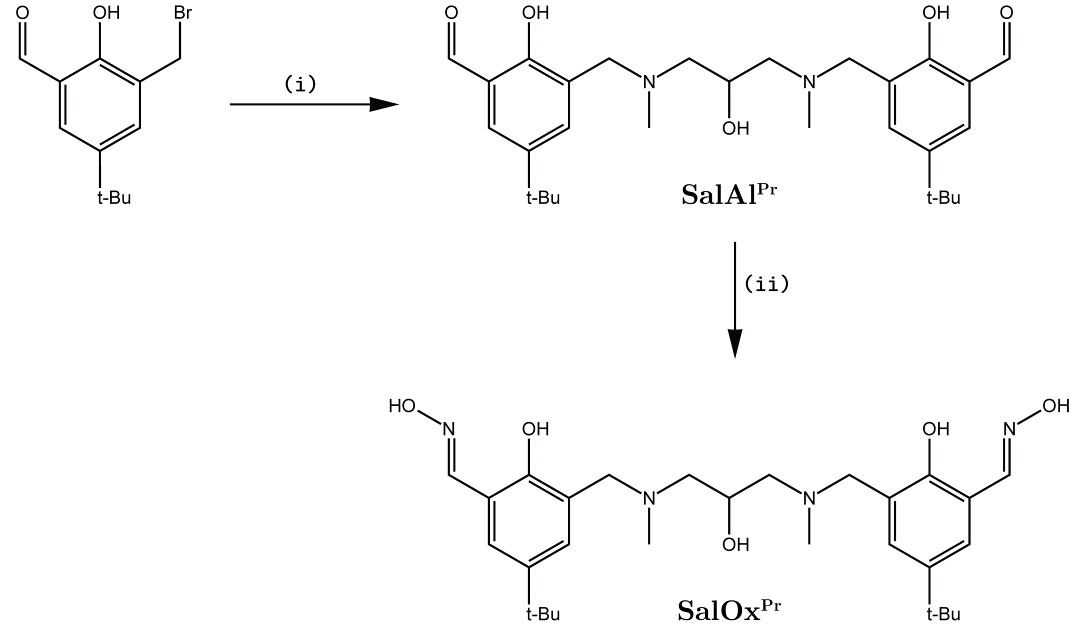

FIGURE C.9: Basic reaction scheme for the preparation of **H_3SalAl^{Pr}** and **H_5SalOx^{Pr}**. (i) 0.5 eq. 1,3-bis(methylamino)propan-2-ol, 2 eq. Et_3N, $CHCl_3$, 24 hr, RT. (ii) 2.5 eq $NH_2OH \cdot HCl$, 2.5 eq. NaOH, EtOH, 48 hr, RT.

$\mathbf{SalAl^{Pr}{}_2Cu_4(OAc)_2(1,4\text{–}dioxane)\cdot 2\,MeOH}$

The complex **$\mathbf{SalAl^{Pr}{}_2Cu_4(OAc)_2(1,4\text{–}dioxane)\cdot 2\,MeOH}$** (Figure C.10) was obtained by the 1:2 reaction of **$\mathbf{H_3SalAl^{Pr}}$** with $Cu(OAc)_2 \cdot H_2O$ in hot methanol. After drying, the brown solids were dissolved in a minimum amount of 1:1 MeOH:1,4-dioxane, and vapour diffused with diethyl ether to yield blue rectangular prisms. Crystallizing in the orthorhombic space group *Pbcn*, with only half of the complex in the asymmetric unit. Each Cu^{II} centre is 5-coordinate square pyramidal, and is bound within an ONO pocket with an acetate bridging the two Cu^{II} centres bound within the same ligand. One of the two coppers in the asymmetric unit has an axially capping 1,4-dioxane molecule, while the other is coordinated by an unbound aldehyde group from the second ligand in the complex, making a 12-membered $Cu_2O_4C_6$ binding ring.

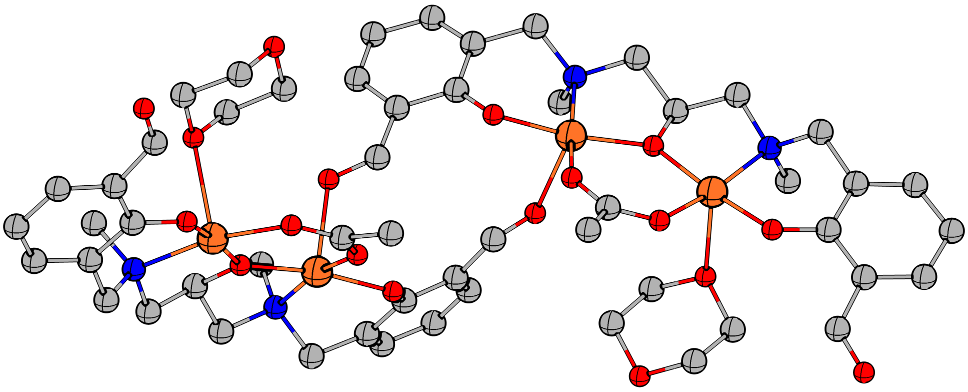

FIGURE C.10: X-ray crystal structure of **$\mathbf{SalAl^{Pr}{}_2Cu_4(OAc)_2(1,4\text{–}dioxane)\cdot 2\,MeOH}$**. Non-coordinated species, hydrogen atoms, and *tert*-butyl groups omitted for clarity. C = grey, Cu = orange, N = blue, O = red.

Crystal Data for $C_{72}H_{108}Cu_4N_4O_{20}$ (M = 1603.78 g mol^{-1}): orthorhombic, space group *Pbcn* (no. 60), a = 26.3922(19) Å, b = 16.7768(7) Å, c = 20.2987(8) Å, V = 8987.8(8) Å^3, Z = 4, T = 100 K, $\mu(\mathrm{CuK}_\alpha)$ = 1.566 mm^{-1}, D_{calc} = 1.185 g cm^{-3} 63643 reflections measured (6.242° $\leq 2\Theta \leq$ 144.224°), 8733 unique (R_{int} = 0.1021, R_{sigma} = 0.0926) which were used in all calculations. The final R_1 was 0.0659 ($I > 2\sigma(I)$) and wR_2 was 0.2041 (all data).

$H_3SalOx^{Pr}Ni_2(OAc)(H_2O)(MeOH) \cdot Cl$

The dinuclear complex, **$H_3SalOx^{Pr}Ni_2(OAc)(H_2O)(MeOH) \cdot Cl$** (Figure C.11), was produced by the same method as $SalAl^{Pr}{}_2Cu_4(OAc)_2$(1,4−dioxane) · 2 MeOH, using the H_5SalOx^{Pr} and $Ni(OAc)_2 \cdot 4\,H_2O$ in place of H_3SalAl^{Pr} and $Cu(OAc)_2 \cdot H_2O$, respectively. **$H_3SalOx^{Pr}Ni_2(OAc)(H_2O)(MeOH) \cdot Cl$** crystallized in the triclinic space group $P\bar{1}$ ($Z' = 1$) as cubic orange crystals. The binding motif exhibited by this complex is incredibly common among transition metal dimers which utilize *valxn* type ligands (*valxn* = Schiff base condensation of *o*-vanillin with *m*,*n*-diamines such as ethylenediamine or *o*-phenylenediamine). Charge balance dictates the oximes and alkyl alcohol must still be protonated due to the presence of a chloride and acetate anion. It is currently unclear what the initial chloride source was, but this complex has been reproduced in small quantities using a 1:1 mixture of $Ni(OAc)_2 \cdot 4\,H_2O$ and $NiCl_2 \cdot 6\,H_2O$.

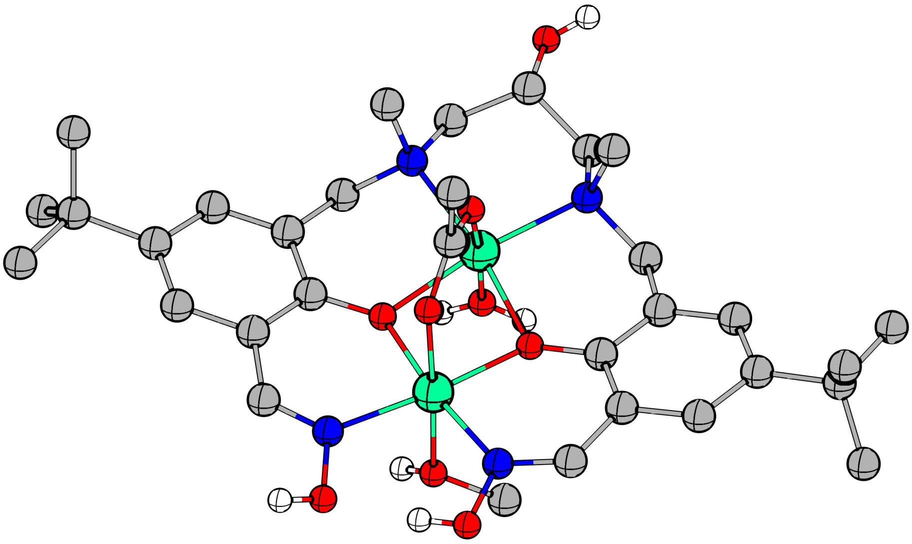

FIGURE C.11: X-ray crystal structure of **$H_3SalOx^{Pr}Ni_2(OAc)(H_2O)(MeOH) \cdot Cl$**. Non-coordinated species and non-acidic hydrogen atoms omitted for clarity. C = grey, N = blue, Ni = pale green, O = red.

Crystal Data for $C_{32}H_{50}ClN_4Ni_2O_9$ (M = 787.63 g mol^{-1}): triclinic, space group $P\bar{1}$ (no. 2), a = 10.1792(5) Å, b = 13.6601(7) Å, c = 14.6298(8) Å, α = 73.077(2)°, β = 80.359(2)°, γ = 73.288(2)°, V = 1856.16(17) Å^3, Z = 2, T = 100.0 K, μ(CuK$_\alpha$) = 2.381 mm^{-1}, D$_{calc}$ = 1.409 g cm^{-3} 27106 reflections measured (6.342° $\leq$ 2Θ $\leq$ 130.164°), 6245 unique (R_{int} = 0.0429, R_{sigma} = 0.0408) which were used in all calculations. The final R_1 was 0.0560 ($I > 2\sigma(I)$) and wR_2 was 0.1563 (all data).

Appendix D

Crystal Structure and Refinement Data

CIFs, Refinement Data, and Reports

The crystal structure and refinement details for complexes reported in Chapters 2 – 6 can be found in this appendix. The same information is printed below the figure of each complex reported in Appendix C.

CIFs and CheckCif reports for all crystal structures reported in Chapters 2 – 6, as well as those in Appendix C, can be found in the enclosed digital appendix.

Some notes on common CheckCif alerts:

- `PLAT410_ALERT_2`
  This alert indicates the relatively close proximity of the protons attached to each aldehyde or imine carbon of **H_2L1** or **H_4L2** with the nearest naphthalene based proton, and is a consequence of the ligands rigidity.
- `PLAT420_ALERT_2`
  This alert most commonly arises as a consequence of the steric bulk of the ligand, excluding lattice solvents from interacting as hydrogen bond acceptors/donors for axially coordinated solvent molecules.
- `PLAT380_ALERT_4`
  Some methyl groups were found to be unstable to free refinement with `AFIX 137`, causing non-negligible shift values, thus had to be restrained using `AFIX 33`.

H_4L2

Crystal structure and refinement data for **H_4L2**.

Empirical formula	$C_{28}H_{30}N_2O_6$
Formula weight /g mol^{-1}	490.54
Temperature /K	100
Crystal system	triclinic
Space group	$P\bar{1}$
a /Å	9.4717(5)
b /Å	11.2928(7)
c /Å	11.7203(8)
α /°	83.287(6)
β /°	79.718(6)
γ /°	87.035(6)
Volume Å^3	1224.39(13)
Z	2
ρ_{calc} /g cm^{-3}	1.331
μ /mm^{-1}	0.769
F(000)	520.0
Crystal size /mm	0.22 × 0.20 × 0.14
Radiation	CuK$_\alpha$ ($\lambda = 1.54178$)
2Θ range for data collection /°	9.496 to 144.214
Index ranges	$-11 \leq h \leq 11$, $-13 \leq k \leq 13$, $-14 \leq l \leq 14$
Reflections collected	25392
Independent reflections	4578 [$R_{\text{int}} = 0.0482$, $R_{\text{sigma}} = 0.0363$]
Data / restraints / parameters	4579/0/445
Goodness-of-fit on F^2	1.201
Final R indices [$I \geq 2\sigma(I)$]	$R_1 = 0.0535$, $wR_2 = 0.1482$
Final R indices [all data]	$R_1 = 0.0644$, $wR_2 = 0.1798$
Largest diff. peak/hole /e Å^{-3}	0.35/-0.29

H_2L3

Crystal structure and refinement data for **H_2L3**.

Empirical formula	$C_{28}Cl_6H_{26}N_4O_2$
Formula weight /g mol^{-1}	663.26
Temperature /K	173
Crystal system	monoclinic
Space group	$C2/c$
a /Å	24.4862(11)
b /Å	10.0342(4)
c /Å	12.3679(9)
α /°	90
β /°	98.066(7)
γ /°	90
Volume Å^3	3008.3(3)
Z	4
ρ_{calc} /g cm^{-3}	1.464
μ /mm^{-1}	5.488
F(000)	1360.0
Crystal size /mm	$0.38 \times 0.35 \times 0.22$
Radiation	CuK$_\alpha$ ($\lambda = 1.54178$)
2Θ range for data collection /°	7.22 to 143.98
Index ranges	$-28 \leq h \leq 30$, $-11 \leq k \leq 12$, $-14 \leq l \leq 12$
Reflections collected	16692
Independent reflections	2909 [$R_{\mathrm{int}} = 0.0923$, $R_{\mathrm{sigma}} = 0.0801$]
Data / restraints / parameters	2909/0/195
Goodness-of-fit on F^2	1.122
Final R indices [$I \geq 2\sigma(I)$]	$R_1 = 0.0629$, $wR_2 = 0.1580$
Final R indices [all data]	$R_1 = 0.0899$, $wR_2 = 0.1876$
Largest diff. peak/hole /e Å^{-3}	0.30/-0.47

hexamineSal

Crystal structure and refinement data for **hexamineSal**.

Empirical formula	$BrC_{20}Cl_6H_{29}N_4O_2$
Formula weight /g mol^{-1}	650.08
Temperature /K	150
Crystal system	triclinic
Space group	$P\bar{1}$
a /Å	9.0701(6)
b /Å	11.0872(8)
c /Å	15.7926(11)
α /°	93.325(7)
β /°	98.145(7)
γ /°	113.143(8)
Volume Å^3	1426.24(19)
Z	2
ρ_{calc} /g cm^{-3}	1.514
μ /mm^{-1}	7.342
F(000)	660.0
Crystal size /mm	0.15 × 0.15 × 0.15
Radiation	CuK$_\alpha$ ($\lambda = 1.54178$)
2Θ range for data collection /°	5.73 to 130.13
Index ranges	$-10 \leq h \leq 10$, $-11 \leq k \leq 12$, $-18 \leq l \leq 18$
Reflections collected	19251
Independent reflections	4790 [$R_{\text{int}} = 0.0923$, $R_{\text{sigma}} = 0.0801$]
Data / restraints / parameters	4790/36/301
Goodness-of-fit on F^2	1.124
Final R indices [$I \geq 2\sigma(I)$]	$R_1 = 0.0637$, $wR_2 = 0.1717$
Final R indices [all data]	$R_1 = 0.0902$, $wR_2 = 0.2014$
Largest diff. peak/hole /e Å^{-3}	0.59/-0.63

Ni_3La

Crystal structure and refinement data for **Ni_3La**.

Empirical formula	$C_{38}H_{46}LaN_3Ni_3O_{33}$
Formula weight /g mol^{-1}	1387.82
Temperature /K	100
Crystal system	monoclinic
Space group	$P2_1/n$
a /Å	10.4295(8)
b /Å	19.2819(15)
c /Å	24.0313(18)
α /°	90
β /°	102.277(3)
γ /°	90
Volume Å^3	4722.2(6)
Z	4
ρ_{calc} /g cm^{-3}	1.952
μ /mm^{-1}	9.197
F(000)	2800.0
Crystal size /mm	0.24 × 0.18 × 0.04
Radiation	CuK$_\alpha$ ($\lambda = 1.54178$)
2Θ range for data collection /°	5.93 to 136.49
Index ranges	$-12 \leq h \leq 11$, $-22 \leq k \leq 21$, $-28 \leq l \leq 25$
Reflections collected	28526
Independent reflections	8337 [$R_{int} = 0.0502$, $R_{sigma} = 0.0494$]
Data / restraints / parameters	8337/4/730
Goodness-of-fit on F^2	1.081
Final R indices [$I \geq 2\sigma(I)$]	$R_1 = 0.0580$, $wR_2 = 0.1659$
Final R indices [all data]	$R_1 = 0.0607$, $wR_2 = 0.1719$
Largest diff. peak/hole /e Å^{-3}	1.92/-2.27

Ni_3Gd

Crystal structure and refinement data for **Ni_3Gd**.

Empirical formula	$C_{45}GdH_{54}N_3Ni_3O_{30}$
Formula weight /g mol^{-1}	1450.29
Temperature /K	100
Crystal system	monoclinic
Space group	$P2_1/n$
a /Å	17.0721(10)
b /Å	18.7861(11)
c /Å	19.1302(10)
α /°	90
β /°	106.716(3)
γ /°	90
Volume Å^3	5261.8(5)
Z	4
ρ_{calc} /g cm^{-3}	1.831
μ /mm^{-1}	10.111
F(000)	2932.0
Crystal size /mm	$0.23 \times 0.10 \times 0.10$
Radiation	CuK$_\alpha$ ($\lambda = 1.54178$)
2Θ range for data collection /°	6.442 to 136.484
Index ranges	$-20 \leq h \leq 20$, $-22 \leq k \leq 22$, $-20 \leq l \leq 20$
Reflections collected	143215
Independent reflections	9641 [$R_{\text{int}} = 0.0509$, $R_{\text{sigma}} = 0.0206$]
Data / restraints / parameters	9641/70/798
Goodness-of-fit on F^2	1.026
Final R indices [$I \geq 2\sigma(I)$]	$R_1 = 0.0232$, $wR_2 = 0.0607$
Final R indices [all data]	$R_1 = 0.0242$, $wR_2 = 0.0614$
Largest diff. peak/hole /e Å^{-3}	0.76/-0.57

Ni_3Eu

Crystal structure and refinement data for **Ni_3Eu**.

Empirical formula	$C_{37.5}EuH_{36}N_3Ni_3O_{28.5}$
Formula weight /g mol^{-1}	1312.78
Temperature /K	100
Crystal system	monoclinic
Space group	$C2/c$
a /Å	12.7986(12)
b /Å	16.5467(16)
c /Å	39.972(4)
α /°	90
β /°	90.203(3)
γ /°	90
Volume Å^3	8464.9(14)
Z	8
ρ_{calc} /g cm^{-3}	2.060
μ /mm^{-1}	12.934
F(000)	5256.0
Crystal size /mm	0.18 × 0.14 × 0.10
Radiation	CuK$_\alpha$ ($\lambda = 1.54178$)
2Θ range for data collection /°	4.422 to 136.462
Index ranges	$-15 \leq h \leq 14$, $-19 \leq k \leq 19$, $-46 \leq l \leq 48$
Reflections collected	129662
Independent reflections	7697 [$R_{\text{int}} = 0.0491$, $R_{\text{sigma}} = 0.0205$]
Data / restraints / parameters	7697/14/682
Goodness-of-fit on F^2	1.048
Final R indices [$I \geq 2\sigma(I)$]	$R_1 = 0.0249$, $wR_2 = 0.0675$
Final R indices [all data]	$R_1 = 0.0250$, $wR_2 = 0.0676$
Largest diff. peak/hole /e Å^{-3}	0.68/-0.72

Ni_3Ba

Crystal structure and refinement data for $\mathbf{Ni_3Ba}$.

Empirical formula	$BaC_{41.5}H_{49.5}N_3Ni_3O_{28}$
Formula weight /g mol^{-1}	1337.80
Temperature /K	100
Crystal system	monoclinic
Space group	$P\bar{1}$
a /Å	11.0862(6)
b /Å	15.5290(9)
c /Å	16.8872(9)
α /°	115.311(4)
β /°	101.491(4)
γ /°	97.235(4)
Volume Å^3	2501.3(3)
Z	2
ρ_{calc} /g cm^{-3}	1.776
μ /mm^{-1}	8.148
F(000)	1353.0
Crystal size /mm	0.21 × 0.20 × 0.16
Radiation	CuK$_\alpha$ ($\lambda = 1.54178$)
2Θ range for data collection /°	6.034 to 130.164
Index ranges	$-11 \leq h \leq 12$, $-18 \leq k \leq 18$, $-19 \leq l \leq 19$
Reflections collected	68110
Independent reflections	8413 [$R_{int} = 0.0916$, $R_{sigma} = 0.0583$]
Data / restraints / parameters	8413/39/682
Goodness-of-fit on F^2	1.052
Final R indices [$I \geq 2\sigma(I)$]	$R_1 = 0.0711$, $wR_2 = 0.1515$
Final R indices [all data]	$R_1 = 0.0926$, $wR_2 = 0.1625$
Largest diff. peak/hole /e Å^{-3}	1.20/-1.19

Ni$_3$Tb

Crystal structure and refinement data for **Ni$_3$Tb**.

Empirical formula	$C_{56}Cl_2H_{52}NNi_3O_{24}Tb$
Formula weight /g mol^{-1}	1313.68
Temperature /K	100
Crystal system	orthorhomibic
Space group	$P2_12_12_1$
a /Å	13.1191(5)
b /Å	17.5642(6)
c /Å	21.1099(7)
α /°	90
β /°	90
γ /°	90
Volume Å^3	4864.3(3)
Z	4
ρ_{calc} /g cm^{-3}	1.794
μ /mm^{-1}	10.070
F(000)	2628.0
Crystal size /mm	0.10 × 0.10 × 0.08
Radiation	CuK$_\alpha$ ($\lambda = 1.54178$)
2Θ range for data collection /°	6.546 to 136.472
Index ranges	$-15 \leq h \leq 15$, $-21 \leq k \leq 20$, $-24 \leq l \leq 25$
Reflections collected	158157
Independent reflections	8628 [$R_{\text{int}} = 0.0552$, $R_{\text{sigma}} = 0.0316$]
Data / restraints / parameters	8628/97/617
Goodness-of-fit on F^2	1.043
Final R indices [$I \geq 2\sigma(I)$]	$R_1 = 0.0584$, $wR_2 = 0.1478$
Final R indices [all data]	$R_1 = 0.0615$, $wR_2 = 0.1501$
Largest diff. peak/hole /e Å^{-3}	0.96/-0.80
Flack Parameter	0.165(7)

Ni_3Gd-Acid

Crystal structure and refinement data for **Ni_3Gd-Acid**.

Empirical formula	$C_{56}H_{52}GdNNi_3O_{28}$
Formula weight /g mol^{-1}	1520.36
Temperature /K	100
Crystal system	monoclinic
Space group	$P2_1/n$
a /Å	11.2553(12)
b /Å	19.402(2)
c /Å	25.293(3)
α /°	90
β /°	96.675(7)
γ /°	90
Volume Å^3	5485.8(11)
Z	4
ρ_{calc} /g cm^{-3}	1.841
μ /mm^{-1}	9.700
F(000)	3068.0
Crystal size /mm	0.21 × 0.08 × 0.08
Radiation	CuK$_\alpha$ ($\lambda = 1.54178$)
2Θ range for data collection /°	5.756 to 136.492
Index ranges	$-12 \leq h \leq 13$, $-23 \leq k \leq 23$, $-30 \leq l \leq 30$
Reflections collected	97593
Independent reflections	10019 [$R_{\mathrm{int}} = 0.1193$, $R_{\mathrm{sigma}} = 0.0610$]
Data / restraints / parameters	10019/3/817
Goodness-of-fit on F^2	1.077
Final R indices [$I \geq 2\sigma(I)$]	$R_1 = 0.0814$, $wR_2 = 0.1870$
Final R indices [all data]	$R_1 = 0.0976$, $wR_2 = 0.1962$
Largest diff. peak/hole /e Å^{-3}	1.78/-0.96

Cu_3La

Crystal structure and refinement data for **Cu_3La**.

Empirical formula	$C_{37}Cu_3H_{26}LaN_3O_{21}$
Formula weight /g mol^{-1}	1164.13
Temperature /K	100
Crystal system	monoclinic
Space group	$C2/c$
a /Å	28.6966(12)
b /Å	16.3850(7)
c /Å	20.3386(11)
α /°	90
β /°	98.064(4)
γ /°	90
Volume Å^3	9375.8(6)
Z	8
ρ_{calc} /g cm^{-3}	1.633
μ /mm^{-1}	9.022
F(000)	4592.0
Crystal size /mm	$0.05 \times 0.05 \times 0.01$
Radiation	CuK_α ($\lambda = 1.54178$)
2Θ range for data collection /°	6.222 to 136.486
Index ranges	$-34 \leq h \leq 34$, $-19 \leq k \leq 19$, $-24 \leq l \leq 24$
Reflections collected	53692
Independent reflections	8685 [$R_{\text{int}} = 0.1965$, $R_{\text{sigma}} = 0.1307$]
Data / restraints / parameters	8685/285/583
Goodness-of-fit on F^2	1.066
Final R indices [$I \geq 2\sigma(I)$]	$R_1 = 0.0966$, $wR_2 = 0.2626$
Final R indices [all data]	$R_1 = 0.1692$, $wR_2 = 0.3175$
Largest diff. peak/hole /e Å^{-3}	1.14/-2.21

Cu_3Gd

Crystal structure and refinement data for **Cu_3Gd**.

Empirical formula	$C_{38}Cu_3GdH_{32}N_3O_{28}$
Formula weight /g mol^{-1}	1306.53
Temperature /K	100
Crystal system	monoclinic
Space group	$C2/c$
a /Å	28.7291(8)
b /Å	16.3936(5)
c /Å	20.1091(9)
α /°	90
β /°	98.124(2)
γ /°	90
Volume Å^3	9375.8(6)
Z	8
ρ_{calc} /g cm^{-3}	1.880
μ /mm^{-1}	11.423
F(000)	5248.0
Crystal size /mm	$0.04 \times 0.04 \times 0.01$
Radiation	CuK_α ($\lambda = 1.54178$)
2Θ range for data collection /°	6.216 to 136.822
Index ranges	$-33 \le h \le 33$, $-19 \le k \le 17$, $-24 \le l \le 23$
Reflections collected	77123
Independent reflections	8563 [$R_{int} = 0.1187$, $R_{sigma} = 0.0776$]
Data / restraints / parameters	8563/394/559
Goodness-of-fit on F^2	1.042
Final R indices [$I \ge 2\sigma(I)$]	$R_1 = 0.0984$, $wR_2 = 0.2593$
Final R indices [all data]	$R_1 = 0.1395$, $wR_2 = 0.2892$
Largest diff. peak/hole /e Å^{-3}	2.16/-1.41

Cu_3Dy

Crystal structure and refinement data for **Cu_3Dy**.

Empirical formula	$C_{37}Cu_3DyH_{26}N_3O_{24}$
Formula weight /g mol^{-1}	1249.73
Temperature /K	100
Crystal system	monoclinic
Space group	$C2/c$
a /Å	28.6992(9)
b /Å	16.3760(5)
c /Å	20.1703(8)
α /°	90
β /°	98.062(3)
γ /°	90
Volume Å^3	9385.9(6)
Z	8
ρ_{calc} /g cm^{-3}	1.769
μ /mm^{-1}	10.677
F(000)	4912.0
Crystal size /mm	$0.10 \times 0.08 \times 0.04$
Radiation	CuK$_\alpha$ ($\lambda = 1.54178$)
2Θ range for data collection /°	6.22 to 152.912
Index ranges	$-33 \leq h \leq 35$, $-18 \leq k \leq 19$, $-25 \leq l \leq 23$
Reflections collected	53922
Independent reflections	9466 [$R_{\text{int}} = 0.0999$, $R_{\text{sigma}} = 0.0761$]
Data / restraints / parameters	9466/400/560
Goodness-of-fit on F^2	1.033
Final R indices [$I \geq 2\sigma(I)$]	$R_1 = 0.1027$, $wR_2 = 0.2672$
Final R indices [all data]	$R_1 = 0.1396$, $wR_2 = 0.2922$
Largest diff. peak/hole /e Å^{-3}	2.16/-1.60

Cu_3Yb

Crystal structure and refinement data for **Cu_3Yb**.

Empirical formula	$C_{40.5}Cu_3H_{38}N_3O_{26.5}Yb$
Formula weight /g mol^{-1}	1354.40
Temperature /K	100
Crystal system	monoclinic
Space group	$C2/c$
a /Å	28.6124(17)
b /Å	16.3599(10)
c /Å	20.3464(16)
α /°	90
β /°	97.601(4)
γ /°	90
Volume Å^3	9440.4(11)
Z	8
ρ_{calc} /g cm^{-3}	1.906
μ /mm^{-1}	5.902
F(000)	5368.0
Crystal size /mm	0.14 × 0.12 × 0.08
Radiation	CuK_α ($\lambda = 1.54178$)
2Θ range for data collection /°	6.232 to 136.484
Index ranges	$-33 \leq h \leq 34$, $-18 \leq k \leq 19$, $-24 \leq l \leq 24$
Reflections collected	37380
Independent reflections	8620 [$R_{int} = 0.0562$, $R_{sigma} = 0.0506$]
Data / restraints / parameters	8620/369/601
Goodness-of-fit on F^2	1.073
Final R indices [$I \geq 2\sigma(I)$]	$R_1 = 0.0966$, $wR_2 = 0.2836$
Final R indices [all data]	$R_1 = 0.1109$, $wR_2 = 0.2947$
Largest diff. peak/hole /e Å^{-3}	2.42/-1.48

Cu_3Ho

Crystal structure and refinement data for **Cu_3Ho**.

Empirical formula	$C_{36.5}Cl_3Cu_3H_{28.5}HoO_{17}$
Formula weight /g mol^{-1}	1200.97
Temperature /K	100
Crystal system	orthorhombic
Space group	*Pbcn*
a /Å	34.591(2)
b /Å	16.5550(10)
c /Å	13.7333(8)
α /°	90
β /°	90
γ /°	90
Volume Å^3	7864.5(8)
Z	8
ρ_{calc} /g cm^{-3}	1.969
μ /mm^{-1}	7.330
F(000)	4572.0
Crystal size /mm	0.10 × 0.10 × 0.04
Radiation	CuK$_\alpha$ ($\lambda = 1.54178$)
2Θ range for data collection /°	5.198 to 136.49
Index ranges	$-40 \leq h \leq 41$, $-19 \leq k \leq 19$, $-16 \leq l \leq 16$
Reflections collected	176922
Independent reflections	7184 [$R_{\text{int}} = 0.0440$, $R_{\text{sigma}} = 0.0155$]
Data / restraints / parameters	7184/22/560
Goodness-of-fit on F^2	1.061
Final R indices [$I \geq 2\sigma(I)$]	$R_1 = 0.0399$, $wR_2 = 0.1055$
Final R indices [all data]	$R_1 = 0.0469$, $wR_2 = 0.1103$
Largest diff. peak/hole /e Å^{-3}	1.57/-0.66

Cu_3Er

Crystal structure and refinement data for **Cu_3Er**.

Empirical formula	$C_{36.5}Cl_3Cu_3ErH_{32.5}O_{19}$
Formula weight /g mol^{-1}	1239.35
Temperature /K	100
Crystal system	orthorhombic
Space group	*Pbcn*
a /Å	34.5966(13)
b /Å	16.5510(6)
c /Å	13.7093(5)
α /°	90
β /°	90
γ /°	90
Volume Å^3	7850.1(5)
Z	8
ρ_{calc} /g cm^{-3}	2.097
μ /mm^{-1}	8.245
F(000)	4876.0
Crystal size /mm	$0.07 \times 0.05 \times 0.01$
Radiation	CuK$_\alpha$ ($\lambda = 1.54178$)
2Θ range for data collection /°	8.756 to 152.51
Index ranges	$-43 \leq h \leq 42$, $-20 \leq k \leq 20$, $-17 \leq l \leq 16$
Reflections collected	202987
Independent reflections	8171 [$R_{\mathrm{int}} = 0.1144$, $R_{\mathrm{sigma}} = 0.0407$]
Data / restraints / parameters	8171/19/552
Goodness-of-fit on F^2	1.025
Final R indices [$I \geq 2\sigma(I)$]	$R_1 = 0.0492$, $wR_2 = 0.1257$
Final R indices [all data]	$R_1 = 0.0737$, $wR_2 = 0.1422$
Largest diff. peak/hole /e Å^{-3}	1.72/-1.65

Cu_3Tb

Crystal structure and refinement data for **Cu_3Tb**.

Empirical formula	$C_{37}Cl_2Cu_3H_{26}NO_{18}Tb$
Formula weight /g mol^{-1}	1193.03
Temperature /K	100
Crystal system	monoclinic
Space group	$P2_1$
a /Å	10.9841(7)
b /Å	16.6805(10)
c /Å	13.6105(8)
α /°	90
β /°	113.771(4)
γ /°	90
Volume Å^3	2282.2(2)
Z	2
ρ_{calc} /g cm^{-3}	1.736
μ /mm^{-1}	10.742
F(000)	1170.0
Crystal size /mm	0.18 × 0.14 × 0.10
Radiation	CuK_α ($\lambda = 1.54178$)
2Θ range for data collection /°	7.096 to 136.488
Index ranges	$-13 \leq h \leq 13$, $-20 \leq k \leq 20$, $-16 \leq l \leq 16$
Reflections collected	74422
Independent reflections	8372 [$R_{int} = 0.1874$, $R_{sigma} = 0.1208$]
Data / restraints / parameters	8372/75/563
Goodness-of-fit on F^2	1.007
Final R indices [$I \geq 2\sigma(I)$]	$R_1 = 0.0782$, $wR_2 = 0.1949$
Final R indices [all data]	$R_1 = 0.1496$, $wR_2 = 0.2374$
Largest diff. peak/hole /e Å^{-3}	1.31/-1.07

Co_3Dy

Crystal structure and refinement data for **Co_3Dy**.

Empirical formula	$C_{41}Co_3DyH_{40}N_3O_{27}$
Formula weight /g mol^{-1}	1346.05
Temperature /K	100
Crystal system	triclinic
Space group	$P\bar{1}$
a /Å	10.2212(8)
b /Å	11.0914(10)
c /Å	22.1617(19)
α /°	91.217(7)
β /°	91.740(6)
γ /°	116.345(6)
Volume Å^3	2248.7(3)
Z	2
ρ_{calc} /g cm^{-3}	1.988
μ /mm^{-1}	18.174
F(000)	1340.0
Crystal size /mm	$0.18 \times 0.18 \times 0.14$
Radiation	CuK$_\alpha$ ($\lambda = 1.54178$)
2Θ range for data collection /°	3.992 to 136.472
Index ranges	$-12 \leq h \leq 11$, $-13 \leq k \leq 12$, $-26 \leq l \leq 26$
Reflections collected	22277
Independent reflections	8044 [$R_{\mathrm{int}} = 0.1035$, $R_{\mathrm{sigma}} = 0.1359$]
Data / restraints / parameters	8044/15/698
Goodness-of-fit on F^2	1.043
Final R indices [$I \geq 2\sigma(I)$]	$R_1 = 0.0873$, $wR_2 = 0.2074$
Final R indices [all data]	$R_1 = 0.1414$, $wR_2 = 0.2413$
Largest diff. peak/hole /e Å^{-3}	1.39/-1.64

Co_3Gd

Crystal structure and refinement data for **Co_3Gd**.

Empirical formula	$C_{40}Co_3GdH_{34}N_3O_{25}$
Formula weight /g mol^{-1}	1290.74
Temperature /K	100
Crystal system	triclinic
Space group	$P\bar{1}$
a /Å	10.1882(12)
b /Å	10.2651(13)
c /Å	23.231(3)
α /°	86.370(8)
β /°	84.284(8)
γ /°	65.297(8)
Volume Å^3	2416.3(4)
Z	2
ρ_{calc} /g cm^{-3}	1.952
μ /mm^{-1}	19.214
F(000)	1280.0
Crystal size /mm	$0.17 \times 0.16 \times 0.14$
Radiation	CuK$_\alpha$ ($\lambda = 1.54178$)
2Θ range for data collection /°	3.824 to 136.488
Index ranges	$-11 \leq h \leq 12$, $-12 \leq k \leq 12$, $-27 \leq l \leq 27$
Reflections collected	76045
Independent reflections	7796 [$R_{int} = 0.1270$, $R_{sigma} = 0.0763$]
Data / restraints / parameters	7796/12/666
Goodness-of-fit on F^2	1.134
Final R indices [$I \geq 2\sigma(I)$]	$R_1 = 0.0590$, $wR_2 = 0.1432$
Final R indices [all data]	$R_1 = 0.0936$, $wR_2 = 0.1602$
Largest diff. peak/hole /e Å^{-3}	0.87/-1.17

Co_3La

Crystal structure and refinement data for **Co_3La**.

Empirical formula	$C_{32}Co_3H_{47}LaN_3O_{29.5}$
Formula weight /g mol^{-1}	1381.52
Temperature /K	100
Crystal system	triclinic
Space group	$P\bar{1}$
a /Å	10.2888(8)
b /Å	15.4555(13)
c /Å	16.0338(13)
α /°	93.324(7)
β /°	108.261(8)
γ /°	90.444(6)
Volume Å^3	2416.3(4)
Z	2
ρ_{calc} /g cm^{-3}	1.899
μ /mm^{-1}	15.544
F(000)	1388.0
Crystal size /mm	0.14 × 0.10 × 0.04
Radiation	CuK$_\alpha$ ($\lambda = 1.54178$)
2Θ range for data collection /°	5.73 to 136.492
Index ranges	$-12 \leq h \leq 11$, $-18 \leq k \leq 18$, $-19 \leq l \leq 18$
Reflections collected	34920
Independent reflections	8664 [$R_{\text{int}} = 0.1021$, $R_{\text{sigma}} = 0.1034$]
Data / restraints / parameters	8664/91/681
Goodness-of-fit on F^2	1.036
Final R indices [$I \geq 2\sigma(I)$]	$R_1 = 0.0804$, $wR_2 = 0.2016$
Final R indices [all data]	$R_1 = 0.1199$, $wR_2 = 0.2235$
Largest diff. peak/hole /e Å^{-3}	1.85/-1.17

Co_3Tb

Crystal structure and refinement data for **Co_3Tb**.

Empirical formula	$C_{39.5}ClCo_3H_{36}N_2O_{23.5}Tb$
Formula weight /g mol^{-1}	1285.86
Temperature /K	100
Crystal system	monoclinic
Space group	$C2/c$
a /Å	14.0045(5)
b /Å	15.7554(5)
c /Å	41.1854(16)
α /°	90
β /°	96.063(2)
γ /°	90
Volume Å^3	9036.6(6)
Z	8
ρ_{calc} /g cm^{-3}	1.890
μ /mm^{-1}	17.370
F(000)	5104.0
Crystal size /mm	$0.12 \times 0.10 \times 0.10$
Radiation	CuK$_\alpha$ ($\lambda = 1.54178$)
2Θ range for data collection /°	8.474 to 136.468
Index ranges	$-15 \leq h \leq 16$, $-18 \leq k \leq 18$, $-49 \leq l \leq 49$
Reflections collected	36728
Independent reflections	8148 [$R_{int} = 0.1009$, $R_{sigma} = 0.0831$]
Data / restraints / parameters	8148/21/645
Goodness-of-fit on F^2	1.029
Final R indices [$I \geq 2\sigma(I)$]	$R_1 = 0.0546$, $wR_2 = 0.1292$
Final R indices [all data]	$R_1 = 0.0924$, $wR_2 = 0.1479$
Largest diff. peak/hole /e Å^{-3}	1.07/-1.26

$\mathbf{Ni_{16}}$–$C2/c$

Crystal structure and refinement data for $\mathbf{Ni_{16}}$–$\mathbf{C2/c}$.

Empirical formula	$C_{128}H_{148}N_8Ni_{16}O_{60}$
Formula weight /g mol^{-1}	3818.00
Temperature /K	100
Crystal system	monoclinic
Space group	$C2/c$
a /Å	62.292(4)
b /Å	22.4830(13)
c /Å	42.170(2)
α /°	90
β /°	118.221(3)
γ /°	90
Volume Å^3	52039(5)
Z	8
ρ_{calc} /g cm^{-3}	0.975
μ /mm^{-1}	1.665
F(000)	15680.0
Crystal size /mm	0.28 × 0.02 × 0.02
Radiation	CuK$_\alpha$ ($\lambda = 1.54178$)
2Θ range for data collection /°	3.22 to 136.492
Index ranges	$-74 \leq h \leq 74$, $-27 \leq k \leq 25$, $-50 \leq l \leq 50$
Reflections collected	493490
Independent reflections	47602 [$R_{\text{int}} = 0.1507$, $R_{\text{sigma}} = 0.0865$]
Data / restraints / parameters	47602/324/1824
Goodness-of-fit on F^2	1.234
Final R indices [$I \geq 2\sigma(I)$]	$R_1 = 0.1233$, $wR_2 = 0.3679$
Final R indices [all data]	$R_1 = 0.1727$, $wR_2 = 0.3989$
Largest diff. peak/hole /e Å^{-3}	0.95/-0.69

$\mathbf{Ni_{16}}$–$P2_1/n$

Crystal structure and refinement data for $\mathbf{Ni_{16}}$–$\boldsymbol{P2_1/n}$.

Empirical formula	$C_{144.5}H_{161}N_8Ni_{16}O_{60}$
Formula weight /g mol^{-1}	3909.16
Temperature /K	100
Crystal system	monoclinic
Space group	$P2_1/n$
a /Å	25.1716(11)
b /Å	44.6220(19)
c /Å	39.0396(17)
α /°	90
β /°	91.394(3)
γ /°	90
Volume Å^3	52039(5)
Z	8
ρ_{calc} /g cm^{-3}	1.185
μ /mm^{-1}	1.987
F(000)	16096.0
Crystal size /mm	0.12 × 0.11 × 0.02
Radiation	CuK$_\alpha$ ($\lambda = 1.54178$)
2Θ range for data collection /°	4.562 to 136.488
Index ranges	$-30 \leq h \leq 28$, $-53 \leq k \leq 39$, $-45 \leq l \leq 45$
Reflections collected	428528
Independent reflections	79176 [$R_{int} = 0.0974$, $R_{sigma} = 0.0821$]
Data / restraints / parameters	79176/560/4158
Goodness-of-fit on F^2	1.063
Final R indices [$I \geq 2\sigma(I)$]	$R_1 = 0.0738$, $wR_2 = 0.2095$
Final R indices [all data]	$R_1 = 0.1146$, $wR_2 = 0.2361$
Largest diff. peak/hole /e Å^{-3}	2.34/-0.64

Ni_{16}–*P*4*nc*

Crystal structure and refinement data for **Ni_{16}–*P*4*nc***.

Empirical formula	$C_{292}H_{344}N_{16}Ni_{32}O_{128}$
Formula weight /g mol^{-1}	8004.53
Temperature /K	100
Crystal system	tetragonal
Space group	$P4nc$
a /Å	24.2318(5)
b /Å	24.2318(5)
c /Å	40.3595(5)
α /°	90
β /°	90
γ /°	90
Volume Å^3	23698.3(13)
Z	2
ρ_{calc} /g cm^{-3}	1.122
μ /mm^{-1}	1.861
F(000)	8256.0
Crystal size /mm	0.18 × 0.16 × 0.10
Radiation	CuK$_\alpha$ ($\lambda = 1.54178$)
2Θ range for data collection /°	4.254 to 152.63
Index ranges	$-28 \leq h \leq 29$, $-27 \leq k \leq 28$, $-26 \leq l \leq 50$
Reflections collected	335181
Independent reflections	23648 [$R_{\text{int}} = 0.0660$, $R_{\text{sigma}} = 0.0314$]
Data / restraints / parameters	23648/20/1094
Goodness-of-fit on F^2	1.026
Final R indices [$I \geq 2\sigma(I)$]	$R_1 = 0.0490$, $wR_2 = 0.1294$
Final R indices [all data]	$R_1 = 0.0727$, $wR_2 = 0.1444$
Largest diff. peak/hole /e Å^{-3}	0.40/-0.34
Flack parameter	0.069(7)

Ni_{16}–formate

Crystal structure and refinement data for **Ni_{16}–formate**.

Empirical formula	$C_{120}H_{112}N_8Ni_{16}O_{60}$
Formula weight /g mol^{-1}	3565.53
Temperature /K	100
Crystal system	trigonal
Space group	$P3_121$
a /Å	26.3591(5)
b /Å	26.3591(5)
c /Å	27.5189(9)
α /°	90
β /°	90
γ /°	120
Volume Å^3	16558.6(8)
Z	3
ρ_{calc} /g cm^{-3}	1.073
μ /mm^{-1}	1.932
F(000)	5448.0
Crystal size /mm	0.14 × 0.12 × 0.08
Radiation	CuK_α ($\lambda = 1.54178$)
2Θ range for data collection /°	5.03 to 144.652
Index ranges	$-32 \leq h \leq 26$, $-32 \leq k \leq 29$, $-25 \leq l \leq 34$
Reflections collected	57752
Independent reflections	20347 [$R_{int} = 0.0264$, $R_{sigma} = 0.0300$]
Data / restraints / parameters	20347/385/859
Goodness-of-fit on F^2	1.114
Final R indices [$I \geq 2\sigma(I)$]	$R_1 = 0.0594$, $wR_2 = 0.1858$
Final R indices [all data]	$R_1 = 0.0685$, $wR_2 = 0.1976$
Largest diff. peak/hole /e Å^{-3}	0.53/-0.39
Flack parameter	0.40(3)

$\mathbf{Cu_{14}}$

Crystal structure and refinement data for $\mathbf{Cu_{14}}$.

Empirical formula	$C_{108}Cu_{14}H_{97}N_9O_{35}$
Formula weight /g mol^{-1}	2970.50
Temperature /K	100
Crystal system	triclinic
Space group	$P\bar{1}$
a /Å	18.3776(13)
b /Å	19.3734(13)
c /Å	23.6144(17)
α /°	66.425(3)
β /°	72.861(3)
γ /°	73.944(3)
Volume Å^3	7241.8(9)
Z	2
ρ_{calc} /g cm^{-3}	1.362
μ /mm^{-1}	2.722
F(000)	2988.0
Crystal size /mm	$0.21 \times 0.14 \times 0.12$
Radiation	CuK$_\alpha$ ($\lambda = 1.54178$)
2Θ range for data collection /°	4.174 to 136.492
Index ranges	$-22 \leq h \leq 21$, $-23 \leq k \leq 23$, $-28 \leq l \leq 28$
Reflections collected	267249
Independent reflections	26452 [$R_{\mathrm{int}} = 0.0742$, $R_{\mathrm{sigma}} = 0.0315$]
Data / restraints / parameters	26452/108/1556
Goodness-of-fit on F^2	1.022
Final R indices [$I \geq 2\sigma(I)$]	$R_1 = 0.0572$, $wR_2 = 0.1657$
Final R indices [all data]	$R_1 = 0.0620$, $wR_2 = 0.1693$
Largest diff. peak/hole /e Å^{-3}	2.08/-0.81

Mn_8

Crystal structure and refinement data for $\mathbf{Mn_8}$.

Empirical formula	$C_{111}H_{112}Mn_8O_{49}$
Formula weight /g mol^{-1}	2669.52
Temperature /K	100
Crystal system	monoclinic
Space group	$P2_1/n$
a /Å	17.1286(13)
b /Å	27.2886(17)
c /Å	24.0193(15)
α /°	90
β /°	106.097(4)
γ /°	90
Volume Å^3	10786.8(13)
Z	4
ρ_{calc} /g cm^{-3}	1.644
μ /mm^{-1}	8.223
F(000)	5480.0
Crystal size /mm	0.34 × 0.30 × 0.05
Radiation	CuK_α ($\lambda = 1.54178$)
2Θ range for data collection /°	5.014 to 137.976
Index ranges	$-20 \leq h \leq 20$, $-32 \leq k \leq 32$, $-28 \leq l \leq 28$
Reflections collected	105874
Independent reflections	19693 [$R_{\mathrm{int}} = 0.0738$, $R_{\mathrm{sigma}} = 0.0644$]
Data / restraints / parameters	19693/3/1268
Goodness-of-fit on F^2	1.070
Final R indices [$I \geq 2\sigma(I)$]	$R_1 = 0.0663$, $wR_2 = 0.1844$
Final R indices [all data]	$R_1 = 0.0835$, $wR_2 = 0.1982$
Largest diff. peak/hole /e Å^{-3}	1.71/-0.76

$\mathbf{MnLa_6}$

Crystal structure and refinement data for $\mathbf{MnLa_6}$.

Empirical formula	$C_{98}H_{72}La_6MnN_4O_{66}$
Formula weight /g mol^{-1}	3429.99
Temperature /K	100
Crystal system	monoclinic
Space group	$C2/c$
a /Å	24.627(3)
b /Å	22.701(2)
c /Å	21.441(2)
α /°	90
β /°	95.454(6)
γ /°	90
Volume Å^3	11933(2)
Z	4
ρ_{calc} /g cm^{-3}	1.809
μ /mm^{-1}	17.968
F(000)	6332.0
Crystal size /mm	0.24 × 0.11 × 0.04
Radiation	CuK$_\alpha$ ($\lambda = 1.54178$)
2Θ range for data collection /°	5.306 to 136.47
Index ranges	$-29 \leq h \leq 29$, $-27 \leq k \leq 26$, $-25 \leq l \leq 25$
Reflections collected	104713
Independent reflections	10883 [$R_{\text{int}} = 0.1324$, $R_{\text{sigma}} = 0.0800$]
Data / restraints / parameters	10883/107/708
Goodness-of-fit on F^2	0.998
Final R indices [$I \geq 2\sigma(I)$]	$R_1 = 0.0744$, $wR_2 = 0.2033$
Final R indices [all data]	$R_1 = 0.1324$, $wR_2 = 0.2427$
Largest diff. peak/hole /e Å^{-3}	1.88/-1.10

Bibliography

(1) C. E. Housecroft and A. G. Sharpe, *Inorganic Chemistry*, Pearson, New York, 4th, 2012.

(2) S. G. Vulfson, *Molecular Magnetochemistry*, Gordon and Breach Science Publishers, 1998.

(3) J. S. Miller and A. J. Epstein, *Angew. Chem. Int. Ed.*, 1994, **33**, 385–415.

(4) W. Brostow and H. E. H. Lobland, *Materials: Introduction and Applications*, John Wiley & Sons, 2016.

(5) O. Kahn, *Molecular Magnetism*, Courier Dover Publications, 2021.

(6) J. M. Coey, *Magnetism and Magnetic Materials*, Cambridge University Press, 2010.

(7) R. L. Carlin, *Magnetochemistry*, Springer Science & Business Media, 2012.

(8) J. L. Atwood, *Comprehensive Supramolecular Chemistry II*, Elsevier, 2017.

(9) R. Sessoli, H. L. Tsai, A. R. Schake, S. Wang, J. B. Vincent, K. Folting, D. Gatteschi, G. Christou and D. N. Hendrickson, *J. Am. Chem. Soc.*, 1993, **115**, 1804–16.

(10) T Lis, *Acta Crystallogr. C*, 1980, **36**, 2042–2046.

(11) D. Gatteschi, R. Sessoli and J. Villain, *Molecular Nanomagnets*, Oxford University Press, 2006.

(12) R. Winpenny, *Molecular Cluster Magnets*, World Scientific Publishing, 2012.

(13) Web Page, 2022.

(14) K. E. Vostrikova, *Coord. Chem. Rev.*, 2008, **252**, 1409–1419.

(15) X. Meng, W. Shi and P. Cheng, *Coord. Chem. Rev.*, 2019, **378**, 134–150.

(16) M. Briganti, F. Totti and M. Andruh, *Dalton Trans.*, 2021, **50**, 15961–15972.

(17) M. G. Vaz and M. Andruh, *Coord. Chem. Rev.*, 2021, **427**, 213611.

(18) H. Russell and F. Saunders, *Atomic Spectra: The Commonwealth and International Library: Selected Readings in Physics*, 2013, 206.

(19) R. Eisberg and R. Resnick, *Quantum Physics of Atoms, Molecules, Solids, Nuclei, and Particles*, 1985.

(20) W. Carnall, P. Fields and K Rajnak, *J. Chem. Phys.*, 1968, **49**, 4424–4442.

(21) C. Benelli and D. Gatteschi, *Introduction to Molecular Magnetism: From Transition Metals to Lanthanides*, John Wiley & Sons, 2015.

(22) J. N. Lalena and D. A. Cleary, *Principles of Inorganic Materials Design*, John Wiley & Sons, 2005.

(23) J. Kanamori, *J. Phys. Chem. Solids*, 1959, **10**, 87–98.

(24) H. Weihe and H. U. Guedel, *Inorg. Chem.*, 1997, **36**, 3632–3639.

(25) N. Steno, *Nicolai Stenonis De solido intra solidum naturaliter contento dissertationis prodromus*, Accademia della Crusca, 1669.

(26) D Coster and K. Knol, *Proc. Royal. Soc. London Ser. A*, 1933, **139**, 459–466.

(27) G. Rhodes, *Crystallography made Crystal Clear: A Guide for Users of Macromolecular Models*, Elsevier, 2010.

(28) J. Gallop, P. Josephs-Franks, J. Davies, L. Hao and J. Macfarlane, *Physica C*, 2002, **368**, 109–113.

(29) M. S. Grinolds, S. Hong, P. Maletinsky, L. Luan, M. D. Lukin, R. L. Walsworth and A. Yacoby, *Nat. Phys.*, 2013, **9**, 215–219.

(30) D. Vasyukov, Y. Anahory, L. Embon, D. Halbertal, J. Cuppens, L. Neeman, A. Finkler, Y. Segev, Y. Myasoedov and M. L. Rappaport, *Nat. Nanotechnol.*, 2013, **8**, 639–644.

(31) L. May, *An Introduction to Mössbauer Spectroscopy*, Springer Science & Business Media, 2012.

(32) R. Herber, *J. Chem. Educ.*, 1965, **42**, 180.

(33) S. Khanra, T. Weyhermueller, E. Bill and P. Chaudhuri, *Inorg. Chem.*, 2006, **45**, 5911–5923.

(34) H. Megaw, *Acta Cryst. Sect. B*, 1968, **24**, 149–153.

(35) S. Stankov, B. Sepiol, T. Kaňuch, D. Scherjau, R. Würschum and M. Miglierini, *J. Phys. Condens. Matter.*, 2005, **17**, 3183.

(36) T. Glaser, *Mössbauer Spectroscopy and Transition Metal Chemistry: Fundamentals and Applications*, John Wiley & Sons, 2011.

(37) M. D. Dyar, D. G. Agresti, M. W. Schaefer, C. A. Grant and E. C. Sklute, *Annu. Rev. Earth Planet. Sci.*, 2006, **34**, 83–125.

(38) L. Walker, G. K. Wertheim and V Jaccarino, *Phys. Rev. Lett.*, 1961, **6**, 98.

(39) M. Ferbinteanu, T. Kajiwara, K.-Y. Choi, H. Nojiri, A. Nakamoto, N. Kojima, F. Cimpoesu, Y. Fujimura, S. Takaishi and M. Yamashita, *J. Am. Chem. Soc.*, 2006, **128**, 9008–9009.

(40) A. Cini, M. Mannini, F. Totti, M. Fittipaldi, G. Spina, A. Chumakov, R. Rüffer, A. Cornia and R. Sessoli, *Nat. Commun.*, 2018, **9**, 1–9.

(41) A. M. Ako, V. Mereacre, Y. Lan, C. E. Anson and A. K. Powell, *Chem. Eur. J.*, 2011, **17**, 4366–4370.

(42) V. Mereacre, D. Prodius, Y. Lan, C. Turta, C. E. Anson and A. K. Powell, *Chem. Eur. J.*, 2011, **17**, 123–128.

(43) A. Baniodeh, I. J. Hewitt, V. Mereacre, Y. Lan, G. Novitchi, C. E. Anson and A. K. Powell, *Dalton Trans.*, 2011, **40**, 4080–4086.

(44) V. Mereacre, A. Baniodeh, C. E. Anson and A. K. Powell, *J. Am. Chem. Soc.*, 2011, **133**, 15335–15337.

(45) V. Mereacre, *Angew. Chem. Int. Ed.*, 2012, **51**, 9922–9925.

(46) G. Abbas, Y. Lan, V. Mereacre, G. Buth, M. T. Sougrati, F. Grandjean, G. J. Long, C. E. Anson and A. K. Powell, *Inorg. Chem.*, 2013, **52**, 11767–11777.

(47) N. K. Kaushik, A. Mishra, A. Ali, J. S. Adhikari, A. K. Verma and R. Gupta, *J. Biol. Inorg. Chem.*, 2012, **17**, 1217–1230.

(48) G.-Y. Wu, X. Shi, H. Phan, H. Qu, Y.-X. Hu, G.-Q. Yin, X.-L. Zhao, X. Li, L. Xu, Q. Yu and H.-B. Yang, *Nat. Commun.*, 2020, **11**, 3178.

(49) J. Ren, X. Wei, R. Xu, Z. Chen, J. Wang, M. Wang, T. Sun, M. Wang and Y. Tang, *J. Mol. Struct.*, 2021, **1229**, 129783.

(50) C.-F. Lee, D. A. Leigh, R. G. Pritchard, D. Schultz, S. J. Teat, G. A. Timco and R. E. P. Winpenny, *Nature*, 2009, **458**, 314–318.

(51) X. Chen, S. Yeganeh, L. Qin, S. Li, C. Xue, A. B. Braunschweig, G. C. Schatz, M. A. Ratner and C. A. Mirkin, *Nano Lett.*, 2009, **9**, 3974–3979.

(52) C. Schouwey, M. Papmeyer, R. Scopelliti and K. Severin, *Dalton Trans.*, 2015, **44**, 2252–2258.

(53) P. Buchwalter, J. Rosé and P. Braunstein, *Chem. Rev.*, 2015, **115**, 28–126.

(54) D. Bansal, S. Pandey, G. Hundal and R. Gupta, *New J. Chem.*, 2015, **39**, 9772–9781.

(55) J.-J. Du, X. Zhang, X.-P. Zhou and D. Li, *Inorg. Chem. Front.*, 2018, **5**, 2772–2776.

(56) X.-R. Wu, S.-Y. Yao, L.-Q. Wei, L.-P. Li and B.-H. Ye, *Inorg. Chim. Acta*, 2018, **482**, 605–611.

(57) M. A. Alabdullah, A. R. Gomez, J. Vittenet, A. Bendjeriou-Sedjerari, W. Xu, I. A. Abba and J. Gascon, *ACS Catal.*, 2020, **10**, 8131–8140.

(58) L. Bogani and W. Wernsdorfer, *Nat. Mater.*, 2008, **7**, 179–186.

(59) J. M. Clemente-Juan, E. Coronado and A. Gaita-Ariño, *Chem. Soc. Rev.*, 2012, **41**, 7464–7478.

(60) D. Dong, *Philos. Mag.*, 2015, **95**, 2948–2954.

(61) S. V. Rao, J. M. Ashtree and A. Soncini, *Physica B*, 2020, **592**, 412237.

(62) D. Asthana, S. J. Lockyer, S. Nawaz, R. J. Woolfson, G. A. Timco, C. A. Muryn, I. J. Vitorica-Yrezabal, D. Collison, N. A. Burton and R. E. P. Winpenny, *Dalton Trans.*, 2021, **50**, 4390–4395.

(63) F.-S. Guo, B. M. Day, Y.-C. Chen, M.-L. Tong, A. Mansikkamaeki and R. A. Layfield, *Angew. Chem. Int. Ed.*, 2017, **56**, 11445–11449.

(64) P. Evans, D. Reta, G. F. Whitehead, N. F. Chilton and D. P. Mills, *J. Am. Chem. Soc.*, 2019, **141**, 19935–19940.

(65) J. D. Rinehart and J. R. Long, *Chem. Sci.*, 2011, **2**, 2078–2085.

(66) B. J. Holliday and C. A. Mirkin, *Angew. Chem. Int. Ed.*, 2001, **40**, 2022–2043.

(67) S. Leininger, B. Olenyuk and P. J. Stang, *Chem. Rev.*, 2000, **100**, 853–908.

(68) R. Chakrabarty, P. S. Mukherjee and P. J. Stang, *Chem. Rev.*, 2011, **111**, 6810–6918.

(69) T. N. Dais, M. J. Brown, M. P. Coles, F. Laur, J. R. Price, G. J. Rowlands and P. G. Plieger, *J. Incl. Phenom. Macrocycl. Chem.*, 2019, **94**, 175–182.

(70) R. W. Hogue, S. Dhers, R. M. Hellyer, J. Luo, G. S. Hanan, D. S. Larsen, A. L. Garden and S. Brooker, *Chem. Eur. J.*, 2017, **23**, 14193–14199.

(71) J. Hausmann, G. B. Jameson and S. Brooker, *Chem. Commun.*, 2003, 2992–2993.

(72) J. Hausmann and S. Brooker, *Chem. Commun.*, 2004, 1530–1531.

(73) X.-P. Zhou, J. Liu, S.-Z. Zhan, J.-R. Yang, D. Li, K.-M. Ng, R. W.-Y. Sun and C.-M. Che, *J. Am. Chem. Soc.*, 2012, **134**, 8042–8045.

(74) L. Qin, G.-J. Zhou, Y.-Z. Yu, H. Nojiri, C. Schroder, R. E. P. Winpenny and Y.-Z. Zheng, *J. Am. Chem. Soc.*, 2017, **139**, 16405–16411.

(75) A. Müller, L. Toma, H. Bögge, M. Schmidtmann and P. Kögerler, *Chem. Commun.*, 2003, 2000–2001.

(76) A. J. Tasiopoulos, A. Vinslava, W. Wernsdorfer, K. A. Abboud and G. Christou, *Angew. Chem. Int. Ed.*, 2004, **43**, 2117–2121.

(77) G. F. Whitehead, F. Moro, G. A. Timco, W. Wernsdorfer, S. J. Teat and R. E. Winpenny, *Angew. Chem. Int. Ed.*, 2013, **52**, 9932–9935.

(78) X. Lu, X. Li, Y. Cao, A. Schultz, J. Wang, C. N. Moorefield, C. Wesdemiotis, S. Z. Cheng and G. R. Newkome, *Angew. Chem. Int. Ed.*, 2013, **52**, 7728–7731.

(79) D. Liu, M. Chen, Y. Li, Y. Shen, J. Huang, X. Yang, Z. Jiang, X. Li, G. R. Newkome and P. Wang, *Angew. Chem. Int. Ed.*, 2018, **57**, 14116–14120.

(80) A. K. Gupta, P. V. Kishore, J.-Y. Cyue, J.-H. Liao, W. Duminy, W. E. van Zyl and C. Liu, *Inorg. Chem.*, 2021, **60**, 8973–8983.

(81) X.-Y. Zheng, Y.-H. Jiang, G.-L. Zhuang, D.-P. Liu, H.-G. Liao, X.-J. Kong, L.-S. Long and L.-S. Zheng, *J. Am. Chem. Soc.*, 2017, **139**, 18178–18181.

(82) S. G. Harris, Thesis, 1999.

(83) J. Wu, X.-L. Li, L. Zhao, M. Guo and J. Tang, *Inorg. Chem.*, 2017, **56**, 4104–4111.

(84) D. P. Goldberg, A. Caneschi and S. J. Lippard, *J. Am. Chem. Soc.*, 1993, **115**, 9299–9300.

(85) R. Sessoli, D. Gatteschi, A. Caneschi and M. A. Novak, *Nature*, 1993, **365**, 141.

(86) H. L. Feltham, R. Clérac and S. Brooker, *Aust. J. Chem.*, 2009, **62**, 1119–1123.

(87) T. L. Gianetti, G. Nocton, S. G. Minasian, N. Kaltsoyannis, A. D. Kilcoyne, S. A. Kozimor, D. K. Shuh, T. Tyliszczak, R. G. Bergman and J. Arnold, *Chem. Sci.*, 2015, **6**, 993–1003.

(88) S. Hazra, C. Rajnák, J. Titiš, M. F. C. Guedes da Silva, R. Boča and A. J. Pombeiro, *Molecules*, 2021, **26**, 1060.

(89) J. T. Henthorn, G. E. Cutsail, T. Weyhermüller and S. DeBeer, *Nat. Chem.*, 2022, 1–6.

(90) C. D. Bérubé, M. Yazdanbakhsh, S. Gambarotta and G. P. Yap, *Organometallics*, 2003, **22**, 3742–3747.

(91) C.-Y. Wang, B. Yu, H. Fu, P. Wang and C.-C. Wang, *Polyhedron*, 2019, **159**, 298–307.

(92) C. A. Gould, K. R. McClain, D. Reta, J. G. Kragskow, D. A. Marchiori, E. Lachman, E.-S. Choi, J. G. Analytis, R. D. Britt and N. F. Chilton, *Science*, 2022, **375**, 198–202.

(93) P. Langan, R. Robinson, P. J. Brown, D. Argyriou, D. Hendrickson and G. Christou, *Acta Cryst. C*, 2001, **57**, 909–910.

(94) S. Osa, T. Kido, N. Matsumoto, N. Re, A. Pochaba and J. Mrozinski, *J. Am. Chem. Soc.*, 2004, **126**, 420–421.

(95) C. M. Zaleski, E. C. Depperman, J. W. Kampf, M. L. Kirk and V. L. Pecoraro, *Angew. Chem. Int. Ed.*, 2004, **43**, 3912–3914.

(96) S. Akine, S. Sunaga, T. Taniguchi, H. Miyazaki and T. Nabeshima, *Inorg. Chem.*, 2007, **46**, 2959–2961.

(97) M. Yamamura, M. Sasaki, M. Kyotani, H. Orita and T. Nabeshima, *Chem. Eur. J.*, 2010, **16**, 10638–10643.

(98) S. Akine, S. Sunaga and T. Nabeshima, *Chem. Eur. J.*, 2011, **17**, 6853–6861.

(99) H. L. C. Feltham, Y. Lan, F. Kloewer, L. Ungur, L. F. Chibotaru, A. K. Powell and S. Brooker, *Chem. Eur. J.*, 2011, **17**, 4362–4365, S4362/1–S4362/9.

(100) H. L. C. Feltham, F. Kloewer, S. A. Cameron, D. S. Larsen, Y. Lan, M. Tropiano, S. Faulkner, A. K. Powell and S. Brooker, *Dalton Trans.*, 2011, **40**, 11425–11432.

(101) A. Yamashita, A. Watanabe, S. Akine, T. Nabeshima, M. Nakano, T. Yamamura and T. Kajiwara, *Angew. Chem. Int. Ed.*, 2011, **50**, 4016–4019.

(102) M. Yamamura, M. Iida, K. Kanazawa, M. Sasaki and T. Nabeshima, *Bull. Chem. Soc. Jpn.*, 2014, **87**, 334–340.

(103) H. Nagae, R. Aoki, S.-n. Akutagawa, J. Kleemann, R. Tagawa, T. Schindler, G. Choi, T. P. Spaniol, H. Tsurugi, J. Okuda and K. Mashima, *Angew. Chem. Int. Ed.*, 2018, **57**, 2492–2496.

(104) H. L. C. Feltham, R. Clerac, A. K. Powell and S. Brooker, *Inorg. Chem.*, 2011, **50**, 4232–4234.

(105) H. L. C. Feltham, R. Clerac, L. Ungur, V. Vieru, L. F. Chibotaru, A. K. Powell and S. Brooker, *Inorg. Chem.*, 2012, **51**, 10603–10612.

(106) H. L. C. Feltham, R. Clerac, L. Ungur, L. F. Chibotaru, A. K. Powell and S. Brooker, *Inorg. Chem.*, 2013, **52**, 3236–3240.

(107) S. Dhers, H. L. C. Feltham, R. Clerac and S. Brooker, *Inorg. Chem.*, 2013, **52**, 13685–13691.

(108) S. Dhers, H. L. C. Feltham, M. Rouzières, R. Clérac and S. Brooker, *Dalton Trans.*, 2016, **45**, 18089–18093.

(109) S. Dhers, H. L. C. Feltham, M. Rouzieres, R. Clerac and S. Brooker, *Inorg. Chem.*, 2019, **58**, 5543–5554.

(110) T. N. Dais, R. Takano, Y. Yamaguchi, T. Ishida and P. G. Plieger, *ACS Omega*, 2022, **7**, 5537–5546.

(111) H. L. C. Feltham, S. Dhers, M. Rouzieres, R. Clerac, A. K. Powell and S. Brooker, *Inorg. Chem. Front.*, 2015, **2**, 982–990.

(112) T. N. Dais, R. Takano, T. Ishida and P. Plieger, *Dalton Trans.*, 2022, **51**, 1446–1453.

(113) H. Asaba, T. Iwasaki, M. Hatazawa, J. Deng, H. Nagae, K. Mashima and K. Nozaki, *Inorg. Chem.*, 2020, **59**, 7928–7933.

(114) T. N. Dais, R. Takano, T. Ishida and P. G. Plieger, *RSC Advances*, 2022, **12**, 4828–4835.

(115) T. Nabeshima, H. Miyazaki, A. Iwasaki, S. Akine, T. Saiki, C. Ikeda and S. Sato, *Chem. Lett.*, 2006, **35**, 1070–1071.

(116) Computer Program, 2016.

(117) G. M. Sheldrick, *Acta Crystallogr. A*, 2015, **71**, 3–8.

(118) G. M. Sheldrick, *Acta Crystallogr. C*, 2015, **71**, 3–8.

(119) O. V. Dolomanov, L. J. Bourhis, R. J. Gildea, J. A. K. Howard and H. Puschmann, *J. Appl. Crystallogr.*, 2009, **42**, 339–341.

(120) S. H. M. Mehr, H. Depmeier, K. Fukuyama, M. Maghami and M. J. MacLachlan, *Org. Biomol. Chem.*, 2017, **15**, 581–583.

(121) J. R. Stevens and P. G. Plieger, *Dalton Trans.*, 2011, **40**, 12235–12241.

(122) D. N. T. De Silva, G. B. Jameson, A. P. S. Pannu, R. Pouhet, M. Wenzel and P. G. Plieger, *Dalton Trans.*, 2015, **44**, 15949–15959.

(123) S. S. Woodhouse, T. N. Dais, E. H. Payne, M. K. Singh, E. K. Brechin and P. G. Plieger, *Dalton Trans.*, 2021, **50**, 5318–5326.

(124) D. N. T. De Silva, T. N. Dais, G. B. Jameson, D. J. Cutler, E. K. Brechin, C. G. Davies, G. N. L. Jameson and P. G. Plieger, *ACS Omega*, 2021, **6**, 16661–16669.

(125) C. Lee, W. Yang and R. G. Parr, *Phys. Rev. B*, 1988, **37**, 785.

(126) S. Grimme, J. Antony, S. Ehrlich and H. Krieg, *J. Chem. Phys.*, 2010, **132**, 154104.

(127) S. Grimme, S. Ehrlich and L. Goerigk, *J. Comput. Chem.*, 2011, **32**, 1456–1465.

(128) D Ramarajan, K Tamilarasan, D Milenković, Z Marković, S Sudha and P Subhapriya, *J. Mol. Struct.*, 2019, **1195**, 73–84.

(129) M. Cossi, N. Rega, G. Scalmani and V. Barone, *J. Comput. Chem.*, 2003, **24**, 669–681.

(130) M. Hagemann, A. Mix, R. J. Berger, T. Pape and N. W. Mitzel, *Inorg. Chem.*, 2008, **47**, 10554–10564.

(131) A. In-Iam, M. Wolf, C. Wilfer, D. Schaniel, T. Woike and P. Klüfers, *Chem. Eur. J.*, 2019, **25**, 1304–1325.

(132) G. Savasci, M. Borges-Martínez, R. J. Berger, C. Ochsenfeld and R. Mera-Adasme, *J. Mol. Model.*, 2019, **25**, 1–8.

(133) M. Pinsky and D. Avnir, *Inorg. Chem.*, 1998, **37**, 5575–5582.

(134) D. Casanova, J. Cirera, M. Llunell, P. Alemany, D. Avnir and S. Alvarez, *J. Am. Chem. Soc.*, 2004, **126**, 1755–1763.

(135) R. Ketkaew, Y. Tantirungrotechai, P. Harding, G. Chastanet, P. Guionneau, M. Marchivie and D. J. Harding, *Dalton Trans.*, 2021, **50**, 1086–1096.

(136) Computer Program, 2005.

(137) A. Cornia, A. C. Fabretti, D. Gatteschi, G. Palyi, E. Rentschler, O. I. Shchegolikhina and A. A. Zhdanov, *Inorg. Chem.*, 1995, **34**, 5383–5387.

(138) M. Fondo, N. Ocampo, A. M. García-Deibe, J. Cano and J. Sanmartín, *Dalton Trans.*, 2010, **39**, 10888–10899.

(139) M. A. Lemes, G. Brunet, A. Pialat, L. Ungur, I. Korobkov and M. Murugesu, *Chem. Commun.*, 2017, **53**, 8660–8663.

(140) C. Janiak, *J. Chem. Soc., Dalton Trans.*, 2000, 3885–3896.

(141) X.-L. Li, F.-Y. Min, C. Wang, S.-Y. Lin, Z. Liu and J. Tang, *Inorg. Chem.*, 2015, **54**, 4337–4344.

(142) A. Dey, J. Acharya and V. Chandrasekhar, *Chem. Asian J.*, 2019, **14**, 4433–4453.

(143) R. Wang, H. Wang, J. Wang, F. Bai, Y. Ma, L. Li, Q. Wang, B. Zhao and P. Cheng, *CrystEngComm*, 2020, **22**, 2998–3004.

(144) G. A. Jeffrey, *An Introduction to Hydrogen Bonding*, Oxford university press New York, 1997, vol. 12.

(145) T. Steiner, *Angew. Chem. Int. Ed.*, 2002, **41**, 48–76.

(146) J. Titiˇs and R. Boca, *Inorg. Chem.*, 2010, **49**, 3971–3973.

(147) J. J. Borrás-Almenar, J. M. Clemente-Juan, E. Coronado and B. S. Tsukerblat, *Inorg. Chem.*, 1999, **38**, 6081–6088.

(148) J. J. Borrás-Almenar, J. M. Clemente-Juan, E. Coronado and B. S. Tsukerblat, *J. Comput. Chem.*, 2001, **22**, 985–991.

(149) J. Bartolomé, G. Filoti, V. Kuncser, G. Schinteie, V. Mereacre, C. E. Anson, A. K. Powell, D. Prodius and C. Turta, *Phys. Rev. B*, 2009, **80**, 014430.

(150) R. Sessoli and A. K. Powell, *Coord. Chem. Rev.*, 2009, **253**, 2328–2341.

(151) K. S. Cole and R. H. Cole, *J. Chem. Phys.*, 1941, **9**, 341–351.

(152) M. Andruh, I. Ramade, E. Codjovi, O. Guillou, O. Kahn and J. C. Trombe, *J. Am. Chem. Soc.*, 1993, **115**, 1822–1829.

(153) J.-P. Costes, F. Dahan, A. Dupuis and J.-P. Laurent, *Inorg. Chem.*, 2000, **39**, 169–173.

(154) T. Shimada, A. Okazawa, N. Kojima, S. Yoshii, H. Nojiri and T. Ishida, *Inorg. Chem.*, 2011, **50**, 10555–10557.

(155) R. Watanabe, K. Fujiwara, A. Okazawa, G. Tanaka, S. Yoshii, H. Nojiri and T. Ishida, *Chem. Commun.*, 2011, **47**, 2110–2112.

(156) P. Mahapatra, N. Koizumi, T. Kanetomo, T. Ishida and A. Ghosh, *New J. Chem.*, 2019, **43**, 634–643.

(157) T. Ishida, IOP Conf. Ser.: Mater. Sci. Eng. IOP Publishing, vol. 202, p. 012001.

(158) T. Kanetomo, T. Kihara, A. Miyake, A. Matsuo, M. Tokunaga, K. Kindo, H. Nojiri and T. Ishida, *Inorg. Chem.*, 2017, **56**, 3310–3314.

(159) R. D. Shannon, *Acta Crystallogr. C*, 1976, **32**, 751–767.

(160) T. Yamane, K. Sugisaki, H. Matsuoka, K. Sato, K. Toyota, D. Shiomi and T. Takui, *Dalton Trans.*, 2018, **47**, 16429–16444.

(161) B. Papánková, R. Boča, Dlháň, I. Nemec, J. Titiš, I. Svoboda and H. Fuess, *Inorg. Chim. Acta*, 2010, **363**, 147–156.

(162) G. Novitchi, S. Jiang, S. Shova, F. Rida, I. Hlavička, M. Orlita, W. Wernsdorfer, R. Hamze, C. Martins, N. Suaud, N. Guihéry, A.-L. Barra and C. Train, *Inorg. Chem.*, 2017, **56**, 14809–14822.

(163) J. Zhou, J. Song, A. Yuan, Z. Wang, L. Chen and Z.-W. Ouyang, *Inorg. Chim. Acta*, 2018, **479**, 113–119.

(164) L. Spillecke, S. Tripathi, C. Koo, A. Bahr, A. Swain, R. Haldar, M. Ansari, J. Jasinski, G. Rajaraman and M. Shanmugam, *Inorg. Chem.*, 2021.

(165) Y. Wu, J. Xi, T. Xiao, J. Ferrando-Soria, Z. Ouyang, Z. Wang, S. Luo, X. Liu and E. Pardo, *Inorg. Chem. Front.*, 2021, **8**, 5158–5168.

(166) Y. Zhao and D. G. Truhlar, *Phys. Chem. Chem. Phys.*, 2008, **10**, 2813–2818.

(167) T. Iwamoto, Y. Watanabe, H. Takaya, T. Haino, N. Yasuda and S. Yamago, *Chem. Eur. J.*, 2013, **19**, 14061–14068.

(168) R. W. Saalfrank, N. Löw, B. Demleitner, D. Stalke and M. Teichert, *Chem. Eur. J.*, 1998, **4**, 1305–1311.

(169) Q. Wang, C. Wilson, A. J. Blake, S. R. Collinson, P. A. Tasker and M. Schröder, *Tetrahedron Lett.*, 2006, **47**, 8983–8987.

DRC 16

MASSEY UNIVERSITY
TE KUNENGA KI PŪREHUROA
UNIVERSITY OF NEW ZEALAND

GRADUATE
RESEARCH
SCHOOL

STATEMENT OF CONTRIBUTION
DOCTORATE WITH PUBLICATIONS/MANUSCRIPTS

We, the candidate and the candidate's Primary Supervisor, certify that all co-authors have consented to their work being included in the thesis and they have accepted the candidate's contribution as indicated below in the *Statement of Originality*.

Name of candidate:	Tyson N. Dais
Name/title of Primary Supervisor:	Professor Paul G. Plieger
In which chapter is the manuscript /published work:	Chapter 3

Please select one of the following three options:

● The manuscript/published work is published or in press

- Please provide the full reference of the Research Output:

T. N. Dais, R. Takano, T. Ishida and P. G. Plieger. Self-assembly of non-macrocyclic Ni_3Ln clusters. *Dalton Trans.*, 2022, **51**, 1446-1453.

○ The manuscript is currently under review for publication – please indicate:

- The name of the journal:
- The percentage of the manuscript/published work that was contributed by the candidate:
- Describe the contribution that the candidate has made to the manuscript/published work:

○ It is intended that the manuscript will be published, but it has not yet been submitted to a journal

Candidate's Signature:	Tyson Dais
Date:	21 March 2022
Primary Supervisor's Signature:	Paul Plieger Digitally signed by Paul Plieger DN: cn=Paul Plieger, c=NZ, o=Massey University, ou=School of Fundamental Sciences, email=p.g.plieger@massey.ac.nz Date: 2022.03.22 11:44:23 +13'00'
Date:	22-Mar-2022

This form should appear at the end of each thesis chapter/section/appendix submitted as a manuscript/ publication or collected as an appendix at the end of the thesis.

GRS Version 5 – 13 December 2019
DRC 19/09/10

MASSEY UNIVERSITY
TE KUNENGA KI PŪREHUROA
UNIVERSITY OF NEW ZEALAND

GRADUATE RESEARCH SCHOOL

STATEMENT OF CONTRIBUTION
DOCTORATE WITH PUBLICATIONS/MANUSCRIPTS

We, the candidate and the candidate's Primary Supervisor, certify that all co-authors have consented to their work being included in the thesis and they have accepted the candidate's contribution as indicated below in the *Statement of Originality*.

Name of candidate:	Tyson N. Dais
Name/title of Primary Supervisor:	Professor Paul G. Plieger

In which chapter is the manuscript /published work: Chapter 4

Please select one of the following three options:

● The manuscript/published work is published or in press

- Please provide the full reference of the Research Output:

T. N. Dais, R. Takano, Y. Yamaguchi, T. Ishida and P. G. Plieger. Metallocyclic Cu^{II}-Ln^{III} single-molecule magnets from the self-assembly of 1,4-diformylnaphthalene-2,3-diol. *ACS Omega*, 2022, **7**(6), 5537-5546.

○ The manuscript is currently under review for publication – please indicate:

- The name of the journal:

- The percentage of the manuscript/published work that was contributed by the candidate:

- Describe the contribution that the candidate has made to the manuscript/published work:

○ It is intended that the manuscript will be published, but it has not yet been submitted to a journal

Candidate's Signature:	Tyson Dais
Date:	21 March 2022
Primary Supervisor's Signature:	Paul Plieger Digitally signed by Paul Plieger DN: cn=Paul Plieger, c=NZ, o=Massey University, ou=School of Fundamental Sciences, email=p.g.plieger@massey.ac.nz Date: 2022.03.22 11:46:48 +13'00'
Date:	22-Mar-2022

This form should appear at the end of each thesis chapter/section/appendix submitted as a manuscript/ publication or collected as an appendix at the end of the thesis.

GRS Version 5 – 13 December 2019
DRC 19/09/10

DRC 16

MASSEY UNIVERSITY
TE KUNENGA KI PŪREHUROA
UNIVERSITY OF NEW ZEALAND

GRADUATE RESEARCH SCHOOL

STATEMENT OF CONTRIBUTION
DOCTORATE WITH PUBLICATIONS/MANUSCRIPTS

We, the candidate and the candidate's Primary Supervisor, certify that all co-authors have consented to their work being included in the thesis and they have accepted the candidate's contribution as indicated below in the *Statement of Originality*.

Name of candidate:	Tyson N. Dais
Name/title of Primary Supervisor:	Professor Paul G. Plieger

In which chapter is the manuscript /published work: Chapter 5

Please select one of the following three options:

● The manuscript/published work is published or in press

- Please provide the full reference of the Research Output:

T. N. Dais, R. Takano, T. Ishida and P. G. Plieger. Lanthanide induced variability in localised Co^{II} geometries of four triangular $L_3Co_3^{II}Ln^{III}$ complexes. *RSC Advances*, 2022, **12**(8), 4828-4835.

○ The manuscript is currently under review for publication – please indicate:

- The name of the journal:

- The percentage of the manuscript/published work that was contributed by the candidate:

- Describe the contribution that the candidate has made to the manuscript/published work:

○ It is intended that the manuscript will be published, but it has not yet been submitted to a journal

Candidate's Signature:	Tyson Dais
Date:	21 March 2022
Primary Supervisor's Signature:	Paul Plieger Digitally signed by Paul Plieger DN: cn=Paul Plieger, c=NZ, o=Massey University, ou=School of Fundamental Sciences, email=p.g.plieger@massey.ac.nz Date: 2022.03.22 11:47:06 +13'00'
Date:	22-Mar-2022

This form should appear at the end of each thesis chapter/section/appendix submitted as a manuscript/ publication or collected as an appendix at the end of the thesis.